Spectral Characterization of Accelerator-Based Epithermal Neutron Beams for BNCT and BNCS Using Neutron Activation Foils

by

Laura Grace Murphy

B.S. Systems Engineering (1997)

United States Naval Academy

Submitted to the Department of Nuclear Engineering
in Partial Fulfillment of the Requirements for the Degree of
Master of Science in Radiation Health Physics

at the

Massachusetts Institute of Technology

February 1999

© 1999 Massachusetts Institute of Technology
All rights reserved.

Signature of Author.....
Department of Nuclear Engineering
January 22, 1999

Certified by .....
Jacquelyn C. Yanch
Associate Professor of Nuclear Engineering
Thesis Supervisor

Reviewed by .....
David W. Nigg
Idaho National Engineering and Environmental Laboratory
Thesis Reader

Accepted by.....
Lawrence M. Lidsky
Chairman, Department Committee on Graduate Studies

MASSACHUSETTS INSTITUTE OF TECHNOLOGY
WITHDRAWN
JUL 20 1999
FROM
MIT LIBRARIES
LIBRARIES

Science

Spectral Characterization of Accelerator-Based Epithermal Neutron Beams for BNCT and BNCS Using Neutron Activation Foils

by

Laura Grace Murphy

Submitted to the Department of Nuclear Engineering
on January 22, 1999 in partial fulfillment of the
requirements for the Degree of Master of Science in
Radiation Health Physics

ABSTRACT

Massachusetts Institute of Technology's Laboratory for Accelerator Beam Applications (MIT LABA) uses a tandem accelerator to create a number of epithermal neutron beams suitable for Boron Neutron Capture Therapy (BNCT) and Boron Neutron Capture Synovectomy (BNCS). The spectra of these epithermal neutron beams are currently modeled using Monte Carlo N-Particle Transport Code (MCNP) and had not previously been experimentally verified. This work experimentally measures the neutron spectra of the accelerator-based BNCT and BNCS beams at MIT LABA created by the 1.5 MeV Be(d,n) reaction using a neutron activation foil method adapted for BNCT applications by the Idaho National Engineering and Environmental Laboratory (INEEL). This method has been previously used to characterize reactor-based epithermal BNCT beams and proton-cyclotron-based fast neutron beams, but had not been used to characterize accelerator-based epithermal neutron beams prior to this work. The induced gamma-ray radioactivity of irradiated neutron activation foils is experimentally measured and then related to the neutron energy spectrum and yield using a closed-form direct unfolding method. While other methods have historically relied on "thin" foils to leave the neutron flux unperturbed, this method uses "thick" foils that significantly deplete the neutron flux within the primary absorption resonance peak. Coordinating the experimental measurements with MCNP simulation, the perturbed to unperturbed flux ratio is accounted for in the final unfolding matrix calculations. The INEEL activation foil method was found to be effective when applied to accelerator-based epithermal neutron beams for BNCT and BNCS. A detailed spectral characterization from thermal neutron energy to 0.5 keV and a coarse characterization of the fast neutron component of each beam were found. The spectral results compared favorably with the MCNP-calculated spectral shape, and an absolute measurement of the neutron yields of the BNCT and BNCS beams at MIT LABA was also made.

Thesis Supervisor: Jacquelyn C. Yanch

Title: Associate Professor of Nuclear Engineering

Table of Contents

1 Introduction 11
1.1 Boron Neutron Capture Therapy 11
1.2 Boron Neutron Capture Synovectomy 14
1.3 BNCT and BNCS Neutron Beams 15
1.3.1 Accelerator-based BNCT/BNCS Neutron Beams 17
2 Neutron Detection and Spectroscopy 21
2.1 Importance to BNCT/BNCS 21
2.2 Methods of Measuring Neutron Beams 23
2.2.1 Thermal 24
2.2.2 Epithermal and Fast 27
2.2.2.1 Neutron Moderation 28
2.2.2.2 Fast Neutron-Induced Reactions 29
2.2.2.3 Fast Neutron Scattering 30
2.2.2.4 Other Fast Neutron Spectroscopy Methods 31
2.3 Historical Use of Activation Foils 31
2.3.1 Thermal Neutron Detection 33
2.3.2 Fast Neutron Spectroscopy 35
2.3.3 Flux Perturbation Corrections 35
3 Methods and Materials 37
3.1 Spectral Characterization Concept 37
3.1.1 Epithermal Neutron Spectral Analysis 37
3.1.2 Direct Unfolding Concept for Activation Foil Data 39
3.2 Facility Description 42
3.2.1 MIT LABA Accelerator 43
3.2.2 BNCT Moderator/Reflector Assembly 44
3.2.3 BNCS Moderator/Reflector Assembly 46
3.3 Activation Foil Experiments 48
3.3.1 Selection of Activation Foil Materials 48
3.3.1.1 Irradiation Configuration in Foil Stacks 50
3.3.2 Determination of Foil Thickness 50
3.3.2.1 Criterion 1 – Linear Independence 51
3.3.2.2 Criterion 2 – Count Time 53
3.3.3 Experiment Layout 54
3.3.3.1 Foil Wheel Experiments 54
3.3.3.2 Boron Sphere Experiments 56
3.3.4 Counting 58
3.4 MCNP Simulation 59
3.4.1 Moderator/Reflector Models 60
3.4.2 Neutron Source Selection 63
3.4.3 Foil Wheel Model 73
3.4.4 Boron Sphere Model 74
3.4.5 Count Time Simulation Runs 75
3.4.6 Effective Cross Section Simulation Runs 76
3.4.6.1 Simulation Run #1 – Numerator 77

3.4.6.2 Simulation Run #2 – Denominator 78
3.4.7 Computer-Calculated Neutron Spectrum 79
4 Data Analysis and Results 81
4.1 Experiments 81
4.2 Reaction Rates 82
4.2.1 Reaction Rate Calculations 82
4.2.1.1 Decay Constant and Branching Ratio 83
4.2.1.2 Detector Efficiency 84
4.2.1.3 Foil Volume 87
4.2.1.4 Number Density 87
4.2.2 Uncertainty of Reaction Rate 87
4.2.2.1 Current-on-target Error 88
4.2.2.2 Counting Error 90
4.2.2.3 Decay Constant Error 90
4.2.2.4 Foil Volume Error 90
4.2.2.5 Detector Efficiency Error 91
4.2.2.6 Branching Ratio Error 91
4.2.3 BNCT Results 92
4.2.4 BNCS Results 95
4.3 MCNP Simulation 97
4.3.1 Full Range Method 97
4.3.2 Independent Point Method 99
4.3.3 Effective Cross Section Calculations and Results 101
4.3.3.1 Foil Thickness Error 101
4.3.3.2 Foil Placement Error 101
4.3.4 MCNP-calculated Neutron Spectra 102
4.4 Spectral Unfolding 107
4.4.1 Spectral Unfolding Calculations 108
4.4.2 Spectral Unfolding Errors 110
4.4.3 Computer Program 111
4.4.4 BNCT Results 112
4.4.5 BNCS Results 118
4.4.6 1.5 MeV Be(d,n) Yield Estimates 126
5 Conclusion and Future Work 137

Appendix A: Neutron Cross Sections of Foil Materials 141
Appendix B: Decay Scheme of Foil Materials 149
Appendix C: Measured Mass and Thicknesses of Foils 167
Appendix D: Detector Efficiency Fit Comparison 173
Appendix E: MCNP Input Files 177
Appendix F: Effective Cross Sections 195
Appendix G: MATLAB Computer Program 205

References 215

List of Figures

Figure 3-1: Layout of MIT LABA Facility 42
Figure 3-2: Tandem Electrostatic Accelerator at MIT LABA 43
Figure 3-3: BNCT Moderator/Reflector Assembly at MIT LABA 45
Figure 3-4: BNCS Moderator/Reflector Assembly at MIT LABA 47
Figure 3-5: $^{186}W(n,\gamma)$ Neutron Cross Section 49
Figure 3-6: Foil Stack Configuration 50
Figure 3-7: MCNP Simulation Geometry for Initial Determination of Foil Thickness 52
Figure 3-8: Foil Wheel Holder in Front of the BNCT Beam 55
Figure 3-9: Schematic of Foil Wheel with Foil Locations 56
Figure 3-10: Boron-10 Sphere. 57
Figure 3-11: Boron Sphere Holder in Front of the BNCT Beam 57
Figure 3-12: MCNP Model Cross Section of BNCT Moderator/Reflector Assembly 61
Figure 3-13: MCNP Model Cross Section of BNCS Moderator/Reflector Assembly 61
Figure 3-14: MCNP Model Cross Section of BNCT Moderator/Reflector Assembly with Variation Reduction Regions 63
Figure 3-15: The Effect of Different Source Spectra on the MCNP-Calculated Unperturbed Neutron Spectrum of the BNCT Beam 65
Figure 3-16: The Effect of Different Source Spectra on the MCNP-Calculated Unperturbed Neutron Spectrum of the BNCS Beam 67
Figure 3-17: Difference in the MCNP-Calculated Unperturbed Neutron Spectrum of the BNCT Beam as a result of using the Guzek Source Spectrum instead of the Whittlestone Source Spectrum 69
Figure 3-18: Difference in the MCNP-Calculated Unperturbed Neutron Spectrum of the BNCS Beam as a result of using the Guzek Source Spectrum instead of the Whittlestone Source Spectrum 71
Figure 3-19: MCNP Foil Wheel Model 73
Figure 3-20: MCNP Boron Sphere Model 74
Figure 3-21: MCNP Geometry Cross Section with BNCS Moderator/Reflector Assembly for Count Time Determination with 23 cm of Moderator 75
Figure 3-22: MCNP Geometry Cross Section with BNCT Moderator/Reflector Assembly for Count Time Determination 76
Figure 3-23: Geometry for MCNP-Calculated In-Air Unperturbed Neutron Spectra 79

Figure 4-1: MCNP-calculated Unperturbed Neutron Spectrum of the BNCT Beam at MIT LABA Using the Guzek Source Spectrum 103
Figure 4-2: MCNP-calculated Unperturbed Neutron Spectrum of the BNCS Beam at MIT LABA Using the Guzek Source Spectrum 105
Figure 4-3: Unperturbed Neutron Spectrum of the BNCT Beam at MIT LABA found by the Full Range Spectral Unfolding Method 113
Figure 4-4: Unperturbed Neutron Spectrum of the BNCT Beam at MIT LABA found by the Independent Point Spectral Unfolding Method 115
Figure 4-5: Unperturbed Neutron Spectrum of the BNCS Beam at MIT LABA found by the Full Range Spectral Unfolding Method 119

Figure 4-6: Unperturbed Neutron Spectrum of the BNCS Beam at MIT LABA found by the Independent Point Spectral Unfolding Method 121
Figure 4-7: Yield Estimate of 1.5 MeV Be(d,n) Reaction from Scaling the MCNP-calculated Unperturbed Neutron Spectrum of the BNCT Beam found from the Guzek Source Spectrum with the Measured Neutron Spectrum 127
Figure 4-8: Yield Estimate of 1.5 MeV Be(d,n) Reaction from Scaling the MCNP-Calculated Unperturbed Neutron Spectrum of the BNCT Beam found from the Whittlestone Source Spectrum with the Measured Neutron Spectrum 129
Figure 4-9: Yield Estimate of 1.5 MeV Be(d,n) Reaction from Scaling the MCNP-Calculated Unperturbed Neutron Spectrum of the BNCS Beam found from the Guzek Source Spectrum with the Measured Neutron Spectrum 131
Figure 4-10: Yield Estimate of 1.5 MeV Be(d,n) Reaction from Scaling the MCNP-Calculated Unperturbed Neutron Spectrum of the BNCS Beam found from the Whittlestone Source Spectrum with the Measured Neutron Spectrum 133

List of Tables

Table 1-1: Primary Thermal Neutron Reaction with Human Tissue in BNCT 13

Table 2-1: Common Thermal Neutron Detection Reactions..... 25
Table 2-2: Common Fast Neutron Spectroscopy Reactions 29

Table 3-1: Foil Materials and Interactions in the INEEL Neutron Activation Method..... 48
Table 3-2: Initial Estimate of Foil Thickness for Input into MCNP Simulations 52
Table 3-3: Foil Materials and Thicknesses Used for MIT LABA Experiments..... 54

Table 4-1: BNCT Experiments..... 81
Table 4-2: BNCS Experiments..... 81
Table 4-3: Decay Constants and Branching Ratios for Each Reaction. 83
Table 4-4: Errors in Measured Reaction Rates for the BNCT and BNCS Beams..... 92
Table 4-5: Un-normalized Volume-Averaged Reaction Rates per Atom for Foils Irradiated in the BNCT Beam at MIT LABA..... 93
Table 4-6: Normalized Volume-Averaged Reaction Rates per Atom per microAmp for Foils Irradiated in the BNCT Beam at MIT LABA. 94
Table 4-7: Un-normalized Volume-Averaged Reaction Rates per Atom for Foils Irradiated in the BNCS Beam at MIT LABA..... 95
Table 4-8: Normalized Volume-Averaged Reaction Rates per Atom per microAmp for Foils Irradiated in the BNCS Beam at MIT LABA. 96
Table 4-9: Selected Energy Regions for the Full Range Method. 98
Table 4-10: Selected Energy Regions for the Independent Point Method..... 100
Table 4-11: Errors in the Calculated Effective Cross Sections for the BNCT and BNCS Beams. 102
Table 4-12: Yield Estimates for the 1.5 MeV Be(d,n) Reaction. 107
Table 4-13: Thermal, Epithermal, Fast, and Total Neutron Flux of the BNCT Beam... 118
Table 4-14: Thermal, Epithermal, Fast, and Total Neutron Flux of the BNCS Beam... 124
Table 4-15: Yield Estimates of the 1.5 MeV Be(d,n) Reaction Including the MIT LABA Estimates Determined by Spectral Scaling. 135

1 Introduction

Accelerator-based Boron Neutron Capture Therapy (BNCT) and Boron Neutron Capture Synovectomy (BNCS) are being investigated at the Massachusetts Institute of Technology (MIT) Laboratory for Accelerator Beam Applications (LABA) [Yanch *et al.* 1992, Yanch *et al.* 1998]. MIT LABA uses a tandem electrostatic accelerator to bombard protons or deuterons at various energies onto a beryllium or lithium target, in conjunction with a moderator and reflector assembly, to produce epithermal neutron beams suitable for either BNCT or BNCS. The experimentally measured epithermal neutron spectra of these beams, using 1.5 MeV deuterons on a beryllium target, will be presented. An epithermal spectral characterization method using neutron activation foils adapted for BNCT applications by the Idaho National Engineering and Environmental Laboratory (INEEL) will be used. The INEEL method has been previously used to characterize reactor-based epithermal neutron [Harker *et al.* 1992, Nigg *et al.* 1997] and cyclotron-based fast neutron beams [Nigg *et al.* 1998], but the experiments presented in this paper represent the first application of the method in its current form to accelerator-based epithermal neutron beams.

1.1 Boron Neutron Capture Therapy

Boron Neutron Capture Therapy (BNCT) is an experimental cancer treatment combining boron and thermal neutrons to preferentially kill tumor cells within healthy tissue. BNCT is primarily targeted at inoperable tumors or tumors that can be difficult to treat with conventional radiation therapy, such as some forms of brain tumors [Zamenhof *et al.* 1975]. The BNCT concept was originally clinically examined in the

1950's; however, initial clinical trials demonstrated unexpected and unacceptable late radiation effects [Slatkin 1991]. After achievements in improving neutron beam delivery and tumor-seeking boron compounds, BNCT is currently being reexamined in clinical trials in the United States at MIT and Brookhaven National Laboratory [Zamenhof *et al.* 1997, Capala *et al.* 1997] and in Europe at Petten [Sauerwein *et al.* 1998] using epithermal neutron beams.

The BNCT concept relies on the synergistic combination of thermal neutrons and boron compounds within a tumor. Thermal neutrons and boron, on the order used in BNCT, do not cause significant damage by themselves, but when combined inside a tumor, tumor killing can result as result of $^{10}B(n,\alpha)$ reactions. In BNCT treatment, a boron compound is systemically administered to the patient by injection or orally [Zamenhof *et al.* 1997]. These compounds are designed to preferentially build up in tumor cells while remaining in lower concentrations in healthy tissue. After administration of the boron compound, the patient is irradiated so that thermal neutrons are delivered to the tumor region.

Thermal neutrons interact with tissue elements through elastic scattering and absorption reactions. However, since the energies of thermal neutrons are generally considered to be below 0.5 eV, elastic scattering does not contribute significantly to tissue nor tumor dose because of the small amount of energy transferred to the recoil nuclei [Turner 1995]. The principle elemental constituents of tissue include hydrogen, carbon, nitrogen, and oxygen; BNCT also introduces boron into tissue. The primary neutron reactions with these elements, which were determined by examining their thermal neutron absorption cross sections, are shown in Table 1-1.

Table 1-1: Primary Thermal Neutron Reactions with Human Tissue in BNCT [Turner 1995].

Reaction	Reaction Products	Q-Value	Thermal Neutron Cross Section
^{1}H(n,γ)	${}_1^1H+{}_0^1n\rightarrow{}_1^2H+{}_0^0\gamma$	2.22 MeV	0.33 barns
^{14}N(n,p)	${}_7^{14}N+{}_0^1n\rightarrow{}_6^{14}C+{}_1^1H$	0.626 MeV	1.70 barns
^{10}B(n,α)	${}^{10}B+{}_0^1n\rightarrow\begin{cases}{}_3^7Li+{}_2^4\alpha & (7\%)\\ {}_3^7Li^*+{}_2^4\alpha+{}_0^0\gamma & (93\%)\end{cases}$	2.8 MeV	3840 barns

The neutron absorption in hydrogen and nitrogen are the predominant thermal neutron reactions in normal soft tissue. The energy released by hydrogen absorption (2.22 MeV) is carried by a gamma-ray and is deposited outside of the local tissue [Turner 1995]. The energy released by nitrogen absorption (0.626 MeV) is distributed between the kinetic energy of the ^{14}C nucleus and the proton and is deposited locally within 100 μm [Turner 1995]. These reactions occur in all soft tissue irradiated by thermal neutrons.

When boron is preferentially added to tissue in BNCT, the ^{10}B neutron capture is the key reaction. The thermal neutron cross section local energy deposition of the boron capture reaction is significantly higher than normal soft tissue reactions. The ^{7}Li and α particles will deposit all of their energy locally, within 10 μm [Yanch *et al.* 1992]. Therefore, if the boron compound delivered to the patient is successful in preferentially loading the tumor cells with boron, the tumor cells will receive much higher doses than the surrounding normal tissue, even though both are being irradiated by thermal neutrons. The current BNCT clinical trials being conducted at the MIT reactor inject the compound boronophenyalaline (BPA) prior to irradiation [Busse *et al.* 1997]. Using BPA, a boron uptake ratio of approximately 3.5 to 1 is found between tumor and blood [Joel *et al.* 1997]. Damage to healthy tissue can be spared while enough dose is

delivered to the tumor to cause reproductive cell death, based on neutron beam design. A detailed discussion of neutron beam design for BNCT is presented in Section 1.3.

1.2 Boron Neutron Capture Synovectomy

Boron Neutron Capture Synovectomy (BNCS) is an application of the BNCT concept to treat rheumatoid arthritis. This application was first suggested by Yanch in 1994 [Johnson *et al.* 1996] and is currently being investigated through animal trials at MIT LABA in collaboration with Brigham and Women's Hospital and Newton Scientific Incorporated [Yanch *et al.* 1998].

Rheumatoid Arthritis (RA) is an autoimmune disease suffered by approximately 1-3% of the adult population in the United States. RA can affect many organs, but in most patients the disease manifests itself as swollen, inflamed, and painful joints, such as the knees. The inflammation occurs in the membrane (synovium) lining articular joints. The cause of the inflammation is unknown. Left untreated, chronic RA leads to destruction of cartilage, ligaments, and bone. The primary treatment for RA is the administration of various drugs to reduce the inflammation of the synovium. However, one or more joints remain unresponsive to the primary treatment in approximately 10% of the affected population. The remaining treatment for these patients is the physical removal of the inflamed synovium (synovectomy). Even after synovectomy, the synovium will eventually fully regenerate and become inflamed again. This is because synovectomy is a treatment of the symptoms of RA and not the cause [Yanch *et al.* 1998].

Surgical synovectomy has shown symptomatic pain relief for 2-5 years; after which, further treatment is necessary. Radiation synovectomy has also been tried. This non-invasive method uses short-lived beta-emitting radionuclides that are injected

directly into the joint to kill the synovial tissue. Radiation synovectomy has had a success rate of up to 80% and also shows pain relief for 2-5 years [Gumpel and Roles 1975, Symposium 1973, Oka 1975, Deckart *et al.* 1979]. Radiation synovectomy has many advantages over surgery, including the elimination of rehabilitation time, reduction in cost and treatment time, and the use of local instead of general anesthesia [Yanch *et al.* 1998]. Radiation synovectomy is widely used in Europe, Australia, and Canada, but concerns over healthy tissue dose caused by leakage of the radionuclides out of the joint has limited its use in the United States [Yanch *et al.* 1998].

Boron Neutron Capture Synovectomy maintains the advantages of radiation synovectomy but avoids the problems caused by radionuclide leakage. Using the same concept in BNCT, a non-radioactive boron compound is injected directly into the joint, and the joint is then irradiated with thermal neutrons. The desire is to produce functional cell death in the synovium by taking advantage of the $^{10}B(n,\alpha)$ reaction. BNCS requires considerably more radiation dose then BNCT because treatment of tumors only requires reproductive cell death. This can be obtained by delivering larger boron concentrations to the target tissue compared to BNCT through direct rather than systemic injection, as suggested by the research to date conducted at MIT LABA [Johnson 1994, Johnson *et al.* 1996, Binello *et al.* 1997a, Binello *et al.* 1997b, Binello *et al.* 1997c, Yanch *et al.* 1998].

1.3 BNCT and BNCS Neutron Beams

The delivery of thermal neutrons to the boron-containing tissue (tumor or synovium) is as important to the effectiveness of the BNCT and BNCS as the preferential uptake of the boron compound. If the target tissue is located at the skin

surface, an external thermal neutron beam can be used to treat the tissue. However, since the target tissue is normally located at depth within healthy tissue, the attenuation and moderation of the neutron beam through soft tissue must be taken into account. The neutron beam is attenuated predominantly by elastic scatter, followed by thermal interactions in $^{1}H(n,\gamma)$ and $^{14}N(n,p)$ reactions, as shown in Table 1-1. In order to deliver a thermal neutron beam deeper within tissue, a slightly higher energy (epithermal) external neutron beam is required. As an epithermal neutron beam travels through soft tissue, the beam energy is moderated primarily through elastic scattering with hydrogen producing a high thermal neutron flux at a given depth within the tissue. An increase in neutron energy increases the depth at which the thermal flux is delivered. However, at higher beam energies, fast neutron collisions with hydrogen produce recoil protons that deposit high doses to surface tissue. Fast neutron dose can be unacceptable and is taken into account when designing optimal neutron beams [Yanch *et al.* 1992].

External neutron beams used for BNCT and BNCS contain a spectrum of thermal, epithermal, and fast neutrons. Optimal beam design aims to reduce the surface tissue dose while maintaining a high epithermal neutron flux to allow acceptable treatment times.

The optimal neutron beams for BNCT and BNCS are considerably different. BNCT focuses on brain tumors that are embedded within several centimeters of healthy brain tissue. Ideal BNCT beam studies by Yanch *et al.* found that neutron beam energies from 4 eV - 40 keV can deliver a therapeutic gain when treating brain tumors at the midline of the brain (approximately 7.5 cm from the skin surface) [Yanch *et al.* 1991a]. Conversely, BNCS focuses on synovium, which is much closer to the surface (0.5-1.5

cm below the skin surface) [Yanch *et al.* 1998]. Binello *et al.* reports that neutron energies from 0.025 eV to approximately 0.5 or 1.0 keV are optimal for BNCS [Binello *et al.* 1997a].

Currently, the neutron beams used for human BNCT trials are produced from nuclear reactors. If BNCT is proven effective in the current clinical trials, hospitals must have a suitable neutron source available for treatment of patients. Widespread use of reactors is considered untenable for the vast majority of hospitals. A more deployable neutron source is necessary for the widespread use of BNCT or BNCS in the future. Accelerators have been suggested as a viable alternative to reactors as neutron-producing sources [Wang *et al.* 1989, Grusell *et al.* 1990, Shefer *et al.* 1990, Wang *et al.* 1990, Shefer *et al.* 1991, Yanch *et al.* 1991a].

1.3.1 Accelerator-based BNCT/BNCS Neutron Beams

Accelerators can be used to produce neutron beams by bombarding charged particles onto a target material that will produce neutrons of various energies. Reactors have the advantage of high neutron fluxes; therefore, accelerator reactions must be able to produce adequately high neutron fluxes to maintain treatment times comparable to reactors. The most common reactions being examined are Li(p,n), Be(p,n), and Be(d,n), by accelerating protons and/or deuterons onto a lithium or beryllium target [Yue *et al.* 1997]. For reasonable treatment times using the Li(p,n) reaction, it is suggested by Shefer *et al.* that an accelerator must be able to put 4 mA - 30 mA of current on target with particle energies ranging from 2-4 MeV [Shefer *et al.* 1994].

Several accelerator types have been examined for use in producing adequate BNCT beams, including electrostatic accelerators, radio frequency quadrupole (RFQ)

accelerators, and electrostatic quadrupole (ESQ) accelerators. MIT LABA uses a tandem electrostatic accelerator which has advantages over other accelerators because the beam energy and current are continuously tunable over a large range, and the current is continuously delivered to the target rather than in pulses as with RFQ's and ESQ's. Tandem electrostatic accelerators can also operate at higher acceleration gradients, and have very high electrical power efficiency with modest cooling requirements. This allows tandem accelerators to be more compact and minimizes facility modifications and operating costs [Shefer *et al.* 1994]. Details on the specifications of the tandem accelerator at MIT LABA are discussed in Section 3.2.1.

The Li(p,n), Be(p,n), and Be(d,n) reactions produce a spectrum of neutrons at high energies, and are not optimal by themselves for BNCT or BNCS. For example, the maximum neutron energy produced from the 2.5 MeV Li(p,n) reaction is 800 keV (at 0^0), with the neutron spectrum peaking at approximately 550 keV (at 0^0) [Yanch *et al.* 1992]. Each neutron beam must be moderated using materials with high scattering cross sections to create a suitable beam. A reflector material is also used to reflect neutrons back into the moderator to reduce the loss of neutron flux during moderation. Experimental verification of the neutron beam characteristics after moderation and reflection is done through various methods.

This thesis describes the method and results of epithermal spectral measurements using neutron activation foils on the BNCT and BNCS beams at MIT LABA. Chapter 2 discusses traditional neutron measurement techniques and their limitations in measuring the neutron spectrum in the epithermal region. Chapter 3 presents the experimental and computational methods and materials used in the spectral

measurements on the BNCT and BNCS beams at MIT LABA, based on the INEEL neutron activation foil method. Chapter 4 presents and discusses the results of the experimental measurements, and Chapter 5 is an overall conclusion on the effectiveness of applying the INEEL neutron activation foil method to the spectral characterization of accelerator-based epithermal neutron beams.

2 Neutron Detection and Spectroscopy

2.1 Importance to BNCT/BNCS

As mentioned in the Chapter 1, a moderator/reflector assembly must be designed to reduce a neutron beam's energy to energies suitable for BNCT or BNCS. The optimal design of the moderating assembly is done primarily through computer simulation codes such as Monte Carlo N-Particle Transport Code (MCNP) [Briesmeister 1997]. This code calculates the transport of neutrons, photons, and electrons through various materials described in a model geometry. The optimization of the beam through different types and sizes of moderator and reflector materials for the BNCT and BNCS beams at MIT LABA was conducted by using MCNP to calculate the expected dose at various depths in a brain phantom or knee model [Yanch *et al.* 1992, Binello *et al.* 1997d, Gierga *et al.* 1999].

An experimentally-determined dose characterization of the BNCT beam at MIT LABA, using the 1.5 MeV Be(d,n) reaction, was conducted by White to verify the MCNP-predicted dose characterization for that beam[1] [White 1998]. The dual ionization chamber method was used to measure the neutron and photon doses at various depths inside a human brain phantom filled with water. Gold activation foils were also used to measure the thermal neutron dose rate. The experimental results were then compared to the expected results determined by MCNP. These results showed that after

[1] These measurements were not conducted to verify the MCNP-determined optimization of the BNCT moderator/reflector assembly, because this assembly was originally designed for the 2.5 MeV Li(p,n) reaction, not the 1.5 MeV Be(d,n) reaction [Yanch *et al.* 1992]. Optimization of the BNCT beam for the 1.5 MeV Be(d,n) reaction is currently being investigated by White.

matching the thermal neutron dose rate with MCNP, the measured fast neutron dose rate was approximately 50% lower than expected from MCNP [White 1998].

An experimentally determined dose characterization of the BNCS beam at MIT LABA, using the 1.5 MeV Be(d,n) reaction, was conducted using the same method[2] [Gierga 1999]. A brain phantom filled with water was used instead of an anatomically realistic knee phantom. This was done because ionization chambers small enough for accurate measurements within the small knee phantom were not available. Again, there were inconsistencies between the measured and MCNP-predicted dose rates. These results showed that although the experimental and simulated thermal neutron dose rates matched, the measured fast neutron dose rate was approximately 75% lower than expected from MCNP [Gierga 1999].

The inconsistencies between the dose rate measurements and simulation results can be due to experimental errors that are specific to the ionization chambers, but another explanation is that the actual neutron spectrum of each beam is not consistent with the MCNP-predicted spectrum [White 1998]. The dose characterization methods do not measure or verify the neutron spectra of the BNCT or BNCS beams. These methods only verify the effects of the neutrons by measuring the dose due to the thermal neutron interactions, fast neutron interactions, and related photons.

A direct experimental measurement of the BNCT and BNCS neutron spectra at MIT LABA is presented in this paper. Spectral characterization of these beams is

[2] These measurements also were not conducted to verify the MCNP-determined optimization of the BNCS moderator/reflector assembly, because this assembly was originally designed for the 2.5 MeV Li(p,n) or 4.0 MeV Be(p,n) reaction, not the 1.5 MeV Be(d,n) reaction [Binello *et al.* 1997a].

important for direct experimental verification of the neutron spectra, MCNP models, and simulations results for the BNCT and BNCS beams at MIT LABA. Difference in the experimentally-measured and MCNP-predicted neutron spectra can be used to determine inaccuracies in the MCNP dose rate simulations used for the BNCT and BNCS beams. Sources of these inaccuracies could be found in the geometric models used for the BNCT and BNCS moderator/reflector assemblies, the neutron interaction cross sections, or the neutron source spectrum used for the 1.5 MeV Be(d,n) reaction. The spectral measurements for the BNCT and BNCS beams should include a measurement of the total thermal and fast neutron fluxes and a more detailed spectral characterization of the epithermal region. Different methods of measuring neutron beams are discussed in the following sections.

2.2 Methods of Measuring Neutron Beams

In most conventional radiation detectors, radiation interaction with the active detector volume causes the appearance of a certain amount of electric charge. This electric charge is collected by the detector by various means and is related to the amount and/or type of radiation interacting with the detector. In some cases, the electric charge can be related to the energy of the incident radiation; this is called spectroscopy. Charged particle radiation can directly create an electric charge in a detector; however, neutral radiation, such as neutrons and photons, must first be converted into charged radiation, such as protons, alpha particles, electrons, etc., which can then produce the electric charge. Generally, neutrons are converted through interactions with target materials that have high neutron interaction cross sections.

Since cross sections can vary drastically with neutron energy, many different neutron detection techniques have been developed for different energy regions.

The neutron energy spectrum is generally broken into two regions: slow and fast; an intermediate or epithermal neutron region is also sometimes distinguished. The energy boundaries of these regions are often arbitrary and depend on the application. For the purposes of measuring the spectra of BNCT or BNCS beams, the epithermal region is extremely important. The BNCT/BNCS epithermal region is generally taken to be between 0.5 eV and 10 keV [Harker *et al.* 1992], consistent with the definition given by the U.S. National Institute of Standards and Technology (NIST). This paper will use these boundaries for the epithermal region and will refer to the neutrons with energies below 0.5 eV as thermal (slow) neutrons and neutrons with energies above 10 keV as fast neutrons. The following sections will describe traditional techniques for neutron detection and/or spectroscopy in each of these regions.

2.2.1 Thermal

The most common reactions used to detect neutrons in the thermal region are neutron absorption reactions that produce heavy charged particles such as protons, alpha particles, fission fragments, and recoil nuclei. The selected conversion reactions are exothermic and have Q-values in the few MeV range. The Q-value directly determines the amount of kinetic energy the heavy charged particles receive in each reaction. A high Q-value is important because it allows simple detector discrimination between the heavy charged particles and photons, which are often also produced after these reactions [Knoll 1989]. However, a high Q-value also provides such high kinetic energy to the reaction products that the relatively small difference in the neutrons'

energies in the thermal region can not be reflected in the final kinetic energy of the reaction products. In other words, the energy of the incident thermal neutron can not be determined using these reactions. Three methods of thermal neutron spectroscopy are time-of-flight measurements, crystal spectrometers, and mechanical monochromators [Knoll 1989, Krane 1988]. These methods are examined later in the section.

Table 2-1 Common Thermal Neutron Detection Reactions [Knoll 1989, Krane 1988].

Reaction	Reaction Products	Q-value	Thermal Neutron* Cross Section
^{10}B(n,α)	$^{10}B+{}_0^1n \rightarrow \begin{cases} {}_3^7Li+{}_2^4\alpha \quad (7\%) \\ {}_3^7Li^*+{}_2^4\alpha+{}_0^0\gamma \ (93\%) \end{cases}$	2.8 MeV	3840 barns
^{6}Li(n,α)	${}_3^6Li+{}_0^1n \rightarrow {}_1^3H+{}_2^4\alpha$	4.78 MeV	940 barns
^{3}He(n,p)	${}_2^3He+{}_0^1n \rightarrow {}_1^3H+{}_1^1p$	0.764 MeV	5330 barns
^{233}U(n,f) ^{235}U(n,f) ^{239}Pu(n,f)	$^{233}U \text{ or } ^{235}U \text{ or } ^{239}Pu + {}_0^1n \rightarrow$ various fission fragments	~160 MeV	530 barns 584 barns 742 barns

* The thermal neutron cross section is for neutrons with an energy of 0.025 eV.

The reactions in Table 2-1 are commonly used in the following detectors: BF_3 proportional counters, lithium-containing scintillators, ^{3}He proportional counters, and fission ionization chambers [Knoll 1989].

The above techniques are active ways of detecting thermal neutrons, one passive method has not been mentioned--neutron activation foils. The response of the active detectors is displayed immediately and can detail any changes in magnitude of the thermal flux. In spectral characterization of BNCT and BNCS beams where the neutron spectrum is kept constant, an immediate response is not needed; therefore, a passive detection method such as neutron activation foils can be used. Neutron activation foils can not only be used for thermal neutron detection, but they can also be

used for spectral measurements of higher energy neutrons. A complete description of activation foil methods is presented in Section 2.3.

The energy of the thermal neutrons can be measured by mechanical monochromators, time-of-flight measurements, and crystal diffraction. Mechanical monochromators use a rotating cylinder, made of a material with a high absorption cross section for thermal neutrons, with one or more helical slots cut into its surface [Krane 1988]. Only neutrons of a certain energy (velocity) will pass through the rotating cylinder based on the length of the cylinder and the angle that it is rotated, creating a monochromatic neutron beam. Changing the rotational velocity of the cylinder allows the selection of different neutron energies. A second method of neutron detection is then needed to measure the amount of neutrons at each energy. Mechanical monochromators are only practical for neutrons in the thermal energy region. This is because the cylinder is made of a material that has a cross section designed to stop thermal neutron passage except through the helical slots; this material would not be effective in stopping epithermal and fast neutrons. In addition, the energy selection is limited to the thermal region by the size and velocity of the cylinder.

The time-of-flight technique can also be used to determine the energy of neutrons in the thermal region by measuring their velocity. By passing the neutron beam in a short pulse, the time it takes for slow neutrons to travel over a few meters can be easily measured. A neutron of 0.025 eV has a velocity of 2200m/s; therefore, it takes 10^{-3}sec to travel 2.2 meters [Krane 1988]. Measurements of neutrons in the epithermal and fast region using this method are achievable but with some limitations, as discussed in Section 2.2.2.4.

Crystal diffraction gives very precise energy measurements in the thermal region. A de Broglie wavelength of 0.1 nm corresponds to neutrons in the thermal region and is about the same as the typical atomic spacing in a crystal lattice. If a polyenergetic neutron beam interacts with a selected crystal at a certain angle, the reflected neutron beam will be monoenergetic. If the incident angle of the neutron beam is changed slightly, the energy of the reflected monoenergetic beam will also change slightly. Similar to the mechanical monochromator, a separate neutron detector is needed. Spectroscopy of epithermal and fast neutrons can not be achieved by crystal diffraction, because energy selection is limited by the range of incident angles with the crystal. This limits the selected energies to slightly higher and lower than thermal neutron energy that corresponds to the atomic spacing of the crystal [Krane 1988].

2.2.2 Epithermal and Fast

The same reactions used to convert thermal neutrons to charged particles can be theoretically used to convert fast neutrons; however, the cross sections of these reactions decrease considerably with neutron energy, and generally make the detector efficiency too small. Therefore, different conversion methods are examined for better detector efficiency. The most important additional conversion method for fast neutrons is elastic scattering [Knoll 1989]. Neutrons collide with nuclei and transfer some of their kinetic energy to the recoil nuclei. For neutrons with energies in or above the keV range, the recoil nucleus is energetic enough to be directly detected with adequate efficiency.

Fast neutron spectroscopy is also achievable. The energy of thermal neutrons could not be determined using the traditional neutron capture reactions because the low

energy of the incident neutrons was lost in the conversion due to high Q-values. When neutrons reach energies of 10-100 keV and above, their energy is no longer negligible compared to the Q-value and can be measured. Alternatively, elastic scattering reactions have Q-values equal to zero, and once the energies of the recoil nuclei are measurable, fast neutron spectroscopy techniques can be applied [Knoll 1989].

The methods used for fast neutron detection and spectroscopy are broken into three categories by Knoll: 1) detectors based on neutron moderation, 2) detectors based on fast neutron-induced reactions, and 3) detectors that utilize fast neutron scattering [Knoll 1989].

2.2.2.1 Neutron Moderation

Slow neutron detectors (such as described in the Section 2.2.1) can be used to detect fast neutrons by surrounding the detector with a moderating material. The moderating material, generally containing a high concentration of hydrogen, reduces the energy of the fast neutrons as they undergo elastic scattering with the hydrogen nuclei in the moderator. The efficiency of thermal neutron detectors increases with decreasing neutron energy. Increasing the thickness of the moderator decreases the energy of the neutrons that pass through it, but at the same time, it reduces the probability that the neutrons will escape the moderator and reach the detector. Using polyethylene or paraffin as moderating materials, the optimal moderator thickness ranges from a few centimeters for incident keV neutrons to tens of centimeters for incident MeV neutrons [Knoll 1989]. The shape and diameter of these types of detectors are designed so that the detector efficiency response versus neutron energy tends to maximize at a specific energy.

Bonner spheres are classic detectors that apply this moderation concept. Bonner spheres use lithium iodide scintillators inside polyethylene spheres of many different diameters. Each sphere diameter has a different response curve. By measuring the response of each sphere to the same neutron beam, the neutron beam spectrum can be found through unfolding techniques. However, this application is limited because the response curves are rather broad. In addition, below 100 keV, direct measurements of the detector efficiency were difficult [Knoll 1989], making this spectroscopy method specifically unsuitable for the BNCT/BNCS epithermal region.

2.2.2.2 Fast Neutron-Induced Reactions

Table 2-2 Common Fast Neutron Spectroscopy Reactions [Knoll 1989].

Reaction	Reaction Products	Q-value	Fast Neutron* Cross Section
^{6}Li(n,α)	${}_3^6Li+{}_0^1n\rightarrow{}_1^3H+{}_2^4\alpha$	4.78 MeV	0.25 barns
^{3}He(n,p)	${}_2^3He+{}_0^1n\rightarrow{}_1^3H+{}_1^1p$	0.764 MeV	0.9 barns

* The fast neutron cross section is for neutrons with an energy of 1 MeV.

The ^{6}Li(n,α) and ^{3}He(n,p) reactions, described in Table 2-2, are common methods for fast neutron spectroscopy. As mentioned earlier, incident neutron energies above 10-100 keV are no longer negligible compared to the Q-value and can be measured. The only limitation is that the fast neutron cross sections are considerably smaller than the thermal neutron cross sections [Knoll 1989].

Typical lithium detectors used for fast neutron spectroscopy are the lithium iodide scintillator and the lithium sandwich spectrometer [Knoll 1989]. However, these two detectors are not suitable for spectroscopy below 100 keV because lower energies are no longer measurable. Therefore, these spectrometers can not be used in the epithermal region.

Typical helium detectors used for fast neutron spectroscopy are the ^{3}He proportional counter, ^{3}He gridded ionization chamber, ^{3}He scintillator, and the ^{3}He semiconductor sandwich spectrometer [Knoll 1989]. These spectrometers are also not suitable for the BNCT/BNCS epithermal region because only neutron energies above 10 keV are measurable for this reaction.

Not all of the reactions in Table 2-1 are viable for the fast neutron region. The $^{10}B(n,\alpha)$ reaction is suitable for thermal neutron detection but not suitable for fast neutrons, because the reaction cross section is too small at high neutron energies. Fission reactions can be used for fast neutron detection, but because the Q-value is so high, the fast neutron energies are still negligible, and spectroscopy is not possible [Knoll 1989].

2.2.2.3 Fast Neutron Scattering

The most common technique for fast neutron spectroscopy is based on elastic scattering [Knoll 1989]. Neutrons collide with nuclei and transfer some of their energy to the recoil target nuclei. The most popular target material is hydrogen; the recoil nuclei from scattering off of hydrogen are called recoil protons. This collision is the basis of the fast neutron spectroscopy method called proton recoil. The Q-value of elastic scattering is zero; therefore, the sum of the kinetic energies of the recoil nuclei and neutron is the same as the incident neutron. The amount of energy transferred to the recoil proton in scattering off of hydrogen can range from zero to the total energy of the incident neutron. The average energy of the recoil proton is half of the initial neutron energy. The proton recoil process can occur inside either hydrogenous scintillation materials or gas recoil proportional counters. Below neutron energies of

100 keV, it becomes more difficult to detect fast neutrons in the presence of gamma rays using the proton recoil method. Addressing this problem, specialized proton recoil detectors have been designed, which can be used to measure neutrons as low as 1 keV; however, this is still not acceptable for spectral analysis of the entire epithermal region, and complicated equipment and calibration methods are required [Knoll 1989].

2.2.2.4 Other Fast Neutron Spectroscopy Methods

Time of flight measurements mentioned in Section 2.2.1 can be used for neutron spectroscopy in the epithermal and fast neutron regions. However, as the neutron energy increases, the distance over which the time of flight is measured must also be increased [Krane 1988]. A neutron of 100 eV has a velocity of 138315m/s; therefore, it takes 10^{-3} sec to travel 138 meters. To cover the entire epithermal region, this method would require an unacceptably large space for spectral measurements of the BNCT and BNCS beams at MIT LABA.

As mentioned previously, neutron activation foils can be used as a passive method of fast neutron spectroscopy and thermal neutron detection. The historical use of neutron activation foils in both of these applications is described in the next section.

2.3 Historical Use of Activation Foils

Neutron detection by activation of materials is used for various applications. The geometric form of these activation materials is typically that of a thin foil or small-diameter wire, in order to leave the neutron flux unperturbed under measurement. This is important because changes in the neutron flux while passing through a foil can not be easily accounted for using the basic reaction rate equation shown below.

$$RR = \Sigma \Phi V = N \sigma \Phi V \qquad [2\text{-}1]$$

where: RR = reaction rate (reactions/sec),
Σ = macroscopic cross section averaged over the neutron spectrum (cm^{-1}),
Φ = neutron flux averaged over the foil surface (n/cm^2 sec), and
V = foil volume (cm^3).

From Equation 2-1, the neutron flux can be determined by measuring the reaction rate of the foil. The following equations show the relationship between the number of counts detected for a foil and the respective reaction rate.

The rate of change of the number of radioactive products in the foil during irradiation is simply the rate of production (reaction rate) minus the rate of decay.

$$\frac{dN}{dt} = RR - \lambda N \qquad [2\text{-}2]$$

where: N = number of radioactive nuclei present, and
λ = decay constant (sec^{-1}).

This assumes that RR is constant with time, implying that the neutron flux did not change during the irradiation. Solving Equation 2-2 and converting N to activity, A, gives Equation 2-3.

$$A(t) = RR\left(1 - e^{-\lambda t}\right) + A_0 e^{-\lambda t} \qquad [2\text{-}3]$$

where: A_0 = activity of foil at the start time of irradiation.

For previously unirradiated foils, A_0 is zero for the purposes of Equation 2-3. If the foil is irradiated for a time significantly longer than the half-life of the decay, the induced activity asymptotically approaches a saturated activity, A_∞, which is equal to the reaction rate.

$$A_\infty = RR = \Sigma\Phi V \qquad [2\text{-}4]$$

The saturated activity (reaction rate) can be determined from the induced activity at the end of the actual irradiation time by Equation 2-5.

$$A_0 = A_\infty\left(1 - e^{-\lambda t_0}\right) \qquad [2\text{-}5]$$

where: A_0 = activity of foil at end of irradiation, and
t_0 = time of irradiation (sec).

The final relationship between detector counts and measured reaction rate is shown in Equation 2-6. It adds on to Equation 2-5 by taking into account the decay during the time after irradiation and before the activity is counted, the decay during counting, the efficiency of the detector, and the branching ratio of the gamma peak.

$$A_\infty = RR = \frac{(C - B)\lambda}{\varepsilon b_\gamma (1 - e^{-\lambda t_i})(1 - e^{-\lambda t_c})e^{-\lambda t_w}} \qquad [2\text{-}6]$$

where: C = counts collected,
B = background counts collected,
ε = detector efficiency (counts/γ),
b_γ = branching ratio of gamma peak (γ / decay),
t_i = time of irradiation (sec),
t_w = time between end of irradiation and start of counting (sec), and
t_c = count time (sec).

2.3.1 Thermal Neutron Detection

Neutron activation foils used for thermal neutron detection are made of materials that undergo a (n,γ) reaction and have large cross sections in the thermal neutron region. The γ's produced by the radioactive decay of the neutron activated nuclei are collected and related to reaction rate and thermal neutron flux as indicated above. Typically, these materials have thermal neutron microscopic cross sections that vary as the inverse of the neutron velocity (1/v). This helps to simplify the relationship between the reaction rate and thermal flux.

$$RR = \Sigma\Phi V = N\sigma n v V \qquad [2\text{-}7]$$

$$\sigma \cong \frac{\sigma_0}{v} \qquad [2\text{-}8]$$

$$RR = NnV\sigma_0 \qquad [2\text{-}9]$$

$$\Phi_0 = nv_0 \qquad [2\text{-}10]$$

where: N = number density of foil material (atoms/cm^3),
σ = microscopic cross section averaged over the neutron spectrum (cm^2/n),
σ_0 = thermal neutron microscopic cross section (cm^2/n),
n = neutron density (n/cm^3),
Φ_0 = thermal neutron flux (n/cm^2 sec), and
v_0 = thermal neutron velocity, 2.2x10^5 cm/sec.

These materials may also have significant cross sections in the resonance region at neutron energies between 1 eV and 1 keV; therefore, the induced activity of the foils is created not only by the absorption of the thermal neutrons but also by the absorption of resonance region neutrons and above. In order to separate the responses of these regions, the special neutron absorption properties of cadmium are used.

Cadmium has a very large neutron cross section (21000 barns) below 0.5 eV [Turner 1995]. Above that energy the cross section drops abruptly and remains very low for all energies above 0.5 eV. This is known as the *cadmium cutoff*. In effect, a thin layer of cadmium (≈0.5mm) absorbs almost all neutrons below 0.5 eV and only allows neutrons above the cutoff to pass through.

Comparing the activities of an irradiated foil and of a cadmium-covered irradiated foil separates the thermal and resonance responses. An uncovered foil is activated by both thermal and resonance neutrons, but a cadmium-covered foil is activated by only the resonance neutrons. Taking the difference between the two activities gives the foil's response only in the thermal region.

2.3.2 Fast Neutron Spectroscopy

The spectral characterization of a fast neutron spectrum uses activation foils made of materials that undergo threshold reactions. This means that only neutrons above a certain threshold energy will allow a reaction to occur. These threshold reactions may be any number of absorption reactions, such as (n,n), (n,2n), (n,p), or (n,α), provided that they leave activated nuclei in an isomeric or unstable state, which then undergoes γ decay. This γ decay is counted and related to the neutron flux, by the same method as described above. Spectral characterization requires a selection of various materials that have thresholds at many different energies that cover the fast neutron range. Irradiating all of these materials at once gives responses that correspond to the flux above various energy points. These results are then unfolded to determine the flux between each threshold point, giving a spectral characterization of the entire fast neutron region.

2.3.3 Flux Perturbation Corrections

Equation 2-1 is a good estimate for the relationship between the reaction rate and the neutron flux; however, in order to be accurate, many corrections must be added to take into account flux perturbations under measurement. As mentioned earlier, this problem is minimized by using thin foils or small diameter wires, but it still exists. As the neutron beam passes through a material, each reaction perturbs the flux within the energy region that the reaction occurred. Reducing the thickness of the foil will reduce the perturbations, but this also reduces the number of reactions occurring in the foil, making counting extremely long and tedious. Beckurts and Wirtz give a complete

analysis of the techniques required for determining adequate correction factors in order to get more accurate flux measurement results [Beckurts and Wirtz 1964].

Compared to the use of time-of-flight techniques for epithermal neutron spectroscopy, the use of neutron activation foils is more convenient for characterizing the accelerator-based BNCT and BNCS neutron beams at MIT LABA because of their small size and because an immediate response is not required. A method in which thick activation foils are used to characterize the epithermal neutron region is described in Chapter 3. This method, adapted for BNCT applications by INEEL, avoids the need for modifying Equation 2.1 with correction factors to account for flux perturbation by using computer simulation to calculate the estimated actual extent of perturbation within each foil, and adjusting the cross sections and average flux accordingly.

3 Methods and Materials

3.1 Spectral Characterization Concept

A method for spectral analysis of epithermal neutrons using activation foils was adapted by the Idaho National Engineering and Environmental Laboratory (INEEL) to characterize BNCT beams. This method has been previously used to characterize the reactor-based BNCT beams at Brookhaven National Laboratory [Harker *et al.* 1992] and The Technical Research Center of Finland [Nigg *et al.* 1997], and the proton-cyclotron-based fast neutron radiotherapy facility at the University of Washington School of Medicine [Nigg *et al.* 1998]. MIT LABA is applying INEEL's activation foil spectrometry method to accelerator-based BNCT/BNCS beams. The concepts described below were used in the spectral characterization measurements at MIT LABA.

3.1.1 Epithermal Neutron Spectral Analysis

The INEEL method uses the same concepts as historical activation foil methods but with a more detailed focus on spectral analysis in the epithermal neutron region, 0.5 eV to 10 keV. As mentioned in the previous chapter, foils can be used to determine the thermal neutron flux and to characterize the spectrum in the fast neutron region using Equation 2-1, by taking advantage of cross section characteristics of the foil material. Epithermal neutrons are absorbed by an activation material within the resonance region of its cross section. Since the cross sections within the resonance region typically contain many structured peaks and valleys, in order to characterize epithermal neutrons, activation materials that contain a predominant primary neutron absorption peak in the resonance region must be used so that the energies under which the

majority of the absorption reactions occur can be determined more precisely [Harker *et al.* 1992]. Foils selected for use in epithermal spectral analysis have large thermal cross sections in addition to a primary resonance absorption peak. This produces the exact same problem as in thermal neutron detection: the foils are activated by both thermal and epithermal neutrons. The problem is also rectified in the same manner. The foils are covered in cadmium while irradiated. This allows them to be activated solely by the neutrons with energies above the thermal region [Nigg *et al.* 1997]. Since the largest cross section above thermal is under the primary resonance peak, it can be assumed that the majority of the foil's activation is due to the neutron flux within the energies under this peak [Harker *et al.* 1992]. Although, this assumption is not necessary since precise spectral responses are calculated for each foil. Using a method similar to fast neutron spectral analysis several foil materials are selected so that their primary resonance peaks cover the entire epithermal region. Then, spectral unfolding is performed to determine the neutron flux between each resonance peak. Adding one foil with a threshold reaction above the resonance region and one foil without a cadmium cover will also give the magnitude of the neutron flux above and below the epithermal region [Harker *et al.* 1992].

As mentioned in Chapter 2, "thin" foils have been historically used in neutron activation foil methods in order to reduce the perturbation of the neutron flux under measurement [Knoll 1989]; however, this produces a counting time problem because only a small number of reactions occur in the thin foil. In addition, many corrections to Equation 2-1 are required to get accurate results in order to account for perturbations [Knoll 1989]. Instead, the INEEL method uses "thick" foils to increase the number of

reactions within each foil and uses computer simulation to determine the extent of perturbation and the effective neutron cross sections for each material [Harker *et al.* 1992]. The Monte Carlo N-Particle Transport Code (MCNP) was used at MIT LABA to conduct these computer simulations [Briesmeister 1997]. The extent of perturbation and effective cross sections are then used in the spectral unfolding procedure to determine the a-priori unperturbed neutron flux of the beam.

3.1.2 Direct Unfolding Concept for Activation Foil Data

The direct unfolding method developed by Nigg and Harker [Nigg and Harker 1998], shown below, determines the unperturbed neutron flux of the beam by using the experimentally determined reaction rates of each foil and the MCNP-calculated effective cross sections for each foil within each energy region. The general equation describing the relationship of the reaction rate and the neutron flux for this method is shown below.

$$R = \int_0^\infty \sigma_f(E)\Psi_f(E)dE \qquad [3\text{-}1]$$

where: R = volume-averaged reaction rate per atom for a foil,
$\sigma_f(E)$ = microscopic reaction cross section for a foil as a function of energy, and
$\psi_f(E)$ = volume-averaged scalar neutron flux within the foil as a function of energy (perturbed).

Equation 3-1 can be rewritten to extract the unperturbed neutron flux, as shown below.

$$R = \int_0^\infty \sigma_f(E)\left(\frac{\Psi_f(E)}{\Psi(E)}\right)\Psi(E)dE = \int_0^\infty \sigma_f(E)P_f(E)\Psi(E)dE \qquad [3\text{-}2]$$

where: $\psi(E)$ = volume-averaged unperturbed neutron flux that would exist at the exact position of the foil, in its absence, and
$P_f(E)$ = perturbed to unperturbed flux ratio as a function of energy.

The full energy spectrum is broken down into energy regions of interest which are determined by whether the "full range" or "independent point" unfolding method is used,

as described in Sections 4.3.1 and 4.3.2 [Nigg *et al.* 1997]. Equation 3-2 can then be expressed in the standard multigroup form shown below.

$$R = \sum_{j=1}^{NG} a_j \Phi_j \qquad [3\text{-}3]$$

$$a_j = \frac{\int_{EL_j}^{EH_j} \sigma_f(E) P_f(E) \Psi(E) dE}{\int_{EL_j}^{EH_j} \Psi(E)} \qquad [3\text{-}4]$$

$$\Phi_j = \int_{EL_j}^{EH_j} \Psi(E) dE \qquad [3\text{-}5]$$

where: NG = number of energy groups,
a_j = effective cross section (activation constant) of a foil in energy group *j*,
Φ_j = unperturbed flux in energy group *j*,
EH_j = upper limit of energy group *j*, and
EL_j = lower limit of energy group *j*.

Equation 3-6 is the expansion of Equation 3-3, taking into account the various foils and reactions.

$$R_i = \sum_{j=1}^{NG} a_{ij} \Phi_j \qquad [3\text{-}6]$$

where: R_i = reaction rate for reaction *i*, and
a_{ij} = effective cross section of reaction *i* in energy group *j*.

The solution of this system of equations is easily found using matrices. Rewriting Equation 3-6 in matrix form gives Equations 3-7 and 3-8.

$$\begin{bmatrix} a_{11} & a_{12} & \cdots & a_{1\,NG} \\ a_{21} & a_{22} & \cdots & a_{2\,NG} \\ \vdots & \vdots & \cdots & \vdots \\ \vdots & \vdots & \cdots & \vdots \\ a_{NF\,1} & a_{NF\,2} & \cdots & a_{NF\,NG} \end{bmatrix} \begin{bmatrix} \Phi_1 \\ \Phi_2 \\ \vdots \\ \Phi_{NG} \end{bmatrix} = \begin{bmatrix} R_1 \\ R_2 \\ \vdots \\ \vdots \\ R_{NF} \end{bmatrix} \qquad [3\text{-}7]$$

$$[\mathbf{A}][\Phi] = [\mathbf{R}] \qquad [3\text{-}8]$$

where: NF = number of reactions.

The values of the effective cross sections, a_{ij}, can be obtained by MCNP simulation. MCNP has the ability to determine an estimate for the unperturbed and perturbed neutron spectra using a model of the experiment layout and foil characteristics. Section 3.4 describes in detail the method used to determine these values for the accelerator-based BNCT and BNCS beams at MIT LABA.

Then, if the volume-averaged reaction rates per atom, R_i, are measured for each foil, as described in Section 3.3, and input into Equation 3-8, the equation can be solved for the unperturbed flux in each energy region. A solution for the system of equations can be determined if the spectral responses are reasonably linearly independent and the number of reactions is greater than or equal to the number of energy regions selected ($NF \geq NG$). If $NF < NG$, the problem is underdetermined, and a solution can not be found without further information. The exact methods of solution for Equation 3-8 for $NF \geq NG$ are shown in Section 4.4.

This unfolding method is used to unfold the epithermal neutron spectrum from the same set of data in two distinct ways: 1) the "full range" method, and 2) the "individual point" method [Nigg *et al.* 1997]. Each method uses different energy regions and the measured reaction rates of different foils to produce the unfolded neutron spectrum. These methods are described in detail in Sections 4.3.1 and 4.3.2.

3.2 Facility Description

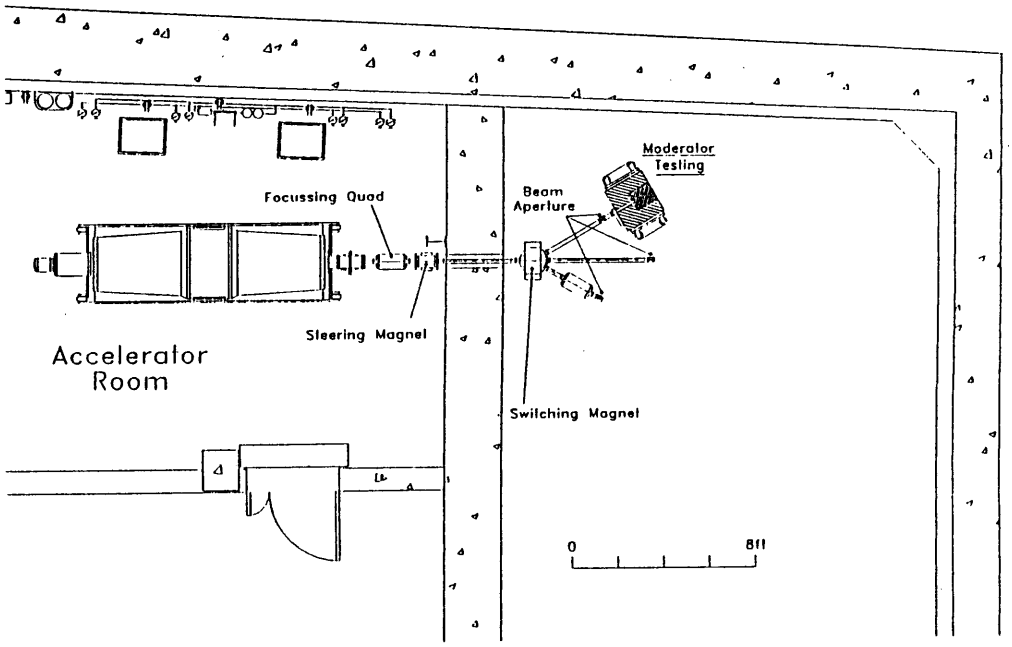

Figure 3-1: Layout of MIT LABA Facility showing the accelerator and experiment room.

The MIT LABA Facility contains a tandem electrostatic accelerator that is capable of accelerating alphas, protons, and deuterons in five separate beam ports. Two of these beam ports are dedicated to producing BNCT and BNCS beams. As part of this work, spectral characterization measurements were conducted on both the BNCT and BNCS beam at MIT LABA. Figure 3-1 is a schematic of the LABA facility. This figure shows the accelerator room separated from the experiment room (a shielded radiation vault) by a 44" thick concrete wall. The beam is passed from the accelerator room to the vault through a small port in the wall. The accelerator is operated and various experimental parameters are monitored in the control room adjacent to the radiation vault. The control room is shielded from the vault by a 3-foot thick concrete wall and 2-foot thick door [Howard *et al.* 1995, Blackburn 1997].

3.2.1 MIT LABA Accelerator

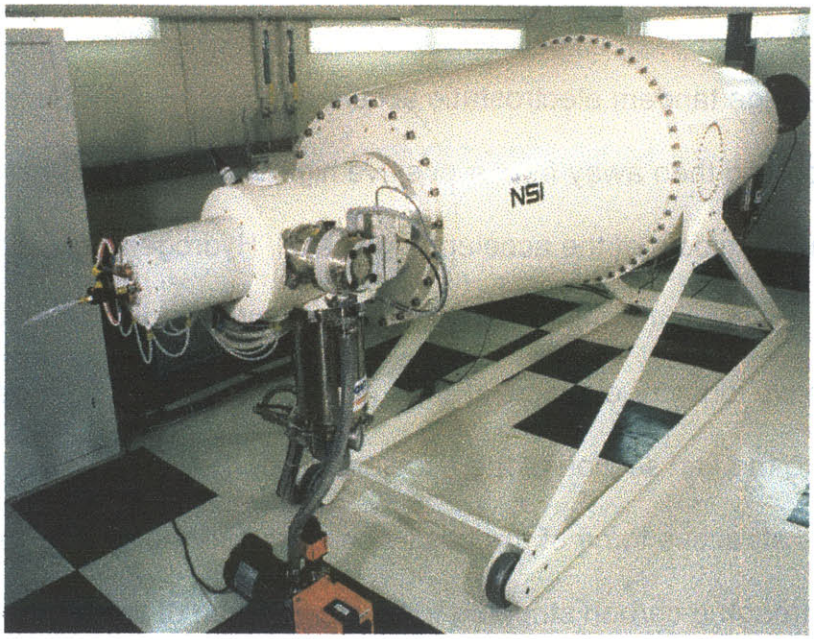

Figure 3-2: Tandem Electrostatic Accelerator at MIT LABA designed by Newton Scientific, Inc.

The two-stage tandem electrostatic accelerator used at LABA, shown in Figure 3-2, was designed and manufactured by Newton Scientific, Inc. in Cambridge, Massachusetts [Yanch *et al.* 1997]. The accelerator weighs approximately 1000 kg, has a total length of 4.3 meters, and has a height of 1.6 meter at the highest point on the pressure vessel. These physical properties make the accelerator suitable for future use in a hospital setting. The accelerator is designed to deliver either protons or deuterons with energies up to 4.1 MeV, beam currents up to 4 mA, and total power levels up to 10 kW [Yanch *et al.* 1997, Blackburn 1997]. Experiments conducted in August 1998 demonstrated that the accelerator is also capable of generating low current beams of alpha particles. Magnetic suppression of secondary particles in the accelerating tubes results in low radiation fields near the accelerator during operation [Yanch *et al.* 1997]. The accelerator is controlled by a PC located in the control room. The following

paragraph is a basic explanation of how the MIT LABA accelerator delivers its particle beam [Blackburn 1997].

The two-stage tandem electrostatic accelerator at LABA accelerates positive particles towards and then away from a positive high-voltage electrostatic field placed on a terminal in the middle of the accelerating vessel. Hydrogen (for protons), deuterium (for deuterons), or helium (for alphas) gas is injected into an ion-source which produces a beam of negative ions, for example H^- ions from hydrogen gas. The negative ions are then injected into the first section of the accelerating column and accelerated toward the terminal due the attractive force of the positive electrostatic field. The negative ion beam passes through a carbon stripping foil at the location of the terminal. The stripping foil removes electrons from the negative ions, producing positive ions, for example converting H^- to H^+. The newly produced positive ion beam is then accelerated away from the terminal, towards the end of the accelerating column, due to the repulsive force of the electrostatic field. For example, with the terminal voltage set at 1 MV, a H^- beam would obtain a kinetic energy of 1 MeV in the first stage of acceleration. Then, after the passing through the stripping foil, the H^+ beam would obtain an additional 1 MeV of kinetic energy in the second acceleration stage. At the end of the accelerator, the positive ion beam has a kinetic energy equal to two times the product of the terminal voltage and the charge of the ion [Blackburn 1997].

3.2.2 BNCT Moderator/Reflector Assembly

The proton or deuteron beam from the LABA accelerator can generate neutron beams in the BNCT and BNCS target assemblies via $^7Li(p,n)$, $^9Be(p,n)$ or $^9Be(d,n)$

reactions. For the spectral characterization measurements, a 3 cm diameter beryllium target, cooled by light water (H_2O), was placed at the end of the beam port.

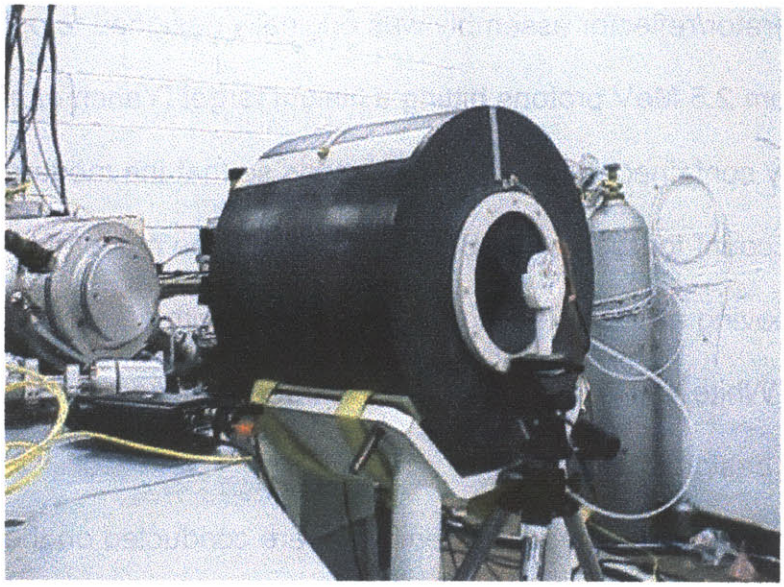

Figure 3-3: BNCT Moderator/Reflector Assembly at MIT LABA

A moderator/reflector assembly, shown in Figure 3-3, surrounds the target to moderate the beam into a suitable epithermal neutron beam for BNCT. A cylindrical heavy water (D_2O) moderator surrounds the target. The moderator has a length of 19 cm and a diameter of 24 cm and is surrounded by 18 cm of lead reflector in three directions, leaving the beam face open [Yanch *et al.* 1992]. The moderator is held inside the reflector shell at the beam face by a 0.3 cm thick Plexiglas cover, which is sealed with a boronated polyethylene cap. The energetic neutrons produced in the target lose energy (moderate) within the heavy water by elastic scattering with deuterium and oxygen. Neutrons are scattered at many energies and angles producing a broad, moderated neutron beam within the moderator. The moderator is designed so that the majority of the neutrons exiting the beam face are in the epithermal region. The

lead reflector is designed so that scattered neutrons are reflected back into the moderator, preventing excessive loss of neutrons [White 1998].

The moderator/reflector assembly was originally designed to optimize a neutron beam created from 2.5 MeV protons hitting a lithium target [Yanch *et al.* 1992]. The original assembly contained removable lead inserts so that the moderator length could be varied. To account for the harder Be(d,n) spectrum, the moderator length was fully extended by removing all of the lead inserts for all runs with deuterons hitting a beryllium target [White 1998]. Section 3.4.1 shows a cross sectional model of the BNCT assembly designed in MCNP.

Spectral characterization measurements were conducted on the BNCT beam using 1.5 MeV deuterons on the beryllium target. During the experiments, the target temperature, beam current on the target, and current on the beam tube were monitored in the control room. The integrated charges on the target and on the beam tube are directly measured, and when divided by the integration time, these measurements give the average beam currents on the target and on the beam tube.

3.2.3 BNCS Moderator/Reflector Assembly

The BNCS moderator/reflector assembly, shown in Figure 3-4, can also convert the proton or deuteron beam into a neutron beam through ^{7}Li(p,n), ^{9}Be(p,n) or ^{9}Be(d,n) reactions. The BNCS assembly currently creates an energetic neutron beam with a beryllium target through Be(d,n) reactions. The target is a single piece of beryllium 0.1905 cm thick and 3.5 cm in diameter mounted at the end of an aluminum target tube [Gierga *et al.* 1998]. The target is cooled with light water using the submerged jet impingement technique [Blackburn *et al.* 1998].

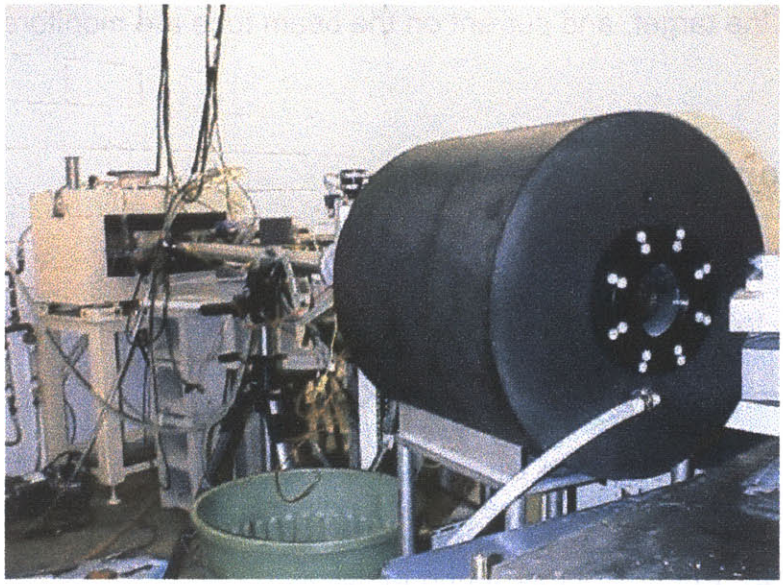

Figure 3-4: BNCS Moderator/Reflector Assembly at MIT LABA.

A moderator/reflector assembly surrounds the target to shape the beam into a suitable epithermal neutron beam for BNCS. The method of neutron beam moderation within the BNCS assembly is the same as in the BNCT assembly, but the reflector is different. The D_2O moderator, up to 23 cm long and 9 cm in diameter, is surrounded by 18 cm of graphite reflector in three directions, leaving the beam face open. Moving the target assembly to any position along the central axis of the moderator can change the length of moderator [Gierga *et al.* 1998]. The moderator is held inside the reflector by a 0.3 cm thick Plexiglas cover that is sealed with a Delrin plastic cap. Section 3.4.1 shows a cross sectional model of the BNCS assembly designed in MCNP.

Spectral characterization measurements on the BNCS beam were conducted using 1.5 MeV deuterons on the beryllium target using 8 cm of moderator. Original plans called for characterization of the BNCS beam with 2.6 MeV deuterons, but these plans were changed in order to match previously run animal irradiations at 1.5 MeV. During the experiments, the target temperature, temperature on the uncooled aperture,

beam current on the target, and current on the beam tube are monitored in the control room.

3.3 Activation Foil Experiments

3.3.1 Selection of Activation Materials

According to Knoll, the following properties must be considered when selecting a material for neutron activation experiments [Knoll 1989]:

1) Shape of the Cross Section;
2) Magnitude of the Cross Section;
3) Decay Constant of the Induced Activity;
4) Purity and Interfering Activities;
5) Nature of the Induced Activity; and
6) Physical Properties.

Based on these considerations, the INEEL method selected several materials for its neutron activation foils, as shown in Table 3-1 [Harker *et al.* 1992]. These materials are also used when applying this method to accelerator-based epithermal neutron beams.

Table 3-1: Foil Materials and Interactions in the INEEL Neutron Activation Method [Nigg *et al.* 1997]. All cross sectional data (ENDF/B-VI) and decay scheme data were provided by the Los Alamos T-2 Nuclear Information Service [LANL 1998].

Foil Material and Interaction	Energy of Primary Response	Magnitude of Cross Section (barns)	Induced Activity	Gamma Decay Energy of Interest	Half-life of Gamma Decay
^{115}In (n,γ)	1.46 eV	29000	^{116}In^{m}	1294 keV 1097 keV 417 keV	54.2 min.
^{197}Au (n,γ)	5 eV	27400	^{198}Au	412 keV	64.7 hr.
^{186}W (n,γ)	18 eV	15400	^{187}W	686 keV	23.9 hr.
^{59}Co (n,γ)	132 eV	850	^{60}Co	1173 keV	5.3 yr.
^{55}Mn (n,γ)	340 eV	45.7	^{56}Mn	847 keV	2.6 hr.
^{63}Cu (n,γ)	580 eV	412	^{64}Cu	511 keV (annihilation)	12.7 hr.
^{115}In (n,n')	339 keV threshold	N/A	^{115}In^{m}	336 keV	4.5 hr.

These materials were chosen because of the criteria they met. Each undergoes a (n,γ) reaction with a reasonably large cross section and has an induced half-life long enough to be counted. In addition, each material is a metal, which can be rolled into a foil. Most importantly, these materials were chosen because of the shape of their reaction cross sections. The (n,γ) cross section for ^{186}W is shown in Figure 3-5.

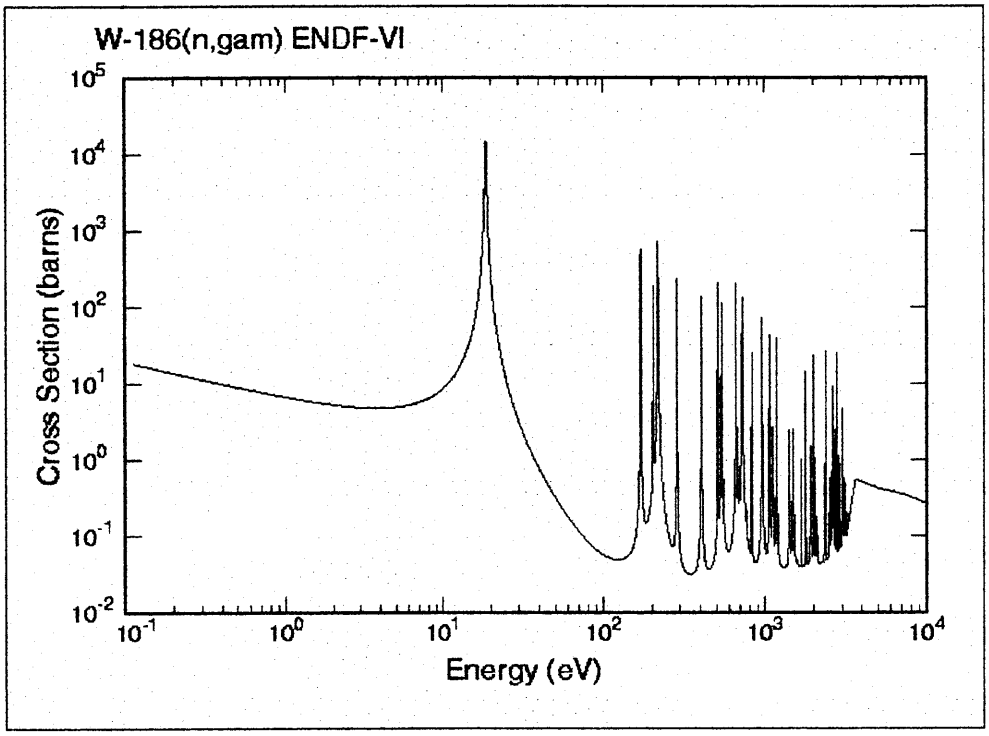

Figure 3-5: $^{186}W(n,\gamma)$ Neutron Cross Section. (taken from the ENDF/B-VI library) [LANL 1998]

This cross section includes an excellent example of a predominant primary resonance peak. It can be assumed that the majority of the (n,γ) reactions in each foil will occur through the absorption of neutrons at the energies under the main resonance peak. As mentioned in Section 3.1.1, the INEEL method uses a combination of historical thermal and fast neutron activation methods to characterize the epithermal

neutron region by selecting materials with primary resonance peaks that cover the epithermal range of interest (0.5 eV – 10 keV) [Harker *et al.* 1992]. By examining column #2 in Table 3-1, it is shown that the selected materials cover this region of interest, including one threshold reaction, ^{115}In(n,n'), to measure the fast neutron flux. This reaction must also meet the criteria above such that cross section and half-life are adequate for standard counting techniques. The cross sections for every isotope are listed in Appendix A, and their decay schemes are listed in Appendix B.

3.3.1.1 Irradiation Configuration in Foil Stacks

All of the foils are irradiated in stacks of five inside a cadmium cover, as shown in Figure 3-6. Each foil stack contains five foils of the same material [Harker *et al.* 1992]. The cadmium cover, manufactured by Reactor Experiments, Inc., is 40 mils thick [Reactor Experiments, Inc. 1998]. For labeling purposes, the foils are numbered one through five, with Foil 1 being closest to the incident neutron beam and Foil 5 being the furthest.

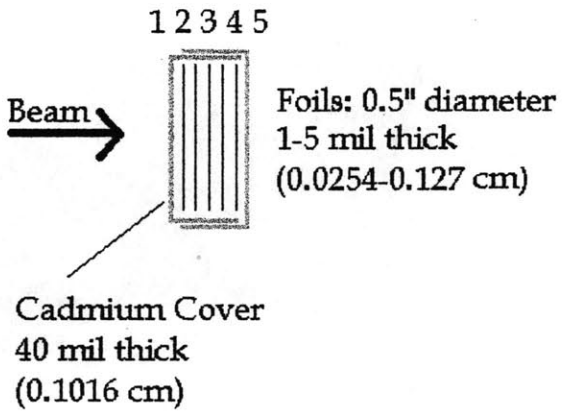

Figure 3-6: Foil Stack Configuration

3.3.2 Determination of Foil Thickness

The foil thickness for each activation material must be sufficient to meet the criteria for good activation data in the unfolding process, as listed below.

1) The effective cross section of Foil 3 as a function of energy should have a strong degree of linear independence from the effective cross section of Foil 1 as a function of energy [Nigg *et al.* 1997].

2) The foil thickness should be thick enough so that each foil has reasonable count times given the flux limitations of an accelerator.

Criterion 2 is important to characterizing accelerator-based epithermal beams or other beams created using a source that has a neutron flux several magnitudes smaller than a reactor. Other criteria to consider are that of the manufacturer. The manufacturer chosen to make the foils was Reactor Experiments, Inc. This company was chosen for consistency, because previous applications of this spectral characterization method have used foils from this company. Reactor Experiments, Inc. makes foils with thicknesses between 1-5 mils [Reactor Experiments, Inc. 1998]; therefore, the foil thickness that meets the unfolding criteria must be rounded to the nearest mil within the range of thickness supplied by the manufacturer.

3.3.2.1 Criterion 1 - Linear Independence

In order to meet criterion 1, it is assumed that sufficient independence can be achieved when the reaction rate of the third foil is one half of that of the first foil, reflecting the fact that the resonance flux is heavily suppressed in the third foil [Nigg 1998]. MCNP is used to determine the foil thickness for each material so that this assumption is met. The estimate of the foil thickness for each material is used as the initial input into the MCNP simulations. This estimate is found by setting the thickness of three foils of each material equal to one mean free path. This is thought to give results close to meeting criterion one [Nigg 1998]. The estimated microscopic cross section was found by averaging the absorption cross section across the full width half maximum of the primary resonance for the isotope of interest of each foil material. This was just an estimate of the foil's cross section, since in several cases the foil is actually made of the natural material, rather than just the isotope of interest. The bolded

numbers in Table 3-2 were used as the initial input in the MCNP simulations. Since the calculated foil thickness was much larger than the maximum thickness supplied by the manufacturer for ^{55}Mn and ^{63}Cu, the maximum thickness of 5 mil was selected. For ^{59}Co, the maximum thickness was also selected, because it was anticipated that its long half-life would prevent this material from meeting criterion 2.

Table 3-2: Initial Estimate of Foil Thickness for Input into MCNP Simulations.

Material	Mean Free Path (cm)	3 Foil Thickness to the nearest mil	Foil Thickness (mil)
^{115}In	0.0012	1	**1**
^{197}Au	0.0008	1	**1**
^{55}Mn	0.3518	139	46 **[5]**
^{63}Cu	0.0521	21	7 **[5]**
^{186}W	0.0049	2	**1**
^{59}Co	0.0168	7	2 **[5]**

The experimental setup was simplified and did not include the source spectrum for the 1.5 MeV Be(d,n) spectrum or the actual BNCT or BNCS moderator/reflector assemblies, as described in Section 3.4. The MCNP geometry for each material is shown in Figure 3-7. The source spectrum used was an isotropic uniform neutron spectrum from 0-1 MeV at a distance of 0.25 cm from the foils. The foils were made of the natural material because they are not manufactured isotropically enriched. In addition, the manganese foils are actually manufactured to be 81.3% Mn and 18.7% Cu [Reactor Experiments, Inc. 1998]. This was also taken into account in the MCNP simulations.

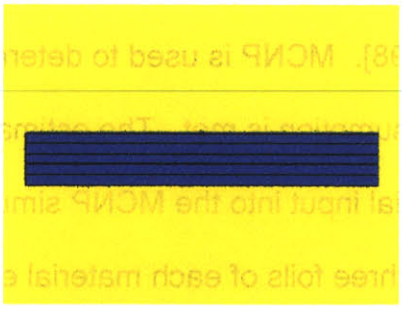

Figure 3-7: MCNP Simulation Geometry for Initial Determination of Foil Thickness

3.3.2.2 Criterion 2 - Count Time

In order to determine if the foil thicknesses are sufficient for adequate count times using the accelerator-based neutron source, MCNP simulations were conducted using accurate models of the BNCT and BNCS moderator/reflector assemblies. Since the original objective of this project was to characterize the BNCS beam using 2.6 MeV deuterons on a Be target, this geometry was first used in the simulations. The MCNP model used for these simulations assumed the largest length of moderation in the BNCS assembly, 23 cm. This provides very conservative simulation results because only 8 cm of moderation was actually used in the BNCS experiments[1]. Count time simulations were also conducted using a BNCT moderator/reflector assembly using 1.5 MeV deuterons on a beryllium target. The exact MCNP geometries and procedures used in both simulations are described in Section 3.4.

From these calculations, it was determined that the cobalt foil had too long a half-life and could not be used on the MIT LABA setup of either the BNCS or BNCT beam. Exceptional count times were needed to get a reasonable counting error for the cobalt foils. Table 3-3 summarizes the foil materials used at MIT LABA and their nominal thicknesses calculated from the above criteria, taking into account the available thicknesses supplied by the manufacturer.

The foils were weighed using a Metler AT201 Microscale in The Environmental Research and Radiochemistry Detector Facility at MIT's Nuclear Reactor Laboratory. The microscale was last calibrated on 5/11/98 and is accurate to within $\pm 5 \times 10^{-5}$ grams.

---

[1] The actual BNCS experiments were conducted using 1.5 MeV deuterons on beryllium with 8 cm of moderation to match the experimental setup of previous rabbit irradiations. Count time calculations were not rerun for this setup because the BNCT beam produces a much lower yield, and any foils that are

The measured mass and thickness of each foil compared to the manufacturer-measured mass and nominal thickness are listed in Appendix C.

Table 3-3: Foil Materials and Thicknesses Used for MIT LABA Experiments. Each calculated foil thickness was determined by independence and counting criteria calculations. The nominal foil thickness of the each foil made by Reactor Experiments is listed as the manufactured foil thickness.

Foil Material	Calculated Foil Thickness (mil)	**Manufactured Foil Thickness (mil)**
In	1	**2***
Au	1	**1**
81.3% Mn / 18.3% Cu	5	**5**
Cu	5	**4****
W	1	**1**

*The indium foils could not be rolled down to 1 mil, the manufactured foil thickness was 2 mil.
**The copper foils were determined to have an average nominal thickness of 4 mil after measuring the mass of the foils received from the manufacturer.

3.3.3 Experiment Layout

The foil stacks are irradiated in a foil wheel for thermal and epithermal neutron measurements and inside a hollow boron sphere for fast neutron measurements [Harker *et al.* 1992]. The following sections describe in detail the specifications of each irradiation configuration.

3.3.3.1 Foil Wheel Experiments

The foil wheel, shown in Figure 3-8, was designed by INEEL for simultaneous irradiation of seven foil stacks so that there is no interference between the stacks [Harker *et al.* 1992, Nigg *et al.* 1997]. The foil wheel is made of Teflon with an outside diameter of 3 inches. In order to hold the foil wheel in front of both the BNCT and BNCS beams, an interchangeable holder design was needed. A similar design was

adequate for use on the BNCT beam can be assumed to be more than adequate for use on the BNCS beam.

needed to hold the boron sphere in position, as described in Section 3.3.3.2. The following criteria were used for both holder designs:

1) Height adjustable to work with both BNCS and BNCT beams,
2) The stacks in the foil wheel must be the same distance from the beam as the stacks in the boron sphere,
3) Placement of holders as close to the beam face as possible,
4) Easy and reliable repositioning (within holder, vertically, distance from the beam, and centered position in beam), and
5) Holder material that won't be activated by the neutron beam and won't significantly perturb the beam.

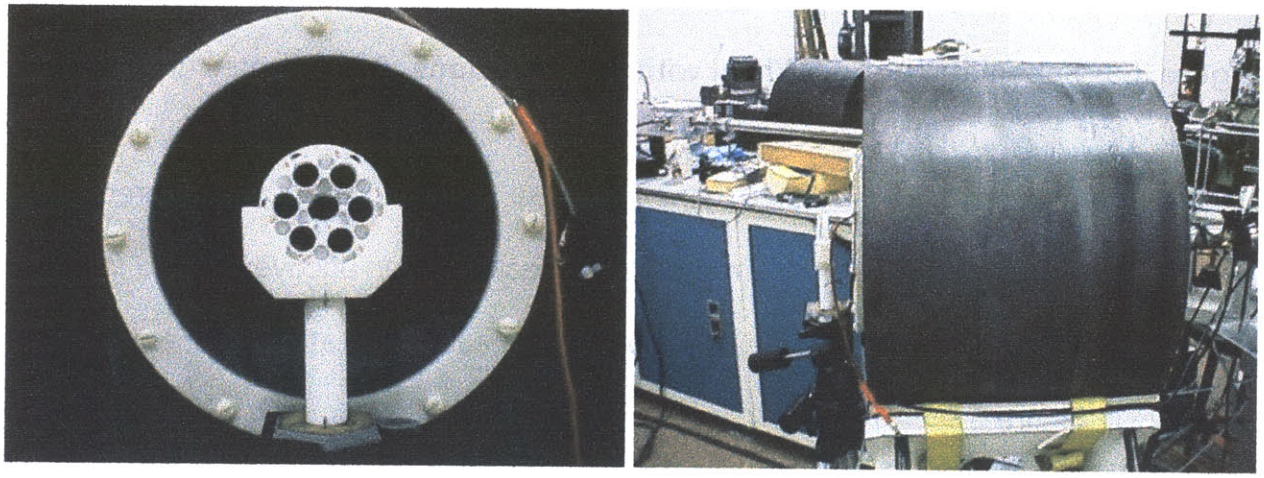

Figure 3-8: Foil Wheel Holder in Front of the BNCT Beam shown in front view (left) and side view (right).

Figure 3-8 shows the designed foil wheel holder in front of the BNCT beam. The holder is made of polyethylene and Teflon. The boron sphere holder is shown in Section 3.3.3.2. The foil wheel slides snuggly into the polyethylene top and was designed so that criterion 2 is met. The Teflon rod is attached to the top of a standard tripod. Once the tripod is in position to meet criterion 3 in front of either the BNCT or BNCS beam, the foil wheel and boron sphere holders can be easily exchanged by removing the top of the tripod. Once the top of the tripod is reattached, the exact position of either holder is reproduced.

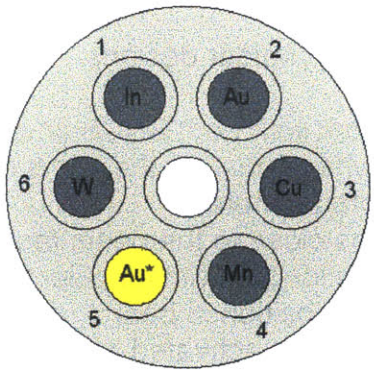

Figure 3-9: Schematic of Foil Wheel with Foil Locations. Au* indicates uncovered gold foils in position 5.

Six foil stacks were irradiated in the foil wheel, including cadmium-covered indium, gold, copper, tungsten, and manganese stacks and an uncovered gold foil stack (for thermal neutron measurements). The position of each foil material in the foil wheel is shown in Figure 3-9.

3.3.3.2 Boron Sphere Experiments

The boron sphere, provided by INEEL, is nearly 100% ^{10}B and is used for suppression of the thermal and epithermal flux before it interacts with the foils [Harker *et al.* 1992]. The primary utility of this suppression is to allow the 336 keV gamma-ray resulting from the inelastic scattering (threshold) reactions in the indium foils to be more easily detected, due to the reduction of interference in the spectrometer from the higher-energy gamma-rays resulting from capture reactions in the indium. One foil stack is irradiated at a time inside the boron sphere and is held inside the sphere using Teflon/silicone tape such that the front of the stack is along the center line of the sphere, as shown in Figure 3-10.

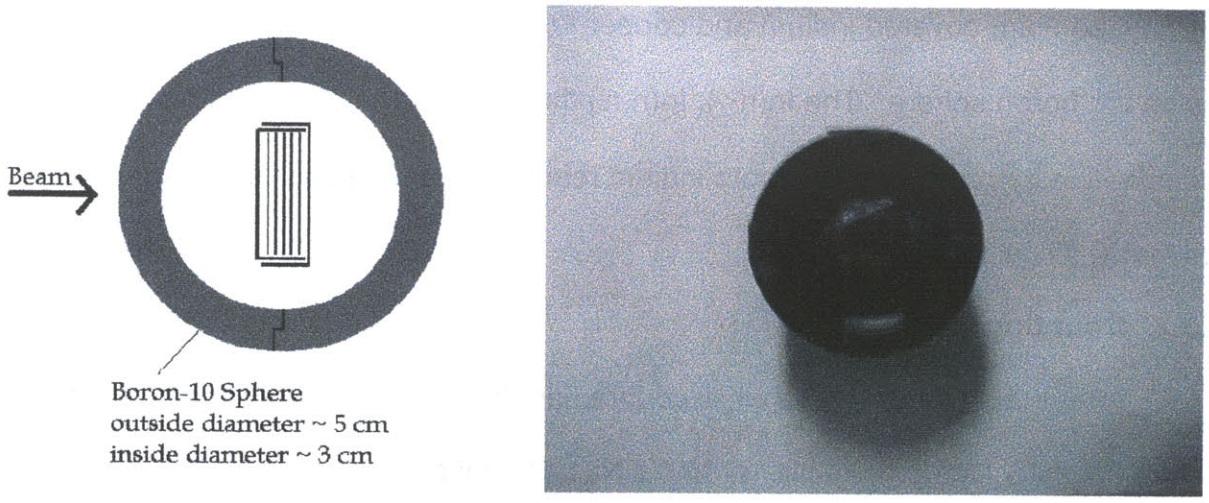

Figure 3-10: Boron-10 Sphere. (left) schematic of boron sphere with foil stack, (right) photograph of one half of the boron sphere with Teflon tape holding foil stack in position.

The holder designed to hold the sphere in front of the neutron beams is a simple Teflon rod with a hollowed-out end so that the sphere can rest on the top, as shown in Figure 3-11. The rod can be attached to the top of the tripod and can be easily repositioned in front of either the BNCT or BNCS beam as described in the previous section.

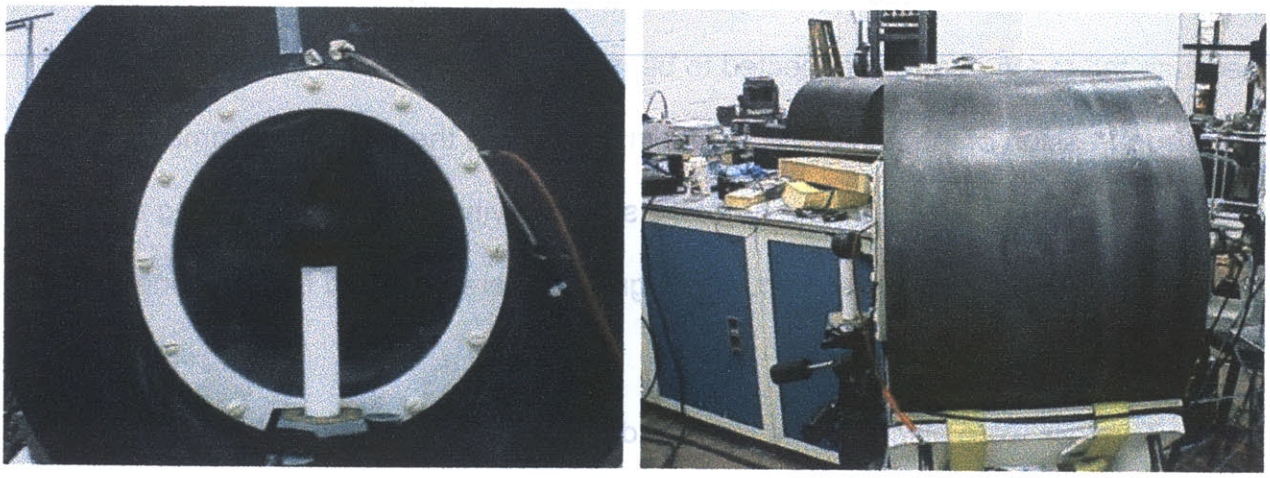

Figure 3-11: Boron Sphere Holder in Front of BNCT Beam shown in front view (left) and side view (right).

Cadmium-covered indium and copper foil stacks were separately irradiated inside the boron sphere. The In(n,γ), In(n,n') threshold, and Cu(n,γ) reactions were examined in this configuration (both indium reactions were measured using the same foil stack) [Nigg *et al.* 1997].

3.3.4 Counting

After irradiation, the foils were counted at The Environmental Research and Radiochemistry Detector Facility at MIT's Nuclear Reactor Laboratory. This facility has four Canberra closed-end coaxial HP(Ge) detectors for gamma spectroscopy [Canberra 1998]. These detectors are read using the Canberra Genie 9900 Multi-Channel Analyzer (MCA) Spectroscopy System [Canberra 1998]. In the existing arrangement, the MCA collects data from 40 keV to 2000 keV.

For the foils irradiated in the foil wheel, Foils 1-3 were counted separately. Foils 4 and 5 were not counted; their primary function in the foil stack was to absorb any backscatter neutrons [Nigg *et al.* 1997]. The five foils in each stack irradiated in the boron sphere were counted together and taken as one large foil. This is required because the reaction rate is expected to be much smaller due to the boron sphere's large suppression of the neutron flux, and in the case of the 336 keV gamma-ray from the indium threshold reaction, the naturally small activity that is induced [Nigg *et al.* 1997]. The net counts (counts minus background) were recorded for each one of the foils described above.

The foils were placed in the HP(Ge) detector on top of two petri dishes. This same geometry was used for all 4 detectors in the facility. The count time for each foil was dictated by the calculated counting error. The foils were counted until the error was

at least below 4%; if time allowed, a counting error of 2% was the goal. After all of the foils from one irradiation run (either a foil wheel or boron sphere) were counted, a standard was counted for five minutes[2] on each detector in the exact counting geometry as the foils to determine the detector efficiency. The Sb-Eu standard is approximately the size of the foils used in the experiment; therefore, it can then be assumed that the solid angles of the standard to the detector and the foils to the detector are equivalent. The final efficiency found from the standard is the absolute efficiency of the detector, taking into account solid angle.

3.4 MCNP Simulation

Monte Carlo N-Particle Transport Code (MCNP) Version 4B was used to model the experimental system [Briesmeister 1997]. MCNP is a computer code that calculates the transport of neutrons, photons, and electrons through a user-defined model geometry, starting with a user-defined source spectrum. MCNP4B uses the ENDF-VI cross sectional data set to simulate the neutron scattering and absorption through each material defined in the model [Briesmeister 1997]. The BNCT and BNCS models contain the moderator/reflector assemblies, foil wheel packets, and foil wheel or boron sphere in their experimental locations. Since MCNP does not track the transport of deuterons, the accelerator and accelerated deuterons hitting the beryllium target was not modeled. The neutron source spectrum input used for these simulations was taken from experimental measurements of the neutron spectrum produced from 1.5 MeV (or 2.6 MeV) deuterons on beryllium [Guzek 1998, Whittlestone 1977, Meadows 1991].

[2] A count time of five minutes was selected to get counting errors below 5% for each gamma peak of interest.

MCNP simulation was used to determine the required foil thicknesses and to estimate the required count time for each foil in both beams, as described in Section 3.3.2. Also, two simulation runs were conducted to determine the effective cross section of the foils in each experimental setup (foil wheel, In foils in boron sphere, and Cu foils in boron sphere) for each beam type (BNCT and BNCS). In addition, one run was conducted to determine the MCNP-calculated in-air unperturbed neutron spectrum from the BNCT and BNCS beams. The following sections discuss the details of the MCNP model and simulation runs.

3.4.1 Moderator/Reflector Models

Accuracy of MCNP simulations relies on the accuracy of the experimental model, the neutron source input, and the interaction cross sections [Briesmeister 1997]. Exact measurements of each part of both moderator/reflector assemblies were used to model each system. Appendix E lists the input file for each model geometry.

The BNCT beam model, designed by Yanch *et al.* [Yanch *et al.* 1992] and modified by White [White 1998], contains the lead reflector, D_2O moderator, beryllium target, Plexiglas cover, and boronated polyethylene cap. The beam tube and target cooling were not included in the model. The neutron source definition input (sdef) was placed at the location of the beryllium target. Figure 3-12 shows a cross section of the MCNP BNCT model used for the simulations.

The BNCS beam model, designed by Gierga [Gierga *et al.* 1998], contains the graphite reflector, D_2O moderator, target (modeled as air instead of beryllium), Plexiglas cover, Delrin plastic caps, aluminum beam tube, and the entire target cooling. The sdef

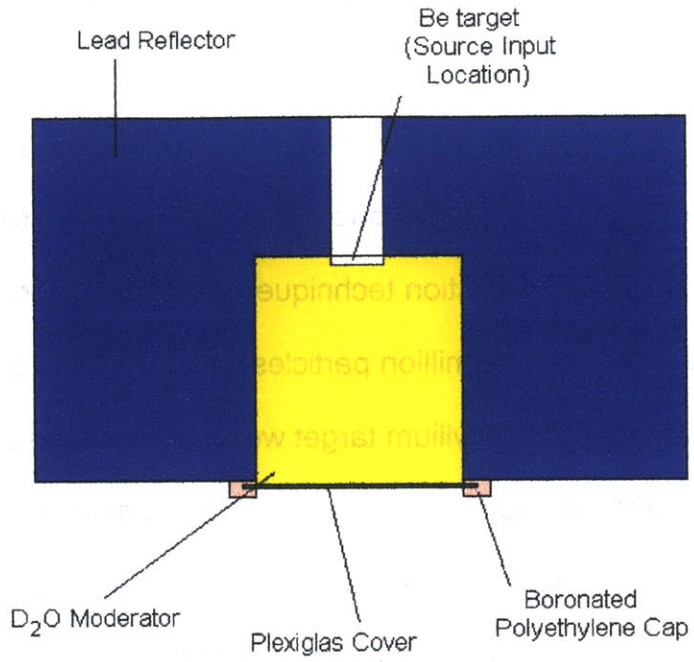

Figure 3-12: MCNP Model Cross Section of the BNCT Moderator/Reflector Assembly.

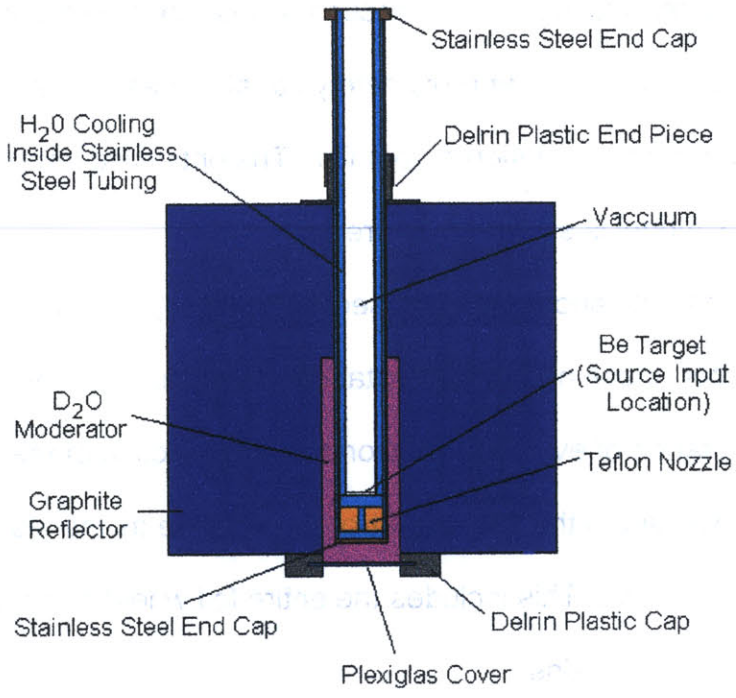

Figure 3-13: MCNP Model Cross Section of the BNCS Moderator/Reflector Assembly.

was placed at the location of the target. Figure 3-13 shows a cross section of MCNP BNCS model.

After initial test simulation runs of the BNCT configuration, it was found that even 100 million starting neutrons could not produce adequately small errors in the estimate of the reaction rates. Variance reduction techniques were then used to increase the statistical precision supplied by 100 million particles [Briesmeister 1997]. The length of moderator and reflector after the beryllium target were broken into several regions. Each section's length (distance down the central axis of the assembly) was initially selected to be approximately equal to the mean free path of a 1 MeV neutron in D_2O. In most MCNP runs (and for all the runs in the simulations used in this work), the neutron importance of each cell in the system was set to 1. For variance reduction, each new section was given a higher neutron importance moving down the projected path of the neutrons. The exact importance of each section is optimized such that the number of neutrons entering each section is approximately equal[3] [Briesmeister 1997]. This can be checked by viewing the simulation output file. The optimized importance of each section in the BNCT model is shown in Figure 3-14.

Even though the variance reduction sections were optimized for neutron passage through the moderator, these neutron importances were carried over to the reflector's sections. The importance of everything beyond the last section of the moderator/ reflector assembly was set to the same neutron importance as the last variance reduction region (imp:n = 8). This includes the entire foil wheel or boron sphere assembly and the foils it contains.

[3] It is better to have the number of neutrons slightly decreasing in each subsequent section rather than rising.

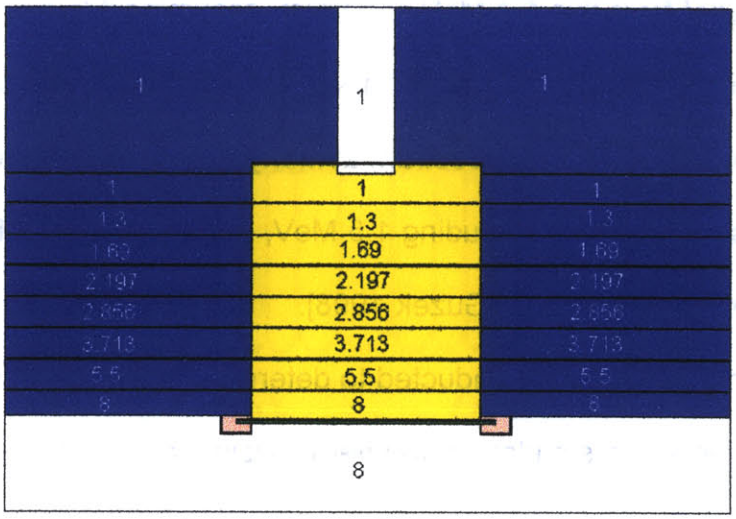

Figure 3-14: MCNP Model Cross Section of BNCT Moderator/Reflector Assembly with Variance Reduction Regions. The neutron importance is shown in each variance reduction region.

The variance reduction regions allowed adequately small errors (less than 6%) in the BNCT simulation results with 100 million starting neutrons in the foil wheel runs and with 200 million starting neutrons in the boron sphere runs. The input file for this geometry is listed in Appendix E.

3.4.2 Neutron Source Selection

The first simulations were conducted using the BNCS beam and 2.6 MeV deuterons on beryllium. Meadows provides experimentally measured neutron spectral data at 0° for high-energy deuterons (2.6 MeV or higher) on beryllium [Meadows 1991]. The 2.6 MeV data were used in the initial count time simulations.

The majority of the simulations used the neutron spectrum from 1.5 MeV deuterons on beryllium. Two sources of neutron spectral data for 1.5 MeV deuterons on beryllium are available. Whittlestone in 1977 experimentally measured the neutron spectrum from 1.4 MeV deuterons on beryllium at 0° [Whittlestone 1977]. Song

created a MCNP sdef from this 1.4 MeV spectrum, assuming it to be isotropic, for use as an approximation to the 1.5 MeV neutron spectrum [Song 1998]. More recently, Guzek has measured the neutron spectrum at many angles from a wide range of deuteron energies on beryllium, including 1.5 MeV, at the Schonland Research Center at the University of Witwatersrand [Guzek 1998].

Several simulations were conducted to determine the effect of using different source spectra in the same simulation geometry. Using the model geometry and method described in Section 3.4.7, the in-air unperturbed neutron spectra from the BNCT and BNCS models were calculated using the Whittlestone, Guzek, and monoenergetic neutron sources. The results of these simulations are shown in Figures 3-15 and 3-16. These figures show that the neutron spectra after moderation produced from the different source spectrum had the same shape (except for the fast neutron region for the monoenergetic sources). This suggests that the BNCT and BNCS beams are fairly insensitive to different source spectra. Figures 3-17 and 3-18 show a direct comparison between the Guzek and Whittlestone source spectrum.

Using the Whittlestone spectrum instead of the Guzek spectrum affects the MCNP-expected unperturbed neutron spectra of the BNCT and BNCS by only ±10% and ±15%, respectively in the lower energy regions. However, there was considerable difference between the Guzek and Whittlestone spectra, 20% and 47%, respectively for the BNCT and BNCS beams, in the highest energy region. If the experimentally-determined unfolded neutron spectra do not match the MCNP-expected neutron spectra, this could be one cause. All simulations in the spectral characterization calculations were conducted using the more complete and more recent Guzek data.

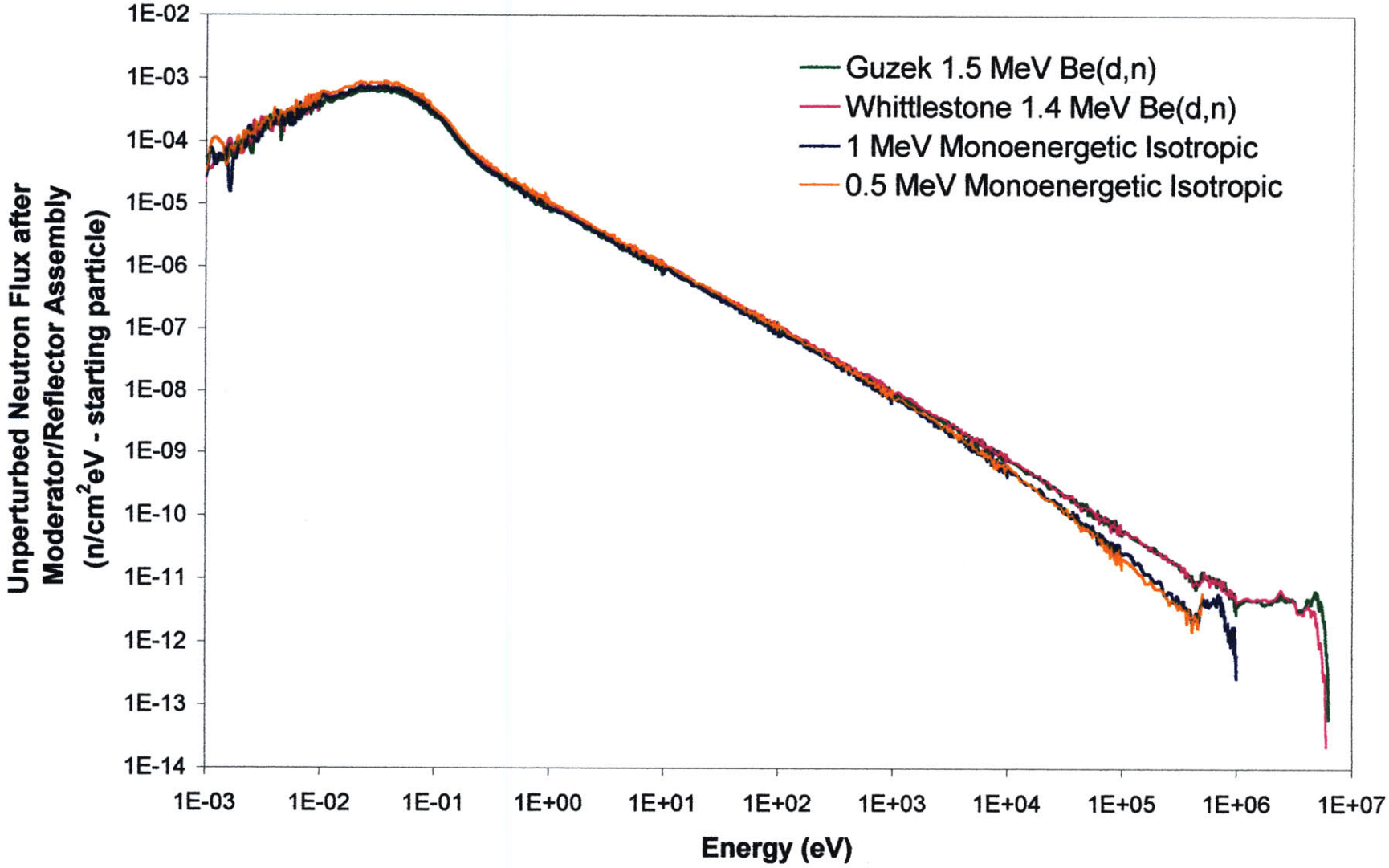

Figure 3-15: The Effect of Different Source Spectra on the MCNP-Calculated Unperturbed Neutron Spectrum of the BNCT Beam.

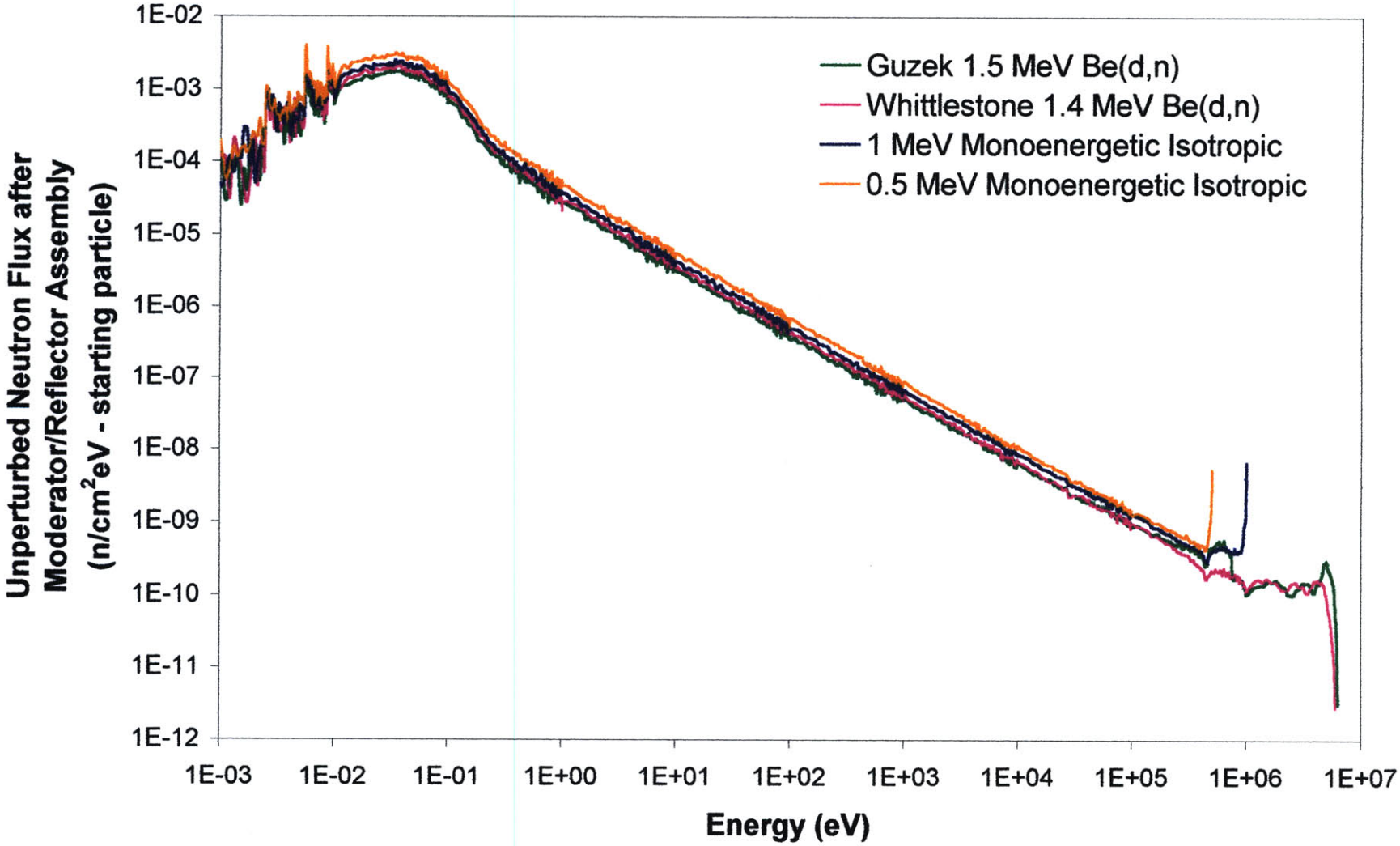

Figure 3-16: The Effect of Different Source Spectra on the MCNP-Calculated Unperturbed Neutron Spectrum of the BNCS Beam.

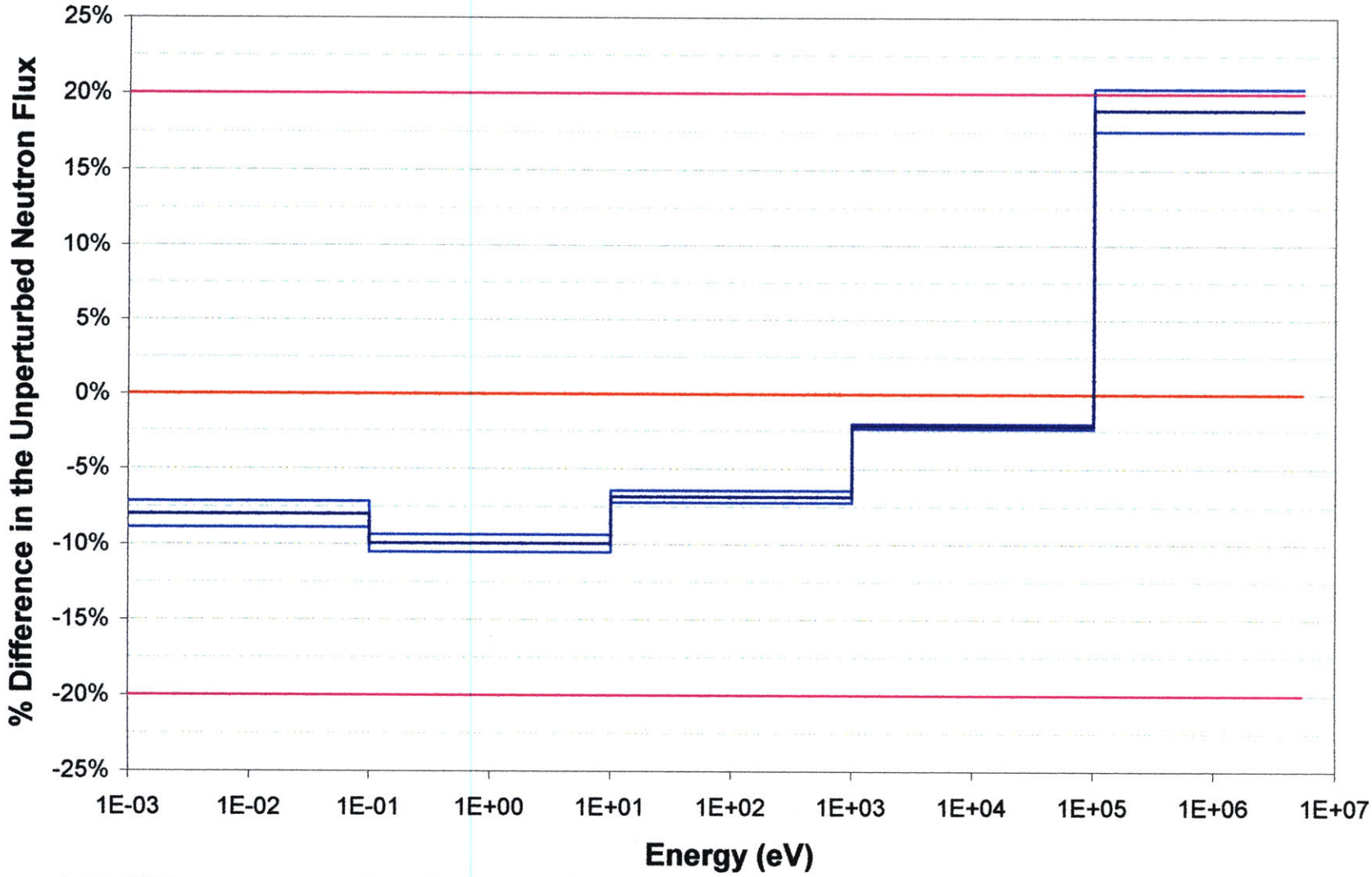

Figure 3-17: Difference in the MCNP-Calculated Unperturbed Neutron Spectrum of the BNCT Beam as a result of using the Guzek Source Spectrum instead of the Whittlestone Source Spectrum. The error bars only include statistical errors and do not include any errors in the Guzek or Whittlestone Source Spectrum.

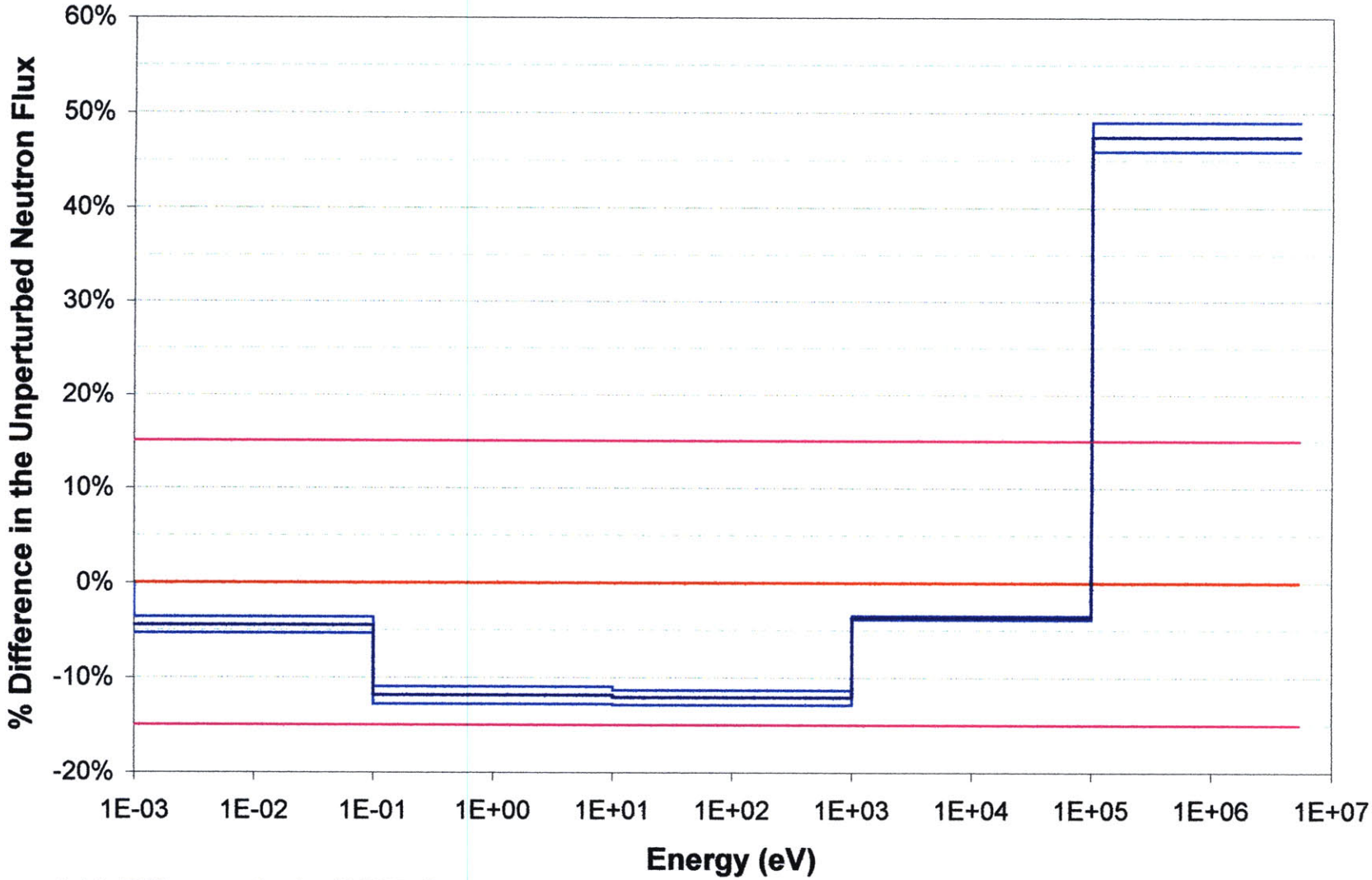

Figure 3-18: Difference in the MCNP-Calculated Unperturbed Neutron Spectrum of the BNCS Beam as a result of using the Guzek Source Spectrum instead of the Whittlestone Source Spectrum. The error bars only include statistical errors and do not include any errors in the Guzek or Whittlestone Source Spectrum.

3.4.3 Foil Wheel Model

The foil wheel model contains the Teflon foil wheel, its polyethylene and Teflon holder, the five cadmium-covered foil stacks, and the one uncovered foil stack. The exact measurements of the foil wheel and holder were used to create the model. The center of the foil wheel was placed at the exact center of beam face and at a distance equal to that in the experiments. The modeled cadmium-covered stacks contain five foils with no space between them and in a position closest to beam within the cover. Each foil stack was placed in the same foil wheel position as used in the experiments, as shown in Figure 3-19. The foils were manufactured from each respective natural element (In, Au, Cu, Mn/Cu, and W); therefore, natural elements were used as each foil material in the model. The nominal manufactured thickness for each foil was used in the model, even though the each foil's exact thickness actually varies up to 18% from this thickness. The measured foil thicknesses for each foil compared to the nominal thicknesses are listed in Appendix C. Appendix E lists the MCNP input for the foil wheel model.

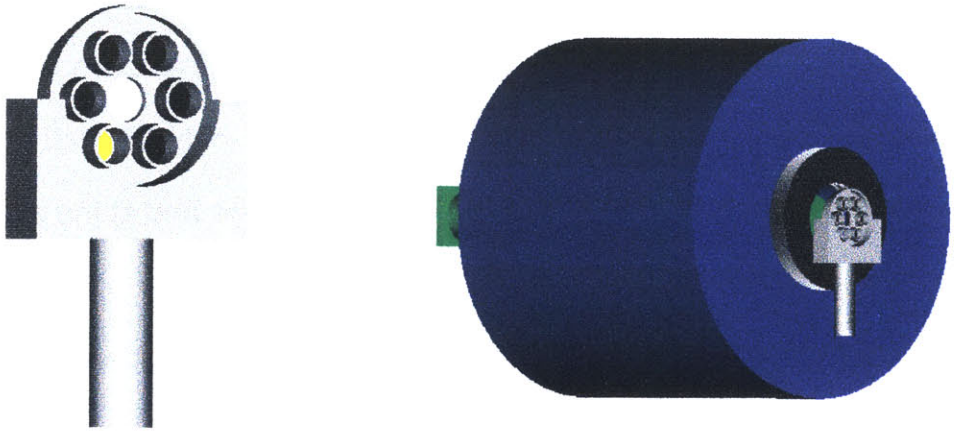

Figure 3-19: MCNP Foil Wheel Model. (left) MCNP foil wheel model with holder and foil stacks. (right) MCNP foil wheel model in experimental position in front of BNCS moderator/reflector model. Both models were plotted in SABRINA (Van Riper 1993).

3.4.4 Boron Sphere Model

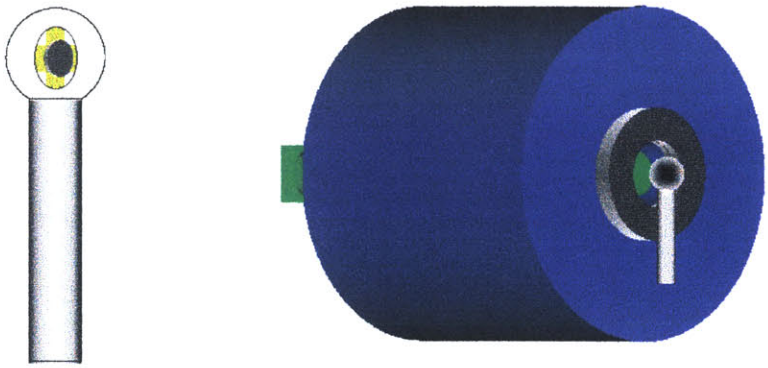

Figure 3-20: MCNP Boron Sphere Model. (left) MCNP boron sphere model with holder. The boron sphere is shown as transparent so that the foil stack can be seen. (right) MCNP boron sphere model in its experimental position in front of BNCS moderator/reflector model. Both models were plotted in SABRINA (Van Riper 1993).

The boron sphere model contains a 100% ^{10}B sphere, its Teflon holder, the Teflon/silicone tape, and the included cadmium-covered foil stack. Two separate boron sphere models were created: one with a cadmium-covered In foil stack, and one with a cadmium-covered Cu foil stack. The exact measurements of the boron sphere, each foil stack, and Teflon holder were used to create the model. The five foils within each foil stack were taken as one cell because the response of all five foils is taken as one datum point, as explained in Section 3.3.4. The nominal thickness of each foil was also used in this model. The front of each foil stack was placed at the center of boron sphere and at the exact experimental distance from the beam face[4], as shown in Figure 3-20. The Teflon/silicone tape used to hold the foil stack in place in the sphere was also modeled. The MCNP inputs for the sphere models are listed in Appendix E.

[4] The experimental distance from the beam face to the front each foil stack is the same for the boron sphere and foil wheel irradiations for each beam.

3.4.5 Count Time Simulation Runs

The count time simulations for the BNCS beam used 2.6 MeV deuterons on beryllium. The model contained moderator/reflector assembly, boron sphere and foil stacks, but not the foil wheel model (Figure 3-21). A separate simulation was run for each foil material. The BNCS moderator/reflector assembly is slightly different from the one described in Section 3.4.1. This assembly has 23 cm of moderation rather than the 8 cm used in the standard model. The MCNP input for this assembly model is listed in Appendix E. Since the exact experimental layout was not yet designed, the simulations assumed that the boron sphere was placed as close to the beam as possible. The first foil in both the boron sphere and foil stack configurations were placed at the same horizontal and vertical position in front of the beam. These simulations were simply used to estimate whether the count times would be reasonable.

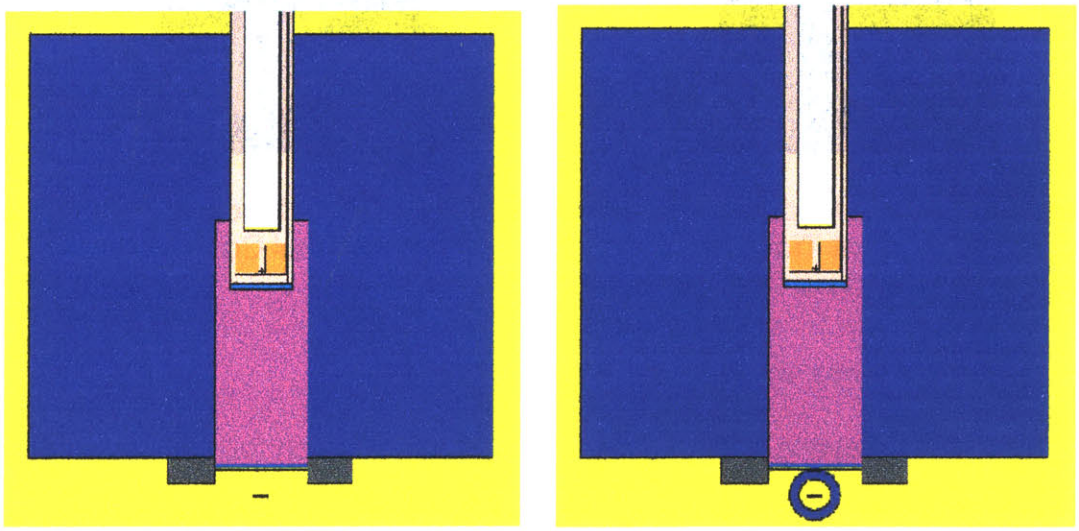

Figure 3-21: MCNP Geometry Cross Section with BNCS Moderator/Reflector Assembly for Count Time Determination with 23 cm of Moderation. (left) Foil Wheel Configuration: Cd-covered foil stack of one material. (right) Boron Sphere Configuration: Cd-covered foil stack inside a boron-10 sphere.

Count time calculations were also done on the BNCT model with a 1.5 MeV Be(d,n) reaction using the BNCT moderator/reflector assembly model without variance reduction, as shown in Figure 3-22. The models include the foil wheel, foil wheel holder, and boron sphere holder. The exact distance of the foils from the moderator/reflector assembly was not used. The boron sphere was placed as close as possible to the assembly, and the foil wheel was placed so that the first foils in both configurations are in the same horizontal position from the assembly.

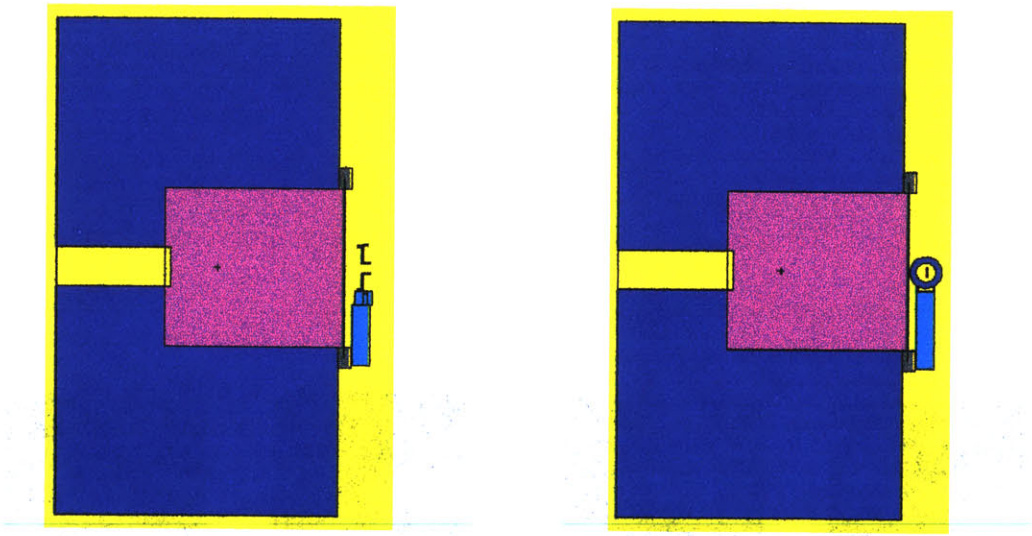

Figure 3-22: MCNP Geometry Cross Section with BNCT Moderator/Reflector Assembly for Count Time Determination. (left) Foil Wheel Configuration. (right) Boron-10 Sphere Configuration.

3.4.6 Effective Cross Section Simulation Runs

MCNP simulations were conducted to determine each foil's effective cross section within each energy region, a_{ij}. Equation 3.4 is restated below to display the components of a_{ij}.

$$a_{ij} = \frac{\int_{EL_j}^{EH_j} \sigma_f(E) P_f(E) \Psi(E) dE}{\int_{EL_j}^{EH_j} \Psi(E)} \qquad [3.9]$$

The numerator is equivalent to the number of expected (n,γ) or (n,n') reactions in each foil within each energy region. The denominator is equivalent to the expected unperturbed neutron flux within the location of each foil in each energy region. The simulation runs for the BNCT beam used the BNCT moderator/ reflector assembly with the variance reduction regions, and the runs for the BNCS beam used the BNCS moderator/reflector assembly with 8 cm of moderation.

3.4.6.1 Simulation Run #1 - Numerator

Using the models described in the previous sections, the following MCNP tally gives the value of the numerator per volume per starting neutron [Briesmeister 1997].

f4:n C_1 C_2
fm4 ρ *m 102* [for (n,γ) reactions] or *fm4* ρ *m 51* [for (n,n') reactions]
e4 E_1 ... E_{NG}

where: f4:n = flux tally per starting neutron
C_1 = cell denoting Foil 1 in any foil stack
C_2 = cell denoting Foil 3 in any foil stack
fm4 = flux tally multiplier with ρ m 102 gives the number of (n,γ) reactions per volume per starting neutron or with ρ m 51 gives the number of (n,n') reactions per volume per starting neutron within C_1 and C_2
ρ = density of foil material
m = foil material
e4 = energy card
$E_{1\text{-}NG}$ = boundaries of each region in MeV, up to NG energy regions.

This tally was used *twice* for each foil stack in the one foil wheel run and two boron sphere runs (In foils and Cu foils) for the BNCT and BNCS beams[5]. The first tally used the energy regions for the full range direct-unfolding method, and the second tally used the energy regions for the independent direct-unfolding method. Both methods will be described in detail in Sections 4.3.1 and 4.3.2. Appendix E lists the numerator tallies for the BNCT and BNCS beams.

3.4.6.2 Simulation Run #2 - Denominator

The denominator is the expected unperturbed neutron flux in each foil. In order to get the unperturbed flux, every material after the beam face must be replaced by air [Nigg and Harker 1998]. This includes the entire foil wheel or boron sphere assembly, including the foils and cadmium covers.

The neutron flux is then tallied in the air-filled location of each foil in each energy region. The following MCNP tally gives the value of the denominator per volume per starting neutron [Briesmeister 1997].

f4:n C_1 C_2
e4 E_1 ... E_{NG}

As in Simulation Run #1, the same two tally runs, with their respective energy regions, were conducted for each foil stack in the foil wheel and boron sphere runs for the BNCS and BNCT beams[6]. The denominator tallies for the BNCT and BNCS beams are listed in Appendix E. Dividing the results of Simulation Runs #1 by #2 for each foil gives the effective cross section in each energy region.

---

[5] For the boron sphere runs only C_1 is used in the f4:n tally. C_1 is the cell denoting all five foils in the foil stack.
[6] The note above also applies to Simulation Run #2 of the boron sphere setup.

3.4.7 Computer-Calculated Neutron Spectrum

MCNP simulation was also used to determine the expected in-air unperturbed neutron spectrum of the BNCT and BNCS beams. One separate simulation was run with each beam assembly to determine the computer-calculated neutron spectrum past the beam face. The neutron spectra of the BNCT and BNCS beams was found by tallying the neutron flux within a thin air cell in front of each beam in small energy increments. Appendix E lists the tallies used to determine the unperturbed neutron flux. Figure 3-23 shows the geometry for each in these simulation runs.

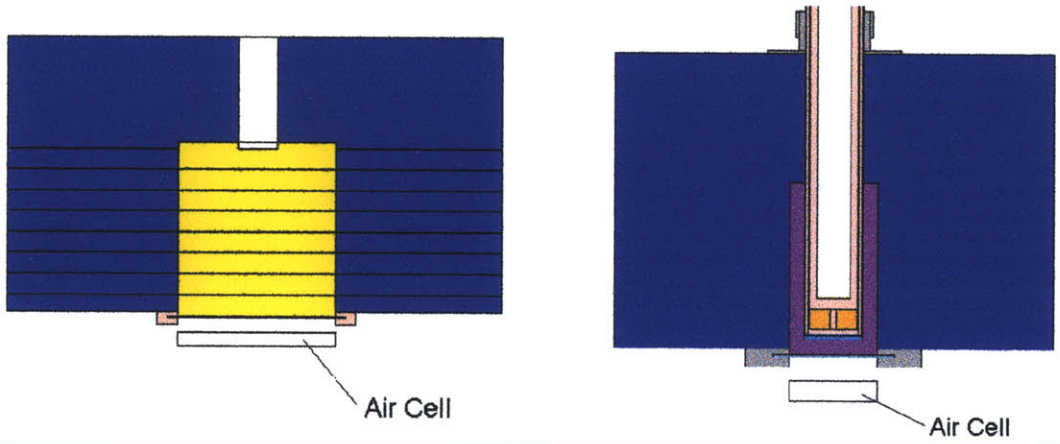

Figure 3-23: Geometry for MCNP-Calculated In-Air Unperturbed Neutron Spectra. (left) BNCT beam using the same variance reduction regions as Figure 3, (right) BNCS beam.

In summary, Chapter 3 described the methods and materials used in the spectral characterization measurements on the BNCT and BNCS beams at MIT LABA. Chapter 4 describes the results of these measurements and discusses these results.

4 Data Analysis and Results

4.1 Experiments

The spectral unfolding experiments on the BNCT and BNCS beams at MIT LABA were conducted between May and November of 1998. The specifications of each experimental run are listed in Tables 4-1 and 4-2.

Table 4-1: BNCT Experiments. Conducted with 19 cm of D_2O moderation and 1.5 MeV deuterons on the beryllium target.

Runs on the BNCT Assembly	Experimental Layout	Average Current on Target (μA)	Irradiation Time (min)	Integrated Charge on Target (C)
Run #1 (5/28/98)	Foil Wheel	75.7 ± 1.5	95.1	0.432
Run #2 (6/17/98)	Sphere (In foils)	97.9 ± 2.0	87.8	0.516
Run #3 (6/17/98)	Sphere (Cu foils)	102.2 ± 2.0	91.7	0.562
Run #4 (6/25/98)	Foil Wheel	115.3 ± 2.3	62.5	0.432
Run #5 (7/17/98)	Foil Wheel	113.1 ± 2.3	63.7	0.432
Run #6 (7/30/98)	Foil Wheel	74.7 ± 1.5	96.4	0.432
Run #7 (8/17/98)	Sphere (In foils)	102.3 ± 2.0	70.8	0.434
Run #8 (8/17/98)	Sphere (Cu foils)	101.7 ± 2.0	70.7	0.432

Table 4-2: BNCS Experiments. Conducted with 8 cm of D_2O moderation and 1.5 MeV deuterons on the beryllium target and 60 V on suppression electrode.

Runs on the BNCS Assembly	Experimental Layout	Average Current on Target (μA)	Irradiation Time (min)	Integrated Charge on Target (C)
Run #1 (11/6/98)	Foil Wheel	100.3 ± 2.0	62.3	0.375
Run #2 (11/6/98)	Sphere (Cu foils)	98.6 ± 2.0	63.4	0.375
Run #3 (11/6/98)	Sphere (In foils)	101.3 ± 2.0	61.7	0.375
Run #4 (11/9/98)	Sphere (Cu foils)	98.2 ± 2.0	63.7	0.375
Run #5 (11/9/98)	Sphere (In foils)	94.3 ± 1.9	59.5	0.337
Run #6 (11/12/98)	Foil Wheel	98.0 ± 2.0	63.7	0.375

4.2 Reaction Rates

The following sections describe the method used to calculate the reaction rate of each foil from its counting results. The method of error propagation is also described. The measured reaction rates are dependent on the average current-on-target of the irradiation run. Therefore, in order to compare the results of each experimental run, the reaction rates must be normalized to the same current-on-target. The calculated un-normalized and normalized reaction rates for each foil are presented and discussed in Sections 4.2.3 and 4.2.4.

4.2.1 Reaction Rate Calculations

The reaction rates used in the spectral unfolding matrix **[R]** in Equation 4-1 are actually the volume-averaged reaction rates per atom per μA.

$$[\mathbf{A}][\Phi] = [\mathbf{R}] \qquad [4\text{-}1]$$

The following equations demonstrate the relationship between RR, A_∞, and R, referencing Equations 2-1, 2-4, and 3-1.

$$R = \int_0^\infty \sigma_f(E)\Psi_f(E)dE \approx \sigma\Phi \qquad [4\text{-}2]$$

$$R = \sigma\Phi = \frac{RR}{NV} = \frac{A_\infty}{NV} \qquad [4\text{-}3]$$

where:
- R = un-normalized volume-averaged reaction rate per atom (reactions/sec-atom),
- $\sigma_f(E)$ = microscopic reaction cross section for a foil as a function of energy (cm^2),
- $\psi_f(E)$ = volume-averaged scalar neutron flux per atom within the foil as a function of energy (perturbed) (n/cm^2-sec-atom)
- RR = reaction rate (reactions/sec),
- N = number density ($atoms/cm^3$), and
- V = foil volume (cm^3).

Given that the saturated activity is found from Equation 2-6, the normalized values of R that are input into the spectral unfolding matrix **[R]** are calculated by Equation 4-4.

$$R_i = \frac{(C_i - B_i)\lambda_i}{\varepsilon_i b_{\gamma_i}(1-e^{-\lambda_i t_{i_i}})(1-e^{-\lambda_i t_{c_i}})e^{-\lambda_i t_{w_i}} N_i V_i A_i} \left(\frac{reactions}{cm^3 \cdot atom \cdot \sec \cdot \mu A}\right) \quad [4\text{-}4]$$

where: R_i = volume averaged reaction rate per atom for reaction *i*,
A_i = average current-on-target for irradiation run of reaction *i* (μA).

The counts, background counts, irradiation time, wait time, counting time, and average current-on-target were measured in the foil wheel and boron sphere experiments as described in Chapter 3. The following sections will discuss the source the remaining elements.

4.2.1.1 Decay Constant and Branching Ratio

Table 4-3 lists the calculated decay constants and branching ratios for each radioactive decay used in the reaction rate calculations.

Table 4-3: Decay Constants and Branching Ratios for each Reaction [LANL 1998].[1] The decay constant for each induced radioactive material was found directly from the half-life listed. The branching ratio for each gamma peak of interest was calculated by multiplying the yield of gamma peak by the discrete spectrum normalization factor for the radiation type, as listed in the LANL data sheets. See Appendix B for the LANL data sheets for each induced radioactive material.

Induced Radioactive Material	Decay Constant (sec^{-1})	Gamma Peak of Interest (keV)	Branching Ratio
$^{116}In^{m}$	2.13E-04	1294	0.8440
^{198}Au	2.98E-06	411	0.9550
^{187}W	8.06E-06	686	0.2639
^{56}Mn	7.47E-05	847	0.9887
^{64}Cu	1.52E-05	511	0.3580
$^{115}In^{m}$	4.29E-05	336	0.4580

[1] LANL data site was chosen over other sources, such as Nuclear Data Sheets, because it presented the uncertainties in each measurement.

4.2.1.2 Detector Efficiency

The Environmental Research and Radiochemistry Detector Facility at MIT provided a Sb-Eu standard for efficiency calculations. As explained in Section 3.3.4, the final detector efficiency found from this standard is the absolute efficiency of the detector, taking into account solid angle. The detector facility supplied an emission rate (and uncertainty) list for each predominant peak of the standard as of 1200 EST September 1, 1998; see Appendix D. For each gamma peak of interest counted, two listed standard peaks directly above and below the energy of gamma peak of interest were selected. The standard emission rate at the time of the experiment for each energy peak was found by taking into account the decay of the standard from the date of the known emission rate, as shown in Equation 4-5.

$$\frac{d\gamma}{dt}(t_1) = \frac{d\gamma}{dt}(t_0)e^{-\lambda_n(t_1-t_0)} \qquad [4\text{-}5]$$

where: $(d\gamma/dt)_n$ = emission rate of peak *n* (γ/sec),
t_0 = 1200 EST September 1, 1988,
t_1 = time of standard count (sec), and
λ_n = decay constant of Sb or Eu (sec^{-1}).

The detector efficiency at the energy of each selected gamma ray peak was calculated by dividing the count rate measured under each selected peak by the $(d\gamma/dt)_n$ at t_1. There is a linear relationship between the natural log of the photon energy and the natural log of the efficiency, ε, as shown in Equation 4-6. Regression analysis is then necessary to determine the detector efficiency at the energy of the foil peaks.

$$\ln(\varepsilon) = m \times \ln(E_\gamma) + b \qquad [4\text{-}6]$$

where: m = slope,
E_γ = gamma ray energy (keV), and
b = intercept.

A linear least-squares fit was first conducted; however, it was found inadequate for this situation. A linear least-squares fit assumes that the error in each of the y-axis data points (in this case, the natural log of the efficiencies) is equal in order to fit a line between the data points. This is not the case. The uncertainties in each of the efficiencies are exactly known and are not equal; therefore, a weighted least-squares fit was selected.

The weighted least-squares fit of the efficiency data takes into account the exact errors in each of the data points and draws a line that best fits the data within the error bars. See Appendix D for a comparison of the best fit lines and extrapolated uncertainties for each regression technique. The weighted least-squares fit method used to determine the slope, m, and intercept, b, of Equation 4-6 is shown in the following three equations [Taylor 1997].

$$\Delta = \sum_{i=1}^{N} w_i \sum_{i=1}^{N} w_i \left(\ln(\varepsilon_i)\right)^2 - \left(\sum_{i=1}^{N} w_i \ln(\varepsilon_i)\right)^2 \qquad [4\text{-}7]$$

$$m = \frac{\sum_{i=1}^{N} w_i \left(\ln(\varepsilon_i)\right)^2 \sum_{i=1}^{N} w_i \ln(E_{\gamma_i}) - \sum_{i=1}^{N} w_i \ln(\varepsilon_i) \sum_{i=1}^{N} w_i \ln(\varepsilon_i) \ln(E_{\gamma_i})}{\Delta} \qquad [4\text{-}8]$$

$$b = \frac{\sum_{i=1}^{N} w_i \sum_{i=1}^{N} w_i \ln(\varepsilon_i) \ln(E_{\gamma_i}) - \sum_{i=1}^{N} w_i \ln(\varepsilon_i) \sum_{i=1}^{N} w_i \ln(E_{\gamma_i})}{\Delta} \qquad [4\text{-}9]$$

where: N = number of selected photon energies for the fitting process, and
w_i = weight assigned to each y-datum point.

The weight assigned to each efficiency datum point is the inverse of the absolute variance in the natural log of the efficiency.[2]

$$w_i = \frac{1}{\sigma^2_{\ln(\varepsilon_i)}} \qquad [4\text{-}10]$$

where: w_i = weight for efficiency *i*, and
$\sigma_{\ln(\varepsilon i)}$ = total **absolute** uncertainty in the natural log of efficiency *i*.

The relative uncertainties in the emission rate data and counting uncertainties contribute to the total efficiency uncertainty. Adding these relative uncertainties in quadrature gives the total relative efficiency uncertainty.

$$\sigma_{\varepsilon_i} = \sqrt{\sigma^2_{std_i} + \sigma^2_{c_i}} \qquad [4\text{-}11]$$

where: $\sigma_{\varepsilon i}$ = total relative uncertainty in efficiency *i*,
σ_{stdi} = relative uncertainty in emission rate *i*, and
σ_{ci} = relative counting uncertainty for standard peak *i*.

The $\sigma_{\ln(\varepsilon i)}$, needed in Equation 4-10, can then be found by multiplying the total relative uncertainty by the natural log of the efficiency, as shown in Equation 4-12 below.

$$\sigma_{\ln(\varepsilon_i)} = \ln(\varepsilon_i) \times \sigma_{\varepsilon_i} \qquad [4\text{-}12]$$

The efficiencies at the energy of the foil peaks measured in each detector are then found by extrapolating from the best fit line, using Equations 4-6, 4-8, and 4-9, at the exact energies of the gamma peaks of interest. The detector efficiencies for these experiments ranged from 0.5% to 2.8%.

---

[2] One standard deviation uncertainties are signified by the variable σ. An unbolded, normal size σ

4.2.1.3 Foil Volume

The volume of each foil is found directly from the measured mass of each foil and the density of the foil material. For the Mn/Cu foil, the density was taken as the weighted average of each element's density, based on its abundance in the foil. Eighty-one percent of the subsequent calculated volume was taken as the volume of natural manganese in the foil.

4.2.1.4 Number Density

The number density of each foil material is found by Equation 4-13. For the Mn/Cu foils, the number density was found only for manganese. The volume calculation takes into account the abundance of manganese in the foil.

$$N_i = \frac{\rho_i N_A}{A_i} \qquad [4\text{-}13]$$

where: N_i = number density (atoms/cm^3)
ρ_i = density of foil for reaction *i* (g/cm^3),
N_A = Avogadro's number of atoms, 6.02E+23 (atoms/mole), and
A = atomic weight of foil for reaction *i* (g/mole).

4.2.2 Uncertainty of Reaction Rate

The uncertainty in the reaction rate from Equation 4-4 needs to be calculated and entered into the final spectral unfolding matrix program in order to find the total uncertainty in the final unfolded flux in each energy region. The uncertainty in the reaction rate is based on the uncertainty of each of its elements. The following is a list of elements that were considered to contribute to the reaction rates' uncertainties:

1. average current-on-target,
2. counting,
3. decay constant,
4. volume,

---

signifies a relative uncertainty. A bolded, slightly larger σ signifies an absolute uncertainty.

5. efficiency, and
6. branching ratio.

The error in the number density and time measurements are considered negligible. Since the listed elements are either multiplied or divided in the reaction rate equation, with one exception[3], the error propagation can be calculated through the quadrature sum of the relative uncertainties of each element, as shown in Equation 4-14.

$$\sigma_{R_i} = \sqrt{(\sigma_m)^2 + (\sigma_{C_i})^2 + (\sigma_{\lambda_i})^2 + (\sigma_{V_i})^2 + (\sigma_{\varepsilon_i})^2 + (\sigma_{b_{\gamma_i}})^2} \qquad [4\text{-}14]$$

where: σ_{Ri} = relative uncertainty in reaction rate *i*,
σ_m = relative uncertainty in current-on-target measurement,
σ_{Ci} = relative uncertainty in counting *i*,
$\sigma_{\lambda i}$ = relative uncertainty in the decay constant *i*,
σ_{vi} = relative uncertainty in foil volume *i*,
$\sigma_{\varepsilon i}$ = relative uncertainty in the fitted detector efficiency *i*, and
$\sigma_{b\gamma i}$ = relative uncertainty in the branching ratio *i*.

4.2.2.1 Current-on-Target Error

The integrated charge-on-target is directly measured in each experiment and when divided by the irradiation time, gives the average current-on-target. The measurement error for the charge-on-target is 2% [White 1998]. The current measurement error is equal to this charge error because the error in time measurements is considered to be negligible.

Another contribution to the error in the current-on-target measurement is the secondary electron effect. When the deuteron beam impinges on the beryllium target, secondary electrons are produced. Some secondary electrons escape the target face

[3] The decay constant is the one exception. It is not only multiplied in the numerator of the reaction rate equation, but is also three times in exponents in the denominator. For simplicity, it is just assumed that the decay constant's uncertainty can simply be added in quadrature with the other elements.

and hit the target housing [White 1998]. This causes incorrect measurements of the charge-on-target and average current-on-target.

When different currents-on-target are selected on the accelerator control panel different focusing specifications are required. This causes the beam impinging on the target to be different in shape depending on the current-on-target. The different shape of the beams can allow different amounts of secondary electrons to escape the target face. Therefore, the measured current-on-target may not be the actual current-on-target. The ratio between the actual and measured currents-on-target is specific to the beam shape and therefore also the magnitude of the measured current-on-target.

A full analysis of the current-on-target measurement problem, including exploration into causes other than the secondary electron effect, has not been conducted for this work. Preliminary experiments suggest that the actual-to-measured current ratios can range from 30-50% for the BNCT beam [White 1998]. For the BNCS beam, the secondary electron effect is suppressed through the use of a suppression electrode. This electrode produces an electric field that helps to reflect escaping secondary electrons back onto the target. The suppression electrode was set to 60 V for the BNCS experiments.

Since the extent at which secondary electrons affect the current measurement has not been determined, this error contribution was not added to the overall error in the normalized reaction rates as listed in Table 4-4. It is important to note that any error in the average current-on-target does not affect the absolute measured un-normalized activation foil reaction rates or the shape and magnitude of the un-normalized unfolded neutron spectrum found by these measurements. The current errors will only affect the

manner in which the absolute measured data are normalized to the same current-on-target.

4.2.2.2 Counting Error

The HP(Ge) detector system used to count the foils uses a multi-channel analyzer computer program described in Section 3.3.4. This program distinguishes the peaks from the background and automatically calculates the counting error under each peak found. The counting error calculated by the program takes into account the statistical error due to the number of counts under the peak and background counts [Canberra 1998]. The relative counting errors found by the detector system for each gamma peak of interest were directly input into Equation 4-14 with no further manipulation.

4.2.2.3 Decay Constant Error

The errors in the decay constants were taken directly from the LANL data sheets, which display the 1-σ relative uncertainty in the half-lives [LANL 1998]. Since the conversion of half-life to decay constant does not contribute any additional errors, the relative uncertainties in the decay constants were assumed to be equal to the relative uncertainties in the half-lives.

4.2.2.4 Foil Volume Error

The foil volume error was set equal to the error in each foil's mass measurement. It is assumed that the error in the density value is negligible. As described in Section 3.3.2.2, the microscale in the Environmental Research and Radiochemistry Detector Facility that was used to weigh the foils is accurate to within $\pm 5 \times 10^{-5}$g. Appendix C lists the measured mass of each foil and its respective measurement error.

4.2.2.5 Detector Efficiency Error

The efficiency estimates found by using the weighted least-squares method have a fitting error. This absolute uncertainty is one value and is the same regardless of the estimated datum point; it is found by Equation 4-15 [Taylor 1997].

$$\sigma_{\ln(\varepsilon)} = \sqrt{\frac{1}{N-2}\sum_{i=1}^{N}\left(\ln(\varepsilon_i)-\left(m\times\ln(E_{\gamma_i})+b\right)\right)^2} \qquad [4\text{-}15]$$

where: $\sigma_{\ln(\varepsilon)}$ = absolute uncertainty in the natural log of efficiency estimates, and
N = number of selected photon energies for the fitting process.

The relative uncertainty in each fitted datum point is found by dividing the absolute uncertainty by the fitted $\ln(\varepsilon_i)$. The relative uncertainty in the $\ln(\varepsilon_i)$ can be assumed to be the relative uncertainty in the ε_i because no errors are added in the conversion of $\ln(\varepsilon_i)$ to ε_i.

$$\sigma_{\varepsilon_i} = \sigma_{\ln(\varepsilon_i)} = \frac{\sigma_{\ln(\varepsilon)}}{\ln(\varepsilon_i)} \qquad [4\text{-}16]$$

where: $\sigma_{\ln(\varepsilon i)}$ = relative uncertainty in the natural log of efficiency *i*.

4.2.2.6 Branching Ratio Error

The error in the yield of each gamma peak and the discrete spectrum normalization factor in the LANL data sheets contribute to the error in the branching ratio [LANL 1998]. Since these factors are multiplied to determine the branching ratio, the relative uncertainty in the branching ratio is found by the quadrature sum of their relative uncertainties. These uncertainties can be found on the LANL data sheets for each reaction and gamma peak [LANL 1998].

Table 4-4 lists the calculated relative errors for each reaction rate component as they contribute to the total reaction rate error for the BNCT and BNCS experiments.

Table 4-4: Errors in Measured Reaction Rates for the BNCT and BNCS Beams.

	BNCT beam	BNCS beam
Current Measurement	2%	2%
Counting	1.3 - 4.1%	1.0 - 2.4 %
Decay Constant	0.1 - 0.4%	0.1 - 0.4%
Foil Volume	0.04 - 0.1%	0.04 - 0.1%
Detector Efficiency	1.4 - 3.1%	1.6 - 3.7%
Branching Ratio	0.1 - 4.1%	0.1 - 4.1%
Number Density	Negligible	Negligible
Time Measurement	Negligible	Negligible

4.2.3 BNCT Results

Table 4-5 lists the un-normalized reaction rates for the experimental runs conducted on the BNCT beam. The data from the first experimental run conducted on 28 May 1998 were not used and are not presented in the table. A change to the accelerator in early June makes comparing the results of this first run to all subsequent runs complicated. Data for Foil 3 in the tungsten interaction of Run #5 are unavailable because the incorrect foil was counted after irradiation. Table 4-6 lists the normalized reaction rates used in the spectral unfolding calculations for the BNCT beam.

Table 4-5: Un-normalized Volume-Averaged Reaction Rates per Atom for Foils Irradiated in the BNCT Beam at MIT LABA (reactions/sec-atom).

Foil Wheel Irradiations (n,gam)	Photon Energy (keV)	Run #4 6/25/98	Run #5 7/17/98	Run #6 7/30/98
In - Foil 1	1294	2.06E-16	1.98E-16	1.58E-16
In - Foil 3	1294	7.95E-17	7.46E-17	4.92E-17
W - Foil 1	686	1.27E-16	1.23E-16	8.52E-17
W - Foil 3	686	5.73E-17	N/A	3.92E-17
Cu - Foil 1	511	9.90E-19	1.20E-18	7.56E-19
Cu - Foil 3	511	8.76E-19	1.05E-18	5.17E-19
Mn -Foil 1	847	4.10E-18	4.27E-18	2.52E-18
Mn - Foil 3	847	2.95E-18	2.96E-18	1.89E-18
Au - Foil 1	411	1.77E-16	1.89E-16	1.28E-16
Au - Foil 3	411	7.76E-17	9.24E-17	5.22E-17
Au* - Foil 1	411	5.01E-16	5.10E-16	3.50E-16
Au* - Foil 3	411	3.84E-16	4.04E-16	2.27E-16

Sphere Irradiations (all 5 foils)	Photon Energy (keV)	Run #2 6/17/98	Run #3 6/17/98	Run #7 8/17/98	Run #8 8/17/98
In(n,gam)	1294	2.64E-19		4.58E-19	
In(n,n')	336	7.06E-20		1.38E-19	
Cu(n,gam)	511		7.25E-20		9.37E-20

Table 4-6: Normalized Volume-Averaged Reaction Rates per Atom per microAmp for Foils Irradiated in the BNCT Beam at MIT LABA (reactions/sec-atom-μA).

Foil Wheel Irradiations (n,gam)	Photon Energy (keV)	Run #4 6/25/98	Run #5 7/17/98	Run #6 7/30/98	Average	Absolute Error
In - Foil 1	1294	1.78E-18	1.75E-18	2.12E-18	1.89E-18	7E-20
In - Foil 3	1294	6.90E-19	6.59E-19	6.59E-19	6.7E-19	3E-20
W - Foil 1	686	1.10E-18	1.09E-18	1.14E-18	1.11E-18	6E-20
W - Foil 3	686	4.97E-19	N/A	5.25E-19	5.1E-19	3E-20
Cu - Foil 1	511	8.59E-21	1.06E-20	1.01E-20	9.76E-21	5E-22
Cu - Foil 3	511	7.60E-21	9.32E-21	6.92E-21	7.9E-21	4E-22
Mn -Foil 1	847	3.55E-20	3.78E-20	3.37E-20	3.6E-20	1E-21
Mn - Foil 3	847	2.56E-20	2.62E-20	2.53E-20	2.6E-20	9E-22
Au - Foil 1	411	1.54E-18	1.67E-18	1.72E-18	1.64E-18	6E-20
Au - Foil 3	411	6.73E-19	8.17E-19	6.99E-19	7.3E-19	3E-20
Au* - Foil 1	411	4.35E-18	4.51E-18	4.68E-18	4.5E-18	1E-19
Au* - Foil 3	411	3.33E-18	3.57E-18	3.04E-18	3.3E-18	1E-19

Sphere Irradiations (all 5 foils)	Photon Energy (keV)	Run #2 6/17/98	Run #3 6/17/98	Run #7 8/17/98	Run #8 8/17/98	Average	Absolute Error
In(n,gam)	1294	2.70E-21		4.47E-21		3.6E-21	2E-22
In(n,n')	336	7.21E-22		1.34E-21		1.03E-21	5E-23
Cu(n,gam)	511		7.09E-22		9.22E-22	8.2E-22	4E-23

4.2.4 BNCS Results

Table 4-7 shows the un-normalized reaction rates for the BNCS beam measurements, and Table 4-8 shows the normalized reaction rates used in the spectral unfolding calculations for the BNCS beam.

Table 4-7: Un-normalized Volume-Averaged Reaction Rates per Atom for Foils Irradiated in the BNCS Beam at MIT LABA (reactions/sec-atom).

Foil Wheel Irradiations (n,gam)	Photon Energy (keV)	Run #1 11/6/98	Run #6 11/12/98
In - Foil 1	1294	8.56E-16	6.83E-16
In - Foil 3	1294	4.30E-16	3.47E-16
W - Foil 1	686	8.26E-16	7.72E-16
W - Foil 3	686	3.85E-16	3.54E-16
Cu - Foil 1	511	6.05E-18	5.94E-18
Cu - Foil 3	511	5.76E-18	5.34E-18
Mn -Foil 1	847	3.03E-17	1.98E-17
Mn - Foil 3	847	2.17E-17	1.78E-17
Au - Foil 1	411	1.14E-15	1.05E-15
Au - Foil 3	411	4.85E-16	4.29E-16
Au* - Foil 1	411	2.88E-15	2.69E-15
Au* - Foil 3	411	2.13E-15	2.01E-15

Sphere Irradiations (all 5 foils)	Photon Energy (keV)	Run #2 11/6/98	Run #3 11/6/98	Run #4 11/9/98	Run #5 11/9/98
In(n,gam)	1294	6.30E-18		5.25E-18	
In(n,n')	336	4.10E-18		3.56E-18	
Cu(n,gam)	511		7.59E-19		6.43E-19

Table 4-8: Normalized Volume-Averaged Reaction Rates per Atom per microAmp for Foils Irradiated in the BNCS Beam at MIT LABA (reactions/sec-atom-μA).

Foil Wheel Irradiations (n,gam)	Photon Energy (keV)	Run #1 11/6/98	Run #6 11/12/98	Average	Absolute Error
In - Foil 1	1294	8.53E-18	6.97E-18	7.8E-18	3E-19
In - Foil 3	1294	4.29E-18	3.54E-18	3.9E-18	2E-19
W - Foil 1	686	8.24E-18	7.88E-18	8.1E-18	5E-19
W - Foil 3	686	3.84E-18	3.62E-18	3.7E-18	2E-19
Cu - Foil 1	511	6.04E-20	6.06E-20	6.1E-20	3E-21
Cu - Foil 3	511	5.74E-20	5.45E-20	5.6E-20	2E-21
Mn -Foil 1	847	3.02E-19	2.02E-19	2.5E-19	1E-20
Mn - Foil 3	847	2.16E-19	1.82E-19	1.99E-19	8E-21
Au - Foil 1	411	1.13E-17	1.07E-17	1.10E-17	5E-19
Au - Foil 3	411	4.83E-18	4.38E-18	4.6E-18	2E-19
Au* - Foil 1	411	2.87E-17	2.75E-17	2.8E-17	1E-18
Au* - Foil 3	411	2.13E-17	2.05E-17	2.1E-17	9E-19

Sphere Irradiations (all 5 foils)	Photon Energy (keV)	Run #2 11/6/98	Run #3 11/6/98	Run #4 11/9/98	Run #5 11/9/98	Average	Absolute Error
In(n,gam)	1294		6.22E-20		5.57E-20	5.9E-20	2.4E-21
In(n,n')	336		4.05E-20		3.77E-20	3.9E-20	1.7E-21
Cu(n,gam)	511	7.69E-21		6.55E-21		7.1E-21	2.9E-22

4.3 MCNP Simulation

MCNP simulation was used to calculate the effective cross sections of each foil in various energy regions and the expected unperturbed neutron spectra from the BNCT and BNCS assemblies. The energy regions over which the effective cross sections were calculated are based on the specific spectral unfolding technique used: "full range" or "independent point" [Nigg *et al.* 1997].

4.3.1 Full Range Method

The full range method is the primary method used to unfold the epithermal neutron spectrum [Nigg *et al.* 1997]. This method takes the reaction rates of the first foils in each foil packet and inputs them into **[R]** of Equation 4-1. The energy regions selected for unfolding are determined by selecting energies in between the resonance peaks of each reaction, including one at the cadmium cutoff and one above the threshold reaction. The upper limit of the highest energy region was set at 14 MeV. These energy regions are used in the MCNP simulation to determine the effective cross sections, which are input into **[A]** in Equation 4-1. The resulting solution of that equation gives the unperturbed neutron flux in every energy region. It is assumed that the unfolded fluxes are constant across their corresponding energy regions, creating a continuous spectrum from the lowest energy region to the highest.

The energy regions selected for the full range method in this paper were taken from the energy regions used in previous applications of the INEEL spectral unfolding method [Nigg *et al.* 1997]. The simulations used to calculate the effective cross sections for the full range method used the following reactions: Au*(n,γ)[4], In(n,γ),

[4] Au*(n,γ) signifies the uncovered gold foils irradiated in the foil wheel.

Au(n,γ), W(n,γ), Mn(n,γ), and Cu(n,γ) in the foil wheel, and In(n,γ), Cu(n,γ), and In(n,n') in the boron sphere. For each of these reactions, the required MCNP tallies to calculate the effective cross sections regions for both the BNCT and BNCS beams (described in Section 3.4.6) were conducted for Foils 1 and 3 in the eight energy regions shown in Table 4-9. Although the results of the third foil for each reaction are not used in this paper in the full range method, it is possible to add the results of the third foils in the future as long as they are independent of the results of the first foils.

Table 4-9: Selected Energy Regions for the Full Range Method. According to MCNP simulation, 99% of the absorption reactions for the Cu(n,gam) reaction in the boron sphere occur between 550 eV and 24 keV [Nigg *et al.* 1997].

	Energy of Primary Peaks	Selected Energy Regions
Lower Limit		**0.001 eV**
Au*(n,gam) Cadmium Cutoff		**0.5 eV**
In(n,gam)	1.46 eV	
		2.44 eV
Au(n,gam)	5 eV	
		6.6 eV
W(n,gam)	18 eV	
		78 eV
Mn(n,gam)	340 eV	
		454 eV
Cu(n,gam)	580 eV	
		690 eV
Cu(n,gam) - sphere	550 eV - 24 keV	
		320 keV
In(n,n') - threshold	339 keV	
Upper Limit		**14 MeV**

4.3.2 Independent Point Method

The independent point method uses the reaction rates of both the first and third foils in each foil packet [Nigg *et al.* 1997]. A separate solution to Equation 4-1 is found for each reaction. The **[R]**'s for each separate reaction are 2x1 matrices that contain the reaction rate information from the first and third foils for that reaction. There are only two energy regions for each solution, making each **[A]** a 2x2 matrix. One energy region is the bounded by the minimum of the primary resonance peak of the particular reaction, and the other energy region is all energies above and below the peak. The solution of Equation 4-1, **[Φ]**, for each reaction contains two results: 1) the neutron flux under the resonance peak, and 2) the neutron flux over all other energies. Only the first result is useful. The overall results of this method will give a flux datum point at each resonance peak.

The energy regions selected for the independent point method in this paper were calculated independently for each reaction. Table 4-10 lists the energy regions selected for each reaction. The boundaries around the primary resonance peak for each (n,γ) reaction were selected at the minimum of each peak (the point at which the peak's edges returned to normal cross section trend line). The reactions used in the independent point method include of all those listed in Table 4-10 and additional $Au^*(n,\gamma)$ and $Au(n,\gamma)$ reactions for the thermal neutron region. The required MCNP tallies to calculate the effective cross sections regions for the BNCT and BNCS beams (described in Section 3.4.6) were obtained from Foils 1 and 3 in the selected energy regions listed to right of the respective reaction in Table 4-10.

Table 4-10: Selected Energy Regions of the Independent Point Method. The reactions used to obtain data in the thermal neutron region were Au*(n,γ) and Au(n,γ) [uncovered and covered].

	Energy of Primary Peaks	Selected Energy Regions
Lower Limit		0.001 eV
Thermal Neutron Region	0.5 eV	**0.5 eV**
Upper Limit		14 MeV
Lower Limit		0.001 eV
		1.1 eV
In(n,gam)	1.46 eV	
		1.8 eV
Upper Limit		14 MeV
Lower Limit		0.001 eV
		4.3 eV
Au(n,gam)	5 eV	
		5.5 eV
Upper Limit		14 MeV
Lower Limit		0.001 eV
		17 eV
W(n,gam)	18 eV	
		20.5 eV
Upper Limit		14 MeV
Lower Limit		0.001 eV
		250 eV
Mn(n,gam)	340 eV	
		410 eV
Upper Limit		14 MeV
Lower Limit		0.001 eV
		570 eV
Cu(n,gam)	580 eV	
		590 eV
Upper Limit		14 MeV
Lower Limit		0.001 eV
		550 eV
Cu(n,gam) - sphere	550 eV - 24 keV	
		24 keV
Upper Limit		14 MeV
Lower Limit		0.001 eV
		320 keV
In(n,n') - threshold	339 keV	
Upper Limit		**14 MeV**

4.3.3 Effective Cross Section Calculations and Results

The effective cross sections were calculated from the tally data obtained from the MCNP simulations. The tallied number of (n,γ) or (n,n') reactions per volume per starting particle was divided by the tallied unperturbed neutron flux per volume per starting neutron in each foil in each respective energy region. Appendix F lists the effective cross sections used in the **[A]** matrix for the BNCT and BNCS beam spectral unfolding calculations.

The errors in the effective cross sections were calculated from the errors in the following items:

1. numerator tally,
2. denominator tally,
3. foil thickness, and
4. foil placement.

The errors in the numerator and denominator tallies, representing the statistical uncertainties in the MCNP calculations, not including any uncertainties in the neutron cross sections or source spectra, were calculated by MCNP [Briesmeister 1997].

4.3.3.1 Foil Thickness Error

The uncertainty in the foil thickness also needs to be considered because the simulations assumed the nominal thickness for each foil. The largest difference between the nominal and measured thickness was used as the uncertainty in the foil thickness for each foil material. Appendix C lists the differences between the nominal and measured thicknesses for each foil.

4.3.3.2 Foil Placement Error

The horizontal distance from the beam face to the first foil in the foil wheel and boron sphere was measured for each beam. This measurement was used in the MCNP

model. The horizontal distance was measured to within ±0.05cm, and the first foils were 6.20 cm and 3.00 cm from the beam face in the BNCT and BNCS beams, respectively. Therefore, the foil placement errors for the BNCT and BNCS beams are 1.0% and 1.5%, respectively.

The relative numerator, denominator, foil thickness, and foil placement uncertainties were added in quadrature to obtain the total error in the effective cross sections. Table 4-11 shows the range of contribution of each component to the effective cross section error in the BNCT and BNCS beams.

Table 4-11: Errors in the Calculated Effective Cross Sections for the BNCT and BNCS Beams.

	BNCT beam	BNCS beam
Numerator Tally	1-8%	1-59%*
Denominator Tally	1-14%	1-8.6%
Indium foil thickness	0.0-18%	0.0-18%
Gold foil thickness	4.0-7.0%	4.0-7.0%
Copper foil thickness	2.0-3.0%	2.0-3.0%
Manganese foil thickness	0.0-4.8%	0.0-4.8%
Tungsten foil thickness	0.0-14%	0.0-14%
Placement of foils	1.0%	1.5%

*98% error was found in one energy region in the In(n,gam) sphere reaction. Due to the high uncertainty, this reaction was not used in the spectral unfolding for the BNCS beam. 59% error was found only in one energy region in the Cu(n,gam) sphere reaction. This reaction was still used.

4.3.4 MCNP-calculated Neutron Spectra

The MCNP-calculated neutron spectra found by the method described in Section 3.4.7 for the BNCT and BNCS beams are shown in Figures 4-1 and 4-2. The error of the flux in each energy bin was found by MCNP and is represented in the figures as error bars. Most errors were below 1%. These errors do not include the errors in the 1.5 MeV Be(d,n) source spectrum measured by Guzek [Guzek 1998]. Since the neutron flux is in units of neutrons/cm^2-eV-starting particle, all MCNP data points must

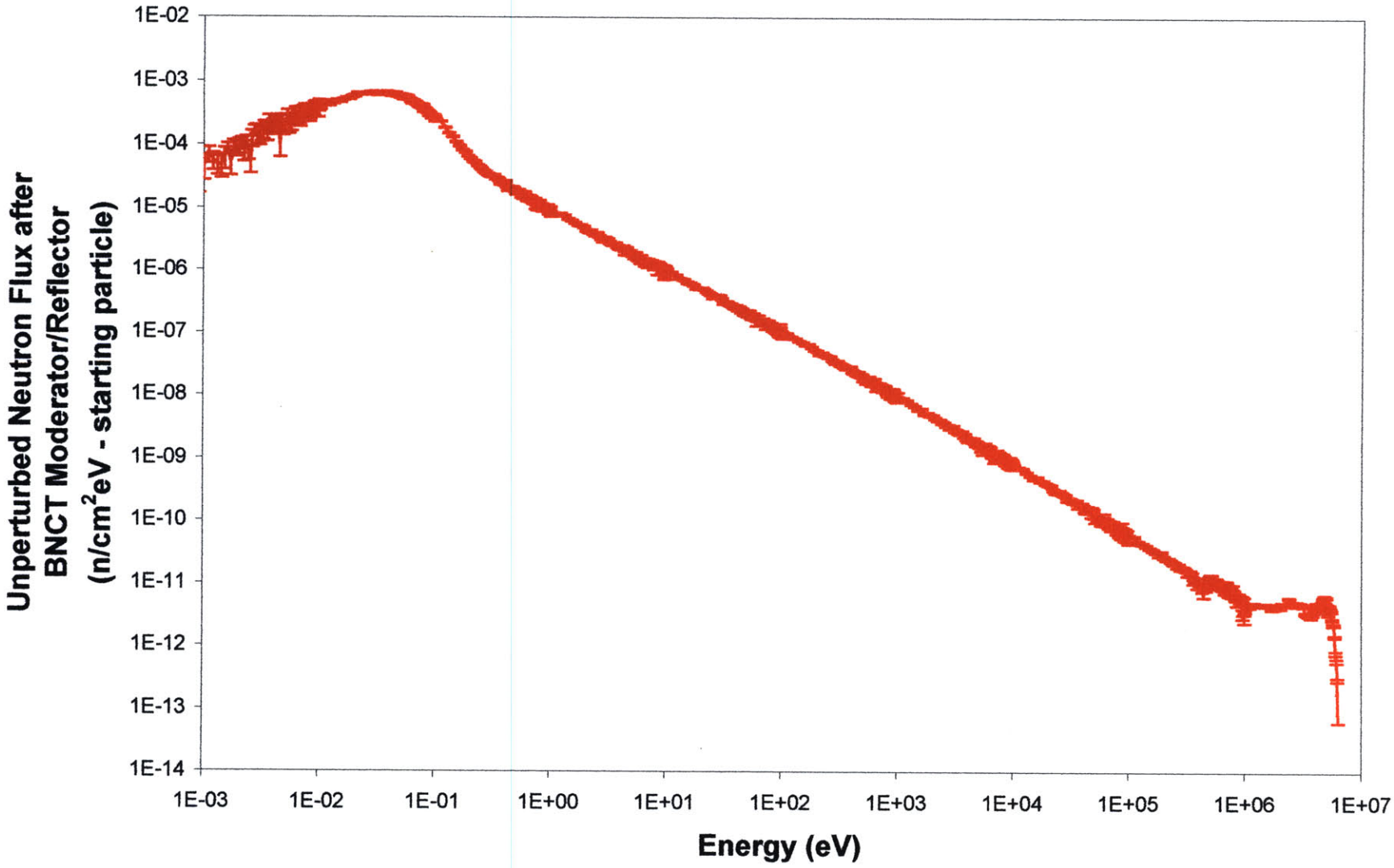

Figure 4-1: MCNP-calculated Unperturbed Neutron Spectrum of the BNCT Beam at MIT LABA Using the Guzek Source Spectrum. The spectrum was not scaled by the yield of the 1.5 MeV Be(d,n) reaction.

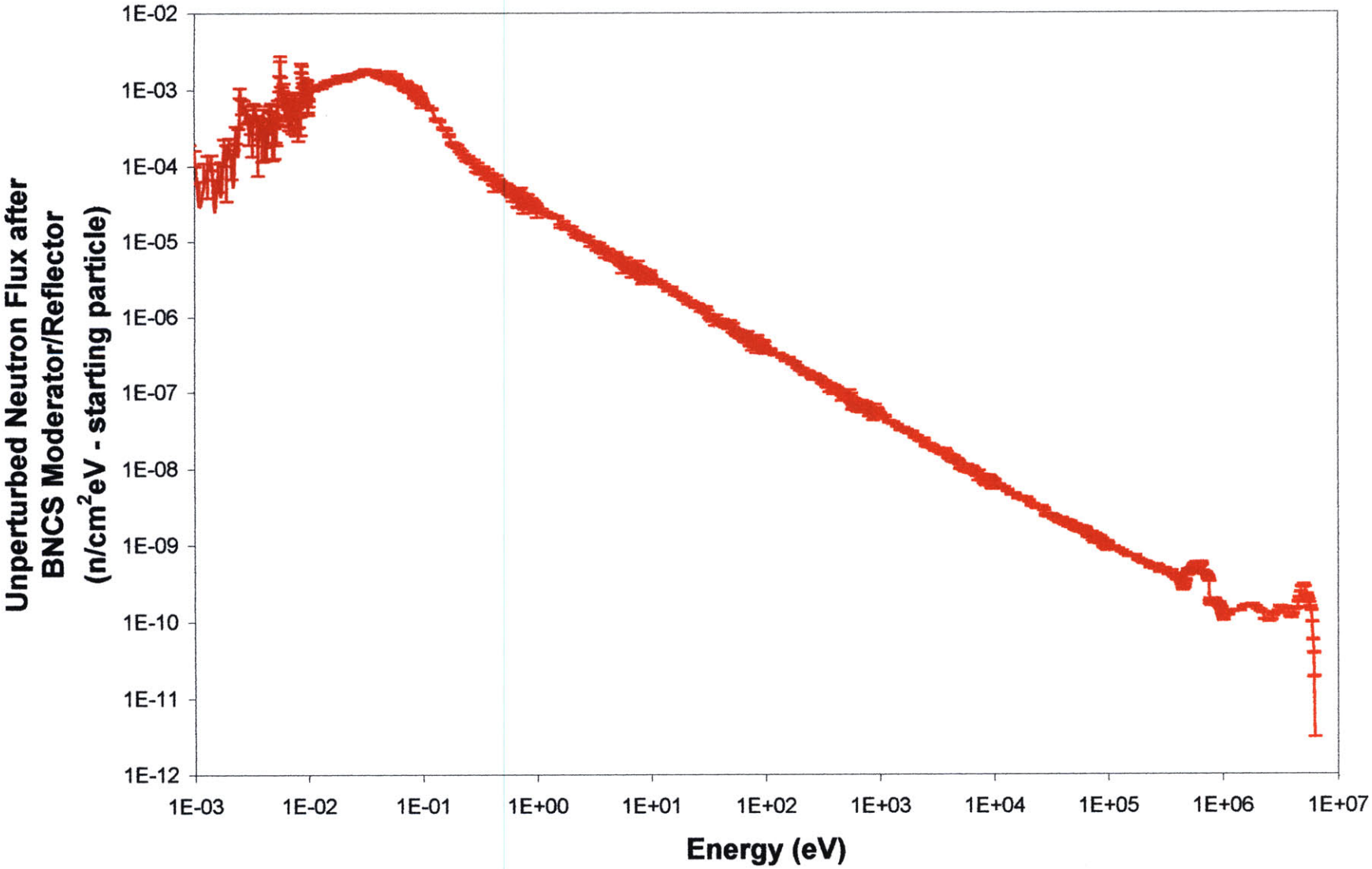

Figure 4-2: MCNP-calculated Unperturbed Neutron Spectrum of the BNCS Beam at MIT LABA Using the Guzek Source Spectrum. The spectrum was not scaled by the yield of the 1.5 MeV Be(d,n) reaction.

be multiplied by the yield of the source 1.5 MeV Be(d,n) reaction to obtain the absolute values of the total neutron yield and spectra of the beams.

The neutron yield of the 1.5 MeV Be(d,n) reaction has been published by several authors as shown in Table 4-12. The cause of the inconsistencies in the yield estimates is unknown.

Table 4-12: Yield Estimates for the 1.5 MeV Be(d,n) Reaction.

	Yield Estimate
Goldie ~ 1959	1.98e+13 n/min-mA
Burrill – 1964	2.64e+13 n/min-mA
Inada *et al.* – 1968	4.8e+13 n/min-mA
Whittlestone – 1977	5.4e+13 n/min-mA
White – 1998	1.8e+13 n/min-mA

The yield estimate found by White is a rough estimate indirectly found by scaling MCNP-predicted thermal neutron dose rates per starting neutron to match experimental thermal neutron dose rate measurements on the BNCT beam at MIT LABA [White 1998]. A similar method is used in this paper to scale the MCNP-calculated spectra. This method is discussed in detail in Section 4.4.4.

4.4 Spectral Unfolding

This section describes the method used to solve for the unfolded spectra for the BNCT and BNCS beams using the measured reaction rates and calculated effective cross sections and Equation 3-8. This method is used to solve for the unfolded spectra for both the full range and independent point methods. A computer program designed to conduct the unfolding manipulations was written in the program code MATLAB® [The Mathworks, Inc. 1994]. The following sections present the spectral unfolding calculations in detail, a description of the MATLAB program, and the complete spectral

unfolding results for the BNCT and BNCS beams based on the measurements conducted at MIT LABA.

4.4.1 Spectral Unfolding Calculations

Prior to solving Equation 4-1 for the unperturbed unfolded fluxes in each energy region, **[A]** must have the number of reactions greater or equal to the number of energy regions, NF≥NG, and all reactions must be reasonably linearly independent. Linear independence can be tested for in several ways; this paper calculates the rank of the **[A]** matrix. The rank of a matrix is the number of linearly independent rows in a matrix. The rank calculations are quickly done in MATLAB using one command [The Mathworks, Inc. 1994]. If the rank of the matrix is equal to the number of rows in the matrix then all of the rows (reactions) are linearly independent.

The spectral unfolding results are found in the flux matrix **[Φ]** in Equation 4-1, where **[A]** are the effective cross sections taken from Appendix F and **[R]** are the measured reaction rates taken from Tables 4-6 and 4-8. The following process for solving for **[Φ]** and propagating errors was developed by Nigg and Harker [Nigg and Harker 1998]. The flux matrix **[Φ]** is found by solving Equation 4-20. If NF=NG, **[A]** is a square matrix, and $\mathbf{[A]}^{-1}$ exists.

$$[\Phi] = [\mathbf{A}]^{-1}[\mathbf{R}] \qquad [4\text{-}20]$$

where: $\mathbf{[A]}^{-1}$ = inverse of **[A]**.

If NF>NG, the problem is over-determined and has extra information; therefore, a fitting process must be used to calculate **[Φ]**. A linear least-squares fitting process is a common method used to solve an over-determined problem. The optimal fitted solution is found by minimizing the sum of the squares of the differences, Δ, between the

measured reaction rates and the calculated reaction rates, obtained by substituting the fitted solution back into Equation 4-20.

$$\Delta = \sum_{i=1}^{NF} \delta_i^2 \qquad [4\text{-}21]$$

$$\delta_i = (R_i - (a_{i1}\Phi_1 + a_{i2}\Phi_2 \cdots + a_{iNG}\Phi_{NG})) \qquad [4\text{-}22]$$

The minima of Δ are found by setting the differential of Equation 4-21 with respect to the flux in each energy group equal to zero. This creates a system of NG equations, which, after some manipulation, is simplified to Equation 4-23; rearrangement of Equation 4-23 gives Equations 4-24 and 4-25.

$$[\mathbf{A}]^T[\mathbf{A}][\Phi] = [\mathbf{A}]^T[\mathbf{R}] \qquad [4\text{-}23]$$

$$[\Phi] = \left([\mathbf{A}]^T[\mathbf{A}]\right)^{-1}[\mathbf{A}]^T[\mathbf{R}] \qquad [4\text{-}24]$$

$$[\Phi] = [\mathbf{B}]^{-1}[\mathbf{A}]^T[\mathbf{R}] \qquad [4\text{-}25]$$

where: $[\mathbf{A}]^T$ = transpose of **[A]**,
$([\mathbf{A}]^T[\mathbf{A}])^{-1}[\mathbf{A}]^T$ = pseudo-inverse of **[A]**, and
$[\mathbf{B}] = [\mathbf{A}]^T[\mathbf{A}]$.

The linear least-squares fit is the most common way of solving problems that have a coefficient matrix, which is not a square matrix, such as when NF>NG in the full-range method in this work. The coefficient matrix in this work is **[A]**. However, just as in the case of the detector efficiency fitting, this fit is based on the assumption that the errors in **[R]** are equal; this assumption is not accurate in this case. The errors in R_i are exactly known and are not equal. A weighted linear least-squares fit is a better fitting process for this situation because it takes into the known errors in **[R]**. In this process, Δ is inversely weighted by the absolute uncertainties in the measured reaction rates, as shown in Equation 4-26. After some manipulation, Equation 4-26 simplifies to Equation

4-27, which can be rearranged into Equation 4-28. Solving Equation 4-28 gives the unfolded neutron flux in each energy group using the weighted least-squares method.

$$\Delta = \sum_{i=1}^{NF} \frac{\delta_i^2}{\sigma_{R_i}^2} \qquad [4\text{-}26]$$

$$[\mathbf{A}]^T[\mathbf{V}][\mathbf{A}][\Phi] = [\mathbf{A}]^T[\mathbf{V}][\mathbf{R}] \qquad [4\text{-}27]$$

$$[\Phi] = \left([\mathbf{A}]^T[\mathbf{V}][\mathbf{A}]\right)^{-1}[\mathbf{A}]^T[\mathbf{V}][\mathbf{R}] \qquad [4\text{-}28]$$

$$[\mathbf{V}] = \begin{bmatrix} \frac{1}{\sigma_{R_1}^2} & 0 & 0 & 0 \\ 0 & \frac{1}{\sigma_{R_2}^2} & 0 & 0 \\ 0 & 0 & \ddots & 0 \\ 0 & 0 & 0 & \frac{1}{\sigma_{R_{NF}}^2} \end{bmatrix} \qquad [4\text{-}29]$$

4.4.2 Spectral Unfolding Errors

The errors of each element of **[R]** must be propagated to determine the total error in the unfolded neutron flux in each energy group. Equation 4-30 determines the error of the unfolded neutron fluxes in each energy group taking into account:

1. the experimental uncertainty of the reaction rates and
2. the variance associated with the fitting process [Nigg and Harker 1998].

$$s_j^2 = \sum_{i=1}^{NF} \left(\frac{\partial \phi_j}{\partial R_i} \right)^2 [\delta_i^2 + u_i^2] \qquad [4\text{-}30]$$

$$[s]^2 = \left(\frac{\partial [\phi]}{\partial [R]} \right)^2 \left[([R] - [A][\phi])^2 + [u]^2 \right] \qquad [4\text{-}31]$$

where: s_j = 1-σ error of the unfolded neutron flux in energy group *j*,
δ_i = variance in fitting process for reaction *i*, and
u_i = absolute uncertainty in reaction *i*

When using the weighted least-squares fitting process:

$$\frac{\partial[\phi]}{\partial[R]} = [B]^{-1}[A]^{T}[V] \qquad [4\text{-}32]$$

$$[\mathbf{B}] = \left([\mathbf{A}]^{\mathrm{T}}[\mathbf{V}][\mathbf{A}]\right) \qquad [4\text{-}33]$$

If NF=NG, there is no fitting process needed. The values of δ_i are by definition equal to zero, and only the experimental uncertainties in the reaction rates are propagated to the errors in the unfolded fluxes. In this case, Equation 4-32 becomes:

$$\frac{\partial[\phi]}{\partial[R]} = [A]^{-1} \qquad [4\text{-}34]$$

4.4.3 Computer Program

In order to perform the spectral unfolding calculations, as described in the previous section, a computer program ("spectrum") was composed in The Student Version of MATLAB 4 [The Mathworks, Inc.1994]. MATLAB is a program specifically designed for matrix manipulation. The flow charts shown in Appendix G graphically show the general actions taken within the program "spectrum" and its subprograms to calculate the unfolded flux matrix and determine its error.

The computer program takes the user-input effective cross sections and reaction rates (and their absolute uncertainties) and calculates the unfolded fluxes in either the full range or independent point unfolding process. The program tests for linear independence by calculating the rank of **[A]** and removes any reaction found not to be independent. If NF>NG, the weighted least-squares method is used to the fit the data. Using the equations in the previous section, the MATLAB program calculates the unfolded flux matrix and its error and saves the results to a data file.

4.4.4 BNCT Results

Figures 4-3 and 4-4 show the neutron spectrum of the BNCT beam found by the full range and independent point methods compared to the MCNP-calculated neutron spectrum. The MCNP-calculated neutron flux in the first energy bin (thermal region: $1x10^3$ – 0.5 eV) was scaled to match the measured thermal neutron flux found by the full range method. This scaling factor was also used when comparing the MCNP spectrum to the measured spectrum found by the independent point method.

The unfolding method used to convert the 9 reactions into 8 energy regions in the full range method does not guarantee that the unfolding solution will have positive flux values [Nigg and Harker 1998]. It was determined that in order to get positive flux values, the BNCT data could only be unfolded into 6 energy regions, as shown in Figure 4-3. Also, in the independent point method, the Cu(n,gam) reaction could not used for this same reason. The method used to determine linear independence only determines whether or not the reactions are independent; it does not determine the extent of independence. If the reactions are not sufficiently independent, negative flux values are possible. The remaining unfolding results for the BNCT beam are sufficient to compare the measured spectra to the MCNP-calculated spectrum.

Figures 4-3 and 4-4 show that the shape of the measured neutron spectra match the MCNP-calculated spectrum. The epithermal region in Figure 4-3 does show some inconsistencies between the measured and expected spectra. These inconsistencies cause the measured BNCT epithermal flux to be 30% or 33% higher than expected from MCNP using the Guzek or Whittlestone source spectra, respectively. The biggest discrepancy between the spectra is in the fast region in Figure 4-4.

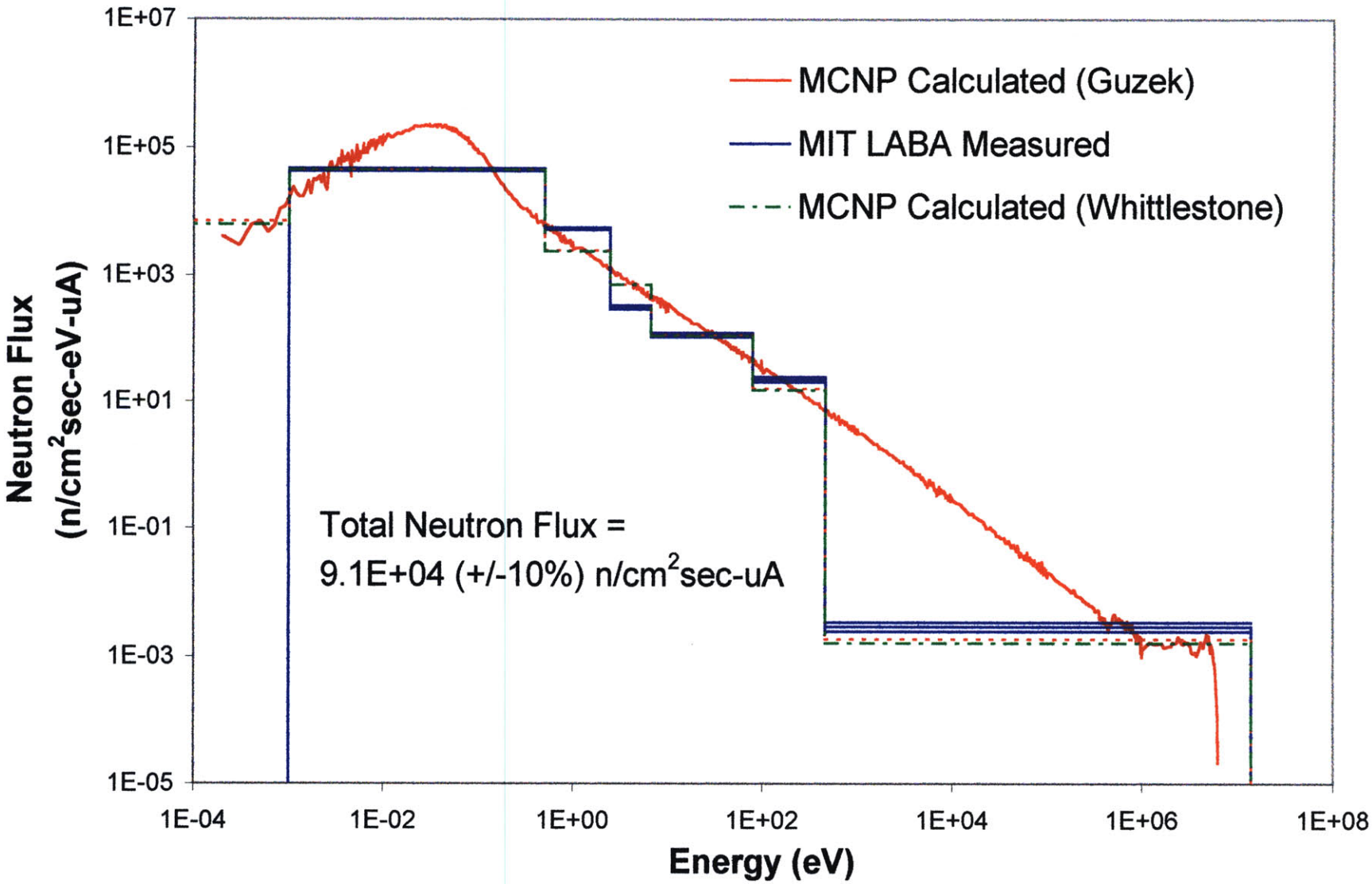

Figure 4-3: Unperturbed Neutron Spectrum of the BNCT Beam at MIT LABA found by the Full Range Spectral Unfolding Method. The measured spectrum is shown in comparison with the MCNP-calculated spectrum scaled to match the measured thermal neutron flux. The dotted red lines indicate the average MCNP-calculated neutron flux found from the Guzek source spectrum over the selected energy region.

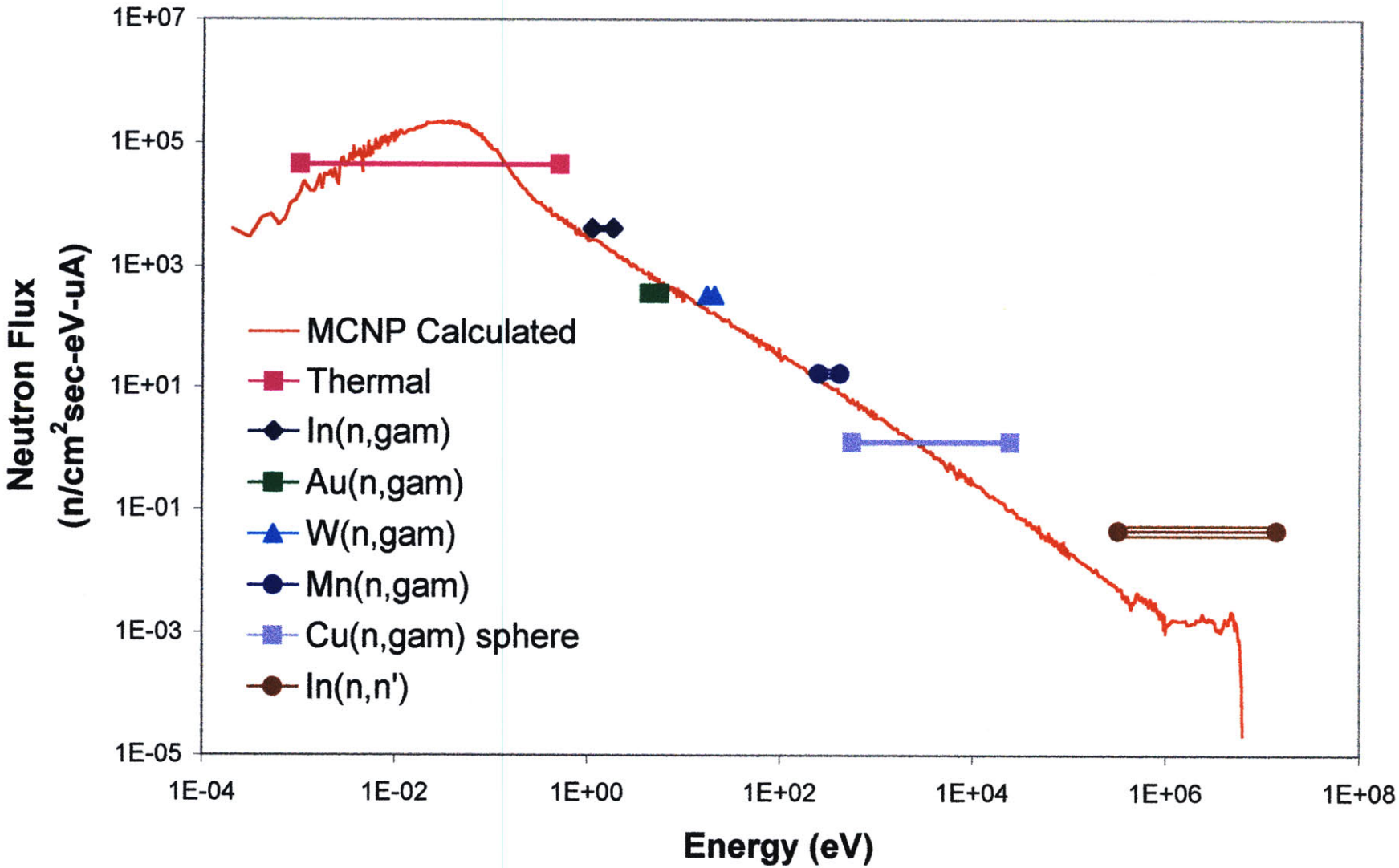

Figure 4-4: Unperturbed Neutron Spectrum of the BNCT Beam at MIT LABA found by the Independent Point Spectral Unfolding Method. The measured spectrum is shown in comparison with the MCNP-calculated spectrum scaled to match the measured thermal neutron flux.

This large discrepancy was unexpected because the fast region ($2.90 \times 10^{-3} \pm 16\%$ n/cm^2-sec-eV-μA) found by the full range method was found to be only 57% or 81% higher than MCNP using the Guzek or Whittlestone source spectra, respectively. Foil placement is one explanation for this discrepancy.

The 6 foils within the foil wheel were placed at radial locations around the center of the beam face, but the boron sphere foils were placed at the center of beam face. For the BNCT and BNCS beams at MIT LABA, it is quite possible that the center of the beam face has a larger fast neutron flux than at other parts because the center of the beam face aligns directly the center of the beryllium target. Any fast neutrons created at the center of the target have less moderator material to transverse through before escaping at the beam face. The fast neutron flux found from the full-range method (Figure 4-3) was unfolded from data of all 9 reactions measured in both the foil wheel and boron sphere, while the fast neutron flux from the independent-point method (Figure 4-4) was unfolded only from the In(n,n') reaction measured in the boron sphere. Therefore, the full-range method is more likely to represent the average fast neutron flux across the entire beam face, which it is compared to, than the independent-point method. The measured fast neutron flux in Figure 4-4 is more representative of the flux at the center of the beam face, and as explained above, the center is expected to have a higher fast neutron flux than expected from MCNP, which is the average flux across the entire beam face.

The activation foil measurements on the BNCT beam found the absolute magnitude of the neutron flux in each region. Table 4-13 lists the magnitude of the measured thermal, epithermal, fast, and total neutron flux of the BNCT beam at 1 μA.

Any future work on determining the actual versus measured current-on-target will only affect the current at which the data were normalized, not the actual measured data. In addition, current corrections will not affect the comparison of the normalized neutron flux with the MCNP-calculated flux due to the nature of the scaling the MCNP results.

Table 4-13: Thermal, Epithermal, Fast, and Total Neutron Flux of the BNCT Beam. There is no difference between the thermal flux because this region was used for scaling.

	MCNP-calculated (Guzek)	MCNP-calculated (Whittlestone)	MIT LABA measured	Difference
Thermal Neutron Flux [0.001 eV– 0.5 eV] (n/cm^2-sec-eV-μA)	4.46×10^4 (±0.4%)*	4.46×10^4 (±0.3%)*	4.46×10^4 (±4.4%)	---
Epithermal Neutron Flux [0.5 eV – 454 eV] (n/cm^2-sec-eV-μA)	4.78×10^1 (±1.0%)*	4.65×10^1 (±1.0%)*	6.20×10^1 (±6.8%)	+30% +33%
Fast Neutron Flux [454 eV – 14 MeV] (n/cm^2-sec-eV-μA)	1.85×10^{-3} (±2.3%)*	1.60×10^{-3} (±1.5%)*	2.90×10^{-3} (±16%)	+57% +81%
Total Neutron Flux (n/cm^2 sec-μA)	---	---	**9.09×10^4 (±10%)**	---

*The errors in the MCNP-calculated flux do not include the uncertainties in the 1.5 MeV Be(d,n) source spectra from Guzek and Whittlestone.

4.4.5 BNCS Results

Figures 4-5 and 4-6 show the neutron spectra of the BNCS beam found by the full range and independent point methods compared to the MCNP-calculated neutron spectrum. The MCNP-calculated neutron spectrum was also scaled to match the measured thermal neutron flux found by the full range method. For the same reason given for the BNCT beam, only six energy regions were used in the full range unfolding method.

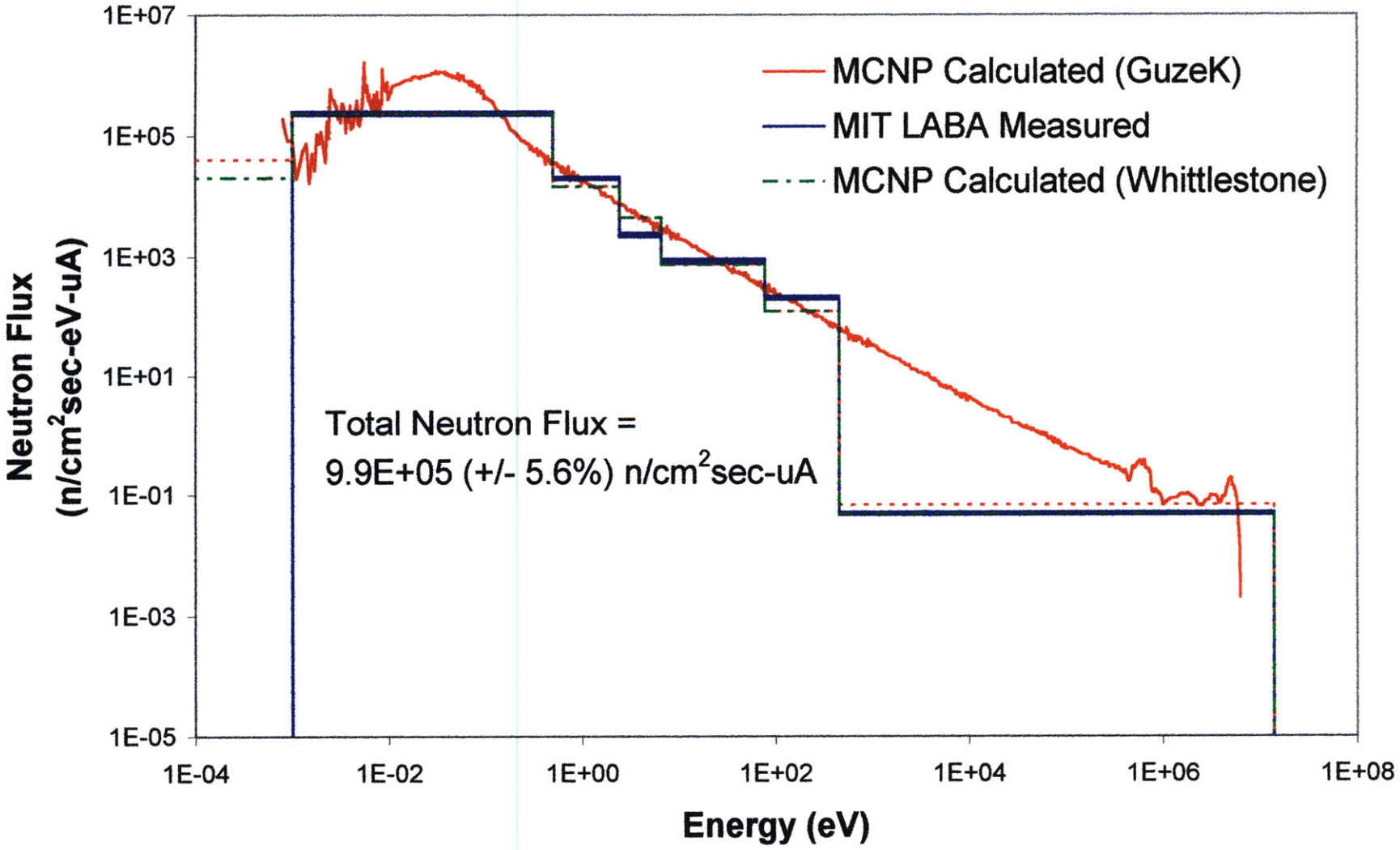

Figure 4-5: Unperturbed Neutron Spectrum of the BNCS Beam at MIT LABA found by the Full Range Spectral Unfolding Method. The measured spectrum is shown in comparison with the MCNP-calculated spectrum scaled to match the measured thermal neutron flux. The dotted red lines indicate the average MCNP-calculated neutron flux found by the Guzek source spectrum over the selected energy region.

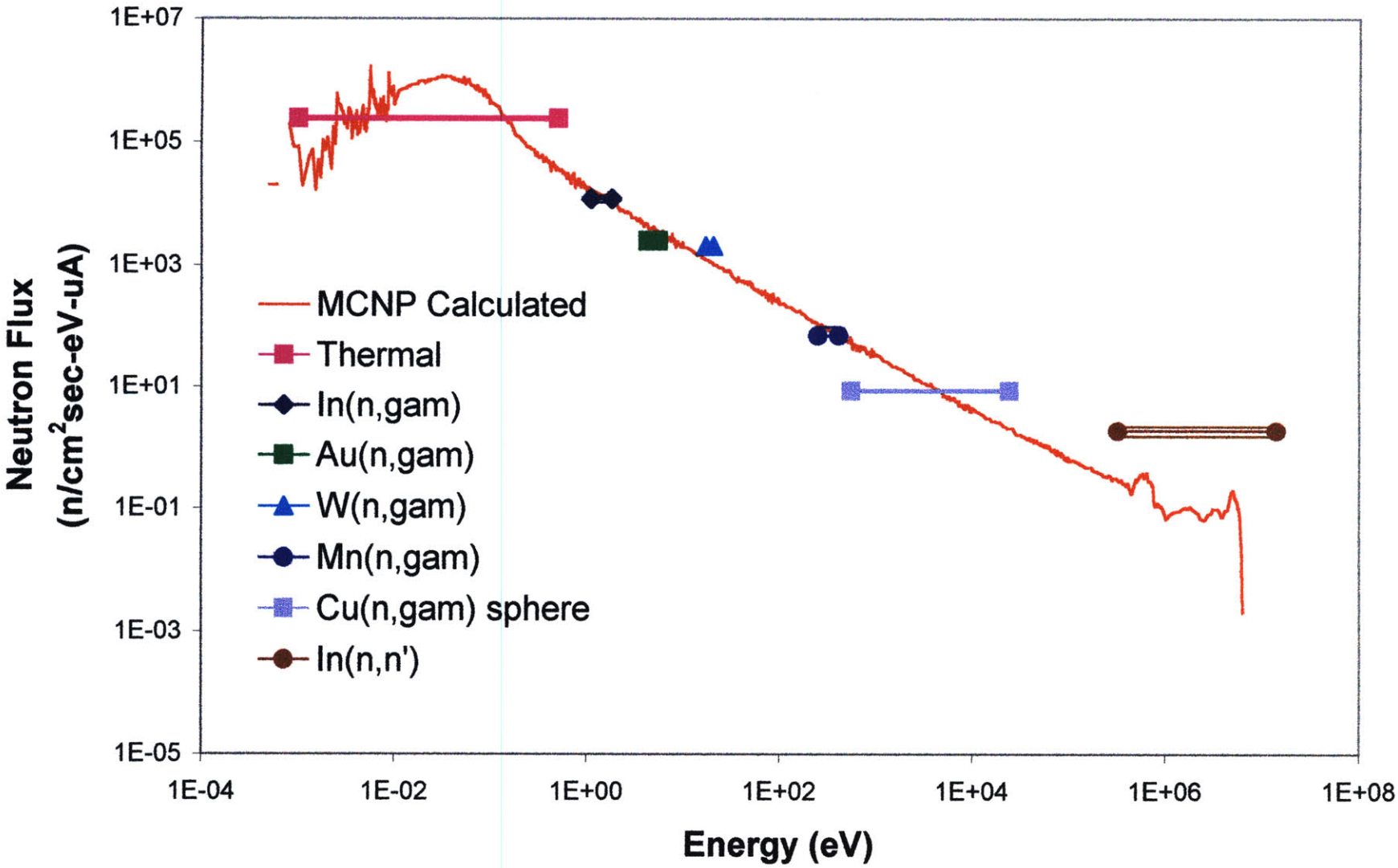

Figure 4-6: Unperturbed Neutron Spectrum of the BNCS Beam at MIT LABA found by the Independent Point Spectral Unfolding Method. The measured spectrum is shown in comparison with the MCNP-calculated spectrum scaled to match the measured thermal neutron flux.

Figures 4-5 and 4-6 show that the shape of the measured neutron spectra match the MCNP-calculated spectrum. The epithermal region in Figure 4-5 does show some inconsistencies between the measured and expected spectra. These inconsistencies cause the measured BNCS epithermal flux to be 27% or 28% higher than expected from MCNP using the Guzek or Whittlestone source spectra, respectively. The biggest discrepancy between the spectra is in the fast region in Figure 4-6. This large discrepancy was unexpected because the fast region ($4.88 \times 10^{-2} \pm 4.8\%$ n/cm^2-sec-eV-μA) found by the full range method was found to be 28% or 0.4% lower than MCNP using the Guzek or Whittlestone source spectra, respectively. A similar discrepancy in the independent point fast neutron region was also found in the BNCT beam results. The proposed explanation for this difference in the BNCT results, foil placement, can also apply to the BNCS results.

The activation foil measurements on the BNCS beam found the absolute magnitude of the neutron flux in each region. Table 4-14 lists the magnitude of the measured thermal, epithermal, fast and total neutron fluxes of the BNCS beam at 1μA. Any future work on determining the actual versus measured current-on-target will only affect the current at which the data were taken, not the actual measured data.

Table 4-14: Thermal, Epithermal, Fast, and Total Neutron Flux of the BNCS Beam. There is no difference between the thermal flux because this region was used for scaling.

	MCNP-calculated (Guzek)	MCNP-calculated (Whittlestone)	MIT LABA measured	Difference
Thermal Neutron Flux [0.001 eV– 0.5 eV] (n/cm^2-sec-eV-μA)	2.35×10^5 (±0.4%)*	2.35×10^5 (±0.4%)*	2.35×10^5 (±4.4%)	---
Epithermal Neutron Flux [0.5 eV – 454 eV] (n/cm^2-sec-eV-μA)	3.22×10^2 (±1.0%)*	3.20×10^2 (±1.5%)*	4.09×10^2 (±7.6%)	+27% +28%
Fast Neutron Flux [454 eV – 14 MeV] (n/cm^2-sec-eV-μA)	6.81×10^{-2} (±1.5%)*	4.86×10^{-3} (±1.4%)*	4.88×10^{-2} (±4.8%)	-28% -0.4%
Total Neutron Flux (n/cm^2 sec-μA)	---	---	**9.86×10^5 (±5.6%)**	---

*The errors in the MCNP-calculated flux do not include the uncertainties in the 1.5 MeV Be(d,n) source spectra from Guzek and Whittlestone.

Even though the general shapes of the measured and MCNP-calculated spectra match, the measured epithermal and fast neutron fluxes of the BNCT and BNCS beams are considerably different than expected from MCNP. This is an unexpected result because the BNCT and BNCS simulations used the same 1.5 Be(d,n) source spectra to calculate the effective cross sections [Guzek 1998]. The unfolded results were compared to the flux expected from MCNP using the Guzek or Whittlestone source spectra in order to determine which source spectrum creates a MCNP-calculated beam spectrum that matches closer to the experimentally measured spectrum.

After matching the thermal neutron flux, the measured epithermal neutron fluxes for the BNCT and BNCS beams were found to be 27%-33% higher than expected from MCNP using the Guzek or Whittlestone source spectra. This difference is consistent for both beams and for both source spectra. Since the epithermal fluxes for the BNCT and

BNCS beams are created from moderation of fast neutrons in the source spectra, these results suggest that the Guzek and Whittlestone 1.5 MeV Be(d,n) source spectrum may not contain all of the high energy neutrons that are actually present.

After matching the thermal neutron flux, the measured fast neutron flux for the BNCT beam was found to be 57% higher than the flux found from MCNP using the Guzek source spectra and 81% higher than found from MCNP using the Whittlestone source spectra. The BNCT fast neutron flux measurements are consistent with the epithermal flux measurements that suggest that the 1.5 MeV Be(d,n) source spectra from Guzek and Whittlestone may not contain all of the high energy neutrons that are actually present. However, these results are completely inconsistent with the dose characterization results on the BNCT beam [White 1998]. Using the Guzek spectrum, the dose characterization measurements conducted on the BNCT beam at MIT LABA found that the experimentally measured fast neutron dose rate was actually 50% lower than the MCNP-calculated fast dose rate, when the thermal neutron dose rate was matched [White 1998].

For the BNCS beam, the measured fast neutron flux was found to be 28% lower than the flux found from MCNP using the Guzek source spectra and matched the flux found from MCNP using the Whittlestone spectra. This is inconsistent with the epithermal flux measurements and the fast flux measurements of the BNCT beam. However, the BNCS results are more consistent with the dose characterization results. Using the Guzek spectrum, the dose characterization measurements conducted on the BNCS beam at MIT LABA found that the experimentally measured fast neutron dose

rate was 75% lower than the MCNP-calculated fast dose rate, when the thermal neutron dose rate was matched [Gierga 1999].

The uncertainties in the 1.5 MeV Be(d,n) source spectra used for the MCNP simulations were not taken into account in the calculated errors of the MCNP-calculated flux. These measurement errors were not provided by the authors [Guzek 1998, Whittlestone 1977]; however other authors suggest that it is reasonable to assume an error of at least 10-15% based on other experiments of this type [Howard 1997]. This assumption brings the experimentally-measured data closer to matching the MCNP-calculated data within error. The conclusion that can be drawn from these results is that a further examination into the source spectrum used in the MCNP simulations for the BNCT and BNCS beams is necessary.

4.4.6 1.5 MeV Be(d,n) Yield Estimates

The factors used to scale the MCNP-calculated spectra to the experimental data can be used to indirectly determine the total neutron yield of the 1.5 MeV Be(d,n) reaction in a method similar to that conducted by White [White 1998]. The spectrum found by MCNP is in units of n/cm^2-eV-starting particle, where the starting particles are neutrons produced by the 1.5 MeV Be(d,n) reaction. The measured normalized neutron spectra are then converted into the units of n/cm^2-eV-min-mA. Therefore, the scaling factor is equivalent to the yield of the 1.5 MeV Be(d,n) reaction in units of n/min-mA. Figures 4-7, 4-8, 4-9 and 4-10 show the reaction yields indirectly found from the measurements on the BNCT and BNCS beams by scaling the MCNP-calculated spectra found from the Guzek or Whittlestone source spectra. The figures present the calculated reaction yield from scaling to the thermal and fast neutrons regions of the

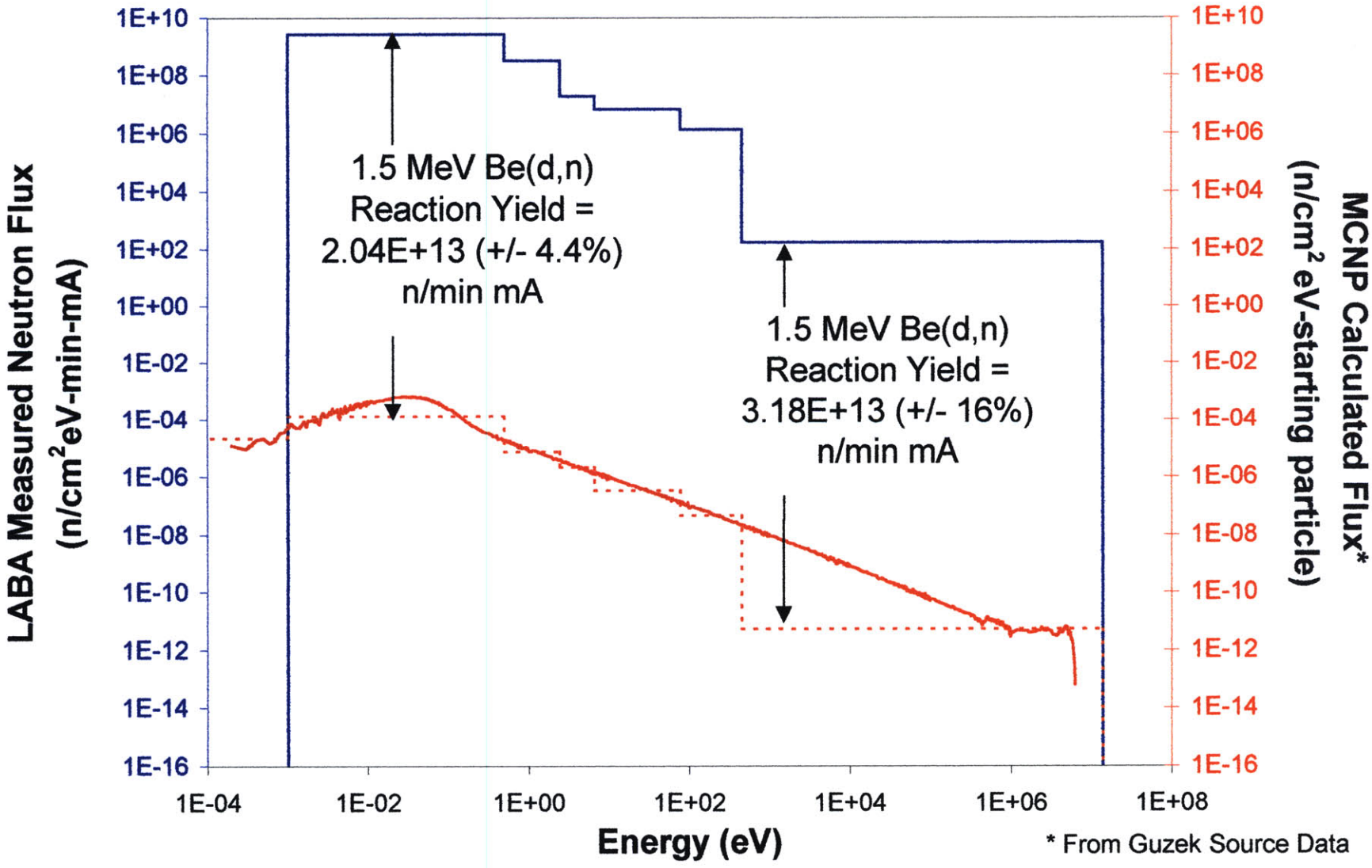

Figure 4-7: Yield Estimate of 1.5 MeV Be(d,n) Reaction from Scaling the MCNP-calculated Unperturbed Neutron Spectrum of the BNCT Beam found from the Guzek Source Spectrum with the Measured Neutron Spectrum. The reaction yield was estimated based on scaling to the thermal and the fast neutron flux.

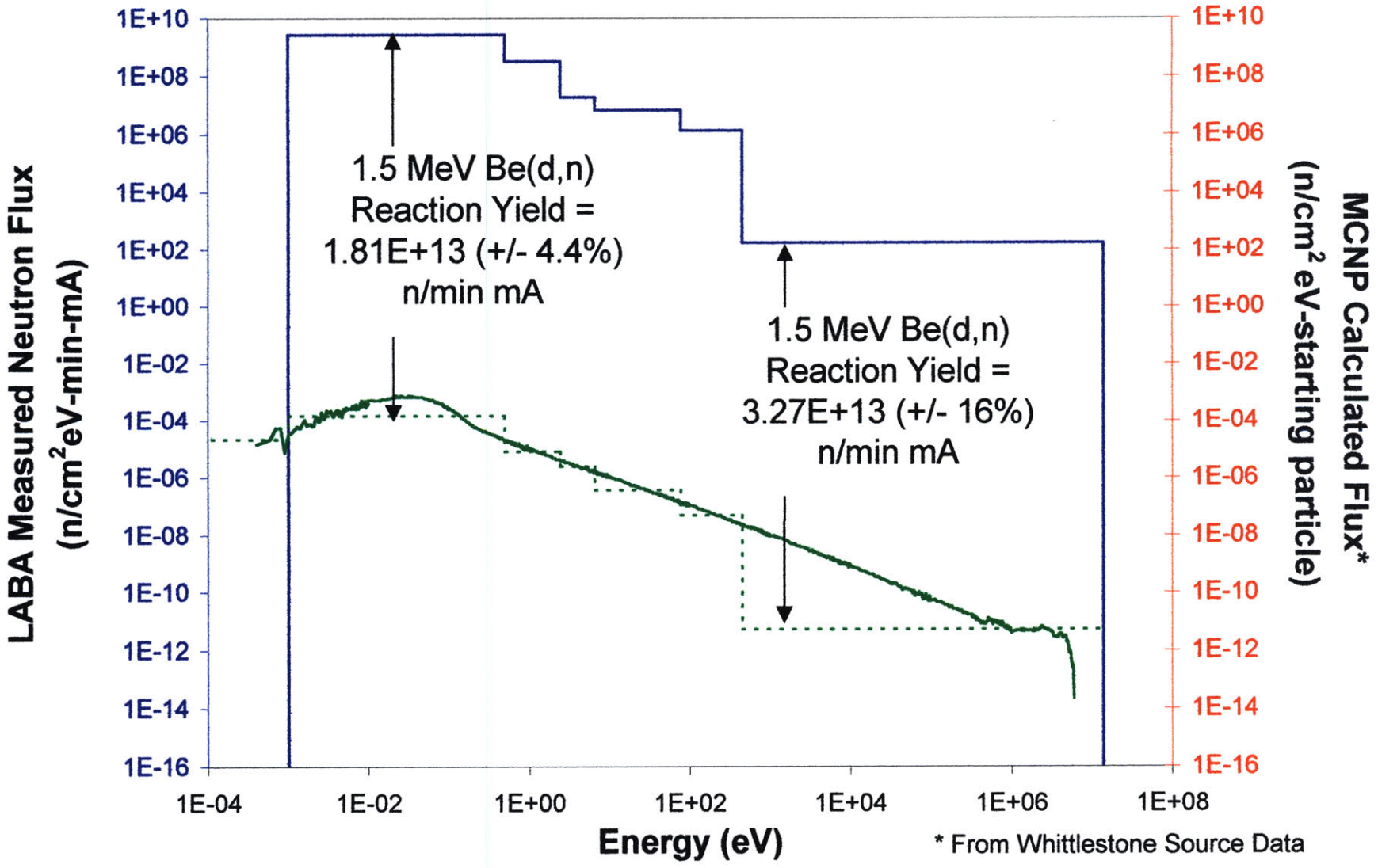

Figure 4-8: Yield Estimate of 1.5 MeV Be(d,n) Reaction from Scaling the MCNP-calculated Unperturbed Neutron Spectrum of the BNCT Beam found from the Whittlestone Source Spectrum with the Measured Neutron Spectrum. The reaction yield was estimated based on scaling to the thermal and the fast neutron flux.

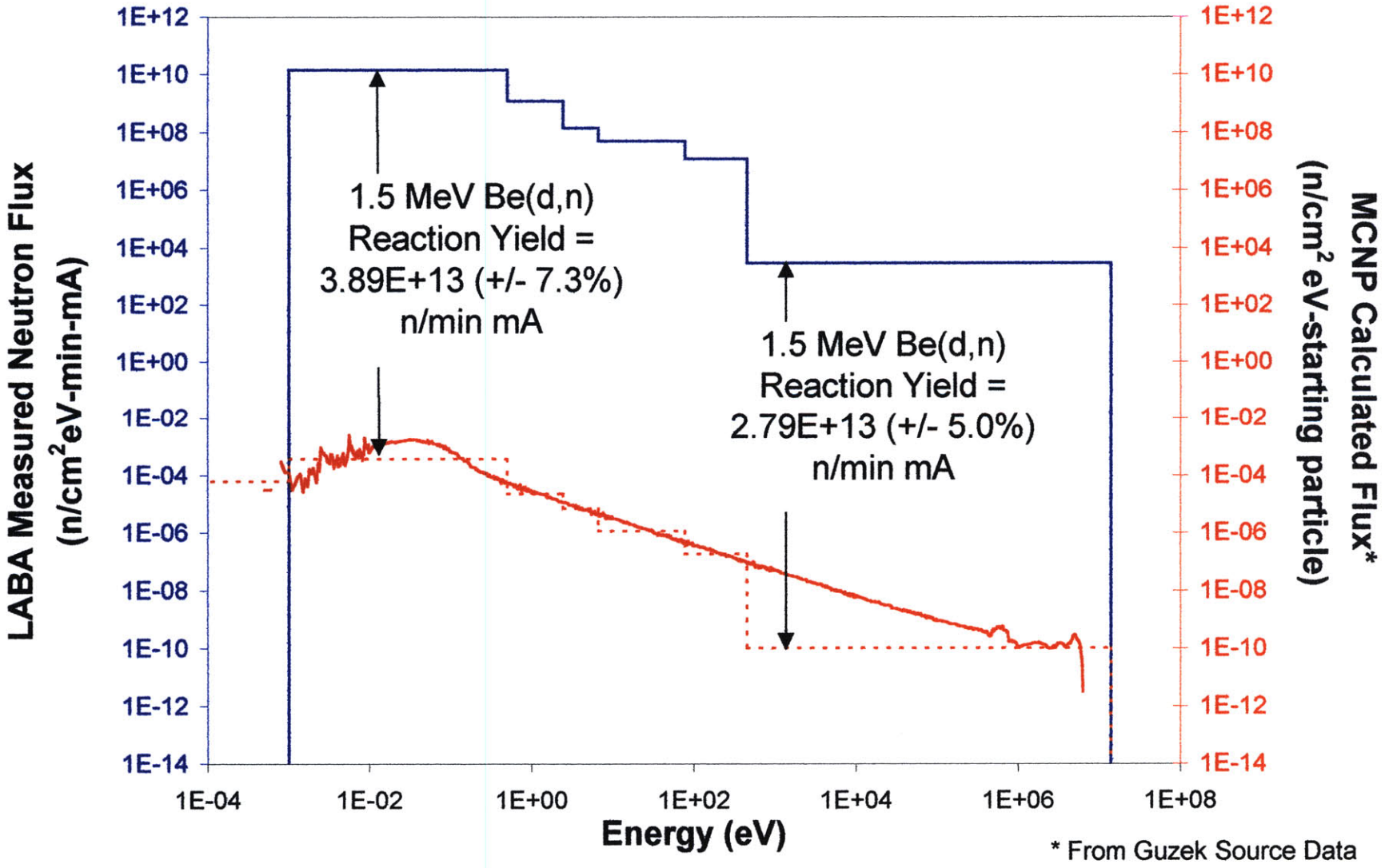

Figure 4-9: Yield Estimate of 1.5 MeV Be(d,n) Reaction from Scaling the MCNP-calculated Unperturbed Neutron Spectrum of the BNCS Beam found from the Guzek Source Spectrum with the Measured Neutron Spectrum. The reaction yield was estimated based on scaling to the thermal and the fast neutron flux.

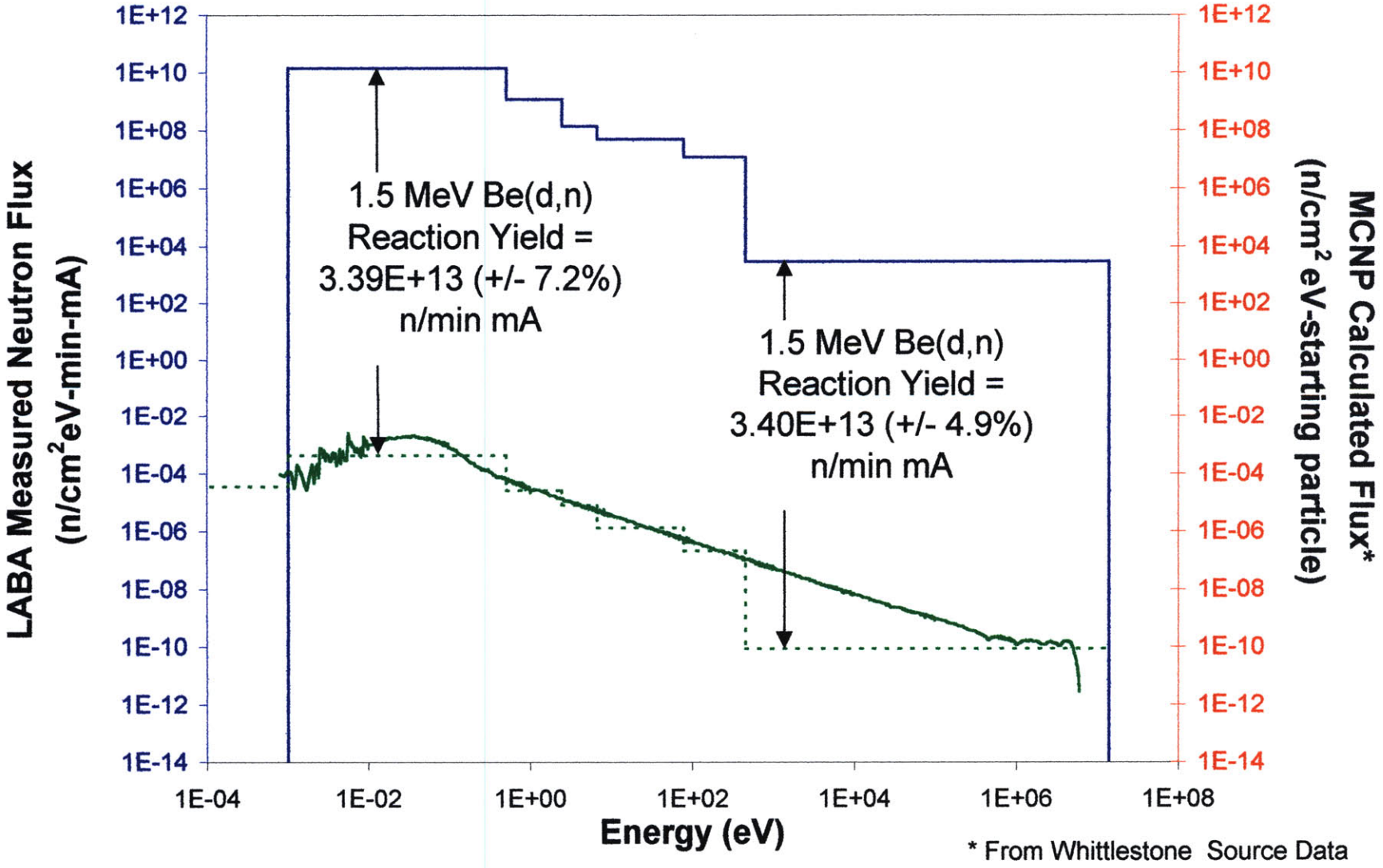

Figure 4-10: Yield Estimate of 1.5 MeV Be(d,n) Reaction from Scaling the MCNP-calculated Unperturbed Neutron Spectrum of the BNCS Beam found from the Whittlestone Source Spectrum with the Measured Neutron Spectrum. The reaction yield was estimated based on scaling to the thermal and the fast neutron flux.

measured spectra. Table 4-15 lists the yields found from scaling with the yields from previous literature.

Table 4-15: Yield Estimates of 1.5 MeV Be(d,n) Reaction Including the MIT LABA Estimates Determined by Spectral Scaling.

	Yield Estimate (n/min-mA)
Goldie ~1959	1.98e+13
Burrill –1964	2.64e+13
Inada *et al.* – 1968	4.8e+13
Whittlestone – 1977	5.4e+13
White – 1998 MIT LABA (dose rates) BNCT Beam – Thermal Scaling	1.8e+13 (Guzek)
MIT LABA (spectra) BNCT Beam – Thermal Scaling	2.04e+13 ± 4.4% (Guzek)* 1.81e+13 ± 4.4% (Whittlestone)*
MIT LABA (spectra) BNCT Beam – Fast Scaling	3.18e+13 ± 16% (Guzek)* 3.27e+13 ± 16% (Whittlestone)*
MIT LABA (spectra) BNCS Beam – Thermal Scaling	3.89e+13 ± 7.3% (Guzek)* 3.39e+13 ± 7.2% (Whittlestone)*
MIT LABA (spectra) BNCS Beam – Fast Scaling	2.79e+13 ± 5.0% (Guzek)* 3.40e+13 ± 4.9% (Whittlestone)*

*The errors in the yield estimate do not include the uncertainties in the 1.5 MeV Be(d,n) source spectra from Guzek and Whittlestone used in the MCNP simulations.

Rough yield estimates were indirectly found from the activation foil measurements on the BNCT and BNCS beams, and any future work on determining the actual versus measured current-on-target will only affect the current of the yield estimate. The estimates found in this work are well within the range of estimates found in previous literature. White's estimate is lower than previous estimates; the cause of the inconsistency is unclear [White 1998]. Even so, the estimates found in this work for the BNCT beam using thermal neutron scaling are consistent with the result found by White.

5 Conclusion and Future Work

The spectral characterization experiments conducted on the BNCT and BNCS beams at MIT LABA demonstrated that the "thick" neutron activation foil method developed by INEEL can be effectively applied to epithermal accelerator-based neutron beams. Only small adjustments were needed to adapt the INEEL method for effectiveness on the accelerator-based beams at MIT LABA. These adjustments included removal of the cobalt foils and increasing the number of foils in the boron sphere from four to five. Additionally, despite any problems with current measurements, such as secondary electron effects, the experimental results demonstrated that the INEEL activation foil method was still effective in giving a spectral characterization of an accelerator-based epithermal beam and in comparing experimental with simulation results.

The measured reaction rates and the MCNP-calculated effective cross sections were used to determine the neutron spectra of the BNCT and BNCS beams by the full range and independent point methods. The unfolded results showed that the measured neutron spectra of each beam matched the basic shape of the MCNP-calculated neutron spectra, with the exception of the fast neutron region in the independent point method.

The full range method provided spectral information in six energy regions (four in the epithermal neutron region). The average measured thermal, epithermal, and fast neutron fluxes were found. When matching the thermal neutron flux, the measured epithermal and fast fluxes did not match with MCNP results. Even though the difference

between the measured and MCNP-determined epithermal neutron flux were consistent between source spectra and beam type, the differences in the fast neutron flux were not consistent between the BNCT and BNCS beams. These results were unexpected because the same 1.5 MeV Be(d,n) source spectrum was used in the MCNP simulations to determine the effective cross sections. In addition, these results contradicted the results found by the dose characterization of the BNCT and BNCS beams at MIT LABA using the Guzek spectra [White 1998, Gierga 1999, Guzek 1998]. The experimental results suggest that the effects of the different source spectra on simulation results should be examined further.

The measured spectra for each beam, however, did not provide further insight into the discrepancies among the neutron yield estimates of the 1.5 MeV Be(d,n) reaction. The experimental results did provide additional yield estimates for the reaction through scaling between simulation and experimental measurements that fell within the range of results of previous literature. In addition, estimates found from spectral measurements were consistent with the estimate that was found by White in the dose characterization of the BNCT at MIT LABA. Further work in determining this yield is important to the effectiveness of determining the dose rate and treatment times for each beam solely through MCNP simulation.

The use of neutron activation foils in characterizing epithermal neutron beams for BNCT and BNCS is advantageous because it is simple, inexpensive, and effective on both reactor-based and accelerator-based beams. The activation foils can also be economically reused for characterization of several beams. The use of neutron activation foils for spectral characterization provides direct experimental verification of

the neutron spectra, MCNP models, and simulation results and is an important addition to the toolbox of methods used to fully characterize BNCT and BNCS beams.

Appendix A:
Neutron Cross Sections of Foil Materials

List of contents:

- In(n,γ) cross section
- ^{197}Au(n,γ) cross section
- ^{186}W(n,γ) cross section
- ^{59}Co(n,γ) cross section
- ^{55}Mn(n,γ) cross section
- ^{63}Cu(n,γ) cross section
- In(n,n') cross section

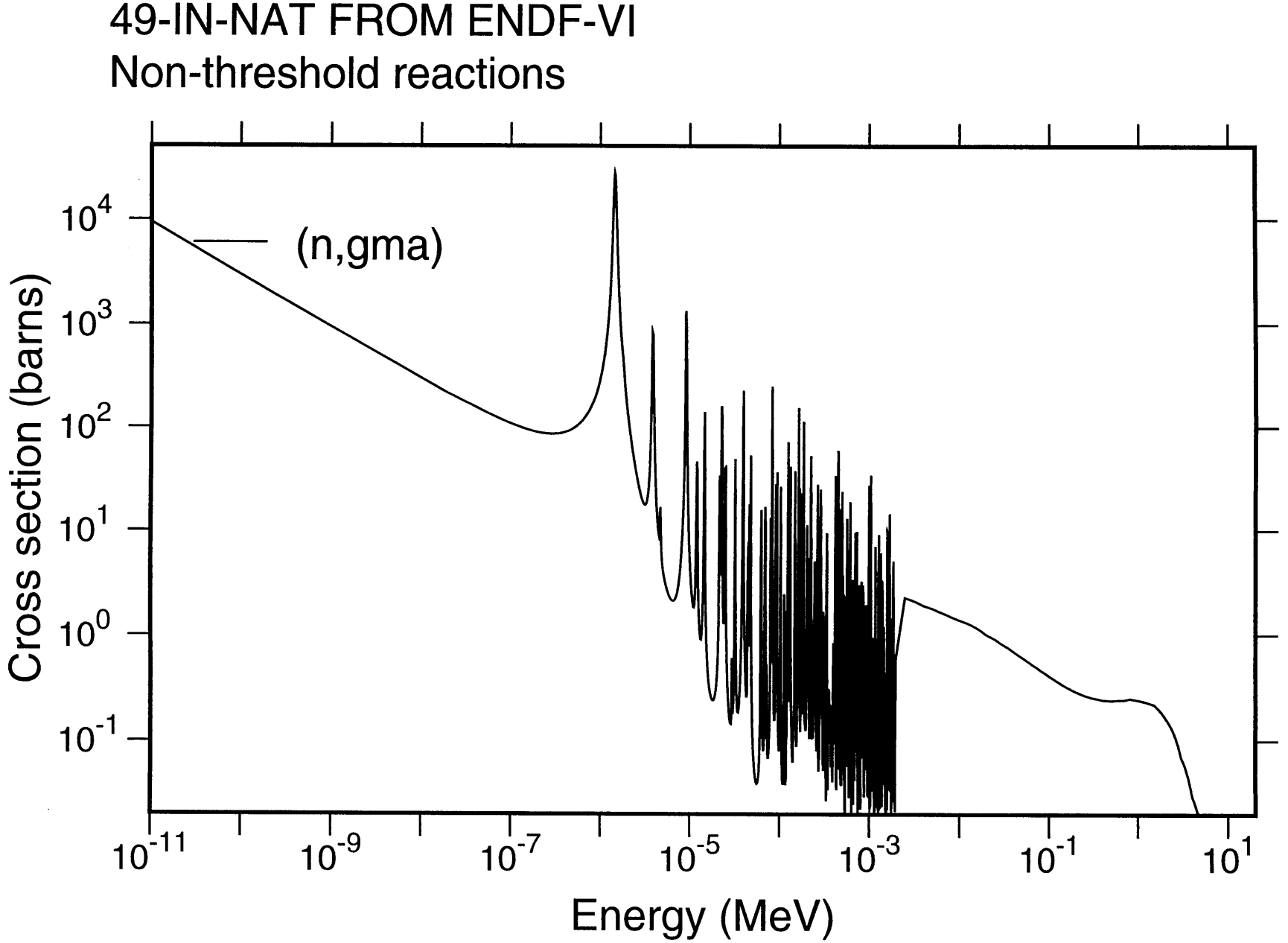
49-IN-NAT FROM ENDF-VI
Non-threshold reactions
(n,gma)
Cross section (barns)
10^{4}
10^{3}
10^{2}
10^{1}
10^{0}
10^{-1}
10^{-11}
10^{-9}
10^{-7}
10^{-5}
10^{-3}
10^{-1}
10^{1}
Energy (MeV)

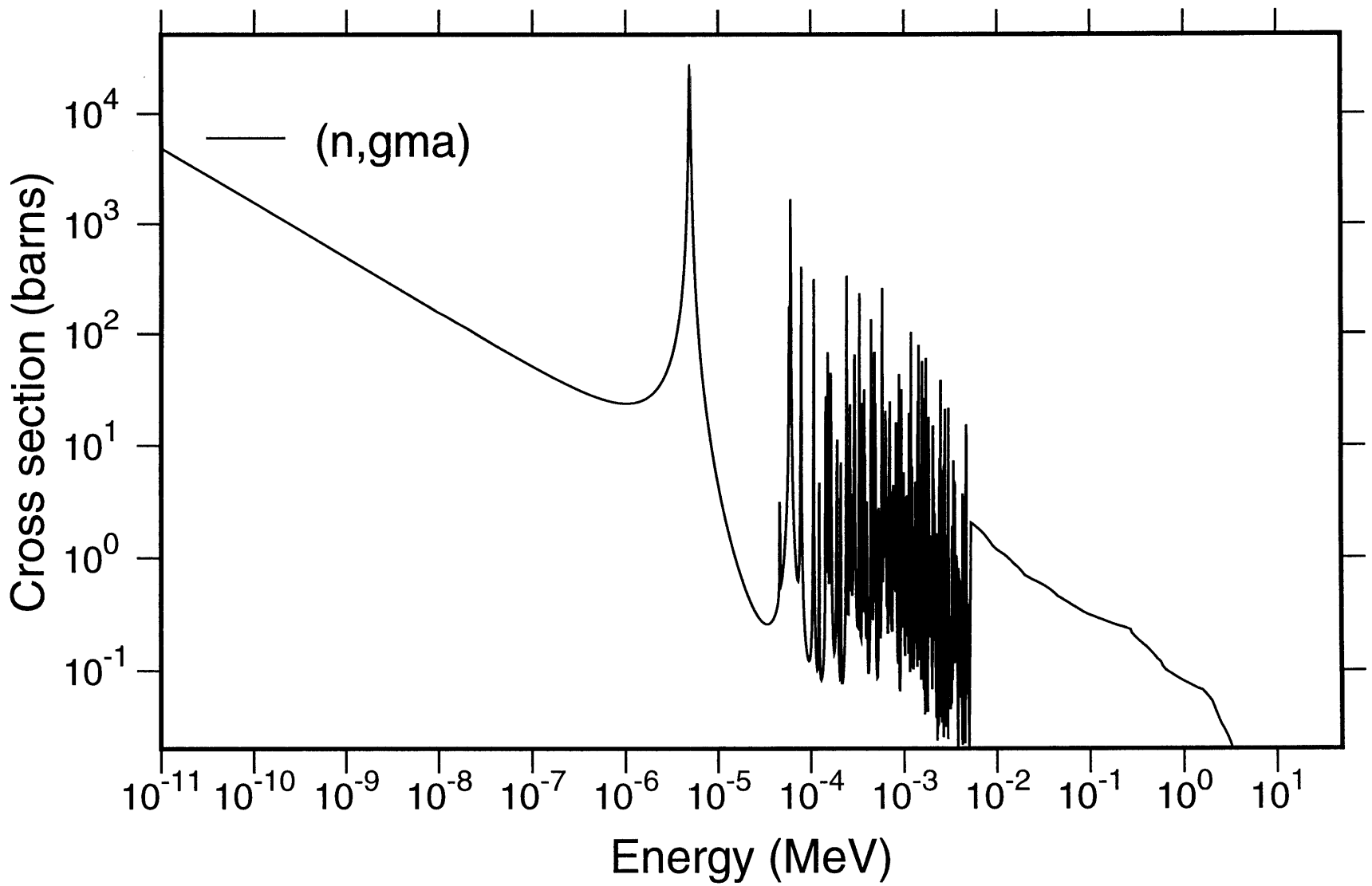
79-AU-197A FROM ENDF-VI.1
Non-threshold reactions
(n,gma)
Cross section (barns)
10^4
10^3
10^2
10^1
10^0
10^-1
10^-11 10^-10 10^-9 10^-8 10^-7 10^-6 10^-5 10^-4 10^-3 10^-2 10^-1 10^0 10^1
Energy (MeV)

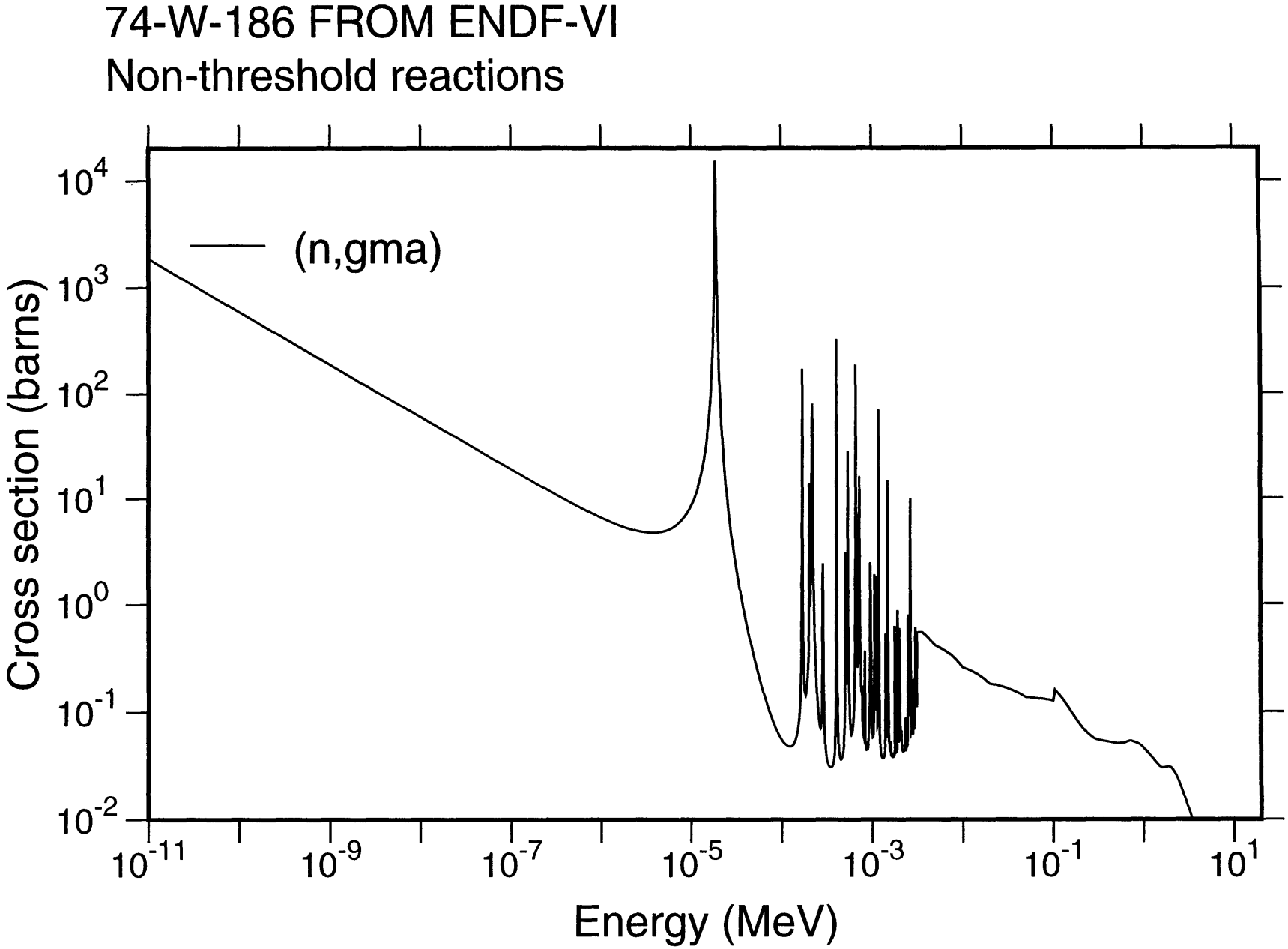
74-W-186 FROM ENDF-VI
Non-threshold reactions
(n,gma)
Cross section (barns)
10^4
10^3
10^2
10^1
10^0
10^-1
10^-2
10^-11
10^-9
10^-7
10^-5
10^-3
10^-1
10^1
Energy (MeV)

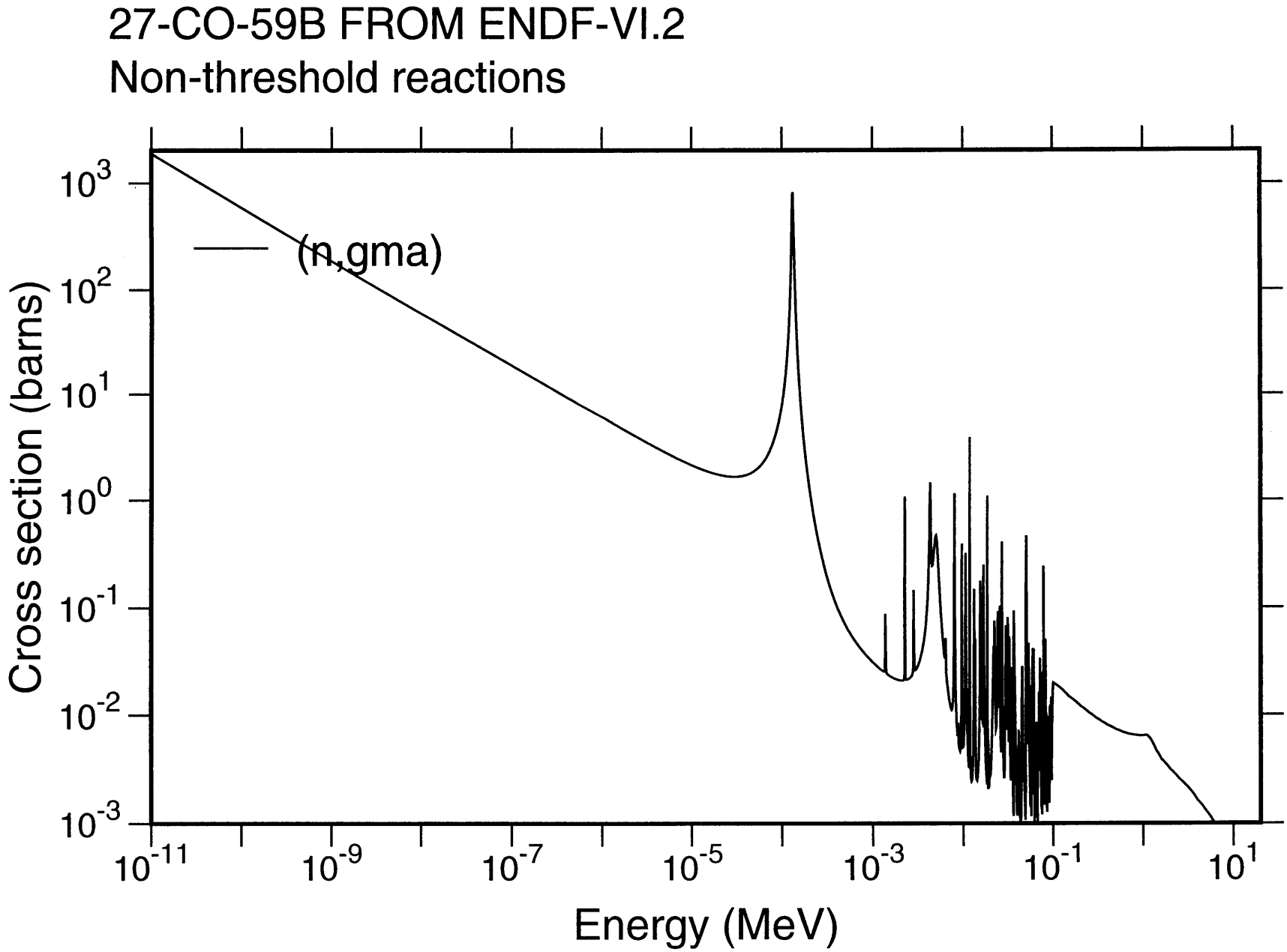
27-CO-59B FROM ENDF-VI.2
Non-threshold reactions
(n,gma)
Cross section (barns)
10^{3}
10^{2}
10^{1}
10^{0}
10^{-1}
10^{-2}
10^{-3}
10^{-11}
10^{-9}
10^{-7}
10^{-5}
10^{-3}
10^{-1}
10^{1}
Energy (MeV)

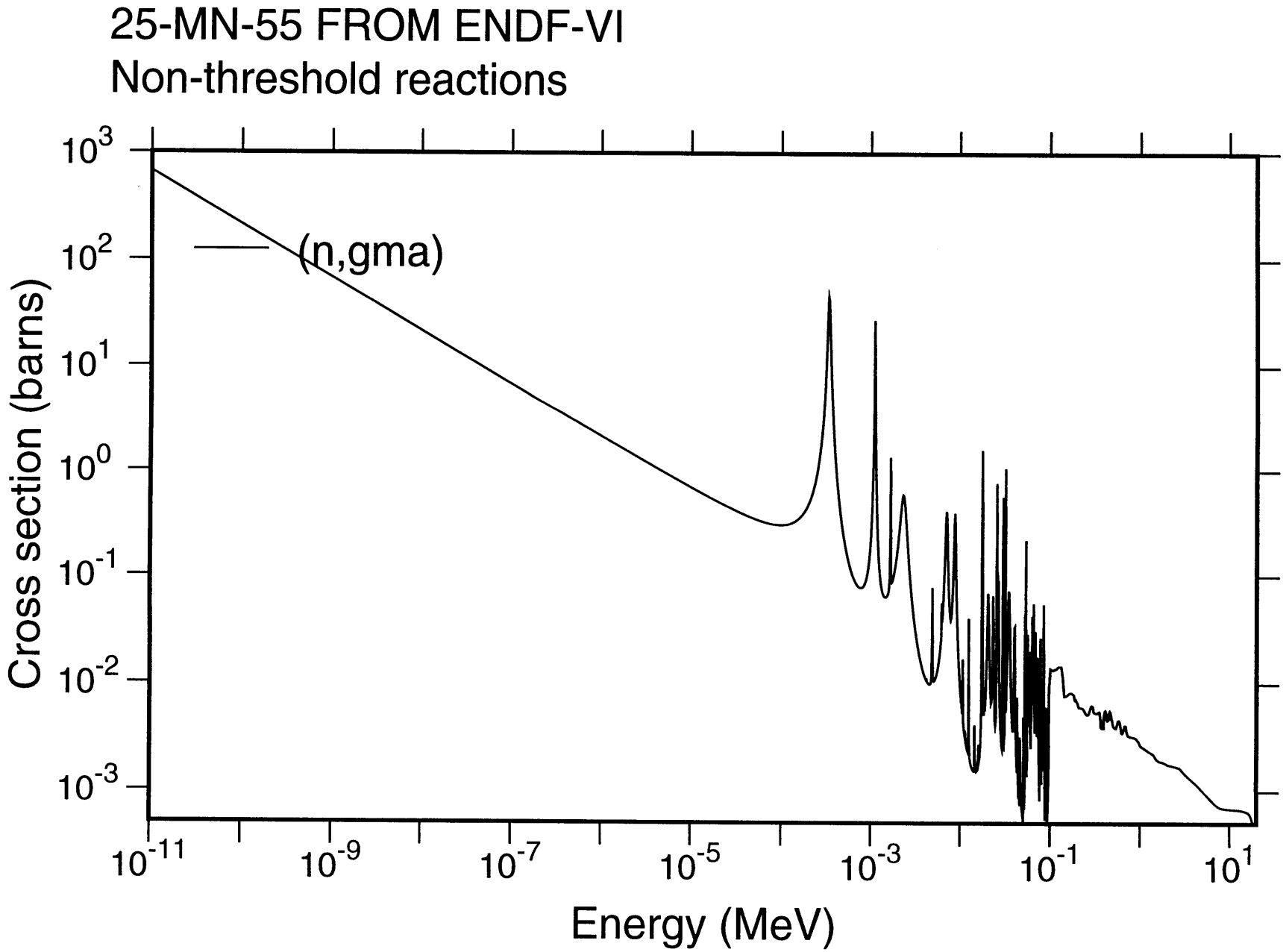
25-MN-55 FROM ENDF-VI
Non-threshold reactions
(n,gma)
Cross section (barns)
Energy (MeV)
10^3
10^2
10^1
10^0
10^-1
10^-2
10^-3
10^-11
10^-9
10^-7
10^-5
10^-3
10^-1
10^1

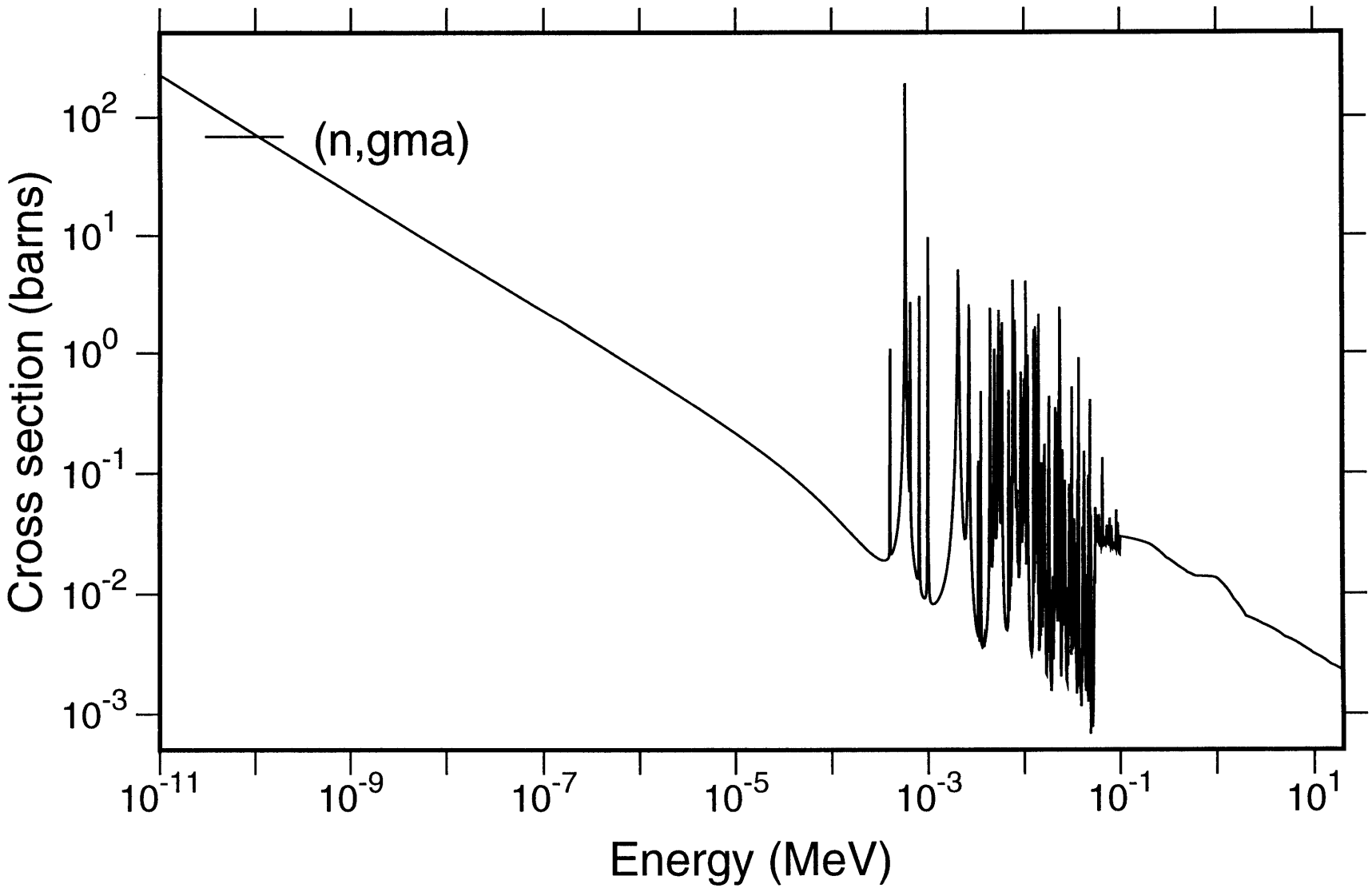
29-CU-63B FROM ENDF-VI.2
Non-threshold reactions
(n,gma)
Cross section (barns)
10^{2}
10^{1}
10^{0}
10^{-1}
10^{-2}
10^{-3}
10^{-11}
10^{-9}
10^{-7}
10^{-5}
10^{-3}
10^{-1}
10^{1}
Energy (MeV)

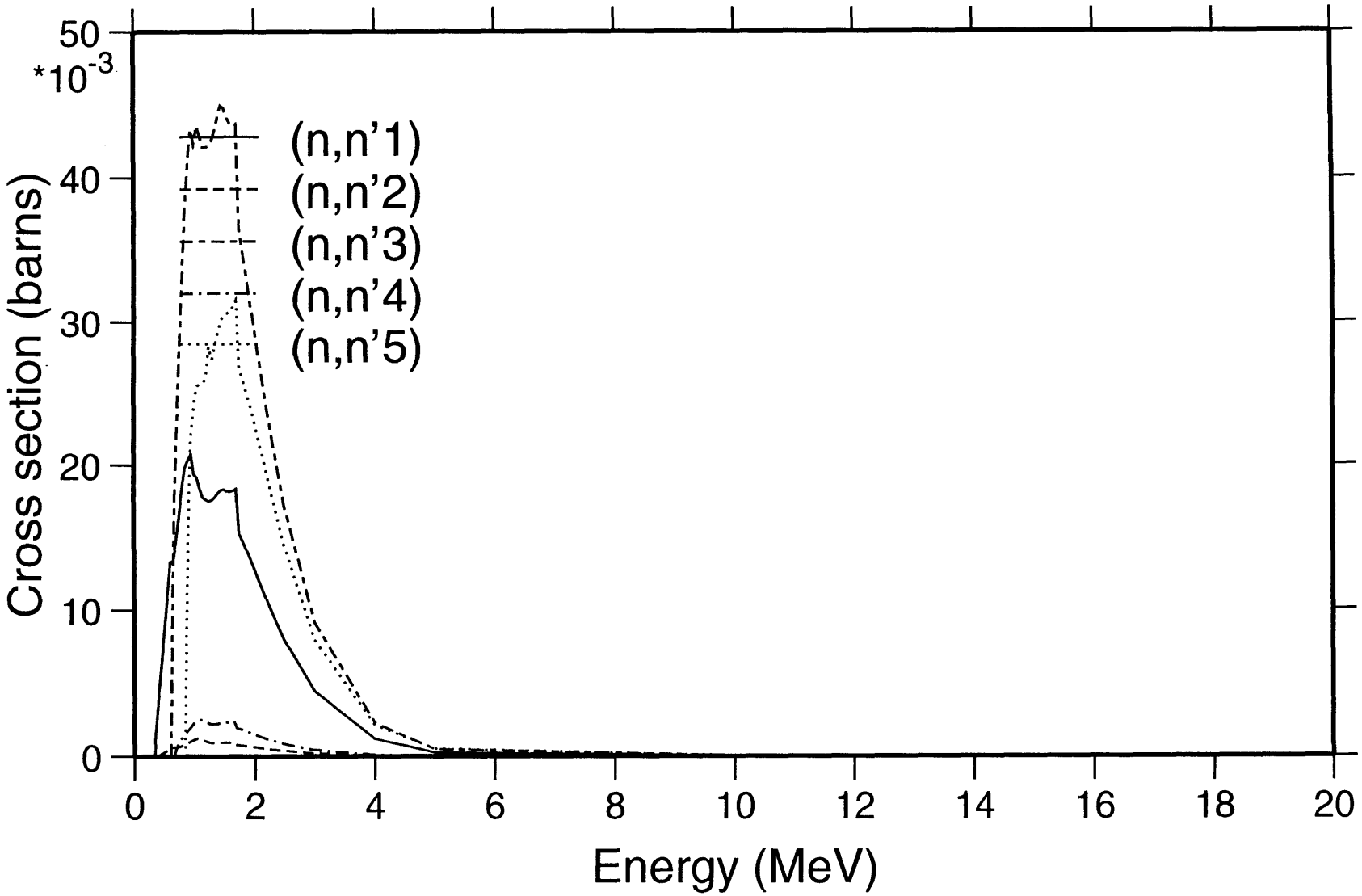
49-IN-NAT FROM ENDF-VI
Inelastic levels
50
*10-3
40
30
20
10
0
Cross section (barns)
(n,n'1)
(n,n'2)
(n,n'3)
(n,n'4)
(n,n'5)
0
2
4
6
8
10
12
14
16
18
20
Energy (MeV)

Appendix B:
Decay Scheme of Foil Materials

List of contents:

- ^{116m}In decay scheme
- ^{198}Au decay scheme
- ^{187}W decay scheme
- ^{60}Co decay scheme
- ^{56}Mn decay scheme
- ^{64}Cu decay scheme
- ^{115m}In decay scheme

49-IN-116M

AWR: 115.003502
Laboratories: INEL
Evaluation Date: FEB88
Evaluators: C.W.REICH
Comments:

```
 116IN B- DECAY (54.15 M)          ENSDF DATED 810528
Q-BETA: A. H. WAPSTRA AND G. AUDI, NUCL. PHYS. A432, 1 (1985).
OTHER: J. BLACHOT ET AL., NUCL. DATA SHEETS 32, 287 91981).
GAMMA NORMALIZATION: FROM RI(1293+1757+2112+2225G)=100.
translated by Fred Mann (WHC)
```

Half life: 3.2490E+03 (3.6000E+00) s, or 54.2 m
Ebeta: 3.1100E+05 (8.0000E+02) eV
Egamma: 2.4730E+06 (0.0000E+00) eV
Ealpha: 0.0000E+00 (0.0000E+00) eV
Spin & Parity: 5.0 plus
Isomer number: 1
Level number: 1

This nuclide has 1 decay mode(s):

Mode: beta-minus
Decay Q: 3.4030E+06 (4.0000E+03) eV

This nuclide has 4 radiation type(s):

Radiation type: gamma
Average decay energy: 2.4730E+06 (3.0000E+04) eV
Discrete spectrum normalization: 8.4400E-03 (4.0000E-05)
41 discrete lines given

9.9818E+04	(1.5000E+01)	0.0200	(0.0080)
1.1650E+05	(1.0000E+03)	0.0590	(0.0240)
1.2475E+05	(7.0000E+01)	0.0120	(0.0060)
1.3833E+05	(8.0000E+00)	3.9000	(0.1400)
1.6260E+05	(5.0000E+02)	0.0830	(0.0240)
1.9650E+05	(5.0000E+02)	0.0590	(0.0240)
2.4500E+05	(3.0000E+02)	0.0440	(0.0090)
2.6295E+05	(8.0000E+01)	0.1400	(0.0300)
2.7240E+05	(8.0000E+02)	0.0940	(0.0350)
2.7849E+05	(8.0000E+01)	0.1700	(0.0200)
3.0380E+05	(7.0000E+01)	0.1400	(0.0200)
3.4520E+05	(8.0000E+02)	0.0350	(0.0120)
3.5536E+05	(4.0000E+01)	0.9800	(0.0500)
4.1686E+05	(3.0000E+01)	34.6000	(1.7000)
4.3490E+05	(7.0000E+02)	0.0430	(0.0170)
4.5850E+05	(5.0000E+02)	0.0830	(0.0240)
4.6314E+05	(1.2000E+02)	0.9800	(0.0600)
5.0010E+05	(8.0000E+02)	0.0350	(0.0120)

5.3600E+05	(6.0000E+02)	0.0410	(0.0150)
5.6740E+05	(4.0000E+02)	0.0490	(0.0150)
6.3910E+05	(1.0000E+03)	0.0350	(0.0120)
6.5570E+05	(4.0000E+02)	0.1300	(0.0500)
6.7990E+05	(1.0000E+03)	0.0350	(0.0120)
6.8900E+05	(3.0000E+02)	0.1900	(0.0300)
7.0570E+05	(3.0000E+02)	0.2000	(0.0300)
7.3070E+05	(3.0000E+02)	0.0800	(0.0300)
7.3600E+05	(0.0000E+00)	0.0035	(0.0000)
7.8110E+05	(8.0000E+02)	0.1300	(0.0240)
8.1870E+05	(2.0000E+02)	13.6000	(0.5000)
8.3090E+05	(4.0000E+02)	0.0620	(0.0120)
9.3180E+05	(5.0000E+01)	0.0900	(0.0190)
9.7255E+05	(2.5000E+01)	0.5380	(0.0190)
1.0724E+06	(4.0000E+01)	0.0240	(0.0180)
1.0973E+06	(2.0000E+02)	66.6000	(1.3000)
1.2355E+06	(1.0000E+03)	0.1100	(0.0200)
1.2541E+06	(1.0000E+03)	0.0470	(0.0230)
1.2935E+06	(4.0000E+01)	100.0000	(2.0000)
1.5074E+06	(2.0000E+02)	11.8000	(0.4000)
1.7538E+06	(6.0000E+02)	2.9100	(0.0900)
2.1121E+06	(4.0000E+02)	18.4000	(0.5000)
2.2253E+06	(8.0000E+01)	0.0610	(0.0100)

Radiation type: beta-minus
Average decay energy: 3.0677E+05 (8.0000E+02) eV
Discrete spectrum normalization: 1.0000E-02 (0.0000E+00)
6 discrete endpoints given

3.0600E+05	(0.0000E+00)	0.3300	(0.0400)	allowed, nonunique
3.5600E+05	(0.0000E+00)	2.7100	(0.1000)	allowed, nonunique
6.0200E+05	(0.0000E+00)	10.2000	(0.4000)	allowed, nonunique
8.7400E+05	(0.0000E+00)	33.8000	(1.5000)	allowed, nonunique
1.0120E+06	(0.0000E+00)	52.1000	(1.2000)	allowed, nonunique
1.1370E+06	(0.0000E+00)	0.0800	(0.0500)	allowed, nonunique

Radiation type: disc. electrons
Average decay energy: 4.2300E+03 (9.0000E+01) eV
Discrete spectrum normalization: 1.0000E-02 (0.0000E+00)
15 discrete lines given

2.9507E+03	(1.0000E+00)	1.1200	(0.0300)
2.1115E+04	(1.0000E+00)	0.1620	(0.0050)
7.0618E+04	(1.5000E+01)	0.0200	(0.0080)
1.0913E+05	(8.0000E+00)	0.6500	(0.0300)
1.3386E+05	(8.0000E+00)	0.0760	(0.0040)
1.3745E+05	(8.0000E+00)	0.0161	(0.0007)
3.2616E+05	(4.0000E+01)	0.0144	(0.0009)
3.8766E+05	(3.0000E+01)	0.3140	(0.0180)
4.1240E+05	(3.0000E+01)	0.0339	(0.0020)
7.8950E+05	(2.0000E+02)	0.0213	(0.0010)
1.0681E+06	(2.0000E+02)	0.0511	(0.0018)
1.0928E+06	(2.0000E+02)	0.0058	(0.0002)
1.2643E+06	(4.0000E+01)	0.0546	(0.0020)
1.2891E+06	(4.0000E+01)	0.0062	(0.0002)
1.4782E+06	(2.0000E+02)	0.0047	(0.0002)

Radiation type: x-rays
Average decay energy: 2.5800E+02 (5.0000E+00) eV

Discrete spectrum normalization: 1.0000E-03 (0.0000E+00)
4 discrete lines given

3.6628E+03	(1.0000E+00)	0.9800 (0.0300)
2.5044E+04	(1.0000E+00)	2.8100 (0.0900)
2.5271E+04	(1.0000E+00)	5.2600 (0.1700)
2.8465E+04	(1.0000E+00)	1.7800 (0.0600)

79-AU-198

AWR: 196.299103
Laboratories: INEL
Evaluation Date: FEB88
Evaluators: C.W.REICH
Comments:

```
 198AU B- DECAY (2.696 D)          ENSDF DATED 840723
Q-BETA: A. H. WAPSTRA AND G. AUDI, NUCL. PHYS. A432, 1 (1985).
OTHER: R. L. AUBLE, NUCL. DATA SHEETS 40, 301 (1983).
E-GAMMA: SEE R. G. HELMER ET AL., AT. DATA AND NUCL. DATA
         TABLES 24, 39 (1979).
GAMMA NORMALIZATION:  0.9548 10 (75HE03); 0.9553 10 (76DEZR)
                      4PIBG-COIN SEMI
translated by Fred Mann (WHC)
```

Half life: 2.3293E+05 (1.7280E+02) s, or 64.7 h
Ebeta: 3.2700E+05 (4.0000E+02) eV
Egamma: 4.0260E+05 (0.0000E+00) eV
Ealpha: 0.0000E+00 (0.0000E+00) eV
Spin & Parity: 2.0 minus
Isomer number: 0
Level number: 0

This nuclide has 1 decay mode(s):

Mode: beta-minus
Decay Q: 1.3726E+06 (6.0000E+02) eV

This nuclide has 4 radiation type(s):

Radiation type: gamma
Average decay energy: 4.0040E+05 (4.0000E+02) eV
Discrete spectrum normalization: 9.5500E-03 (1.0000E-05)
3 discrete lines given

4.1180E+05 (1.1000E+00)	100.0000 (0.0000)	
6.7589E+05 (1.9000E+00)	0.8410 (0.0030)	
1.0877E+06 (3.0000E+00)	0.1664 (0.0021)	

Radiation type: beta-minus
Average decay energy: 3.1170E+05 (2.0000E+02) eV
Discrete spectrum normalization: 1.0000E-02 (0.0000E+00)
3 discrete endpoints given

2.8490E+05 (0.0000E+00)	1.3000 (0.1000)	allowed, nonunique
9.6080E+05 (0.0000E+00)	98.7000 (0.1000)	allowed, nonunique
1.3726E+06 (0.0000E+00)	0.0250 (0.0050)	allowed, nonunique

Radiation type: disc. electrons
Average decay energy: 1.5300E+04 (3.0000E+02) eV
Discrete spectrum normalization: 1.0000E-02 (0.0000E+00)
8 discrete lines given

7.6041E+03	(1.0000E+00)	2.0900	(0.0400)
5.6610E+04	(1.0000E+00)	0.0980	(0.0030)
3.2870E+05	(1.1000E+00)	2.8800	(0.0900)
3.9697E+05	(1.1000E+00)	0.4060	(0.0120)
3.9760E+05	(1.1000E+00)	0.4290	(0.0130)
3.9952E+05	(1.1000E+00)	0.1840	(0.0060)
4.0851E+05	(1.1000E+00)	0.2560	(0.0050)
4.1100E+05	(1.1000E+00)	0.0830	(0.0020)

Radiation type: x-rays
Average decay energy: 2.1800E+03 (4.0000E+01) eV
Discrete spectrum normalization: 1.0000E-02 (0.0000E+00)
5 discrete lines given

1.1824E+04	(1.0000E+00)	1.2800	(0.0300)
6.8894E+04	(1.0000E+00)	0.8100	(0.0200)
7.0818E+04	(1.0000E+00)	1.3800	(0.0400)
8.0040E+04	(1.0000E+00)	0.4770	(0.0140)
8.2302E+04	(1.0000E+00)	0.1320	(0.0040)

74-W -187

AWR: 185.393600
Laboratories: INEL
Evaluation Date: FEB88
Evaluators: C.W.REICH
Comments:

```
 187W B- DECAY                        ENSDF DATED 861029
Q-BETA: A. H. WAPSTRA AND G. AUDI, NUCL. PHYS. A432, 1 (1985).
OTHER: Y. A. ELLIS- AKOVALI, NUCL. DATA SHEETS 36, 559 (1982).
GAMMA NORMALIZATION: ABSOLUTE INTENSITIES WERE OBTAINED BY NDS
AUTHOR FROM INTENSITY BALANCE AT THE 685.74 LEVEL, WHERE THE
B- FEEDING IS 53.1% 16 (70HE14).
translated by Fred Mann (WHC)
```

Half life: 8.6040E+04 (3.6000E+02) s, or 23.9 h
Ebeta: 2.9600E+05 (4.0000E+03) eV
Egamma: 4.2600E+05 (0.0000E+00) eV
Ealpha: 0.0000E+00 (0.0000E+00) eV
Spin & Parity: 1.5 minus
Isomer number: 0
Level number: 0

This nuclide has 1 decay mode(s):

Mode: beta-minus
Decay Q: 1.3124E+06 (1.7000E+03) eV

This nuclide has 4 radiation type(s):

Radiation type: gamma
Average decay energy: 4.1500E+05 (1.5000E+04) eV
Discrete spectrum normalization: 8.3500E-04 (2.9000E-05)
58 discrete lines given

1.6610E+04	(2.0000E+01)	0.0700	(0.0100)
2.9230E+04	(3.0000E+01)	0.0440	(0.0100)
4.0920E+04	(5.0000E+01)	0.0200	(0.0100)
4.3660E+04	(6.0000E+01)	0.0200	(0.0100)
7.2002E+04	(4.0000E+00)	129.0000	(1.9000)
7.7370E+04	(5.0000E+01)	0.0800	(0.0200)
9.3220E+04	(5.0000E+01)	0.0700	(0.0100)
1.0014E+05	(2.0000E+01)	0.1000	(0.0200)
1.0660E+05	(1.3000E+01)	0.2950	(0.0100)
1.1375E+05	(8.0000E+00)	0.8900	(0.0300)
1.2379E+05	(1.1000E+02)	0.0300	(0.0100)
1.3425E+05	(7.0000E+00)	102.5000	(2.1000)
1.3850E+05	(6.0000E+01)	0.0500	(0.0200)
1.6567E+05	(4.0000E+02)	0.0100	(0.0040)
1.6850E+05	(4.0000E+02)	0.0300	(0.0110)
1.9834E+05	(1.2000E+02)	0.0200	(0.0050)

2.0625E+05	(1.9000E+01)	1.6500 (0.0600)
2.0829E+05	(1.6000E+02)	0.0080 (0.0030)
2.3920E+05	(2.4000E+01)	1.0000 (0.0500)
2.4628E+05	(2.2000E+01)	1.3800 (0.0500)
2.7561E+05	(1.2000E+02)	0.0240 (0.0070)
3.0270E+05	(5.0000E+02)	0.0060 (0.0030)
3.5286E+05	(1.7000E+02)	0.0180 (0.0070)
3.7431E+05	(1.4000E+02)	0.0300 (0.0100)
3.7593E+05	(1.3000E+02)	0.0400 (0.0100)
4.5492E+05	(2.0000E+01)	0.3400 (0.0200)
4.7957E+05	(3.0000E+01)	253.0000 (6.0000)
4.8415E+05	(3.0000E+01)	0.2000 (0.0100)
4.9280E+05	(2.0000E+02)	0.3000 (0.1000)
5.1165E+05	(5.0000E+01)	7.4700 (0.0800)
5.5152E+05	(4.0000E+01)	58.9000 (1.2000)
5.6462E+05	(1.9000E+02)	0.1400 (0.0500)
5.7371E+05	(1.4000E+02)	0.0060 (0.0020)
5.7631E+05	(8.0000E+01)	0.0770 (0.0120)
5.7872E+05	(1.1000E+02)	0.0110 (0.0040)
5.8896E+05	(6.0000E+01)	1.4100 (0.0300)
6.1290E+05	(5.0000E+02)	0.0240 (0.0120)
6.1828E+05	(6.0000E+01)	72.7000 (1.5000)
6.2554E+05	(1.0000E+02)	12.6000 (0.3000)
6.3865E+05	(1.3000E+02)	0.0370 (0.0120)
6.4730E+05	(3.0000E+02)	0.0090 (0.0040)
6.8234E+05	(2.0000E+02)	0.0800 (0.0800)
6.8574E+05	(5.0000E+01)	316.0000 (7.0000)
6.9306E+05	(2.2000E+02)	0.0150 (0.0090)
7.4529E+05	(1.0000E+02)	3.4500 (0.0800)
7.6740E+05	(8.0000E+02)	0.0180 (0.0070)
7.7291E+05	(6.0000E+01)	47.7000 (1.0000)
8.1656E+05	(2.0000E+01)	0.1140 (0.0090)
8.2590E+05	(3.0000E+02)	0.0027 (0.0004)
8.2665E+05	(2.5000E+02)	0.0027 (0.0004)
8.4470E+05	(5.0000E+02)	0.0028 (0.0016)
8.6471E+05	(1.8000E+02)	3.8900 (0.0900)
8.7956E+05	(1.9000E+02)	1.6400 (0.0400)
9.6017E+05	(5.0000E+01)	0.0153 (0.0009)
1.0562E+06	(5.0000E+01)	0.0026 (0.0007)
1.1904E+06	(1.2000E+02)	0.0025 (0.0003)
1.2208E+06	(3.0000E+02)	0.0002 (0.0001)
1.2301E+06	(4.0000E+01)	0.0153 (0.0018)

Radiation type: beta-minus
Average decay energy: 2.7400E+05 (4.0000E+03) eV
Discrete spectrum normalization: 1.0000E-02 (0.0000E+00)
16 discrete endpoints given

8.1900E+04	(0.0000E+00)	0.0033 (0.0011)	allowed, nonunique
9.1600E+04	(0.0000E+00)	0.0001 (0.0000)	allowed, nonunique
1.2200E+05	(0.0000E+00)	0.0120 (0.0050)	allowed, nonunique
3.5220E+05	(0.0000E+00)	0.0015 (0.0001)	allowed, nonunique
4.3280E+05	(0.0000E+00)	0.5200 (0.0600)	allowed, nonunique
4.4780E+05	(0.0000E+00)	0.6700 (0.0800)	allowed, nonunique
4.6770E+05	(0.0000E+00)	0.0002 (0.0001)	allowed, nonunique
4.8580E+05	(0.0000E+00)	0.0023 (0.0009)	allowed, nonunique
4.9580E+05	(0.0000E+00)	0.0380 (0.0130)	allowed, nonunique
5.3950E+05	(0.0000E+00)	4.2000 (0.4000)	allowed, nonunique
6.2670E+05	(0.0000E+00)	53.1000 (1.6000)	allowed, nonunique
6.6510E+05	(0.0000E+00)	0.0008 (0.0004)	allowed, nonunique
6.8690E+05	(0.0000E+00)	5.2000 (0.5000)	allowed, nonunique
6.9410E+05	(0.0000E+00)	5.2000 (0.5000)	allowed, nonunique

1.1782E+06	(0.0000E+00)	0.7000 (0.3000)	allowed, nonunique
1.3124E+06	(0.0000E+00)	30.0000 (2.0000)	allowed, nonunique

Radiation type: disc. electrons
Average decay energy: 2.2600E+04 (5.0000E+02) eV
Discrete spectrum normalization: 1.0000E-02 (0.0000E+00)
18 discrete lines given

6.7035E+03	(1.0000E+00)	13.1000 (0.5000)
4.2070E+04	(8.0000E+00)	0.2270 (0.0130)
4.9182E+04	(1.0000E+00)	0.7100 (0.0300)
5.9475E+04	(4.0000E+00)	0.7900 (0.0400)
6.0043E+04	(4.0000E+00)	0.3230 (0.0160)
6.1467E+04	(4.0000E+00)	0.3730 (0.0180)
6.2571E+04	(7.0000E+00)	15.9000 (0.8000)
6.9300E+04	(4.0000E+00)	0.3390 (0.0140)
1.2172E+05	(7.0000E+00)	2.3100 (0.1200)
1.2229E+05	(7.0000E+00)	0.3040 (0.0150)
1.3137E+05	(7.0000E+00)	0.6200 (0.0300)
1.3362E+05	(7.0000E+00)	0.1900 (0.0100)
1.3457E+05	(1.9000E+01)	0.3600 (0.0200)
4.0789E+05	(3.0000E+01)	0.3870 (0.0200)
4.6704E+05	(3.0000E+01)	0.0510 (0.0030)
5.4660E+05	(6.0000E+01)	0.1560 (0.0150)
6.1406E+05	(5.0000E+01)	0.0850 (0.0040)
7.0123E+05	(6.0000E+01)	0.0630 (0.0090)

Radiation type: x-rays
Average decay energy: 1.1000E+04 (3.0000E+02) eV
Discrete spectrum normalization: 1.0000E-02 (0.0000E+00)
5 discrete lines given

1.0010E+04	(1.0000E+00)	5.9000 (0.2000)
5.9718E+04	(1.0000E+00)	4.8000 (0.2000)
6.1141E+04	(1.0000E+00)	8.3000 (0.4000)
6.9152E+04	(1.0000E+00)	2.8300 (0.1300)
7.1051E+04	(1.0000E+00)	0.7400 (0.0300)

27-CO- 60

AWR: 59.484570
Laboratories: INEL
Evaluation Date: FEB88
Evaluators: C.W.REICH
Comments:

```
 60CO B- DECAY (5.2704 Y)          ENSDF DATED 860805
Q-BETA: A. H. WAPSTRA AND G. AUDI, NUCL. PHYS. A432, 1 (1985).
OTHER: P. ANDERSSON ET AL.,NUCL. DATA SHEETS 48, 251 (1986).
PRECISE E-GAMMA VALUES: R. G. HELMER ET AL., AT. DATA AND NUCL.
                        DATA TABLES 24, 39 (1979).
GAMMA NORMALIZATION: FROM I(1332G+2159G)=100 AND
                     I(2159G)/I(1332G)=1.11E-5 18.
translated by Fred Mann (WHC)
```

Half life: 1.6635E+08 (1.5778E+04) s, or 5.3 a
Ebeta: 9.6400E+04 (7.0000E+01) eV
Egamma: 2.5044E+06 (0.0000E+00) eV
Ealpha: 0.0000E+00 (0.0000E+00) eV
Spin & Parity: 5.0 plus
Isomer number: 0
Level number: 0

This nuclide has 1 decay mode(s):

Mode: beta-minus
Decay Q: 2.8236E+06 (1.1000E+02) eV

This nuclide has 4 radiation type(s):

Radiation type: gamma
Average decay energy: 2.5044E+06 (2.0000E+02) eV
Discrete spectrum normalization: 1.0000E-02 (0.0000E+00)
6 discrete lines given

```
3.4693E+05 (7.0000E+01)     0.0076 ( 0.0005)
8.2628E+05 (9.0000E+01)     0.0076 ( 0.0008)
1.1732E+06 (4.0000E+00)    99.9000 ( 0.0200)
1.3325E+06 (5.0000E+00)    99.9820 ( 0.0010)
2.1588E+06 (9.0000E+01)     0.0011 ( 0.0002)
2.5050E+06 (0.0000E+00)     0.0000 ( 0.0000)
```

Radiation type: beta-minus
Average decay energy: 9.6030E+04 (7.0000E+01) eV
Discrete spectrum normalization: 1.0000E-02 (0.0000E+00)
2 discrete endpoints given

```
3.1787E+05 (0.0000E+00)    99.9250 ( 0.0200)     allowed, nonunique
```

1.4911E+06 (0.0000E+00)	0.0570 (0.0200)	allowed, nonunique

Radiation type: disc. electrons
Average decay energy: 3.7000E+02 (7.0000E+00) eV
Discrete spectrum normalization: 1.0000E-04 (0.0000E+00)
6 discrete lines given

8.4750E+02 (1.0000E+00)	3.9000 (0.0800)
6.6062E+03 (1.0000E+00)	1.5500 (0.0300)
1.1649E+06 (4.0000E+00)	1.5000 (0.0500)
1.1722E+06 (4.0000E+00)	0.1450 (0.0040)
1.3242E+06 (5.0000E+00)	1.1400 (0.0300)
1.3315E+06 (5.0000E+00)	0.1110 (0.0030)

Radiation type: x-rays
Average decay energy: 8.3000E-01 (1.2000E-02) eV
Discrete spectrum normalization: 1.0000E-05 (0.0000E+00)
4 discrete lines given

8.6830E+02 (1.0000E+00)	0.1490 (0.0030)
7.4609E+03 (1.0000E+00)	3.2500 (0.0700)
7.4781E+03 (1.0000E+00)	6.4000 (0.1400)
8.2647E+03 (1.0000E+00)	1.3000 (0.0300)

25-MN- 56

AWR: 55.518929
Laboratories: INEL
Evaluation Date: FEB88
Evaluators: C.W.REICH
Comments:

```
 56MN B- DECAY                        ENSDF DATED 870727
Q-BETA: A. H. WAPSTRA AND G. AUDI, NUCL. PHYS. A432, 1 (1985).
OTHER: HUO JUNDE ET AL., NUCL DATA SHEETS 51, 1 (1987).
GAMMA NORMALIZATION: BASED ON NO B-DECAY TO THE GROUND STATE
                     AND INTENSITY BALANCE.
translated by Fred Mann (WHC)
```

Half life: 9.2826E+03 (2.1600E+00) s, or 2.6 h
Ebeta: 8.3100E+05 (6.0000E+03) eV
Egamma: 1.6920E+06 (0.0000E+00) eV
Ealpha: 0.0000E+00 (0.0000E+00) eV
Spin & Parity: 3.0 plus
Isomer number: 0
Level number: 0

This nuclide has 1 decay mode(s):

Mode: beta-minus
Decay Q: 3.6957E+06 (9.0000E+02) eV

This nuclide has 4 radiation type(s):

Radiation type: gamma
Average decay energy: 1.6920E+06 (1.7000E+04) eV
Discrete spectrum normalization: 9.8870E-03 (3.0000E-06)
10 discrete lines given

8.4675E+05	(2.0000E+01)	100.0000 (0.3000)
1.0378E+06	(2.2000E+01)	0.0400 (0.0050)
1.2383E+06	(2.6000E+01)	0.1000 (0.0100)
1.8107E+06	(4.0000E+01)	27.5000 (0.8000)
2.1130E+06	(4.0000E+01)	14.5000 (0.4000)
2.5229E+06	(6.0000E+01)	1.0000 (0.0300)
2.5984E+06	(5.0000E+01)	0.0190 (0.0020)
2.6574E+06	(5.0000E+01)	0.6600 (0.0200)
2.9598E+06	(6.0000E+01)	0.3100 (0.0100)
3.3696E+06	(7.0000E+01)	0.1700 (0.0100)

Radiation type: beta-minus
Average decay energy: 8.3100E+05 (6.0000E+03) eV
Discrete spectrum normalization: 1.0000E-02 (0.0000E+00)
7 discrete endpoints given

2.5050E+05	(0.0000E+00)	0.0188	(0.0020)	allowed, nonunique
3.2600E+05	(0.0000E+00)	1.1600	(0.0400)	allowed, nonunique
5.7280E+05	(0.0000E+00)	0.0400	(0.0050)	allowed, nonunique
7.3580E+05	(0.0000E+00)	14.6000	(0.4000)	allowed, nonunique
1.0382E+06	(0.0000E+00)	27.9000	(0.8000)	allowed, nonunique
1.6107E+06	(0.0000E+00)	0.0590	(0.0110)	allowed, nonunique
2.8489E+06	(0.0000E+00)	56.3000	(1.0000)	allowed, nonunique

Radiation type: disc. electrons
Average decay energy: 2.9400E+02 (7.0000E+00) eV
Discrete spectrum normalization: 1.0000E-04 (0.0000E+00)
6 discrete lines given

7.0160E+02	(1.0000E+00)	4.3400	(0.1200)
5.6821E+03	(1.0000E+00)	1.8500	(0.0500)
8.3964E+05	(2.0000E+01)	2.6600	(0.0800)
8.4591E+05	(2.0000E+01)	0.2480	(0.0070)
1.8036E+06	(4.0000E+01)	0.1270	(0.0050)
2.1059E+06	(4.0000E+01)	0.0510	(0.0020)

Radiation type: x-rays
Average decay energy: 6.3900E-01 (1.2000E-02) eV
Discrete spectrum normalization: 1.0000E-05 (0.0000E+00)
4 discrete lines given

7.1750E+02	(1.0000E+00)	0.1350	(0.0040)
6.3909E+03	(1.0000E+00)	2.9200	(0.0800)
6.4032E+03	(1.0000E+00)	5.7600	(0.1600)
7.0580E+03	(1.0000E+00)	1.1700	(0.0300)

29-CU- 64

AWR: 63.450199
Laboratories: INEL
Evaluation Date: JAN88
Evaluators: C.W.REICH
Comments:

```
  64CU B- DECAY                        ENSDF DATED 800723
  64CU B+ DECAY                        ENSDF DATED 800723
 Q VALUES: A. H. WAPSTRA AND G. AUDI, NUCL. PHYS. A432, 1 (1985).
 OTHER: M. L. HALBERT, NUCL. DATA SHEETS 28, 179 (1979).
translated by Fred Mann (WHC)
```

Half life: 4.5724E+04 (7.2000E+00) s, or 12.7 h
Ebeta: 1.2240E+05 (9.0000E+02) eV
Egamma: 1.9070E+05 (0.0000E+00) eV
Ealpha: 0.0000E+00 (0.0000E+00) eV
Spin & Parity: 1.0 plus
Isomer number: 0
Level number: 0

This nuclide has 2 decay mode(s):

Mode: beta-minus
Decay Q: 5.7820E+05 (8.0000E+02) eV
Branching: 37.1000 (0.4000) percent

Mode: e.c. or beta-plus
Decay Q: 1.6745E+06 (4.0000E+02) eV
Branching: 62.9000 (0.4000) percent

This nuclide has 5 radiation type(s):

Radiation type: gamma
Average decay energy: 6.5000E+03 (5.0000E+02) eV
Discrete spectrum normalization: 6.2900E-03 (4.0000E-05)
1 discrete lines given

```
1.3458E+06 (6.0000E+01)      0.7700 ( 0.0600)
```

Radiation type: beta-minus
Average decay energy: 7.0600E+04 (8.0000E+02) eV
Discrete spectrum normalization: 1.0000E-02 (0.0000E+00)
1 discrete endpoints given

```
5.7820E+05 (0.0000E+00)    37.1000 ( 0.4000)      allowed, nonunique
```

Radiation type: e.c. or beta-plus
Average decay energy: 4.9800E+04 (5.0000E+02) eV
Discrete spectrum normalization: 1.0000E-02 (0.0000E+00)
2 discrete lines given

3.2870E+05	(0.0000E+00)	0.4800 (0.0400)	allowed, nonunique
1.6745E+06	(0.0000E+00)	62.4000 (0.4386)	allowed, nonunique

Radiation type: disc. electrons
Average decay energy: 2.0470E+03 (1.4000E+01) eV
Discrete spectrum normalization: 1.0000E-02 (0.0000E+00)
2 discrete lines given

8.4750E+02	(1.0000E+00)	59.2000 (0.5000)
6.6062E+03	(1.0000E+00)	23.4000 (0.2000)

Radiation type: x-rays
Average decay energy: 1.8420E+05 (1.8000E+03) eV
Discrete spectrum normalization: 1.0000E-02 (0.0000E+00)
5 discrete lines given

8.6830E+02	(1.0000E+00)	0.2258 (0.0019)
7.4609E+03	(1.0000E+00)	4.9000 (0.0400)
7.4781E+03	(1.0000E+00)	9.6500 (0.0900)
8.2647E+03	(1.0000E+00)	1.9650 (0.0180)
5.1100E+05	(1.0000E+00)	35.8000 (0.4000)

49-IN-115M

AWR: 114.012100
Laboratories: INEL
Evaluation Date: JAN88
Evaluators: C.W.REICH
Comments:

```
  115IN B- DECAY (4.486 H)          ENSDF DATED 800716
  115IN IT DECAY (4.486 H)          ENSDF DATED 800716
 Q-BETA: A. H. WAPSTRA AND G. AUDI, NUCL. PHYS. A432, 1 (1985).
 OTHER: J. BLACHOT AND G. MARGUIER, NUCL. DATA SHEETS 52, 565 (198
translated by Fred Mann (WHC)
```

Half life: 1.6150E+04 (1.4400E+01) s, or 4.5 h
Ebeta: 1.6900E+05 (4.0000E+03) eV
Egamma: 1.6240E+05 (0.0000E+00) eV
Ealpha: 0.0000E+00 (0.0000E+00) eV
Spin & Parity: 0.5 minus
Isomer number: 1
Level number: 1

This nuclide has 2 decay mode(s):

Mode: beta-minus
Decay Q: 8.3300E+05 (4.0000E+03) eV
Branching: 5.0000 (0.7000) percent

Mode: IT
Decay Q: 3.3624E+05 (3.0000E+01) eV
Branching: 95.0000 (0.7000) percent

This nuclide has 4 radiation type(s):

Radiation type: gamma
Average decay energy: 1.5420E+05 (1.0000E+03) eV
Discrete spectrum normalization: 1.0000E-02 (0.0000E+00)
2 discrete lines given

```
3.3624E+05 (2.5000E+01)     45.8000 ( 0.3000)
4.9737E+05 (2.9000E+01)      0.0470 ( 0.0000)
```

Radiation type: beta-minus
Average decay energy: 1.4000E+04 (7.0000E+01) eV
Discrete spectrum normalization: 1.0000E-02 (0.0000E+00)
2 discrete endpoints given

```
3.3600E+05 (0.0000E+00)      0.0470 ( 0.0000)      allowed, nonunique
8.3300E+05 (0.0000E+00)      5.0000 ( 0.7000)      allowed, nonunique
```

Radiation type: disc. electrons
Average decay energy: 1.5500E+05 (4.0000E+03) eV
Discrete spectrum normalization: 1.0000E-02 (0.0000E+00)
7 discrete lines given

2.8362E+03	(1.0000E+00)	41.0000	(1.0000)
2.0272E+04	(1.0000E+00)	5.7900	(0.1800)
3.0830E+05	(3.0000E+01)	38.5000	(1.2000)
3.3200E+05	(3.0000E+01)	5.6600	(0.1700)
3.3230E+05	(3.0000E+01)	0.9700	(0.0300)
3.3251E+05	(3.0000E+01)	1.4800	(0.0500)
3.3546E+05	(3.0000E+01)	1.6700	(0.0400)

Radiation type: x-rays
Average decay energy: 8.1800E+03 (1.6000E+02) eV
Discrete spectrum normalization: 1.0000E-02 (0.0000E+00)
8 discrete lines given

3.4872E+03	(1.0000E+00)	3.2300	(0.0800)
3.6628E+03	(1.0000E+00)	0.0000	(0.0000)
2.4002E+04	(1.0000E+00)	9.3000	(0.3000)
2.4210E+04	(1.0000E+00)	17.5000	(0.5000)
2.5044E+04	(1.0000E+00)	0.0001	(0.0000)
2.5271E+04	(1.0000E+00)	0.0002	(0.0000)
2.7257E+04	(1.0000E+00)	5.8200	(0.1800)
2.8465E+04	(1.0000E+00)	0.0001	(0.0000)

Appendix C:
Measured Mass and Thicknesses of Foils

List of Contents:

Measured Mass
- Indium Foils
- Gold Foils
- Copper Foils
- Manganese Foils
- Tungsten Foils

Measured Thickness Compared to Nominal Thickness
- Indium Foils
- Gold Foils
- Copper Foils
- Manganese Foils
- Tungsten Foils

Indium Foils:

FOIL #	SPEC. SHEET MASS (g)	MEASURED MASS (g) #1	MEASURED MASS (g) #2	MEASURED MASS (g) #3	AVG. MEASURED MASS (g)	ERROR (%)
A	0.0490	0.04881	0.04898	0.04891	0.04890	0.1%
B	0.0523	0.05305	0.05314	0.05303	0.05307	0.1%
C	0.0424	0.04286	0.04301	0.04277	0.04288	0.1%
D	0.0530	0.05337	0.05328	0.05331	0.05332	0.1%
E	0.0406	0.04074	0.04075	0.04032	0.04075	0.1%
F	0.0472	0.04734	0.04737	0.04725	0.04732	0.1%
G	0.0534	0.05342	0.05355	0.05353	0.05350	0.1%
H	0.0430	0.04314	0.04316	0.04315	0.04315	0.1%
I	0.0482	0.04836	0.04842	0.04833	0.04837	0.1%
J	0.0545	0.05529	0.05525	0.05534	0.05529	0.1%
K	0.0500	0.05064	0.05052	0.05055	0.05057	0.1%
L	0.0500	0.05035	0.05026	0.05025	0.05029	0.1%
M	0.0464	0.04676	0.04664	0.04669	0.04670	0.1%
N	0.0447	0.04478	0.04469	0.04477	0.04475	0.1%
O	0.0468	0.04687	0.04687	0.04694	0.04689	0.1%
P	0.0513	0.05174	0.05170	0.05176	0.05173	0.1%
R	0.0505	0.05072	0.05079	0.05079	0.05077	0.1%
S	0.0555	0.05554	0.05557	0.05551	0.05554	0.1%
T	0.0500	0.05015	0.05023	0.05022	0.05020	0.1%
U	0.0469	0.04710	0.04720	0.04715	0.04715	0.1%

Gold Foils:

FOIL #	SPEC. SHEET MASS (g)	MEASURED MASS (g) #1	MEASURED MASS (g) #2	MEASURED MASS (g) #3	AVG. MEASURED MASS (g)	ERROR (%)
A	0.0654	0.06551	0.06549	0.06550	0.06550	0.08%
B	0.0651	0.06511	0.06511	0.06512	0.06511	0.08%
C	0.0650	0.06487	0.06483	0.06484	0.06485	0.08%
D	0.0664	0.06612	0.06617	0.06611	0.06613	0.08%
E	0.0658	0.06564	0.06571	0.06563	0.06566	0.08%
F	0.0657	0.06589	0.06579	0.06588	0.06585	0.08%
G	0.0655	0.06590	0.06593	0.06585	0.06589	0.08%
H	0.0649	0.06499	0.06496	0.06496	0.06497	0.08%
I	0.0649	0.06539	0.06544	0.06539	0.06541	0.08%
J	0.0654	0.06539	0.06539	0.06537	0.06538	0.08%
K	0.0649	0.06530	0.06530	0.06522	0.06527	0.08%
L	0.0653	0.06548	0.06549	0.06544	0.06547	0.08%
M	0.0662	0.06588	0.06586	0.06586	0.06587	0.08%
N	0.0656	0.06576	0.06571	0.06570	0.06572	0.08%
O	0.0650	0.06517	0.06511	0.06515	0.06514	0.08%
P	0.0656	0.06573	0.06581	0.06591	0.06582	0.08%
R	0.0657	0.06565	0.06577	0.06580	0.06574	0.08%
S	0.0646	0.06477	0.06478	0.06472	0.06476	0.08%
T	0.0659	0.06570	0.06570	0.06573	0.06571	0.08%
U	0.0660	0.06585	0.06570	0.06583	0.06579	0.08%

Copper Foils:

FOIL #	SPEC. SHEET MASS (g)	MEASURED MASS (g)	MEASURED MASS (g) #2	MEASURED MASS (g) #3	AVG. MEASURED MASS (g)	ERROR (%)
A	0.1126	0.11284	0.11273	0.11283	0.11280	0.04%
B	0.1127	0.11304	0.11311	0.11306	0.11307	0.04%
C	0.1122	0.11254	0.11259	0.11250	0.11254	0.04%
D	0.1125	0.11290	0.11293	0.11290	0.11291	0.04%
E	0.1126	0.11282	0.11285	0.11288	0.11285	0.04%
F	0.1121	0.11250	0.11259	0.11253	0.11254	0.04%
G	0.1126	0.11291	0.11286	0.11288	0.11288	0.04%
H	0.1123	0.11280	0.11284	0.11284	0.11283	0.04%
I	0.1125	0.11242	0.11242	0.11239	0.11241	0.04%
J	0.1126	0.11272	0.11271	0.11268	0.11270	0.04%
K	0.1130	0.11248	0.11246	0.11246	0.11247	0.04%
L	0.1123	0.11258	0.11272	0.11262	0.11264	0.04%
M	0.1125	0.11309	0.11308	0.11320	0.11312	0.04%
N	0.1128	0.11248	0.11246	0.11261	0.11252	0.04%
O	0.1117	0.11293	0.11302	0.11304	0.11300	0.04%
P	0.1240	0.11295	0.11297	0.11294	0.11295	0.04%
R	0.1122	0.11288	0.11297	0.11297	0.11294	0.04%
S	0.1125	0.11307	0.11311	0.11313	0.11310	0.04%
T	0.1120	0.11242	0.11248	0.11248	0.11246	0.04%
U	0.1122	0.11288	0.11284	0.11290	0.11287	0.04%

Manganese Foils:

FOIL #	SPEC. SHEET MASS (g)	MEASURED MASS (g)	MEASURED MASS (g) #2	MEASURED MASS (g) #3	AVG. MEASURED MASS (g)	ERROR (%)
A	0.1158	0.11627	0.11618	0.11624	0.11623	0.04%
B	0.1200	0.12026	0.12035	0.12029	0.12030	0.04%
C	0.1211	0.12096	0.12105	0.12103	0.12101	0.04%
D	0.1174	0.11726	0.11734	0.11731	0.11730	0.04%
E	0.1195	0.11956	0.11964	0.11957	0.11959	0.04%
F	0.1203	0.12056	0.12055	0.12056	0.12056	0.04%
G	0.1208	0.12007	0.12013	0.12006	0.12009	0.04%
H	0.1202	0.12064	0.12065	0.12067	0.12065	0.04%
I	0.1231	0.12269	0.12270	0.12275	0.12271	0.04%
J	0.1166	0.11651	0.11648	0.11653	0.11651	0.04%
K	0.1206	0.12019	0.12024	0.12022	0.12022	0.04%
L	0.1205	0.12006	0.12007	0.12010	0.12008	0.04%
M	0.1235	0.12323	0.12321	0.12324	0.12323	0.04%
N	0.1241	0.12367	0.12369	0.12374	0.12370	0.04%
O	0.1217	0.12169	0.12174	0.12170	0.12171	0.04%
P	0.1219	0.12144	0.12149	0.12145	0.12146	0.04%
R	0.1197	0.11916	0.11913	0.11911	0.11913	0.04%
S	0.1196	0.11862	0.11872	0.11874	0.11869	0.04%
T	0.1190	0.11820	0.11816	0.11822	0.11819	0.04%
U	0.1207	0.12059	0.12062	0.12068	0.12063	0.04%

Tungsten Foils:

FOIL #	SPEC. SHEET MASS (g)	MEASURED MASS (g)	MEASURED MASS (g) #2	MEASURED MASS (g) #3	AVG. MEASURED MASS (g)	ERROR (%)
A	0.0569	0.05950	0.05953	0.05954	0.05952	0.08%
B	0.0601	0.06035	0.06036	0.06042	0.06038	0.08%
C	0.0532	0.05353	0.05348	0.05356	0.05352	0.09%
D	0.0568	0.05715	0.05725	0.05718	0.05719	0.09%
E	0.0542	0.05404	0.05404	0.05402	0.05403	0.09%
F	0.0638	0.06415	0.06399	0.06410	0.06408	0.08%
G	0.0541	0.05413	0.05418	0.05415	0.05415	0.09%
H	0.0609	0.06115	0.06117	0.06114	0.06115	0.08%
I	0.0645	0.06462	0.06470	0.06466	0.06466	0.08%
J	0.0554	0.05544	0.05539	0.05534	0.05539	0.09%
K	0.0558	0.05577	0.05586	0.05591	0.05585	0.09%
L	0.0622	0.06240	0.06243	0.06242	0.06242	0.08%
M	0.0665	0.06673	0.06670	0.06676	0.06673	0.07%
N	0.0575	0.05789	0.05791	0.05788	0.05789	0.09%
O	0.0629	0.06319	0.06320	0.06319	0.06319	0.08%
P	0.0539	0.05432	0.05432	0.05431	0.05432	0.09%
R	0.0611	0.06141	0.06135	0.06111	0.06129	0.08%
S	0.0562	0.05628	0.05634	0.05635	0.05632	0.09%
T	0.0575	0.05759	0.05753	0.05754	0.05755	0.09%
U	0.0582	0.05846	0.05838	0.05842	0.05842	0.09%

Indium Foils:

FOIL #	MEASURED THICKNESS DIFF. (mil)	NOMINAL THICKNESS (mil)	% DIFFERENCE
A	2.08	2.0	4.0%
B	2.26	2.0	13.0%
C	1.82	2.0	9.0%
D	2.27	2.0	13.5%
E	1.73	2.0	13.5%
F	2.01	2.0	0.5%
G	2.27	2.0	13.5%
H	1.83	2.0	8.5%
I	2.06	2.0	3.0%
J	2.35	2.0	17.5%
K	2.15	2.0	7.5%
L	2.14	2.0	7.0%
M	1.99	2.0	0.5%
N	1.90	2.0	5.0%
O	1.99	2.0	0.5%
P	2.20	2.0	10.0%
R	2.16	2.0	8.0%
S	2.36	2.0	18.0%
T	2.14	2.0	7.0%
U	2.00	2.0	0.0%

Gold Foils:

FOIL #	MEASURED THICKNESS DIFF. (mil)	NOMINAL THICKNESS (mil)	% DIFFERENCE
A	1.05	1.0	5.0%
B	1.05	1.0	5.0%
C	1.04	1.0	4.0%
D	1.07	1.0	7.0%
E	1.06	1.0	6.0%
F	1.06	1.0	6.0%
G	1.06	1.0	6.0%
H	1.05	1.0	5.0%
I	1.05	1.0	5.0%
J	1.05	1.0	5.0%
K	1.05	1.0	5.0%
L	1.05	1.0	5.0%
M	1.06	1.0	6.0%
N	1.06	1.0	6.0%
O	1.05	1.0	5.0%
P	1.06	1.0	6.0%
R	1.06	1.0	6.0%
S	1.04	1.0	4.0%
T	1.06	1.0	6.0%
U	1.06	1.0	6.0%

Copper Foils:

FOIL #	MEASURED THICKNESS DIFF. (mil)	NOMINAL THICKNESS (mil)	% DIFFERENCE
A	3.91	4.0	2.3%
B	3.92	4.0	2.0%
C	3.90	4.0	2.5%
D	3.92	4.0	2.0%
E	3.91	4.0	2.3%
F	3.90	4.0	2.5%
G	3.92	4.0	2.0%
H	3.91	4.0	2.3%
I	3.90	4.0	2.5%
J	3.91	4.0	2.3%
K	3.90	4.0	2.5%
L	3.91	4.0	2.3%
M	3.93	4.0	1.8%
N	3.90	4.0	2.5%
O	3.92	4.0	2.0%
P	3.92	4.0	2.0%
R	3.92	4.0	2.0%
S	3.92	4.0	2.0%
T	3.90	4.0	2.5%
U	3.92	4.0	2.0%

Mangense Foils:

FOIL #	MEASURED THICKNESS DIFF. (mil)	NOMINAL THICKNESS (mil)	% DIFFERENCE
A	4.76	5.0	4.8%
B	4.91	5.0	1.8%
C	4.94	5.0	1.2%
D	4.79	5.0	4.2%
E	4.88	5.0	2.4%
F	4.91	5.0	1.8%
G	4.91	5.0	1.8%
H	4.94	5.0	1.2%
I	5.00	5.0	0.0%
J	4.76	5.0	4.8%
K	4.91	5.0	1.8%
L	4.91	5.0	1.8%
M	5.03	5.0	0.6%
N	5.07	5.0	1.4%
O	4.97	5.0	0.6%
P	4.97	5.0	0.6%
R	4.88	5.0	2.4%
S	4.85	5.0	3.0%
T	4.82	5.0	3.6%
U	4.94	5.0	1.2%

Tungsten Foils:

FOIL #	MEASURED THICKNESS DIFF. (mil)	NOMINAL THICKNESS (mil)	% DIFFERENCE
A	0.96	1.0	4.3%
B	0.97	1.0	2.7%
C	0.86	1.0	13.9%
D	0.92	1.0	8.0%
E	0.87	1.0	13.0%
F	1.03	1.0	3.0%
G	0.87	1.0	12.7%
H	0.99	1.0	1.5%
I	1.04	1.0	4.0%
J	0.89	1.0	10.8%
K	0.90	1.0	10.2%
L	1.00	1.0	0.0%
M	1.08	1.0	8.0%
N	0.93	1.0	6.8%
O	1.02	1.0	2.0%
P	0.87	1.0	12.7%
R	0.99	1.0	1.2%
S	0.91	1.0	9.2%
T	0.93	1.0	7.4%
U	0.94	1.0	5.8%

Appendix D:
Detector Efficiency Fit Comparison

List of Contents:
- Emission Rate Table for Sb-Eu standard.
- Comparison of Linear vs. Weighted Least-squares Fit.

(This comparison is one example of the difference between the weighted least-squares and linear least-squares fit for detector efficiency data. The weighted least-squares line should pass through the error bars of nearly every data point.)

Emission Rate Table for Sb-Eu standard

Radionuclide	Photon Energy (keV)	Emission Rate ($x\ s^{-1}$) or ($\gamma\ s^{-1}$) 1200 EST September 1, 1988	Total Estimated Uncertainty (%)*
^{125}Sb-^{125m}Te	Kα, 27.4	4.704×10^4	1.3
^{154}Eu-^{155}Eu	Kα, 42.8	2.775×10^4	1.3
^{155}Eu	86.5	1.062×10^4	0.9
^{155}Eu	105.3	7.396×10^3	1.3
^{154}Eu	123.1	4.321×10^4	0.8
^{125}Sb	176.3	5.162×10^3	0.6
^{154}Eu	247.7	7.325×10^3	0.6
^{125}Sb	427.9	2.244×10^4	0.8
^{125}Sb	463.4	7.888×10^3	0.7
^{154}Eu	591.8	5.242×10^3	0.6
^{125}Sb	600.6	1.333×10^4	0.7
^{125}Sb	635.9	8.518×10^3	0.6
^{154}Eu	723.3	2.127×10^4	0.6
^{154}Eu	873.2	1.291×10^4	0.7
^{154}Eu	996.3	1.105×10^4	0.9
^{154}Eu	1004.7	1.917×10^4	0.7
^{154}Eu	1274.5	3.694×10^4	0.5
^{154}Eu	1596.4	1.878×10^3	0.7

* Estimated total uncertainties have the significance of one standard deviation of the mean.

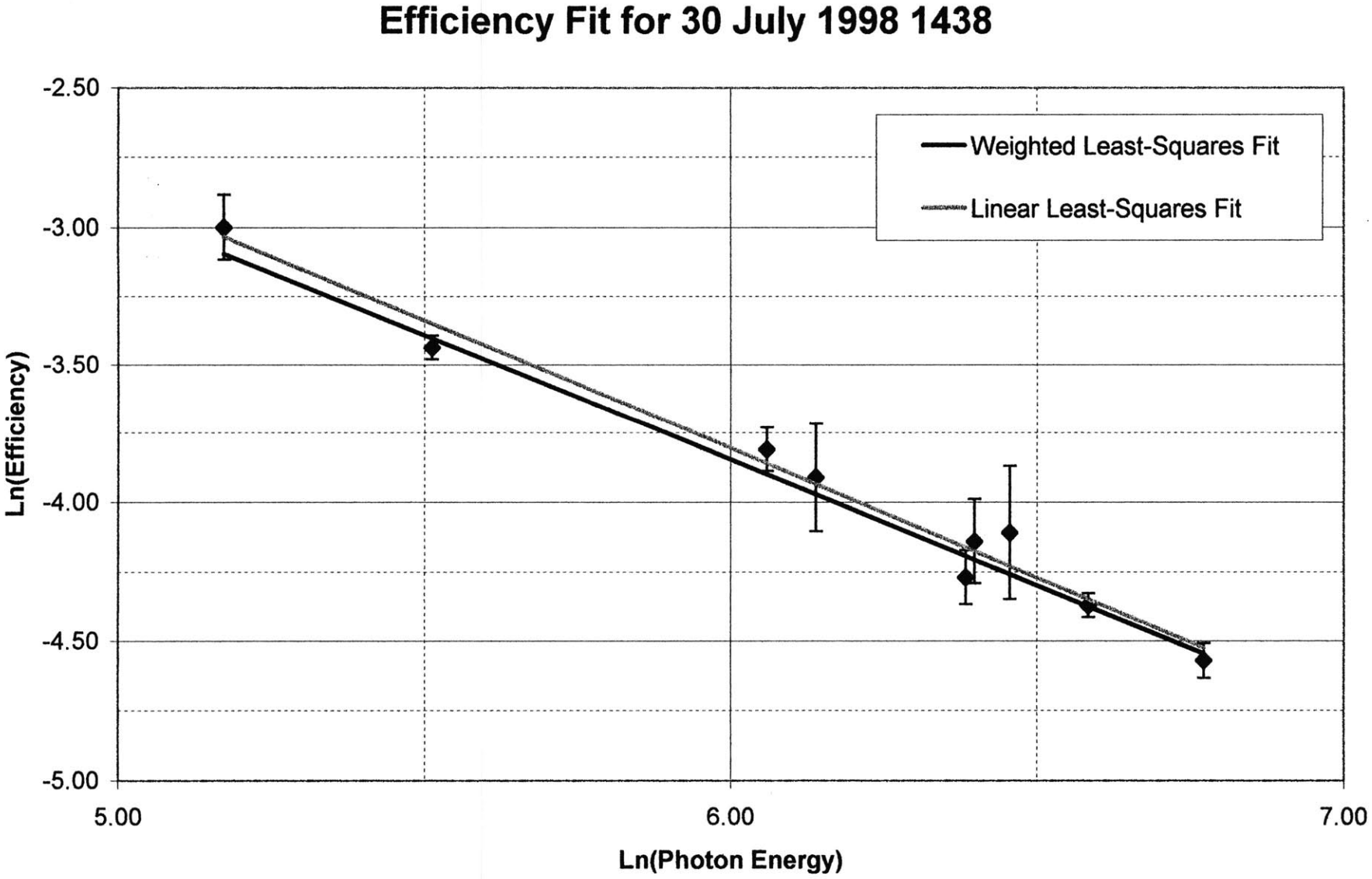
Efficiency Fit for 30 July 1998 1438
-2.50
-3.00
-3.50
-4.00
-4.50
-5.00
Ln(Efficiency)
5.00
6.00
7.00
Ln(Photon Energy)
Weighted Least-Squares Fit
Linear Least-Squares Fit

Appendix E:
MCNP Input Files

List of Contents:

Models
- BNCT Moderator/Reflector Model
- BNCT Moderator/Reflector Model with Variance Reduction
- BNCS Moderator/Reflector Model with 8 cm of moderation
- BNCS Moderator/Reflector Model with 23 cm of moderation
- Foil Wheel Model
- Boron Sphere with In foils Model
- Boron Sphere with Cu foils Model

Effective Cross Section
- Foil Wheel Numerator Tallies
- Boron Sphere with In foils Numerator Tallies
- Boron Sphere with Cu foils Numerator Tallies
- Foil Wheel Denominator Tallies
- Boron Sphere with In foils Denominator Tallies
- Boron Sphere with Cu foils Denominator Tallies

Unpertured Neutron Flux
- Unperturbed Neutron Flux Tallies

MCNP Models

BNCT Moderator/Reflector Model:

```
c
c     DEFINING CELLS:
c
3  5 -1.105 (-5 6 2 -43):(-6 18 -43)     $ moderator
4  2 -11.35 (-4 5 -3 2):(-5 7 43 -3)   $ Lead reflector
5  1 -1.3e-3 -2 -5 6                $ Target
6  1 -1.3e-3 -2 5 -4                $ ion cavity before target
7  3 -1.17 -44 -18 8                  $ plexiglass cover
8  6 -0.93 (-19 44 9 -7):(-7 18 43 -44):(-8 9 43 -44) $ boronated polyethylene cap
c
c     SURFACES
2   cz 3
3   cz 38
4   pz 52.89875
5   pz 36.68125
6   pz 35.68125
7   pz 10.28125
8   pz 9.28125
9   pz 8.28125
18  pz 9.58125
19  cz 15.24
43  cz 12.065
44  cz 13.65
```

BNCT Moderator/Reflector Model with Variance Reduction:

```
c Added variance reduction regions with weighting factor
c increase of 1.3 for each region with increased importance
c in last two regions
c
c Added imp to rest of experiment equal to last region
c and added imp.  to air region past beam.
c
c     DEFINING CELLS:
c
3  5 -1.105 (-5 6 2 -43):(-6 90 -43)     $ moderator 1
4  2 -11.35 (-4 5 -3 2):(-5 6 43 -3)   $ Lead reflector
5  1 -1.3e-3 -2 -5 6                $ Target
6  1 -1.3e-3 -2 5 -4                $ ion cavity before target
7  3 -1.17 -44 -18 8                  $ plexiglass cover
8  6 -0.93 (-19 44 9 -7):(-7 18 43 -44):(-8 9 43 -44) $ boronated polyethylene cap
9  5 -1.105 -90 91 -43               $ moderator 2
10 5 -1.105 -91 92 -43               $ moderator 3
11 5 -1.105 -92 93 -43               $ moderator 4
12 5 -1.105 -93 94 -43               $ moderator 5
13 5 -1.105 -94 95 -43               $ moderator 6
14 5 -1.105 -95 96 -43               $ moderator 7
15 5 -1.105 -96 18 -43               $ moderator 8
16 2 -11.35 -6 90 43 -3              $ lead reflector 2
17 2 -11.35 -90 91 43 -3              $ lead refelctor 3
18 2 -11.35 -91 92 43 -3              $ lead reflector 4
19 2 -11.35 -92 93 43 -3              $ lead reflector 5
```

```
20 2 -11.35 -93 94 43 -3          $ lead reflector 6
21 2 -11.35 -94 95 43 -3          $ lead reflector 7
22 2 -11.35 -95 96 43 -3          $ lead reflector 8
23 2 -11.35 -96 7 43 -3           $ lead reflector 9

c    SURFACES
c
2  cz 3
3  cz 38
4  pz 52.89875
5  pz 36.68125
6  pz 35.68125
7  pz 10.28125
8  pz 9.28125
9  pz 8.28125
18  pz 9.58125
19  cz 15.24
43  cz 12.065
44  cz 13.65
c
c  VARIANCE REDUCTION
c
90 pz 32.43125
91 pz 29.18125
92 pz 25.93125
93 pz 22.68125
94 pz 19.43125
95 pz 16.18125
96 pz 12.93125
97 pz 0
```

BNCT Moderator/Reflector Model Materials:

```
c   Air
m1   7014 -0.755 8016 -0.232 18000 -0.013
c
c   Lead
m2   82000.50 1
c
c   Plexiglass
m3   6000 4 1001 6 8016 2 $ rho=1.17
c
c   Heavy Water
m5   1002 2 8016 1
mt5  hwtr.01
c
c   Boronated Polyethylene     $ rho=0.93
m6   5010 -0.05 6012 -0.814 1001 -0.136
mt6 poly.01t
```

BNCS Moderator/Reflector Model:

```
c   BNCS Moderator/Reflector Assembly
c   includes improved model of target and reflector geometry
c   distance from target to D2O end (at plexiglass) = 8 cm
c   FIXED moderator dimensions
```

```
c   single (or paralled opposed) beam irradiation
c   1.5 MeV deuterons on Be target
c
c     DEFINING CELLS:
c
3 2 -1.1034 (302 -223 -1):(221 -2 -1 223)    $ moderator
4 3 -2.1 (3 -2 1 -4):(2 -5 221 -4)        $ reflector
5 4 -2.6989 -900 201 240 -241              $ al. target tube
c
7 0 -900 201 -240                $ void inside beam tube
13 11 -2.25 205 -210 -206 207        $ teflon nozzle
14 11 -2.25 210 -211 -212 207        $ extra teflon
15 12 -7.9874 -900 212 210 -211     $ inner stainless tube
16 12 -7.9874 -230 222 220 -221     $ outer stainless tube
17 12 -7.9874 -222 223 -221         $ outer s.s end cap
20 12 -7.9874 -900 230 -231 232 -233 234 211 $ s.s. block
c
c water coolant
c
50 9 -1.0 222 -230 -220 211
51 9 -1.0 222 -207 -211
52 9 -1.0 -206 207 -205
53 9 -1.0 -210 206 -202
54 9 -1.0 202 -900 241 -210
c
c plastic and plexiglass end holders
c
60 13 -1.429 -3 300 -301 1 #61
61 14 -1.17 -302 303 -304
62 13 -1.429 5 -310 221 -313
63 13 -1.429 221 310 -311 5 -312
64 13 -1.429 221 315 312 -311 -314

c   surfaces
c
1 cz 4.4958          $ moderator
2 pz 30.3425      $ moderator
3 pz 7.3425     $ moderator
4 cz 22.5                $ reflector
5 pz 48.3425     $ reflector
c
c improved target
c
c be target end
201 pz 14.3773
202 pz 14.1868
c teflon nozzle
205 cz 0.3175
206 pz 12.8773
207 pz 10.0773
c inner stainless tube
210 cz 2.4511
211 cz 2.54
212 pz 10.3773
c outer stainless tube
220 cz 2.92735
```

```
221 cz 3.01625
222 pz 9.1773
223 pz 8.6773
c block of stainless
230 pz 69.9773
231 py 3.81
232 py -3.81
233 px 3.81
234 px -3.81
c aluminum target tube
240 cz 1.661
241 cz 1.75
900 pz 71.1773
c
c  plastic end pieces for sealing D2O
c
300 pz 4.8025   $ plastic cylinder
301 cz 8.9573
302 pz 6.3773 $ plexiglass end piece
303 pz 6.0725
304 cz 6.1633
c
c back piece
c
310 pz 48.7855
311 pz 54.2594
312 cz 3.65125
313 cz 6.82625
314 cz 3.95355
315 pz 50.5764
```

BNCS Moderator/Reflector Model with 23 cm of moderation:

```
c   BNCS Moderator/Reflector Assembly
c   includes improved model of target and reflector geometry
c   distance from target to D2O end (at plexiglass) = 23 cm
c   single (or paralled opposed) beam irradiation
c   2.6 MeV deuterons on Be target (1/2 beam diameter)
c   includes 10 cm graphite back reflector
c
c   CELLS
c
2 5 -1.3e-3 -241 -201 202   $ target (filled with air)
3 2 -1.1034 (302 -223 -1):(221 -2 -1 223)   $ moderator
4 3 -2.1 (3 -2 1 -4):(2 -5 221 -4)        $ reflector
5 4 -2.6989 -900 201 240 -241             $ al. target tube
7 0 -900 201 -240                $ void inside beam tube
13 11 -2.0 205 -210 -206 207        $ teflon nozzle
14 11 -2.0 210 -211 -212 207        $ extra teflon
15 12 -7.9874 -900 212 210 -211     $ inner stainless tube
16 12 -7.9874 -230 222 220 -221     $ outer stainless tube
17 12 -7.9874 -222 223 -221         $ outer s.s end cap
20 12 -7.9874 -900 230 -231 232 -233 234 211 $ s.s. block
c
c water coolant
```

```
c
50 9 -1.0 222 -230 -220 211
51 9 -1.0 222 -207 -211
52 9 -1.0 -206 207 -205
53 9 -1.0 -210 206 -202
54 9 -1.0 202 -900 241 -210
c
c plastic and plexiglass end holders
60 13 -1.429 -3 300 -301 1
61 14 -1.17 -302 303 -1
c

c   surfaces
c
1 cz 4.4958              $ moderator
2 pz 29.9                $ moderator
3 pz 6.9                 $ moderator
4 cz 22.5                $ reflector
5 pz 47.9                $ reflector
c
c
c improved target
c
c be target end
201 pz 28.9348
202 pz 28.7443
c teflon nozzle
205 cz 0.3175
206 pz 27.4348
207 pz 24.6348
c inner stainless tube
210 cz 2.4511
211 cz 2.54
212 pz 24.9348
c outer stainless tube
220 cz 2.92735
221 cz 3.01625
222 pz 23.7348
223 pz 23.2348
c block of stainless
230 pz 84.4648
231 py 3.81
232 py -3.81
233 px 3.81
234 px -3.81
c aluminum target tube
240 cz 1.661
241 cz 1.75
900 pz 85.7348
c
c  plastic end pieces for sealing D2O
c
300 pz 4.36   $ plastic cylinder
301 cz 8.9573
302 pz 5.9348  $ plexiglass end piece
303 pz 5.63
```

BNCS Moderator/Reflector Model Materials:

```
c
c   target: 9Be
m1   4009 1
c
c   moderator: D20
m2   1002 2 8016 1
mt2   hwtr.01
c
c   reflector: graphite
m3   6012 1
mt3   grph.01
c
c   proton beam: aluminum
m4   13027 1
c
c   air
m5      7014 -0.755 8016 -0.232 18000 -0.013
c
c   fluid (water)
m9    1001 2 8016 1
mt9   lwtr.01
c
c stainless
m12 24000 -8.0 26000 -74.0 28000 -18.0 $ rho=7.9874
c
c following compositions from TRIM code
c teflon
m11 6000 2 9019 4 $ rho=2.0
c
c delrin plastic
m13 6000 1 1001 2 8016 1  $ rho=1.429
mt13 poly.01t
c
c plexiglass
m14 6000 4 1001 6 8016 2  $ rho=1.17
mt14 poly.01t
c
```

Foil Wheel Model:

```
c Includes teflon foil wheel, poly wheel holder, and
c teflon rod in correct position.  with added foils.
c Pos.  1:  In 2 mil Pos.  2:  Au 1 mil Pos.  3:  Cu 4 mil
c Pos.  4:  Mn 5 mil Pos.  5:  Au (not covered) 1 mil
c Pos.  6:  W 1 mil.
c
c Added experimental layout:  with foils 6.19125 cm away [BNCT]
c Added experimental layout:  with foils 2.9825 cm away [BNCS]
c from plexiglass as in experiment, with actual Cd cover
c dimensions, and using nominal thicknesses for foils.
c
c     DEFINING CELLS:
```

```
c
c foil wheel  holder
c
30 13 -1.429 -11 10 22 -14 40 -16 17
31 13 -1.429 -11 10 20 -40 41 -16 17
32 13 -1.429 -11 10 22 -41 15 -16 17
33 11 -2.25 -12 -10 13
c
c foil wheel
c
40 11 -2.25 -38 39 -22 21
41 11 -2.25 -39 40 -22 24 26 28 30 32 34 36
42 11 -2.25 -40 41 -20 22
43 11 -2.25 -80 42 45 -30
44 11 -2.25 -80 42 46 -32
45 11 -2.25 -80 42 44 -28
46 11 -2.25 -80 42 47 -34
47 11 -2.25 -80 42 43 -26
48 11 -2.25 -39 42 37 -36
c
c foils
c
70 20 -8.65 -39 50 -31
71 22 -7.31 -50 52 -66
72 22 -7.31 -52 54 -66
73 22 -7.31 -54 57 -66
74 22 -7.31 -57 58 -66
75 22 -7.31 -58 59 -66
76 20 -8.65 -79 80 -30
77 20 -8.65 -50 79 -30 66
78 20 -8.65 -39 50 -33
79 21 -19.3 -50 51 -65
80 21 -19.3 -51 52 -65
81 21 -19.3 -52 53 -65
82 21 -19.3 -53 54 -65
83 21 -19.3 -54 55 -65
84 20 -8.65 -79 80 -32
85 20 -8.65 -50 79 -32 65
86 20 -8.65 -39 50 -29
87 23 -8.96 -50 54 -70
88 23 -8.96 -54 58 -70
89 23 -8.96 -58 76 -70
90 23 -8.96 -76 77 -70
91 23 -8.96 -77 62 -70
92 20 -8.65 -79 80 -28
93 20 -8.65 -50 79 -28 70
94 20 -8.65 -39 50 -35
95 24 -7.61 -50 55 -69
96 24 -7.61 -55 59 -69
97 24 -7.61 -59 61 -69
98 24 -7.61 -61 62 -69
99 24 -7.61 -62 63 -69
100 20 -8.65 -79 80 -34
101 20 -8.65 -50 79 -34 69
102 21 -19.3 -39 71 -68
103 21 -19.3 -71 72 -68
```

```
104 21 -19.3 -72 73 -68
105 21 -19.3 -73 74 -68
106 21 -19.3 -74 75 -68
107 20 -8.65 -39 50 -27
108 25 -19.3 -50 51 -67
109 25 -19.3 -51 52 -67
110 25 -19.3 -52 53 -67
111 25 -19.3 -53 54 -67
112 25 -19.3 -54 55 -67
113 20 -8.65 -79 80 -26
114 20 -8.65 -50 79 -26 67

c     SURFACES
c
c foil wheel holder
c
10 py -5.588
11 py 0
12 c/y 0 3.09 1.269
13 py -14.78026
14 pz 3.979
15 pz 1.439
16 px 4.7625
17 px -4.7625
c
c foil wheel
c
20 cz 3.81
21 cz 3.175
22 cz 3.4925
24 cz 0.889
26 c/z 2.159 0 0.889
27 c/z 2.159 0 0.762
28 c/z -2.159 0 0.889
29 c/z -2.159 0 0.762
30 c/z 1.0795 1.86944 0.889
31 c/z 1.0795 1.86944 0.762
32 c/z -1.0795 1.86944 0.889
33 c/z -1.0795 1.86944 0.762
34 c/z -1.0795 -1.86944 0.889
35 c/z -1.0795 -1.86944 0.762
36 c/z 1.0795 -1.86944 0.889
37 c/z 1.0795 -1.86944 0.73025
38 pz 3.725
39 pz 3.09
40 pz 2.7725
41 pz 2.1375
42 pz 1.82
43 c/z 2.159 0 0.73025
44 c/z -2.159 0 0.73025
45 c/z 1.0795 1.86944 0.73025
46 c/z -1.0795 1.86944 0.73025
47 c/z -1.0795 -1.86944 0.73025
c
c foils
c
```

```
50 pz 2.9884
51 pz 2.98586
52 pz 2.98332
53 pz 2.98078
54 pz 2.97824
55 pz 2.9757
57 pz 2.97316
58 pz 2.96808
59 pz 2.963
61 pz 2.9503
62 pz 2.9376
63 pz 2.9249
65 c/z -1.0795 1.86944 0.635
66 c/z 1.0795 1.86944 0.635
67 c/z 2.159 0 0.635
68 c/z 1.0795 -1.86944 0.635
69 c/z -1.0795 -1.86944 0.635
70 c/z -2.159 0 0.635
71 pz 3.08746
72 pz 3.08492
73 pz 3.08238
74 pz 3.07984
75 pz 3.0773
76 pz 2.95792
77 pz 2.94776
79 pz 2.836
80 pz 2.7344
```

Foil Wheel Model Materials:

```
c teflon
m11 6000 2 9019 4 $ rho=2.0
c
c delrin plastic
m13 6000 1 1001 2 8016 1  $ rho=1.429
mt13 poly.01t
c
c cadmium
m20 48000 1
c
c gold
m21 79197 1
c
c indium
m22 49000 1
c
c copper
m23 29000 1
c
c 81.3% Mn
m24 25055 -.813 29000 -0.187
c
c tungsten
m25 74000 1
```

Boron Sphere-In foils Model:

```
c   With Boron-10 Sphere and teflon rod.
c   With 5 Indium Foils 2 mil Inside.
c
c   Added experimental layout: with foils 6.19125 cm away from
c   plexiglass as in experiment, with actual Cd cover dimensions,
c   and using nominal thicknesses for foils.  With teflon tape.
c
c     DEFINING CELLS:
c
c foils
c
30 20 -8.65 -10 11 -13
31 21 -7.31 -11 12 -15
32 20 -8.65 -16 17 -14
33 20 -8.65 -11 16 -14 15
c
c boron sphere
c
40 22 -1.65 20 -21
c
c boron sphere holder
c
45 11 -2.0 (21 -30 32 33 -34):
     (-30 -33 31)
c
c teflon tape
c
50 11 -2.0 -40 41 -49 45 -20
51 12 -2.0 -40 41 -45 46 -20
52 11 -2.0 -42 48 -46 47 -20
53 12 -2.0 -42 48 -47 10 -20

c     SURFACES
c
c foils
c
10 pz 3.09
11 pz 2.9884
12 pz 2.963
14 cz 0.889
15 cz .635
16 pz 2.836
17 pz 2.7344
13 cz .762
c
c
c boron sphere
c
20 sz 3.09 1.50876    $inside boron sphere radius
21 sz 3.09 2.39268     $ outside boron sphere rad.
c
c boron sphere holder
c
```

```
30 c/y 0 3.09 1.27
31 py -14.78026
32 c/y 0 3.09 1.17
33 py -3.02768
34 py 0
c
c teflon tape
c
40 py 0.635
41 py -0.635
42 px 0.635
45 pz 3.10143
46 pz 3.09762
47 pz 3.09381
48 px -0.635
49 pz 3.10524
```

Boron Sphere-In foils Model Materials:

```
c teflon
m11 6000 2 9019 4 $ rho=2.0
c
c silicone
m12 6000 2 1001 6 14000 1 8016 1  $ assume rho same as teflon
c
c cadmium
m20 48000 1
c
c indium
m21 49000 1
c
c boron
m22 5010 1
c
```

Boron Sphere-Cu foils Model:

```
c   With Boron-10 Sphere and teflon rod.
c   With 5 Copper Foils 4 mil inside
c
c   Added experimental layout: with foils 6.19125 cm away from
c   plexiglass as in experiment, with actual Cd cover dimensions,
c   and using nominal thicknesses for foils.  With teflon tape.
c
c     DEFINING CELLS:
c
c foils
c
30 20 -8.65 -10 11 -13
31 21 -8.96 -11 12 -15
32 20 -8.65 -16 17 -14
33 20 -8.65 -11 16 -14 15
c
c boron sphere
c
```

```
40 22 -1.65 20 -21
c
c boron sphere holder
c
45 11 -2.0 (21 -30 32 33 -34):
     (-30 -33 31)
c
c teflon tape
c
50 11 -2.0 -40 41 -49 45 -20
51 12 -2.0 -40 41 -45 46 -20
52 11 -2.0 -42 48 -46 47 -20
53 12 -2.0 -42 48 -47 10 -20

c     SURFACES
c
c foils
c
10 pz 3.09
11 pz 2.9884
12 pz 2.9376
14 cz 0.889
15 cz .635
16 pz 2.836
17 pz 2.7344
13 cz .762
c
c
c boron sphere
c
20 sz 3.09 1.50876     $inside boron sphere radius
21 sz 3.09 2.39268      $ outside boron sphere rad.
c
c boron sphere holder
c
30 c/y 0 3.09 1.27
31 py -14.78026
32 c/y 0 3.09 1.17
33 py -3.02768
34 py 0
c
c teflon tape
c
40 py 0.635
41 py -0.635
42 px 0.635
45 pz 3.10143
46 pz 3.09762
47 pz 3.09381
48 px -0.635
49 pz 3.10524
```

Boron Sphere-Cu foils Model Materials:

```
c teflon
m11 6000 2 9019 4 $ rho=2.0
c
c silicone
m12 6000 2 1001 6 14000 1 8016 1  $ assume rho same as teflon
c
c cadmium
m20 48000 1
c
c copper
m21 29000 1
c
c boron
m22 5010 1
c
```

Effective Cross Section Simulations

Foil Wheel Neutron Tallies [NUMERATOR]:

```
c   Full Range Method
c
fc4 # of Absorption Reactions in In
f4:n 71 73
fm4 -7.31 22 102
e4 1e-9 5e-7 2.44e-6 6.60e-6 7.8e-5
     4.54e-4 6.90e-4 3.20e-1 14
c
fc14 # of Absorption Reactions in Au
f14:n 79 81
fm14 -19.3 21 102
e14 1e-9 5e-7 2.44e-6 6.60e-6 7.8e-5
     4.54e-4 6.90e-4 3.20e-1 14
c
fc24 # of Absorption Reactions in Cu
f24:n 87 89
fm24 -8.96 23 102
e24 1e-9 5e-7 2.44e-6 6.60e-6 7.8e-5
     4.54e-4 6.90e-4 3.20e-1 14
c
fc34 # of Absorption Reactions in Mn
f34:n 95 97
fm34 -7.61 24 102
e34 1e-9 5e-7 2.44e-6 6.60e-6 7.8e-5
     4.54e-4 6.90e-4 3.20e-1 14
c
fc44 # of Absorption Reactions in Au*
f44:n 102 104
fm44 -19.3 21 102
e44 1e-9 5e-7 2.44e-6 6.60e-6 7.8e-5
     4.54e-4 6.90e-4 3.20e-1 14
c
fc54 # of Absorption Reactions in W
```

```
f54:n 108 110
fm54 -19.3 25 102
e54 1e-9 5e-7 2.44e-6 6.60e-6 7.8e-5
     4.54e-4 6.90e-4 3.20e-1 14
c
c  Independent Point Method
c
fc64 # of Absorption Reactions in In
f64:n 71 73
fm64 -7.31 22 102
e64 1e-9 1.1e-6 1.8e-6 14
c
fc74 # of Absorption Reactions in Au
f74:n 79 81
fm74 -19.3 21 102
e74 1e-9 4.3e-6 5.5e-6 14
c
fc84 # of Absorption Reactions in Cu
f84:n 87 89
fm84 -8.96 23 102
e84 1e-9 5.7e-4 5.9e-4 14
c
fc94 # of Absorption Reactions in Mn
f94:n 95 97
fm94 -7.61 24 102
e94 1e-9 2.5e-4 4.1e-4 14
c
fc104 # of Absorption Reactions in Au* threshold
f104:n 102 104
fm104 -19.3 21 102
e104 1e-9 5e-7 14
c
fc114 # of Absorption Reactions in W
f114:n 108 110
fm114 -19.3 25 102
e114 1e-9 1.7e-5 2.05e-5 14
c
fc124 # of Absorption Reactions in Au threshold
f124:n 79 81
fm124 -19.3 21 102
e124 1e-9 5e-7 14
c
```

Foil Wheel Neutron Tallies [DENOMINATOR]:

```
c
c   Full Range Method
c
fc4 Unperturbed Flux in In
f4:n 71 73
e4 1e-9 5e-7 2.44e-6 6.60e-6 7.8e-5
     4.54e-4 6.90e-4 3.20e-1 14
c
fc14 Unperturbed Flux in Au
f14:n 79 81
```

```
e14 1e-9 5e-7 2.44e-6 6.60e-6 7.8e-5
     4.54e-4 6.90e-4 3.20e-1 14
c
fc24 Unperturbed Flux in Cu
f24:n 87 89
e24 1e-9 5e-7 2.44e-6 6.60e-6 7.8e-5
     4.54e-4 6.90e-4 3.20e-1 14
c
fc34 Unperturbed Flux in Mn
f34:n 95 97
e34 1e-9 5e-7 2.44e-6 6.60e-6 7.8e-5
     4.54e-4 6.90e-4 3.20e-1 14
c
fc44 Unperturbed Flux in Au*
f44:n 102 104
e44 1e-9 5e-7 2.44e-6 6.60e-6 7.8e-5
     4.54e-4 6.90e-4 3.20e-1 14
c
fc54 Unperturbed Flux in W
f54:n 108 110
e54 1e-9 5e-7 2.44e-6 6.60e-6 7.8e-5
     4.54e-4 6.90e-4 3.20e-1 14
c
c  Independent Point Method
c
fc64 Unperturbed Flux in In
f64:n 71 73
e64 1e-9 1.1e-6 1.8e-6 14
c
fc74 Unperturbed Flux in Au
f74:n 79 81
e74 1e-9 4.3e-6 5.5e-6 14
c
fc84 Unperturbed Flux in Cu
f84:n 87 89
e84 1e-9 5.7e-4 5.9e-4 14
c
fc94 Unperturbed Flux in Mn
f94:n 95 97
e94 1e-9 2.5e-4 4.1e-4 14
c
fc104 Unperturbed Flux in Au* threshold
f104:n 102 104
e104 1e-9 5e-7 14
c
fc114 Unperturbed Flux in W
f114:n 108 110
e114 1e-9 1.7e-5 2.05e-5 14
c
fc124 Unperturbed Flux in Au threshold
f124:n 79 81
e124 1e-9 5e-7 14
c
```

Boron Sphere-In foils Neutron Tallies [NUMERATOR]:

```
c  FULL RANGE
c
fc4 # of Absorption Reactions in In
f4:n 31
fm4 -7.31 21 102
e4 1e-9 5e-7 2.44e-6 6.60e-6 7.8e-5
     4.54e-4 6.90e-4 3.20e-1 14
c
fc14 # of (n,n') Reactions in In
f14:n 31
fm14 -7.31 21 51
e14 1e-9 5e-7 2.44e-6 6.60e-6 7.8e-5
     4.54e-4 6.90e-4 3.20e-1 14
c
c  INDEPENDENT POINT
c
fc24 # of Absorption Reactions in In
f24:n 31
fm24 -7.31 21 102
e24 1e-9 1.1e-6 1.8e-6 14
c
fc34 # of (n,n') Reactions in In
f34:n 31
fm34 -7.31 21 51
e34 1e-9 .32 14
c
```

Boron Sphere-In foils Neutron Tallies [DENOMINATOR]:

```
c  FULL RANGE
c
fc4 Unperturbed Flux in In
f4:n 31
e4 1e-9 5e-7 2.44e-6 6.60e-6 7.8e-5
     4.54e-4 6.90e-4 3.20e-1 14
c
c  INDEPENDENT POINT
c
fc14 Unperturbed Flux in In
f14:n 31
e14 1e-9 1.1e-6 1.8e-6 .32 14
c
```

Boron Sphere-Cu foils Neutron Tallies [NUMERATOR]:

```
c   FULL RANGE
c
fc4 # of Absorption Reactions in Cu
f4:n 31
fm4 -8.96 21 102
e4 1e-9 5e-7 2.44e-6 6.60e-6 7.8e-5
     4.54e-4 6.90e-4 3.20e-1 14
c
```

```
c    INDEPENDENT POINT
c
fc14 # of Absorption Reactions in Cu
f14:n 31
fm14 -8.96 21 102
e14 1e-9 5.50e-4 2.4e-2 14
c
```

Boron Sphere-Cu foils Neutron Tallies [DENOMINATOR]:

```
c   FULL RANGE
c
fc4 Unperturbed Flux in Cu
f4:n 31
e4 1e-9 5e-7 2.44e-6 6.60e-6 7.8e-5
     4.54e-4 6.90e-4 3.20e-1 14
c
c    INDEPENDENT POINT
c
fc14 Unperturbed Flux in Cu
f14:n 31
e14 1e-9 5.50e-4 2.4e-2 14
c
```

Unperturbed Neutron Flux Simulations

Unperturbed Neutron Flux Tallies:

```
fc4 Unperturbed Flux
f4:n 26 [BNCT]
f4:n 21 [BNCS]
e4 1e-10 2e-10 3e-10 4e-10 5e-10 6e-10 7e-10 8e-10
    9e-10 1e-09 1.1e-09 1.2e-09 1.3e-09 1.4e-09 1.5e-09 1.6e-09
    1.7e-09 1.8e-09 1.9e-09 2e-09 2.1e-09 2.2e-09 2.3e-09 2.4e-09
    2.5e-09 2.6e-09 2.7e-09 2.8e-09 2.9e-09 3e-09 3.1e-09 3.2e-09
    3.3e-09 3.4e-09 3.5e-09 3.6e-09 3.7e-09 3.8e-09 3.9e-09 4e-09
    4.1e-09 4.2e-09 4.3e-09 4.4e-09 4.5e-09 4.6e-09 4.7e-09 4.8e-09
    4.9e-09 5e-09 5.1e-09 5.2e-09 5.3e-09 5.4e-09 5.5e-09 5.6e-09
    5.7e-09 5.8e-09 5.9e-09 6e-09 6.1e-09 6.2e-09 6.3e-09 6.4e-09
    6.5e-09 6.6e-09 6.7e-09 6.8e-09 6.9e-09 7e-09 7.1e-09 7.2e-09
    7.3e-09 7.4e-09 7.5e-09 7.6e-09 7.7e-09 7.8e-09 7.9e-09 8e-09
    8.1e-09 8.2e-09 8.3e-09 8.4e-09 8.5e-09 8.6e-09 8.7e-09 8.8e-09
    8.9e-09 9e-09 9.1e-09 9.2e-09 9.3e-09 9.4e-09 9.5e-09 9.6e-09
    9.7e-09 ...
    ... 8.5E+01 8.6E+01 8.7E+01 8.8E+01 8.9E+01 9.0E+01 9.1E+01
    9.2E+01 9.3E+01 9.4E+01 9.5E+01 9.6E+01 9.7E+01 9.8E+01 9.9E+01
    1.0E+02 1.1E+02 1.2E+02 1.3E+02 1.4E+02
c
fc14 Unperturbed Flux Binned
f14:n 26 [BNCT]
f14:n 21 [BNCS]
e14 1e-9 5e-7 2.44e-6 6.60e-6 7.8e-5
     4.54e-4 6.90e-4 3.20e-1 14
```

Appendix F:
Effective Cross Sections

List of Contents:

- BNCT Effective Cross Sections
- BNCS Effective Cross Sections

BNCT Beam Effective Cross Sections

Au*(n,gam) [THERMAL REGION] - Full Range Method

Foil 1

Energy Region	Cross Section	Absolute Error	Relative Error
1.00E-09			
5.00E-07	1.20E+02	8.59E+00	7.1%
2.44E-06	3.94E+01	2.93E+00	7.5%
6.60E-06	7.61E+02	6.23E+01	8.2%
7.80E-05	2.21E+01	2.28E+00	10.3%
4.54E-04	1.73E+01	1.52E+00	8.8%
6.90E-04	1.50E+01	1.67E+00	11.2%
3.20E-01	3.69E+00	2.82E-01	7.7%
1.40E+01	5.37E-02	3.96E-03	7.4%

Foil 3

Energy Region	Cross Section	Absolute Error	Relative Error
1.00E-09			
5.00E-07	1.16E+02	8.31E+00	7.1%
2.44E-06	3.93E+01	2.93E+00	7.5%
6.60E-06	2.46E+02	1.96E+01	8.0%
7.80E-05	1.24E+01	1.10E+00	8.9%
4.54E-04	1.49E+01	1.30E+00	8.7%
6.90E-04	1.23E+01	1.25E+00	10.2%
3.20E-01	3.39E+00	2.59E-01	7.6%
1.40E+01	5.33E-02	3.91E-03	7.3%

Au*(n,gam) [THERMAL REGION] - Independent Point Method

Foil 1

Energy Region	Cross Section	Absolute Error	Relative Error
1.00E-09			
5.00E-07	1.20E+02	8.59E+00	7.1%
1.40E+01	5.90E+01	4.49E+00	7.6%

Foil 3

Energy Region	Cross Section	Absolute Error	Relative Error
1.00E-09			
5.00E-07	1.16E+02	8.31E+00	7.1%
1.40E+01	2.44E+01	1.79E+00	7.3%

Au(n,gam) [THERMAL REGION] - Independent Point Method

Foil 1

Energy Region	Cross Section	Absolute Error	Relative Error
1.00E-09			
5.00E-07	3.12E-01	2.63E-02	8.4%
1.40E+01	5.34E+01	4.08E+00	7.6%

Foil 3

Energy Region	Cross Section	Absolute Error	Relative Error
1.00E-09			
5.00E-07	3.10E-01	2.61E-02	8.4%
1.40E+01	2.08E+01	1.54E+00	7.4%

In(n,gam) - Full Range Method

Foil 1

Energy Region	Cross Section	Absolute Error	Relative Error
1.00E-09			
5.00E-07	2.49E-01	4.63E-02	18.6%
2.44E-06	1.74E+02	3.18E+01	18.3%
6.60E-06	1.61E+01	3.00E+00	18.6%
7.80E-05	6.65E+00	1.23E+00	18.5%
4.54E-04	2.02E+00	3.73E-01	18.4%
6.90E-04	9.26E-01	1.84E-01	19.8%
3.20E-01	4.37E-01	7.92E-02	18.1%
1.40E+01	3.13E-02	5.67E-03	18.1%

Foil 3

Energy Region	Cross Section	Absolute Error	Relative Error
1.00E-09			
5.00E-07	2.45E-01	4.57E-02	18.6%
2.44E-06	5.20E+01	9.48E+00	18.3%
6.60E-06	1.29E+01	2.39E+00	18.5%
7.80E-05	5.00E+00	9.29E-01	18.6%
4.54E-04	1.90E+00	3.51E-01	18.5%
6.90E-04	9.20E-01	1.83E-01	19.8%
3.20E-01	4.32E-01	7.84E-02	18.1%
1.40E+01	3.17E-02	5.75E-03	18.1%

In(n,gam) - Independent Point Method

Foil 1

Energy Region	Cross Section	Absolute Error	Relative Error
1.00E-09			
1.10E-06	3.95E+00	7.16E-01	18.1%
1.80E-06	4.78E+02	8.88E+01	18.6%
1.40E+01	3.46E+00	6.29E-01	18.1%

resonance	4.78E+02	8.88E+01	18.6%
other	3.64E+00	6.56E-01	18.0%

Foil 3

Energy Region	Cross Section	Absolute Error	Relative Error
1.00E-09			
1.10E-06	3.56E+00	6.46E-01	18.1%
1.80E-06	8.92E+01	1.67E+01	18.7%
1.40E+01	2.85E+00	5.16E-01	18.1%

resonance	8.92E+01	1.67E+01	18.7%
other	3.10E+00	5.59E-01	18.0%

Au(n,gam) - Full Range Method

Foil 1

Energy Region	Cross Section	Absolute Error	Relative Error
1.00E-09			
5.00E-07	3.12E-01	2.63E-02	8.4%
2.44E-06	2.84E+01	2.12E+00	7.5%
6.60E-06	7.43E+02	6.10E+01	8.2%
7.80E-05	1.73E+01	1.75E+00	10.1%
4.54E-04	1.62E+01	1.39E+00	8.6%
6.90E-04	1.65E+01	1.72E+00	10.5%
3.20E-01	3.36E+00	2.58E-01	7.7%
1.40E+01	5.12E-02	3.76E-03	7.3%

Foil 3

Energy Region	Cross Section	Absolute Error	Relative Error
1.00E-09			
5.00E-07	3.10E-01	2.61E-02	8.4%
2.44E-06	2.82E+01	2.11E+00	7.5%
6.60E-06	2.23E+02	1.80E+01	8.1%
7.80E-05	1.11E+01	1.06E+00	9.5%
4.54E-04	1.41E+01	1.21E+00	8.6%
6.90E-04	1.37E+01	1.43E+00	10.4%
3.20E-01	3.13E+00	2.41E-01	7.7%
1.40E+01	5.12E-02	3.76E-03	7.3%

Au(n,gam) - Independent Point Method

Foil 1

Energy Region	Cross Section	Absolute Error	Relative Error
1.00E-09			
4.30E-06	1.24E+01	9.06E-01	7.3%
5.50E-06	2.43E+03	2.29E+02	9.4%
1.40E+01	9.50E+00	7.27E-01	7.7%
resonance	2.43E+03	2.29E+02	9.4%
other	1.07E+01	7.58E-01	7.1%

Foil 3

Energy Region	Cross Section	Absolute Error	Relative Error
1.00E-09			
4.30E-06	1.17E+01	8.54E-01	7.3%
5.50E-06	4.80E+02	4.80E+01	10.0%
1.40E+01	7.65E+00	5.73E-01	7.5%
resonance	4.80E+02	4.80E+01	10.0%
other	9.31E+00	6.62E-01	7.1%

W(n,gam) - Full Range Method

Foil 1

Energy Region	Cross Section	Absolute Error	Relative Error
1.00E-09			
5.00E-07	5.65E-02	3.23E-03	5.7%
2.44E-06	4.23E+00	1.02E-01	2.4%
6.60E-06	1.03E+02	5.69E+00	5.5%
7.80E-05	9.88E+01	3.65E+00	3.7%
4.54E-04	1.16E+01	4.79E-01	4.1%
6.90E-04	5.82E+00	3.89E-01	6.7%
3.20E-01	1.55E+00	3.45E-02	2.2%
1.40E+01	3.68E-02	7.17E-04	1.9%

Foil 3

Energy Region	Cross Section	Absolute Error	Relative Error
1.00E-09			
5.00E-07	5.67E-02	3.24E-03	5.7%
2.44E-06	4.26E+00	1.06E-01	2.5%
6.60E-06	6.27E+01	3.73E+00	6.0%
7.80E-05	4.69E+01	1.78E+00	3.8%
4.54E-04	9.79E+00	4.05E-01	4.1%
6.90E-04	5.46E+00	3.62E-01	6.6%
3.20E-01	1.51E+00	3.57E-02	2.4%
1.40E+01	3.51E-02	1.81E-03	5.1%

W(n,gam) - Independent Point Method

Foil 1

Energy Region	Cross Section	Absolute Error	Relative Error
1.00E-09			
1.70E-05	1.25E+01	1.82E+00	14.6%
2.05E-05	5.77E+02	1.21E+02	21.0%
1.40E+01	1.06E+01	1.55E+00	14.6%
resonance	5.77E+02	1.21E+02	21.0%
other	1.15E+01	1.62E+00	14.1%

Foil 3

Energy Region	Cross Section	Absolute Error	Relative Error
1.00E-09			
1.70E-05	8.82E+00	1.28E+00	14.6%
2.05E-05	1.94E+02	4.12E+01	21.3%
1.40E+01	6.34E+00	9.21E-01	14.5%
resonance	1.94E+02	4.12E+01	21.3%
other	7.48E+00	1.06E+00	14.2%

Mn(n,gam) - Full Range Method

Foil 1

Energy Region	Cross Section	Absolute Error	Relative Error
1.00E-09			
5.00E-07	1.83E-02	1.60E-03	8.7%
2.44E-06	1.24E+00	6.82E-02	5.5%
6.60E-06	8.10E-01	4.67E-02	5.8%
7.80E-05	3.58E-01	1.89E-02	5.3%
4.54E-04	1.81E+00	1.04E-01	5.8%
6.90E-04	1.88E-01	1.28E-02	6.8%
3.20E-01	1.27E-01	7.58E-03	6.0%
1.40E+01	1.95E-03	1.02E-04	5.2%

Foil 3

Energy Region	Cross Section	Absolute Error	Relative Error
1.00E-09			
5.00E-07	1.75E-02	1.31E-03	7.5%
2.44E-06	1.23E+00	6.78E-02	5.5%
6.60E-06	8.08E-01	4.69E-02	5.8%
7.80E-05	3.49E-01	1.84E-02	5.3%
4.54E-04	8.72E-01	5.19E-02	6.0%
6.90E-04	1.74E-01	1.20E-02	6.9%
3.20E-01	9.54E-02	7.27E-03	7.6%
1.40E+01	1.92E-03	1.00E-04	5.2%

Mn(n,gam) - Independent Point Method

Foil 1

Energy Region	Cross Section	Absolute Error	Relative Error
1.00E-09			
2.50E-04	2.94E-01	1.48E-02	5.0%
4.10E-04	5.83E+00	3.86E-01	6.6%
1.40E+01	8.32E-02	4.69E-03	5.6%

resonance	5.83E+00	3.86E-01	6.6%
other	2.07E-01	1.03E-02	4.9%

Foil 3

Energy Region	Cross Section	Absolute Error	Relative Error
1.00E-09			
2.50E-04	2.91E-01	1.46E-02	5.0%
4.10E-04	2.45E+00	1.72E-01	7.0%
1.40E+01	6.50E-02	4.38E-03	6.7%

resonance	2.45E+00	1.72E-01	7.0%
other	1.98E-01	9.85E-03	5.0%

Cu(n,gam) - Full Range Method

Foil 1

Energy Region	Cross Section	Absolute Error	Relative Error
1.00E-09			
5.00E-07	7.20E-03	4.31E-04	6.0%
2.44E-06	4.58E-01	1.86E-02	4.1%
6.60E-06	2.83E-01	1.24E-02	4.4%
7.80E-05	9.39E-02	3.51E-03	3.7%
4.54E-04	7.86E-02	3.16E-03	4.0%
6.90E-04	5.11E-01	3.03E-02	5.9%
3.20E-01	8.69E-02	3.04E-03	3.5%
1.40E+01	6.00E-03	2.16E-04	3.6%

Foil 3

Energy Region	Cross Section	Absolute Error	Relative Error
1.00E-09			
5.00E-07	6.93E-03	3.95E-04	5.7%
2.44E-06	4.51E-01	1.81E-02	4.0%
6.60E-06	2.79E-01	1.21E-02	4.4%
7.80E-05	9.27E-02	3.49E-03	3.8%
4.54E-04	7.95E-02	3.26E-03	4.1%
6.90E-04	5.19E-01	3.15E-02	6.1%
3.20E-01	8.51E-02	2.99E-03	3.5%
1.40E+01	6.06E-03	2.20E-04	3.6%

Cu(n,gam) - Independent Point Method

Foil 1

Energy Region	Cross Section	Absolute Error	Relative Error
1.00E-09			
5.70E-04	1.03E-01	3.45E-03	3.3%
5.90E-04	7.09E-01	1.15E-01	16.2%
1.40E+01	6.19E-02	2.17E-03	3.5%

resonance	7.09E-01	1.15E-01	16.2%
other	8.76E-02	2.95E-03	3.4%

Foil 3

Energy Region	Cross Section	Absolute Error	Relative Error
1.00E-09			
5.70E-04	1.02E-01	3.42E-03	3.3%
5.90E-04	6.93E-01	1.16E-01	16.7%
1.40E+01	6.03E-02	2.09E-03	3.5%

resonance	6.93E-01	1.16E-01	16.7%
other	8.65E-02	2.91E-03	3.4%

Cu(n,gam) [SPHERE] - Full Range Method

All 5 Foils

Energy Region	Cross Section	Absolute Error	Relative Error
1.00E-09			
5.00E-07	0.00E+00	0.00E+00	0.0%
2.44E-06	0.00E+00	0.00E+00	0.0%
6.60E-06	0.00E+00	0.00E+00	0.0%
7.80E-05	1.50E-05	4.41E-06	29.5%
4.54E-04	1.73E-03	1.21E-04	7.0%
6.90E-04	2.89E-02	2.15E-03	7.4%
3.20E-01	2.39E-02	8.26E-04	3.5%
1.40E+01	4.31E-03	1.52E-04	3.5%

Cu(n,gam) [SPHERE] - Independent Point Method

All 5 Foils

Energy Region	Cross Section	Absolute Error	Relative Error
1.00E-09			
5.50E-04	4.81E-04	3.05E-05	6.3%
2.40E-02	2.83E-02	1.03E-03	3.6%
1.40E+01	8.07E-03	2.77E-04	3.4%

resonance	2.83E-02	1.03E-03	3.6%
other	2.60E-03	8.35E-05	3.2%

In(n,gam) [SPHERE] - Full Range Method

All 5 Foils

Energy Region	Cross Section	Absolute Error	Relative Error
1.00E-09			
5.00E-07	0.00E+00	0.00E+00	0.0%
2.44E-06	0.00E+00	0.00E+00	0.0%
6.60E-06	0.00E+00	0.00E+00	0.0%
7.80E-05	9.49E-05	4.77E-05	50.2%
4.54E-04	4.68E-02	1.10E-02	23.5%
6.90E-04	6.38E-02	1.51E-02	23.7%
3.20E-01	1.60E-01	2.89E-02	18.1%
1.40E+01	2.77E-02	5.02E-03	18.1%

In(n,n') [FAST REGION] - Full Range Method

All 5 Foils

Energy Region	Cross Section	Absolute Error	Relative Error
1.00E-09			
5.00E-07	0.00E+00	0.00E+00	0.0%
2.44E-06	0.00E+00	0.00E+00	0.0%
6.60E-06	0.00E+00	0.00E+00	0.0%
7.80E-05	0.00E+00	0.00E+00	0.0%
4.54E-04	0.00E+00	0.00E+00	0.0%
6.90E-04	0.00E+00	0.00E+00	0.0%
3.20E-01	0.00E+00	0.00E+00	0.0%
1.40E+01	1.65E-03	2.99E-04	18.1%

In(n,n') [FAST REGION] - Independent Point Method

All 5 Foils

Energy Region	Cross Section	Absolute Error	Relative Error
1.00E-09			
3.20E-01	0.00E+00	0.00E+00	0.0%
1.40E+01	1.65E-03	2.99E-04	18.1%

below threshold	0	0	0.0%
above threshold	1.65E-03	2.99E-04	18.1%

BNCS Beam Effective Cross Sections

Au*(n,gam) [THERMAL REGION] - Full Range Method

Foil 1

Energy Region	Cross Section	Absolute Error	Relative Error
1.00E-09			
5.00E-07	1.33E+02	9.65E+00	7.2%
2.44E-06	4.27E+01	3.22E+00	7.5%
6.60E-06	7.54E+02	6.32E+01	8.4%
7.80E-05	2.19E+01	2.30E+00	10.5%
4.54E-04	1.98E+01	1.70E+00	8.6%
6.90E-04	1.80E+01	1.80E+00	10.0%
3.20E-01	2.38E+00	1.80E-01	7.6%
1.40E+01	5.80E-02	4.17E-03	7.2%

Foil 3

Energy Region	Cross Section	Absolute Error	Relative Error
1.00E-09			
5.00E-07	1.26E+02	9.12E+00	7.2%
2.44E-06	4.26E+01	3.24E+00	7.6%
6.60E-06	2.36E+02	1.91E+01	8.1%
7.80E-05	1.46E+01	1.42E+00	9.8%
4.54E-04	1.65E+01	1.41E+00	8.5%
6.90E-04	1.47E+01	1.48E+00	10.1%
3.20E-01	2.25E+00	1.69E-01	7.5%
1.40E+01	5.80E-02	4.17E-03	7.2%

Au*(n,gam) [THERMAL REGION] - Independent Point Method

Foil 1

Energy Region	Cross Section	Absolute Error	Relative Error
1.00E-09			
5.00E-07	1.33E+02	9.65E+00	7.2%
1.40E+01	1.59E+01	1.24E+00	7.8%

Foil 3

Energy Region	Cross Section	Absolute Error	Relative Error
1.00E-09			
5.00E-07	1.26E+02	9.12E+00	7.2%
1.40E+01	6.89E+00	5.12E-01	7.4%

Au(n,gam) [THERMAL REGION] - Independent Point Method

Foil 1

Energy Region	Cross Section	Absolute Error	Relative Error
1.00E-09			
5.00E-07	2.71E-01	2.64E-02	9.8%
1.40E+01	1.43E+01	1.14E+00	8.0%

Foil 3

Energy Region	Cross Section	Absolute Error	Relative Error
1.00E-09			
5.00E-07	2.69E-01	2.61E-02	9.7%
1.40E+01	6.16E+00	4.64E-01	7.5%

In(n,gam) - Full Range Method

Foil 1

Energy Region	Cross Section	Absolute Error	Relative Error
1.00E-09			
5.00E-07	2.62E-01	5.00E-02	19.1%
2.44E-06	1.85E+02	3.39E+01	18.4%
6.60E-06	1.60E+01	3.00E+00	18.7%
7.80E-05	6.54E+00	1.23E+00	18.9%
4.54E-04	2.22E+00	4.12E-01	18.5%
6.90E-04	9.56E-01	1.83E-01	19.1%
3.20E-01	3.37E-01	6.10E-02	18.1%
1.40E+01	3.47E-02	6.27E-03	18.1%

Foil 3

Energy Region	Cross Section	Absolute Error	Relative Error
1.00E-09			
5.00E-07	2.52E-01	4.81E-02	19.1%
2.44E-06	5.43E+01	9.96E+00	18.3%
6.60E-06	1.31E+01	2.46E+00	18.8%
7.80E-05	5.23E+00	9.84E-01	18.8%
4.54E-04	2.07E+00	3.83E-01	18.6%
6.90E-04	9.57E-01	1.83E-01	19.2%
3.20E-01	3.35E-01	6.07E-02	18.1%
1.40E+01	3.46E-02	6.25E-03	18.1%

In(n,gam) - Independent Point Method

Foil 1

Energy Region	Cross Section	Absolute Error	Relative Error
1.00E-09			
1.10E-06	4.61E+00	8.41E-01	18.2%
1.80E-06	4.97E+02	9.26E+01	18.6%
1.40E+01	9.97E-01	1.81E-01	18.2%

resonance	4.97E+02	9.26E+01	18.6%
other	1.37E+00	2.47E-01	18.1%

Foil 3

Energy Region	Cross Section	Absolute Error	Relative Error
1.00E-09			
1.10E-06	4.13E+00	7.55E-01	18.3%
1.80E-06	9.14E+01	1.73E+01	18.9%
1.40E+01	8.47E-01	1.54E-01	18.2%

resonance	9.14E+01	1.73E+01	18.9%
other	1.19E+00	2.14E-01	18.1%

Au(n,gam) - Full Range Method

Foil 1

Energy Region	Cross Section	Absolute Error	Relative Error
1.00E-09			
5.00E-07	2.71E-01	2.64E-02	9.8%
2.44E-06	3.02E+01	2.27E+00	7.5%
6.60E-06	7.16E+02	6.17E+01	8.6%
7.80E-05	1.86E+01	2.00E+00	10.7%
4.54E-04	1.60E+01	1.39E+00	8.7%
6.90E-04	1.58E+01	1.69E+00	10.7%
3.20E-01	2.12E+00	1.59E-01	7.5%
1.40E+01	5.82E-02	4.18E-03	7.2%

Foil 3

Energy Region	Cross Section	Absolute Error	Relative Error
1.00E-09			
5.00E-07	2.69E-01	2.61E-02	9.7%
2.44E-06	3.06E+01	2.37E+00	7.8%
6.60E-06	2.28E+02	1.90E+01	8.3%
7.80E-05	1.25E+01	1.28E+00	10.2%
4.54E-04	1.39E+01	1.21E+00	8.7%
6.90E-04	1.39E+01	1.38E+00	9.9%
3.20E-01	2.05E+00	1.54E-01	7.5%
1.40E+01	5.82E-02	4.18E-03	7.2%

Au(n,gam) - Independent Point Method

Foil 1

Energy Region	Cross Section	Absolute Error	Relative Error
1.00E-09			
4.30E-06	1.54E+01	1.18E+00	7.7%
5.50E-06	2.45E+03	2.39E+02	9.8%
1.40E+01	2.92E+00	2.25E-01	7.7%
resonance	2.45E+03	2.39E+02	9.8%
other	4.42E+00	3.17E-01	7.2%

Foil 3

Energy Region	Cross Section	Absolute Error	Relative Error
1.00E-09			
4.30E-06	1.40E+01	1.05E+00	7.5%
5.50E-06	5.08E+02	5.30E+01	10.4%
1.40E+01	2.47E+00	1.88E-01	7.6%
resonance	5.08E+02	5.30E+01	10.4%
other	3.86E+00	2.77E-01	7.2%

W(n,gam) - Full Range Method

Foil 1

Energy Region	Cross Section	Absolute Error	Relative Error
1.00E-09			
5.00E-07	5.96E-02	3.64E-03	6.1%
2.44E-06	4.38E+00	1.25E-01	2.9%
6.60E-06	1.06E+02	7.46E+00	7.1%
7.80E-05	9.53E+01	3.87E+00	4.1%
4.54E-04	1.33E+01	5.18E-01	3.9%
6.90E-04	5.73E+00	3.58E-01	6.3%
3.20E-01	1.00E+00	1.55E-02	1.5%
1.40E+01	3.96E-02	2.39E-04	0.6%

Foil 3

Energy Region	Cross Section	Absolute Error	Relative Error
1.00E-09			
5.00E-07	5.91E-02	3.59E-03	6.1%
2.44E-06	4.27E+00	1.01E-01	2.4%
6.60E-06	6.14E+01	4.59E+00	7.5%
7.80E-05	4.30E+01	1.70E+00	3.9%
4.54E-04	1.11E+01	4.59E-01	4.1%
6.90E-04	5.60E+00	4.05E-01	7.2%
3.20E-01	9.93E-01	1.90E-02	1.9%
1.40E+01	3.94E-02	2.10E-04	0.5%

W(n,gam) - Independent Point Method

Foil 1

Energy Region	Cross Section	Absolute Error	Relative Error
1.00E-09			
1.70E-05	1.42E+01	2.13E+00	15.0%
2.05E-05	6.60E+02	1.04E+02	15.8%
1.40E+01	2.64E+00	3.89E-01	14.7%
resonance	6.60E+02	1.04E+02	15.8%
other	4.28E+00	6.08E-01	14.2%

Foil 3

Energy Region	Cross Section	Absolute Error	Relative Error
1.00E-09			
1.70E-05	9.41E+00	1.40E+00	14.9%
2.05E-05	2.14E+02	3.46E+01	16.1%
1.40E+01	1.70E+00	2.46E-01	14.5%
resonance	2.14E+02	3.46E+01	16.1%
other	2.79E+00	3.97E-01	14.2%

Mn(n,gam) - Full Range Method

Foil 1

Energy Region	Cross Section	Absolute Error	Relative Error
1.00E-09			
5.00E-07	1.89E-02	1.76E-03	9.3%
2.44E-06	1.26E+00	7.04E-02	5.6%
6.60E-06	8.32E-01	4.93E-02	5.9%
7.80E-05	3.67E-01	1.98E-02	5.4%
4.54E-04	1.95E+00	1.12E-01	5.8%
6.90E-04	2.01E-01	1.26E-02	6.2%
3.20E-01	8.59E-02	4.97E-03	5.8%
1.40E+01	2.07E-03	1.05E-04	5.1%

Foil 3

Energy Region	Cross Section	Absolute Error	Relative Error
1.00E-09			
5.00E-07	1.93E-02	1.79E-03	9.3%
2.44E-06	1.25E+00	6.94E-02	5.6%
6.60E-06	8.03E-01	4.70E-02	5.9%
7.80E-05	3.65E-01	1.95E-02	5.3%
4.54E-04	9.49E-01	5.66E-02	6.0%
6.90E-04	1.88E-01	1.16E-02	6.2%
3.20E-01	6.28E-02	3.59E-03	5.7%
1.40E+01	2.05E-03	1.04E-04	5.1%

Mn(n,gam) - Independent Point Method

Foil 1

Energy Region	Cross Section	Absolute Error	Relative Error
1.00E-09			
2.50E-04	3.27E-01	1.69E-02	5.2%
4.10E-04	5.72E+00	3.54E-01	6.2%
1.40E+01	3.05E-02	1.70E-03	5.6%
resonance	5.72E+00	3.54E-01	6.2%
other	8.84E-02	4.46E-03	5.0%

Foil 3

Energy Region	Cross Section	Absolute Error	Relative Error
1.00E-09			
2.50E-04	3.21E-01	1.65E-02	5.2%
4.10E-04	2.45E+00	1.63E-01	6.6%
1.40E+01	2.33E-02	1.28E-03	5.5%
resonance	2.45E+00	1.63E-01	6.6%
other	8.12E-02	4.10E-03	5.1%

Cu(n,gam) - Full Range Method

Foil 1

Energy Region	Cross Section	Absolute Error	Relative Error
1.00E-09			
5.00E-07	6.97E-03	5.13E-04	7.4%
2.44E-06	4.58E-01	1.89E-02	4.1%
6.60E-06	3.05E-01	1.37E-02	4.5%
7.80E-05	1.03E-01	4.07E-03	4.0%
4.54E-04	9.24E-02	3.78E-03	4.1%
6.90E-04	5.14E-01	2.72E-02	5.3%
3.20E-01	6.63E-02	2.31E-03	3.5%
1.40E+01	6.48E-03	2.20E-04	3.4%

Foil 3

Energy Region	Cross Section	Absolute Error	Relative Error
1.00E-09			
5.00E-07	6.65E-03	4.98E-04	7.5%
2.44E-06	4.61E-01	1.96E-02	4.3%
6.60E-06	3.09E-01	1.43E-02	4.6%
7.80E-05	9.89E-02	3.78E-03	3.8%
4.54E-04	9.10E-02	3.74E-03	4.1%
6.90E-04	4.99E-01	2.52E-02	5.0%
3.20E-01	6.51E-02	2.26E-03	3.5%
1.40E+01	6.49E-03	2.20E-04	3.4%

Cu(n,gam) - Independent Point Method

Foil 1

Energy Region	Cross Section	Absolute Error	Relative Error
1.00E-09			
5.70E-04	1.17E-01	4.13E-03	3.5%
5.90E-04	6.97E-01	1.03E-01	14.8%
1.40E+01	2.72E-02	9.39E-04	3.5%
resonance	6.97E-01	1.03E-01	14.8%
other	4.62E-02	1.59E-03	3.4%

Foil 3

Energy Region	Cross Section	Absolute Error	Relative Error
1.00E-09			
5.70E-04	1.16E-01	4.15E-03	3.6%
5.90E-04	6.24E-01	8.04E-02	12.9%
1.40E+01	2.67E-02	9.17E-04	3.4%
resonance	6.24E-01	8.04E-02	12.9%
other	4.57E-02	1.57E-03	3.4%

Cu(n,gam) [SPHERE] - Full Range Method

All 5 Foils

Energy Region	Cross Section	Absolute Error	Relative Error
1.00E-09			
5.00E-07	0.00E+00	0.00E+00	0.0%
2.44E-06	0.00E+00	0.00E+00	0.0%
6.60E-06	0.00E+00	0.00E+00	0.0%
7.80E-05	2.72E-05	1.62E-05	59.5%
4.54E-04	2.60E-03	2.45E-04	9.5%
6.90E-04	3.64E-02	3.51E-03	9.6%
3.20E-01	2.66E-02	8.85E-04	3.3%
1.40E+01	5.28E-03	1.69E-04	3.2%

Cu(n,gam) [SPHERE] - Independent Point Method

All 5 Foils

Energy Region	Cross Section	Absolute Error	Relative Error
1.00E-09			
5.50E-04	8.59E-04	6.87E-05	8.0%
2.40E-02	3.58E-02	1.28E-03	3.6%
1.40E+01	7.38E-03	2.36E-04	3.2%

resonance	3.58E-02	1.28E-03	3.6%
other	6.24E-03	1.98E-04	3.2%

In(n,gam) [SPHERE] - Full Range Method

All 5 Foils

Energy Region	Cross Section	Absolute Error	Relative Error
1.00E-09			
5.00E-07	0.00E+00	0.00E+00	0.0%
2.44E-06	0.00E+00	0.00E+00	0.0%
6.60E-06	0.00E+00	0.00E+00	0.0%
7.80E-05	1.04E-03	1.04E-03	99.8%
4.54E-04	4.57E-02	1.16E-02	25.3%
6.90E-04	7.85E-02	2.05E-02	26.1%
3.20E-01	1.47E-01	2.65E-02	18.1%
1.40E+01	2.76E-02	4.97E-03	18.0%

In(n,n') [FAST REGION] - Full Range Method

All 5 Foils

Energy Region	Cross Section	Absolute Error	Relative Error
1.00E-09			
5.00E-07	0.00E+00	0.00E+00	0.0%
2.44E-06	0.00E+00	0.00E+00	0.0%
6.60E-06	0.00E+00	0.00E+00	0.0%
7.80E-05	0.00E+00	0.00E+00	0.0%
4.54E-04	0.00E+00	0.00E+00	0.0%
6.90E-04	0.00E+00	0.00E+00	0.0%
3.20E-01	0.00E+00	0.00E+00	0.0%
1.40E+01	1.59E-03	2.86E-04	18.0%

In(n,n') [FAST REGION] - Independent Point Method

All 5 Foils

Energy Region	Cross Section	Absolute Error	Relative Error
1.00E-09			
3.20E-01	0.00E+00	0.00E+00	0.0%
1.40E+01	1.59E-03	2.86E-04	18.0%

below threshold	0	0	0.0%
above threshold	1.59E-03	2.86E-04	18.0%

Appendix G:
MATLAB Computer Program

List of Contents:

Flow Chart
- "spectrum.m"
- subprogram "fullflux.m"
- subprogram "ptflux.m"
- subprogram "activate.m"
- subprogram "inrate.m"

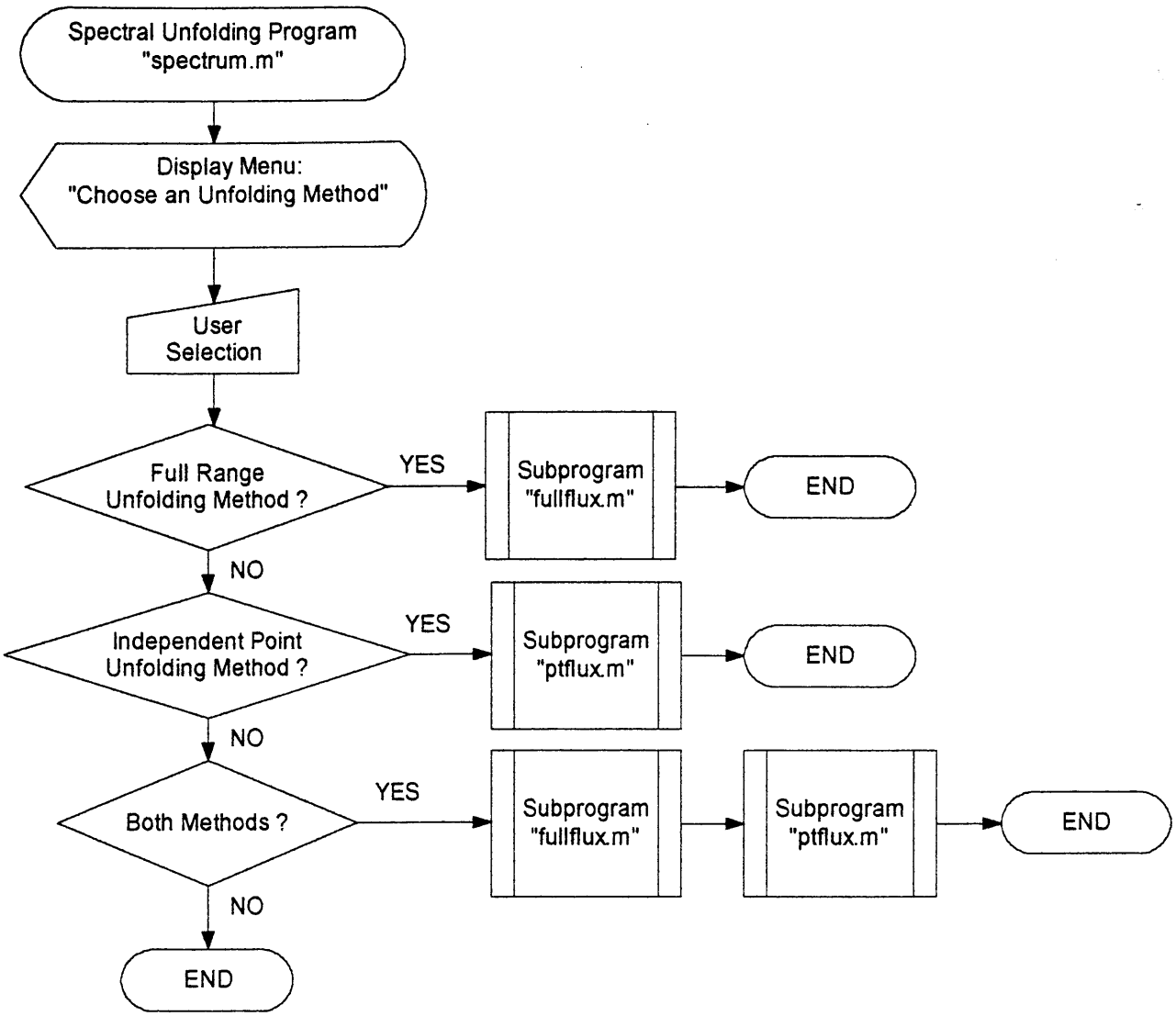
Spectral Unfolding Program
"spectrum.m"
Display Menu:
"Choose an Unfolding Method"
User
Selection
Full Range
Unfolding Method ?
YES
Subprogram
"fullflux.m"
END
NO
Independent Point
Unfolding Method ?
YES
Subprogram
"ptflux.m"
END
NO
Both Methods ?
YES
Subprogram
"fullflux.m"
Subprogram
"ptflux.m"
END
NO
END

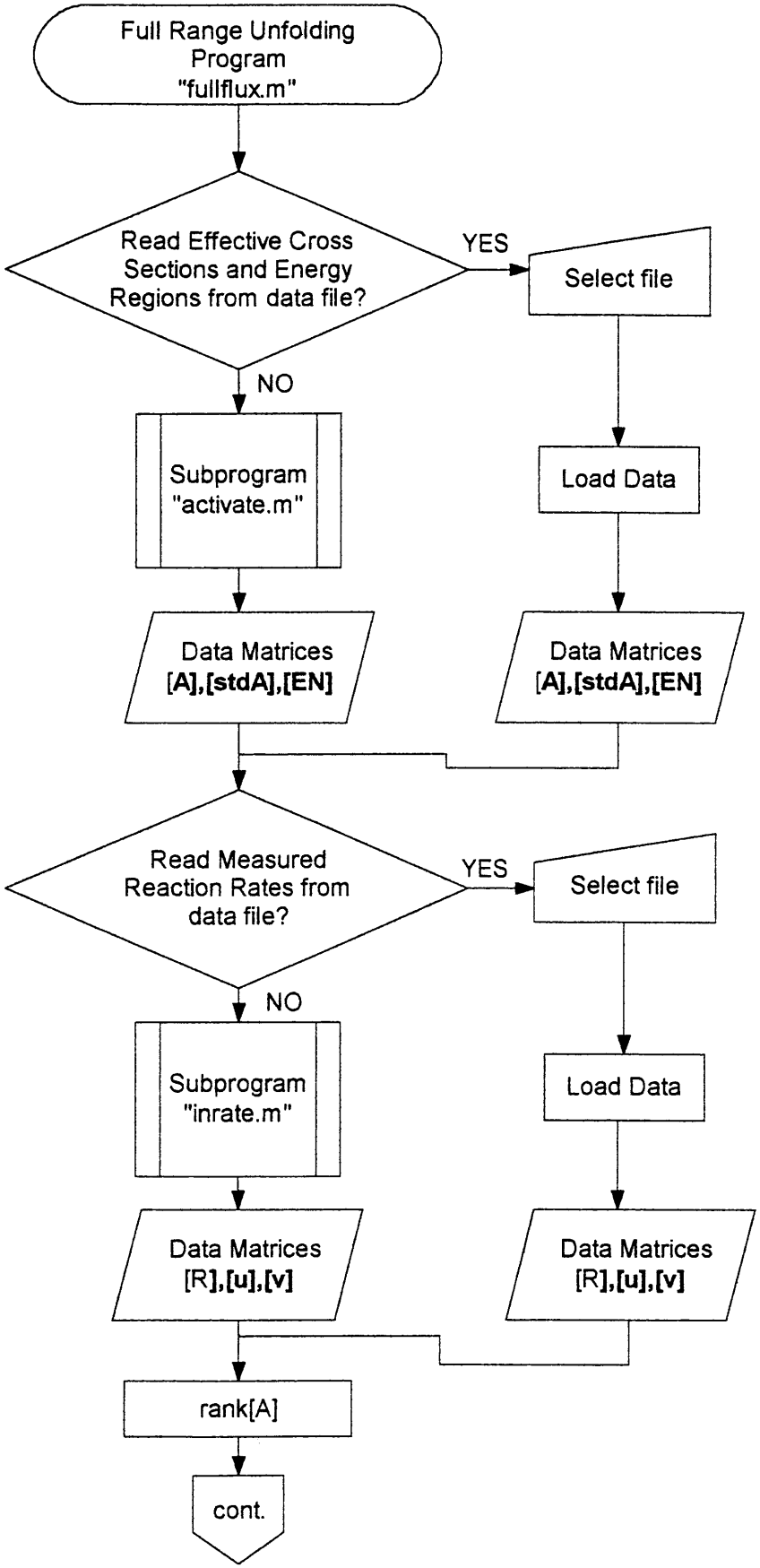
Full Range Unfolding Program "fullflux.m"
Read Effective Cross Sections and Energy Regions from data file?
YES
Select file
NO
Subprogram "activate.m"
Load Data
Data Matrices [A],[stdA],[EN]
Data Matrices [A],[stdA],[EN]
Read Measured Reaction Rates from data file?
YES
Select file
NO
Subprogram "inrate.m"
Load Data
Data Matrices [R],[u],[v]
Data Matrices [R],[u],[v]
rank[A]
cont.

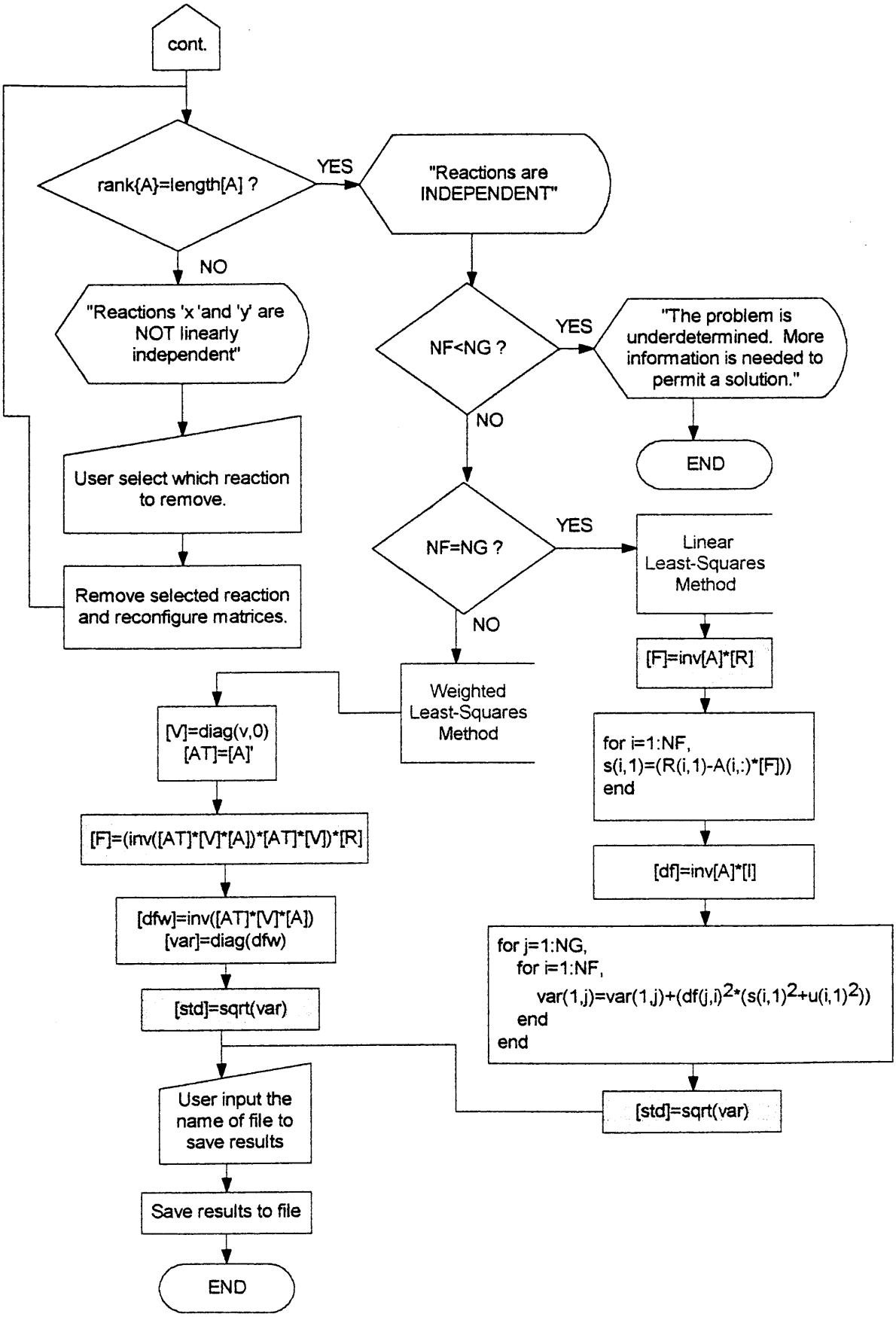
cont.
rank{A}=length[A] ?
YES
"Reactions are INDEPENDENT"
NO
"Reactions 'x 'and 'y' are NOT linearly independent"
User select which reaction to remove.
Remove selected reaction and reconfigure matrices.
NF<NG ?
YES
"The problem is underdetermined. More information is needed to permit a solution."
END
NO
NF=NG ?
YES
Linear Least-Squares Method
[F]=inv[A]*[R]
for i=1:NF,
s(i,1)=(R(i,1)-A(i,:)*[F]))
end
[df]=inv[A]*[I]
for j=1:NG,
for i=1:NF,
var(1,j)=var(1,j)+(df(j,i)^2*(s(i,1)^2+u(i,1)^2))
end
end
[std]=sqrt(var)
NO
Weighted Least-Squares Method
[V]=diag(v,0)
[AT]=[A]'
[F]=(inv([AT]*[V]*[A])*[AT]*[V])*[R]
[dfw]=inv([AT]*[V]*[A])
[var]=diag(dfw)
[std]=sqrt(var)
User input the name of file to save results
Save results to file
END

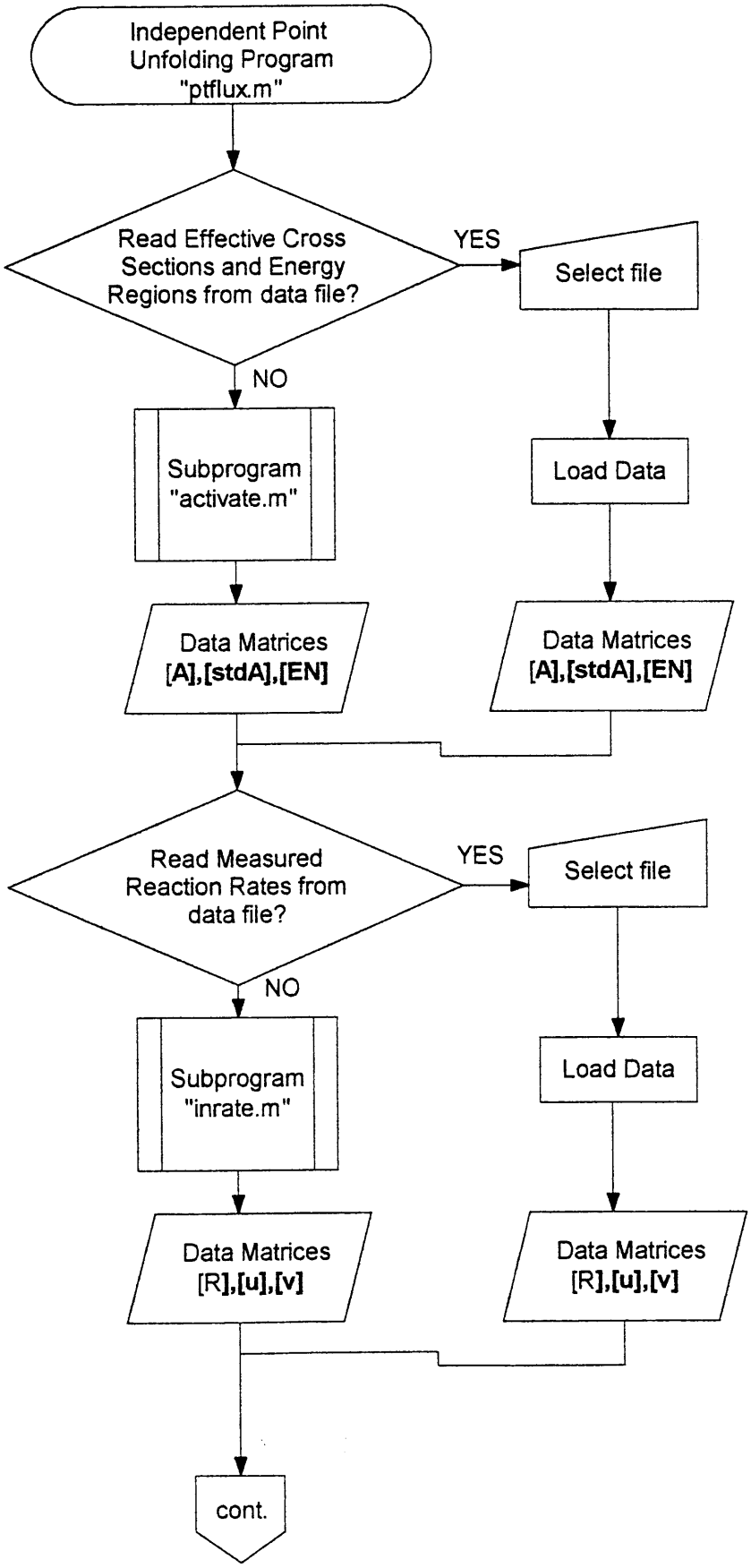
Independent Point Unfolding Program "ptflux.m"
Read Effective Cross Sections and Energy Regions from data file?
YES
Select file
NO
Subprogram "activate.m"
Load Data
Data Matrices [A],[stdA],[EN]
Data Matrices [A],[stdA],[EN]
Read Measured Reaction Rates from data file?
YES
Select file
NO
Subprogram "inrate.m"
Load Data
Data Matrices [R],[u],[v]
Data Matrices [R],[u],[v]
cont.

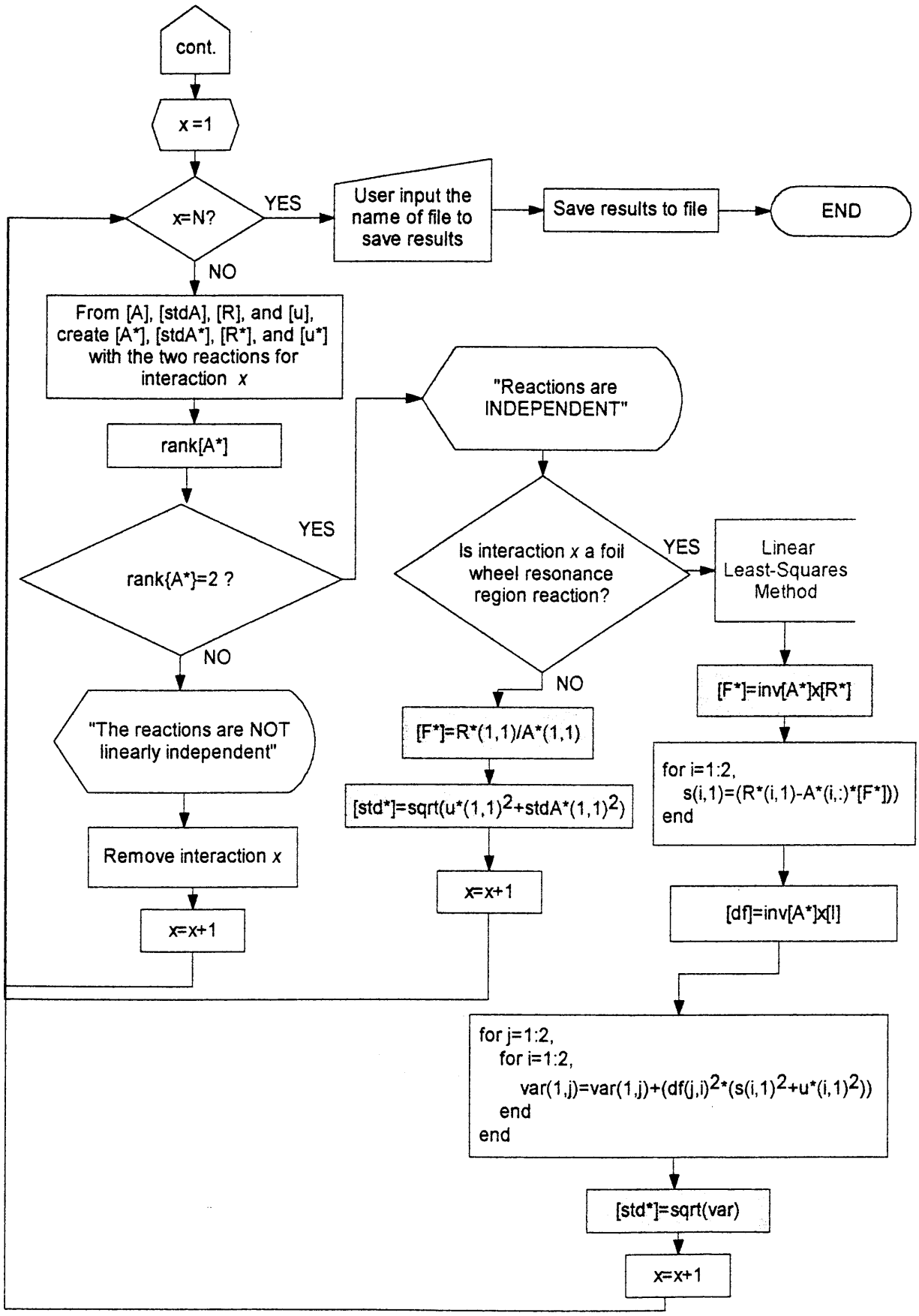
cont.
x =1
x=N?
YES
NO
User input the name of file to save results
Save results to file
END
From [A], [stdA], [R], and [u], create [A*], [stdA*], [R*], and [u*] with the two reactions for interaction x
rank[A*]
rank{A*}=2 ?
YES
NO
"The reactions are NOT linearly independent"
Remove interaction x
x=x+1
"Reactions are INDEPENDENT"
Is interaction x a foil wheel resonance region reaction?
YES
NO
Linear Least-Squares Method
[F*]=R*(1,1)/A*(1,1)
[std*]=sqrt(u*(1,1)^2+stdA*(1,1)^2)
x=x+1
[F*]=inv[A*]x[R*]
for i=1:2,
s(i,1)=(R*(i,1)-A*(i,:)*[F*])
end
[df]=inv[A*]x[I]
for j=1:2,
for i=1:2,
var(1,j)=var(1,j)+(df(j,i)^2*(s(i,1)^2+u*(i,1)^2))
end
end
[std*]=sqrt(var)
x=x+1

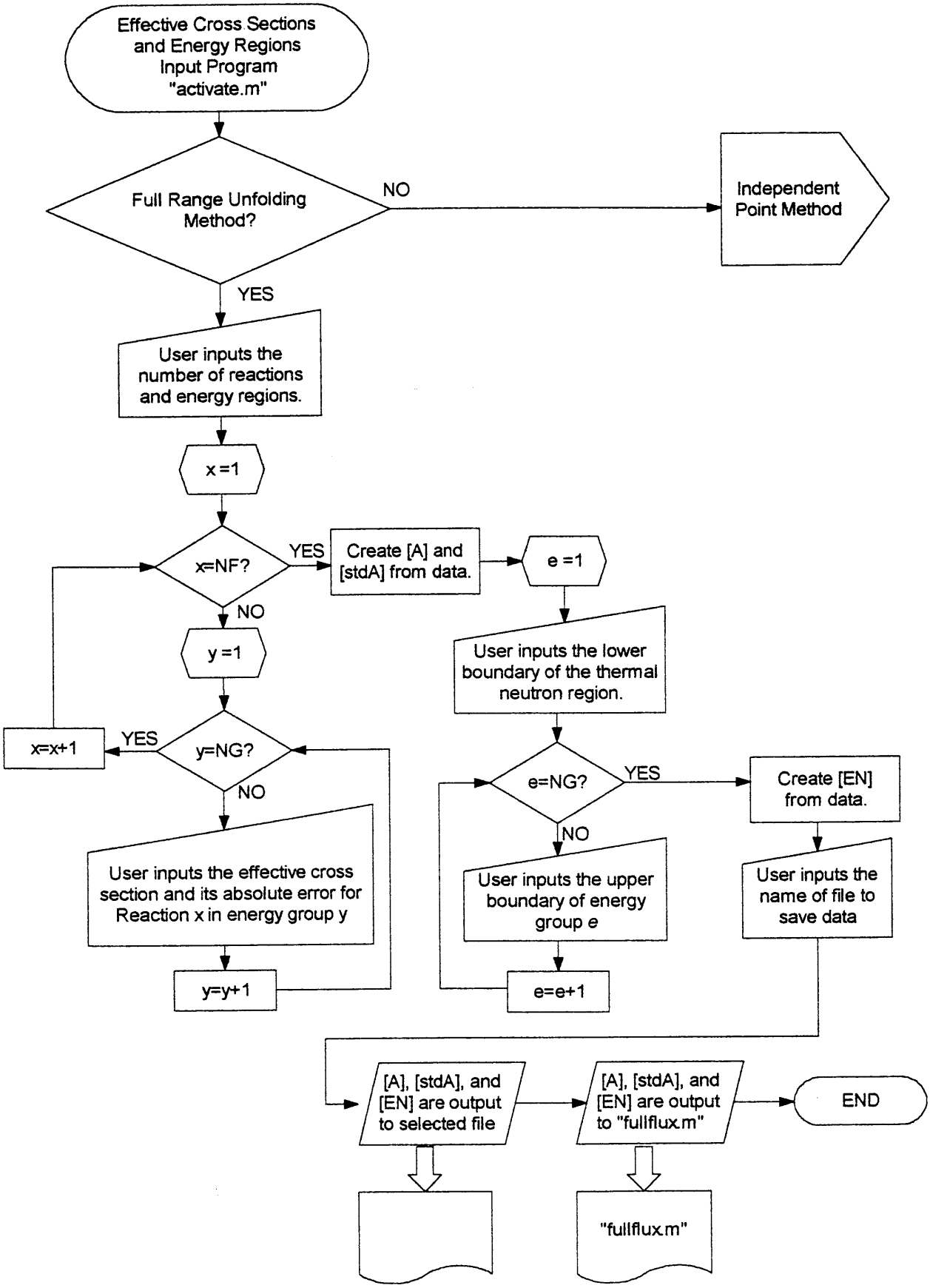
Effective Cross Sections and Energy Regions Input Program "activate.m"
Full Range Unfolding Method?
NO
Independent Point Method
YES
User inputs the number of reactions and energy regions.
x =1
x=NF?
YES
Create [A] and [stdA] from data.
e =1
NO
y =1
User inputs the lower boundary of the thermal neutron region.
x=x+1
YES
y=NG?
NO
e=NG?
YES
Create [EN] from data.
NO
User inputs the effective cross section and its absolute error for Reaction x in energy group y
User inputs the upper boundary of energy group e
User inputs the name of file to save data
y=y+1
e=e+1
[A], [stdA], and [EN] are output to selected file
[A], [stdA], and [EN] are output to "fullflux.m"
END
"fullflux.m"

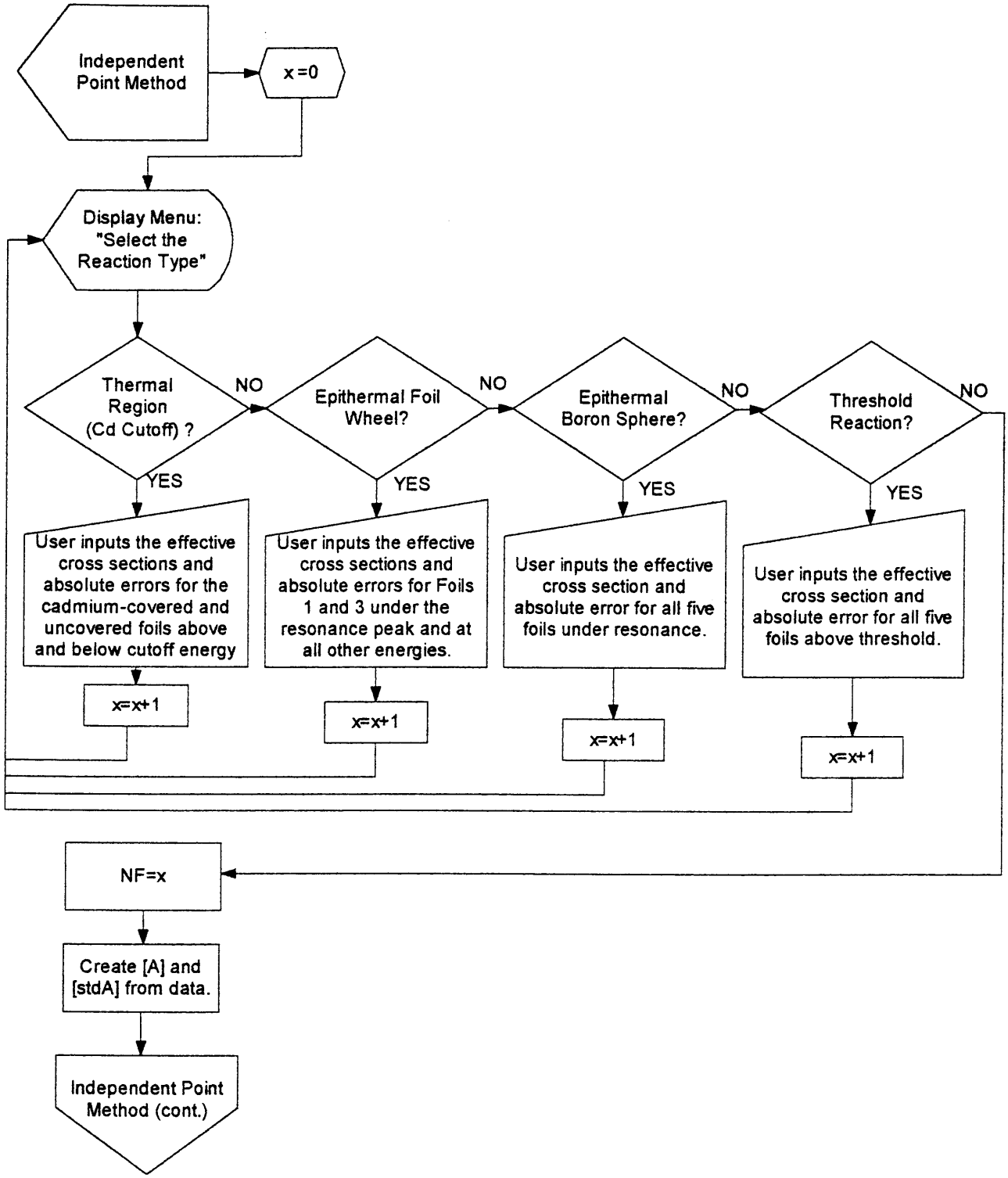
Independent Point Method
x=0
Display Menu: "Select the Reaction Type"
Thermal Region (Cd Cutoff) ?
NO
Epithermal Foil Wheel?
NO
Epithermal Boron Sphere?
NO
Threshold Reaction?
NO
YES
YES
YES
YES
User inputs the effective cross sections and absolute errors for the cadmium-covered and uncovered foils above and below cutoff energy
User inputs the effective cross sections and absolute errors for Foils 1 and 3 under the resonance peak and at all other energies.
User inputs the effective cross section and absolute error for all five foils under resonance.
User inputs the effective cross section and absolute error for all five foils above threshold.
x=x+1
x=x+1
x=x+1
x=x+1
NF=x
Create [A] and [stdA] from data.
Independent Point Method (cont.)

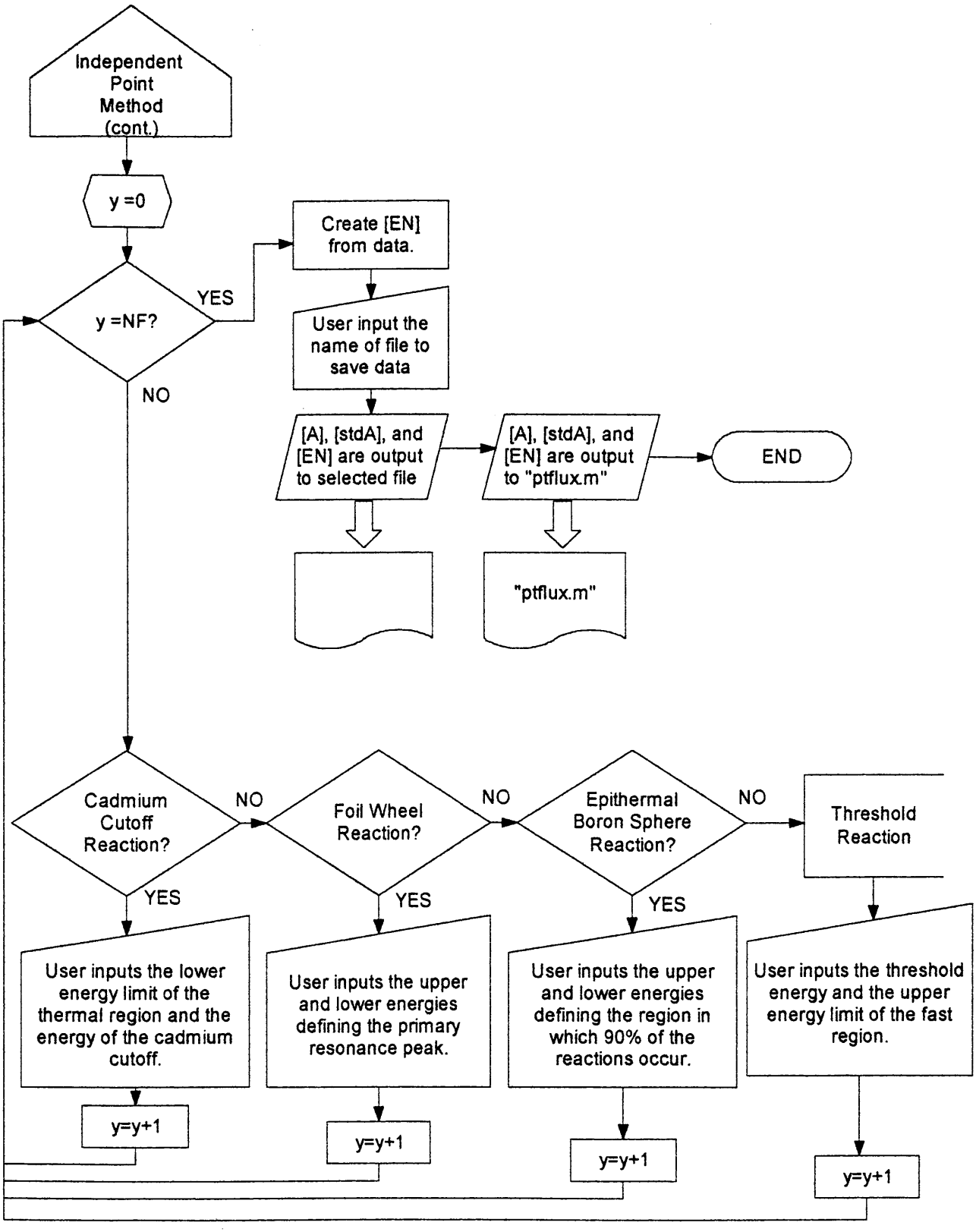
Independent Point Method (cont.)
y =0
y =NF?
YES
NO
Create [EN] from data.
User input the name of file to save data
[A], [stdA], and [EN] are output to selected file
[A], [stdA], and [EN] are output to "ptflux.m"
END
"ptflux.m"
Cadmium Cutoff Reaction?
NO
Foil Wheel Reaction?
NO
Epithermal Boron Sphere Reaction?
NO
Threshold Reaction
YES
YES
YES
User inputs the lower energy limit of the thermal region and the energy of the cadmium cutoff.
User inputs the upper and lower energies defining the primary resonance peak.
User inputs the upper and lower energies defining the region in which 90% of the reactions occur.
User inputs the threshold energy and the upper energy limit of the fast region.
y=y+1
y=y+1
y=y+1
y=y+1

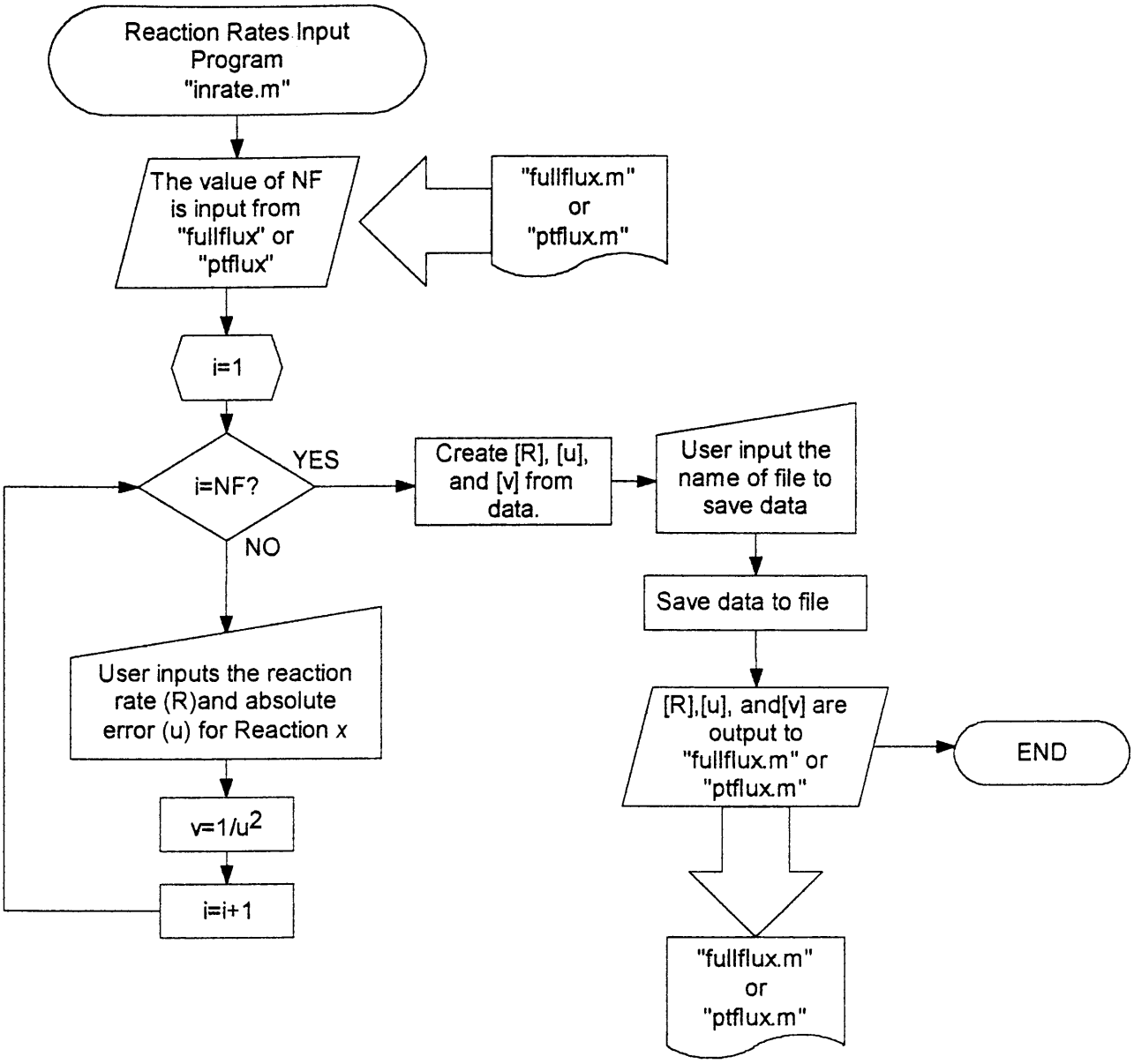
Reaction Rates Input Program "inrate.m"
The value of NF is input from "fullflux" or "ptflux"
"fullflux.m" or "ptflux.m"
i=1
i=NF?
YES
NO
Create [R], [u], and [v] from data.
User input the name of file to save data
Save data to file
User inputs the reaction rate (R)and absolute error (u) for Reaction x
v=1/u2
i=i+1
[R],[u], and[v] are output to "fullflux.m" or "ptflux.m"
END
"fullflux.m" or "ptflux.m"

References

Beckurts, K. H., and Wirtz K. *Neutron Physics.* New York, Springer-Verlag ,1964.

Blackburn, B. W. "Characterization of a High-Current Tandem Accelerator and Associated Development of a Water-Cooled Beryllium Target for the Production of Intense Neutron Beams." M.S. Thesis, Department of Nuclear Engineering, Massachusetts Institute of Technology, Cambridge, MA, Jan. 1997.

Blackburn, B.W., Yanch, J.C., and Klinkowstein, R. E. "Development of a High-power water-cooled beryllium target for use in accelerator-based boron neutron capture therapy." *Med. Phys.,* 25:1967-1974, 1998.

Binello, E., Shefer, R. E., and Yanch, J. C. " Neutron Beam Design for Boron Neutron Capture Synovectomy." in *Advances in Neutron Capture Therapy, Volume Ii, Chemistry and Biology*, Larsson B., Crawford, J. Weinrich, R., Eds., pp. 459-463. Proceedings of the Seventh International Symposium on Neutron Capture Therapy for Cancer. Amsterdam, Elsevier Science, 1997.

Binello, E., Shortkroff, S., Jones, A., Viveiros, C., Ly, A., Sledge, C. B., Davison, A., Shefer, R. E., and Yanch, J. C. "Research in Boron Neutron Capture Synovectomy." in *International Conference: Neutrons in Research and Industry*, George Vourvopouls, Ed., pp. 68-71, Proceedings from the SPIE 2867, 1997.

Binello, E., Shortkroff, S., and Yanch, J. C. "The PGNAA of Human Arthritic Synovium for Boron Neutron Capture Synovectomy." *Transactions of the American Nuclear Society,* TANSAO 77:548-549, 1997.

Binello, E., Yanch, J. C., Shortkroff, S., Viveiros, C., Young, G., Jones, A., Sledge, C. B., and Davison, A. "In Vitro Analysis of ^{10}B Uptake for Boron Neutron Capture Synovectomy." in *Advances in Neutron Capture Therapy, Volume Ii, Chemistry and Biology*, Larsson B., Crawford, J. Weinrich, R., Eds., pp. 609-613. Proceedings of the Seventh International Symposium on Neutron Capture Therapy for Cancer. Amsterdam, Elsevier Science, 1997.

Briesmeister, J. F. *MCNP – A General Monte Carlo N-Particle Transport Code, Version 4B*, Los Alamos, NM, Los Alamos National Laboratory, 1997.

Burrill, E. A. *Neutron Production and Protection.* Burlington, MA., High Voltage Engineering Corporation, 1964.

Busse, P.M., Zamenhof, R., Madoc-Jones, H., Solares, G., Kiger, S., Riley, K., Chuang, C., Rogers, G., and Harling, O. "Clinical follow-up of patients with melanoma of the extremity treated in the phase I boron neutron capture therapy protocol." in *Advances in Neutron Capture Therapy, Volume I, Medicine and Physics*, Larsson B., Crawford, J. Weinrich, R., Eds., pp. 60-64. Proceedings of the Seventh

International Symposium on Neutron Capture Therapy for Cancer. Amsterdam, Elsevier Science, 1997.

Canberra, *Canberra Nuclear Instruments Catalog*, 9th ed., Meridian, Connecticut, 1998.

Capala, J., Chadha, M., Coderre, J. A., Diaz, A. Z., Liu H. B., Wheeler, F. J., Wessol, D. E., Wielopolski, L., and Chanana, A. D. 'Radiation doses to brain under BNCT protocols at Brookhaven National Laboratory." in *Advances in Neutron Capture Therapy, Volume I, Medicine and Physics*, Larsson B., Crawford, J. Weinrich, R., Eds., pp. 51-55. Proceedings of the Seventh International Symposium on Neutron Capture Therapy for Cancer. Amsterdam, Elsevier Science, 1997.

Deckart, H., Tamaschke, J., Ertl, S., Tautz, M. and Knap, G. "Radiosynovectomy of the knee-joint with ^{198}Au colloid, ^{90}Y-ferric hydrate colloid, and ^{186}Re-sulphide colloid." *Radiobiol. Radiother.* 2:363-370, 1979.

Gierga, D. P., Yanch, J. C., Shefer, R. E., and Blackburn, B. "Construction of an accelerator based neutron beamline for treatment of arthritic joints." submitted for publication in *Frontiers in Neutron Capture Therapy*, Hawthorne, M. F., Shelly, K., and Wiersema, R. J., Eds., Proceedings of the Eighth International Symposium on Neutron Capture Therapy for Cancer, September 1998.

Gierga, D. P., Yanch, J. C., and Shefer, R. E. "Design of an neutron beamline for accelerator-based boron neutron capture synovectomy." submitted for publication in *Med. Phys.*, January 1999.

Gierga, D. P. Personal Communication, January 1999.

Gumpel, J. M., and Roles, N. C. "A controlled trial of intra-articular radiocolloids versus surgical synovectomy in persistent synovitis." *Lancet* 1:448-489, 1975.

Grusell, E., Condé, H., Larsson, B., Rönnqvist, T., Sornsuntisook, O., Crawford, J., Reist, H., Dahl, B., Sjöstrand, N. G., and Russel, G. "The possible use of a spallation neutron source for neutron capture therapy with epithermal neutrons." in *Neutron Beam Design, Development and Performance for Neutron Capture Therapy*, Harling, O. K., Bernard, J. A., and Zamenhof, R. G., Eds., New York, Plenum Press, 1990.

Guzek, J. Ph.D. Thesis, University of Witwatersrand, Johannesburg, South Africa, in preparation, 1998.

Harker, Y. D., Anderl, R. A., Becker, G. K., and Miller, L. G. "Spectral Characterization of the Epithermal Neutron Beam at the Brookhaven Medical Research Reactor." *Nucl. Sci. Eng.* 110:355-368, 1992.

Howard, W. B. and Yanch, J. C. "Shielding Design and Dose Assessment for Accelerator-Based Neutron Capture Therapy." *Health Phys.* 68(5):723-730, 1995.

Howard, W. B., Grimes, S. M., Massey, T. N., Al-Quaraishi, S.I., Jacobs, D. K., Brient, C. E., and Yanch, J. C. "Measurement of the Thick Target ^{9}Be(p,n) Neutron Energy Spectra." submitted for publication in *Nucl. Sci. Eng.,* November 1997.

Inada T., Kawachi, K., and Hiramoto, T. "Neutrons from thick target beryllium (d,n) reactions at 1.0 MeV to 3.0 MeV." *J. Nucl. Sci. Tech.* 5:22-29, 1968.

Johnson, L. S. "Beta-particle Dosimetry in Radiation Synovectomy and Use of the ^{10}B(n,α) Nuclear Reaction to Examine the Pathology of Rheumatoid Arthritis." Ph.D. thesis, Massachusetts Institute of Technology, Cambridge, MA, May 1994.

Johnson, L. S., Yanch, J. C., Shortkroff, S., and Sledge, C. "Temporal and Spatial Distribution of Boron Uptake in Excised Human Synovium." in *Cancer Neutron Capture Therapy*, Y. Mishima, Ed., pp. 183-188. Proceedings of the Sixth International Symposium on Neutron Capture Therapy for Cancer. Kobe, Japan, Plenum Press, 1996.

Joel, D. D., Chadha, M., Chanana, A. D., Coderre, J. A., Elowitz, E. H., Gebbers, J-O., Liu, H. B., Micca, P. L., Nawrocky, M. M., Shady, M., and Slatkin, D. N. "Uptake of BPA into glioblastoma multiforme correlates with tumor cellularity." in *Advances in Neutron Capture Therapy, Volume Ii, Chemistry and Biology*, Larsson B., Crawford, J. Weinrich, R., Eds., pp. 225-228. Proceedings of the Seventh International Symposium on Neutron Capture Therapy for Cancer. Amsterdam, Elsevier Science, 1997.

Klinkowstein, R. E., Shefer, R. E., Yanch, J. C., Howard, W. B., Song, H., Binello, E., Blackburn, B. W., Daigle, J. L., Sears, S. M., Goldie, C. H., and Ledoux, R. J. "Operation of a high current tandem electrostatic accelerator for boron neutron capture therapy." in *Advances in Neutron Capture Therapy, Volume I, Medicine and Physics*, Larsson B., Crawford, J. Weinrich, R., Eds., pp. 522-527. Proceedings of the Seventh International Symposium on Neutron Capture Therapy for Cancer. Amsterdam, Elsevier Science, 1997.

Krane, K. S., *Introductory Nuclear Physics*, New York, John Wiley & Sons, Inc., 1988.

Knoll, G. F. *Radiation Detection and Measurement*, 2nd Ed. New York, John Wiley & Sons, Inc., 1989.

LANL Data Sheets. "T-2 Information Service" URL http://t2.lanl.gov, Los Alamos National Laboratory,1998.

Mathworks, Inc. *MATLAB, High Performance Numeric Computation and Visualization Software: Reference Guide*, Natick, Massachusetts, Mathworks, Inc.,1992.

Meadows, J. W. "The thick target Be(d,n) neutron spectra for neutron energies between 2.6 and 7.0 MeV." in *Argonne National Laboratory Nuclear Data and Measurement Series*, ANL/NDM-124, 1991.

Nigg, D. W., Harker, Y. D., Hartwell, J. K., Wemple, C. A., Seppälä, T., Serén, T., Kaita, K., and Auterin, I. "Collaborative Spectral Characterization of the Finnish Epithermal-Neutron Beam Facility for BNCT." in *INEEL BNCT Research Program Annual Report-1996*, INEEL/EXT-97-00319, 1997.

Nigg, D. W., Wemple, C. A., Hartwell, J. K., Harker, Y. D., Venhuizen, J. R., and Risler, R. "Validation of Neutron Production and Beam Line Modeling for the University of Washington Fast-Neutron Facility." in *INEEL BNCT Research Program Annual Report-1997*, INEEL/EXT-98-00327, 1998.

Nigg, D. W., and Harker, Y. D. "Method Used for Direct Unfolding of Neutron Spectra from Activation Data." in *INEEL BNCT Research Program Annual Report-1997*, INEEL/EXT-98-00327, 1998.

Nigg, D. W. Personal Communication, February 18, 1998.

Oka, M. "Radiation synovectomy of the rheumatoid knee with Yttrium 90." *Ann. Clin. Res.* 7:205-210, 1975.

Reactor Experiments, Inc. *Catalog 24*, Sunnyvale, California, 1990.

Shefer, R. E., Klinkowstein, R. E., Yanch, J. C., and Brownell, G. L. "A versatile, new accelerator design for epithermal neutron production for boron neutron capture therapy." in *Neutron Beam Design, Development and Performance for Neutron Capture Therapy*, Harling, O. K., Bernard, J. A., and Zamenhof, R. G., Eds., New York, Plenum Press, 1990.

Shefer, R. E., Klinkowstein, R. E., Yanch, J. C., and Brownell, G. L. "An epithermal neutron source for BNCT using a tandem cascade accelerator." in *Progress in Neutron Capture Therapy for Cancer*, Allen, B., Moore, D., and Harrington, B., Eds., pp. 119-122, Proceedings of the Fourth International Symposium on Boron Neutron Capture Therapy, New York, Plenum Press, 1991

Shefer, R. E., Klinkowstein, R. E., Yanch, J. C., and Howard, W. B. "Tandem electrostatic accelerators for BNCT." in *Proceeding of the 1st International Workshop on Accelerator-Based Neutron Sources for Boron Neutron Capture Therapy*, pp. 89-97. Jackson, WY, INEL CONF-940976, 1994.

Slatkin, D. N. "A History of Boron Neutron Capture Therapy of Brain Tumors. Postulation of a Brain Radiation Dose Toleration Limit." *Brain.* 114(4):1609-1629, 1991.

Song, H. "Accelerator-Based Neutron Brachytherapy" Ph.D. Thesis, Department of Physics, Massachusetts Institute of Technology, Cambridge, MA, September 1998.

Symposium on radioactive colloids in the treatment of arthritis. *Ann. Rheum. Dis.* 32:(Supplemental 6), 1973.

Taylor, J. R. *An Introduction to Error Analysis.* 2nd Ed. Sausalito, California, University Science Books, 1997.

Turner, J. E., *Atoms, Radiation, and Radiation Protection*, 2nd Ed. New York, John Wiley & Sons, Inc., 1995.

Van Riper, K. A. *SABRINA User's Guide: for SABRINA Version 3.54.* Los Alamos, NM, Los Alamos National Laboratory, 1993.

Wang, C. K., Blue, T. E., and Gahbauer, R. "A neutronic study of an accelerator-based neutron irradiation facility for boron neutron capture therapy." *Nucl. Tech.* 84:93-107, 1989.

Wang, C. K., Blue, T. E., and Blue, J. W. "An experimental study of the moderator assembly for a low-energy proton accelerator neutron irradiation facility of BNCT." in *Neutron Beam Design, Development and Performance for Neutron Capture Therapy*, Harling, O. K., Bernard, J. A., and Zamenhof, R. G., Eds., New York, Plenum Press, 1990.

White, S. "Beam Characterization for Accelerator-Based Boron Neutron Capture Therapy Using the ^{9}Be(d,n) Nuclear Reaction." M.S. Thesis, Department of Nuclear Engineering, Massachusetts Institute of Technology, Cambridge, MA, June 1998.

Whittlestone, S. "Neutron distributions from the deuteron bombardment of a thick beryllium target." *J. Phys. D. Appl. Phys.*, 10:1715-1723, 1977.

Yanch, J. C., Zhou, X-L, Shefer, R. E., Klinkowstein, R. E., and Brownell, G. L. "Design of an accelerator-based epithermal neutron beam for boron neutron capture therapy." in *Progress in Neutron Capture Therapy for Cancer*, Allen, B., Moore, D., and Harrington, B., Eds., pp. 107-112, Proceedings of the Fourth International Symposium on Boron Neutron Capture Therapy, New York, Plenum Press, 1991.

Yanch, J. C., Zhou, X-L, and Brownell, G. L. "A Monte-Carlo investigation of the dosimetric properties of monoenergetic neutron beams for neutron capture therapy. " *Rad. Res.* 126:1-20, 1991.

Yanch, J. C., Zhou, X-L, Shefer, R. E., and Klinkowstein, R. E. "Accelerator-based epithermal neutron beam design for neutron capture therapy." *Med. Phys.* 19(3):709-721, 1992.

Yanch, J. C., Shefer, R. E., Klinkowstein, R. E., Howard, W. B., Song, H., Blackburn, B., Binello, E. "Research in Boron Neutron Capture Therapy at MIT LABA." *AIP Conference Proceedings* 392(2):1281, 1997

Yanch, J.C., Shortkroff, S., Shefer, R. E., Johnson, S., Binello, E., Gierga, D., Jones, A. G., Young, G., Viveiros, C., Davison, A., and Sledge, C. "Boron Neutron Capture Synovectomy: Treatment of Rheumatoid Arthritis Based on the $^{10}Be(n,\alpha)^{7}Li$ Nuclear Reaction." Submitted for publication in *Med. Phys.*, November 1998.

Yue, G., Chen, J., Song, R., and Bao, S. "Measurements of neutron energy spectra from a thick beryllium target with incident proton energies from 3 to 4 MeV." in *Advances in Neutron Capture Therapy, Volume I, Medicine and Physics*, Larsson B., Crawford, J. Weinrich, R., Eds., pp. 505-510. Proceedings of the Seventh International Symposium on Neutron Capture Therapy for Cancer. Amsterdam, Elsevier Science, 1997.

Zamenhof, R. G., Murray, B. W., Brownell, G. L. Wellum, G. R., and Tolpin, E. I. "Boron Neutron Capture Therapy for the Treatment of Cerebral Gliomas. I: Theoretical Evaluation of the Efficacy of Various Neutron Beams." *Med. Phys.* 2:47-60, 1975.

Zamenhof, R. G., Solares, G. R., Kiger, W. S., Riley, K. J., Busse, P. M., Fischer E., Norregaard, T., and Harling, O. K. "Clinical Treatment Planning of Subjects Undergoing Boron Neutron Capture Therapy." in *Advances in Neutron Capture Therapy, Volume Ii, Chemistry and Biology*, Larsson B., Crawford, J. Weinrich, R., Eds., pp. 614-620. Proceedings of the Seventh International Symposium on Neutron Capture Therapy for Cancer. Amsterdam, Elsevier Science, 1997.

4156